Tweaking EMT and MDR Dynamics by Co-targeting Signaling Pathways in Triple Negative Breast Cancer

A Thesis

Submitted in Partial Fulfillment of the Requirements for the award of the degree of

DOCTOR OF PHILOSOPHY

by

Rajib Shome

(Roll No. - 166106002)

Department of Biosciences and Bioengineering

Indian Institute of Technology Guwahati

Guwahati, 781039, Assam, India

December 2021

Dedicated to My Family

Declaration

I, hereby, declare that the research embodied in this thesis entitled "**Tweaking EMT and MDR Dynamics by Co-targeting Signaling Pathways in Triple Negative Breast Cancer"** is the result of investigations carried out by me under the supervision of Prof. Siddhartha Sankar Ghosh, Department of Biosciences and Bioengineeing, Indian Institute of Technology Guwahati, India for the award of Degree of Doctor of Philosophy. This work has not been submitted elsewhere for any degree, diploma, etc. of any Institute or University to the best of my knowledge and belief.

Rajib Shome

Date: 20.12.2021 **Rajib Shome**

Place: Guwahati Roll No. 166106002

Indian Institute of Technology Guwahati

Department of Biosciences and Bioengineering

Certificate

This is to certify that the thesis entitled "**Tweaking EMT and MDR Dynamics by Co-targeting Signaling Pathways in Triple Negative Breast Cancer"** being submitted to the **Indian Institute of Technology Guwahati** by **Rajib Shome** (Roll No. **166106002)** for the award of the degree of **Doctor of Philosophy** in Department of Biosciences and Bioengineering, is a bonafide record of research work carried out by him. The contents of this thesis have not been submitted to any other University or Institute for the award of any degree or diploma.

Date: 20.12.2021
Place: Guwahati

Prof. Siddhartha Sankar Ghosh
(Thesis Supervisor)

Dr. Siddhartha Sankar Ghosh
Professor
Department of Biosciences and Bioengineering
Indian Institute of Technology Guwahati
Guwahati-781039, Assam, India

Acknowledgment

I want to use this opportunity to express my heartfelt gratitude to everyone who have played a pivotal role in helping me reach this destination and supported me throughout my journey. First of all, I would like to thank my Ph.D. supervisor Professor Siddhartha Sankar Ghosh, for giving me this wonderful opportunity to work in his lab and taking care of all the facilities to carry out my research. It was for his constant support and guidance that has helped me to stay motivated throughout the tenure of Ph.D. and helped me to nurture myself in every aspect of life. I am thankful to him for providing me enough support and for believing in my capabilities. I whole heartedly thank sir for being the inspiration I will always look forward to in my life.

I also want to thank my doctoral committee members for evaluating my work time and again, and for giving constructive ideas throughout this tenure, which have helped me improve and understand my research work better. I am highly indebted to the Department of Biosciences and Bioengineering, Centre for Nanotechnology, Central instrumentation Facility, IIT Guwahati and DBT Program Support Facility for providing the support and assistance required out carry out my thesis work. I am also thankful to the faculty, staff and others members of the Department of BSBE and Centre for Nanotechnology.

I sincerely appreciate all my senior and junior lab members for their love and support. I am thankful to them for providing an amicable work environment. I would also like to thank all the members under the DBT program support facility.

I am also thankful to my parents for providing me the love, care and support, without which I would not have been in this position. Even in the most difficult situations, they have always supported me to choose the career I wished. It was indeed an experience of a lifetime, a lovely and pleasant stay at this splendid campus of IIT Guwahati. Moreover, I will always remain indebted to the Almighty God for being the guiding light at all times.

Rajib Shome.

Rajib Shome

Table of Contents

Abstract

Triple-negative breast cancer (TNBC), the most aggressive subtype of breast cancer, which lacks effective targeted therapies due to lack of expression of the targetable bioreceptors. On account of this, patients with metastatic TNBC (mTNBC) exhibits poor clinical outcome with a median overall survival (OS) of approximately 13–16 months. Additionally, hypoxic condition in solid tumors contributes to the epithelial to mesenchymal transition (EMT), which aggravates cancer progression, multidrug resistance (MDR), migration, and stemness of TNBC. There is a strong correlation between various drug efflux mechanisms, cancer stem cells and tumor microenvironments, which in turn is synchronized by complex signaling crosstalk between EMT and MDR. It is hypothesized that combining these regulatory connections with targeted combinatorial therapies may be a practical approach to annihilate the progression/metastasis of TNBC.

The current thesis work focuses on exploring cancer signaling pathways and targeting significant vulnerabilities to alter EMT and MDR dynamics in TNBC. **Section 1** comprises the **Introduction and Review of Literature**, which describes in detail the complex molecular signaling process that leads to metastasis, cancer progression, and relapse. In this section, basic biology and molecular aspects of EMT have been described. Furthermore, the role of aberrant induction of EMT in metastasis, cancer stemness, and MDR has been elucidated. The panorama of prominent cancer signaling pathways contributing to EMT and MDR has been consolidated. The objectives of the thesis have been fabricated to alter EMT and MDR dynamics by exploiting these signaling pathways. Finally, the salient features of this thesis have been delineated. **Section 2** comprises a thorough explanation of the **Materials and Methods** used for the experiments in the current thesis. This section also encompasses the details of the protocols, along with the induction of EMT and modifications to develop hypoxic conditions. **Section 3** describes **Results and Discussions**. In this section, firstly an attempt was persuaded to alter EMT and MDR dynamics in TNBC by co-targeting EGFR and Wnt/β-catenin signaling.

Given the strong implication of EGFR and Wnt/β-catenin signaling in the molecular pathogenesis of TNBC through EMT and MDR, it was hypothesized that an effective combination of inhibitors, one directed against EGFR (lapatinib) and the other directed against TNSK1 (XAV939), maybe a strategy to accomplish profound therapeutic effects in TNBC. Hence, the effect of the inhibitor combination was explored on TNBC

cells by analyzing molecular changes in EMT markers in both monolayer cultures and multicellular tumor spheroids, which mimic *in vivo* conditions. The expression levels of genes contributing to EMT and MDR were found to be significantly reduced. The invasive nature and migratory potential of the TNBC cells were also found to be downregulated by several-folds.

In the subsequent endeavor, second approach was to alter EMT and MDR dynamics in TNBC by co-targeting Wnt/β-catenin and SQSTM1 signaling. SQSTM1 is a multifunctional stress-inducible scaffold protein involved in diverse cellular processes. Besides, SQSTM1 acts as a substrate and regulator of autophagy, and oxidative detoxifying protein promoter, and a modulator of genomic integrity and mitotic transfer. It is also known to induce and stabilize prominent EMT factors, thereby facilitating cancer dissemination. It was reported that EMT-related signal pathways significantly influence autophagy; conversely, autophagy activation can suppress or strengthen EMT by regulating various signaling pathways. However, SQSTM1 is critically involved at the interface of autophagy and EMT; all crucial events in the control of cell growth and cancer. Therefore, an effective combination therapy module was devised to target Wnt/β-catenin signaling (FH535) and SQSTM1 (siRNA), simultaneously. The effect of an inhibitor (FH535) with combination of siRNA against SQSTM1 was investigated in TNBC cells to explore molecular alterations of EMT and MDR markers. Following combination therapy, cytotoxicity tests on TNBC cells revealed a significant dose-dependent reduction in cell viability and a synergistic interaction between inhibitors. The migration and invasion assay revealed downregulations of the metastatic property.

In the final part of the thesis, a nontherapeutic approach was implemented with FDA-approved drugs and biocompatible nanocarrier in the quest for successful targeted therapy. In this work, a novel therapeutic module has been fabricated by coating a non-toxic, biodegradable PLGA nanoparticle core with D-penicillamine templated Au-Cu bimetallic nanoclusters. Further, the resultant nanomaterials were coated with recombinant transferrin protein to specifically target transferrin receptor overexpressing cancer cells. The present work is the first attempt to alter EMT and MDR dynamics in TNBC by application of novel nanocomposites. Application of the nanocomposites incurred the phase transition from EMT to MET (mesenchymal to epithelial transition). The nanocomposites successfully downregulated the expression of ABC transporters ABCB1 and ABCC1 responsible for multidrug resistance (MDR). Regulation of EMT and MDR adroitly inhibited the migration capacity of TNBC cell line MDA-MB-231 and MDA-MB-468. The detailed molecular changes in downstream signaling have been delineated. Nonetheless, the current findings highlight the

potential of incapacitating EMT and MDR by nanocomposites for better efficacy in TNBC.

Conclusion and Future Prospects in **Section 4** summarizes the key findings of this current thesis. In pursuit of effective therapy, multiple critical signaling pathways underlying EMT were targeted which resulted in reversal of EMT, MDR and stemness of TNBC cells. Overall, the obtained results emphasize a potential combined application of crucial pathways inhibitors in the targeted therapy of TNBC.

List of Abbreviations and Acronyms

ABC Transporter	ATP-Binding Cassette Transporters
APC	Adenomatous Polyposis Coli
ATP	Adenosine Triphosphate
APS	Ammonium Persulfate
BCA	Bicinchoninic acid
bHLH	Basic Helix Loop Helix
BSA	Bovine Serum Albumin
CCCP	Carbonyl Cyanide 3-Chlorophenylhydrazone
CD	Circular Dichroism
CDK-4	Cyclin Dependent Kinase-4
CSC	Cancer Stem Cell
CPTAC	Clinical Proteomic Tumor Analysis Consortium
CTCF	Corrected Total Cell Fluorescence
Da	Dalton
DAPI	4′,6-diamidino-2-phenylindole
DCFDA	Dichlorodihydrofluorescein Diacetate
DLS	Dynamic Light Scattering
DMEM	Dulbecco's Modified Eagle's Medium
DMSO	Dimethyl Sulfoxide
EDTA	Ethylenediaminetetraacetic Acid
EDX	Energy Dispersive X-Ray

EGF	Epidermal Growth Factor
EGFR	Epidermal Growth Factor Receptor
EMT	Epithelial to Mesnchymal Transition
ER	Estrogen Receptor
ERK 2	Extracellular Signal-Regulated Kinases
FBS	Fetal Bovine Serum
FDA	Food and Drug Administration
FESEM	Field Emission Scanning Electron Microscopy
FITC	Fluorescein Isothiocyanate
FTIR	Fourier Transform Infrared
GAPDH	Glyceraldehyde 3-phosphate dehydrogenase
GEPIA	Gene Expression Profiling Interactive Analysis
GSK-3β	Glycogen synthase kinase 3 beta
GTEx	Genotype-Tissue Expression
h	Hour
HER-2	Human Epidermal Growth Factor Receptor 2
HCl	Hydro Chloric acid
H_2O_2	Hydrogen Peroxide
IC	Inhibitory Concentration
JC-1	Tetraethyl-benzimidazolylcarbocyanine Iodide
LC-3	Microtubule-associated protein 1A/1B-light chain 3
LEF	Lymphoid Enhancer Factor
MCF	Michigan Cancer Foundation
MDR	Multi Drug Resistance
MET	Mesenchymal to Epithelial Transistion
NCCS	National Centre for Cell Science

NF-κB	Nuclear factor kappa-light-chain-enhancer of activated B
OD	Optical Density
PBS	Phosphate Buffer Saline
PBST	Phosphate Buffer Saline with 0.1% Tween
PCR	Polymerase Chain Reaction
PE	Phycoerythrin
P-GP	P-glycoprotein
PI	Propidium Iodide
PLGA	poly(lactic-co-glycolic acid)
PMSF	Phenylmethanesulfonyl fluoride
PR	Progesterone Receptor
PVA	Poly(vinyl alcohol)
PVDF	Polyvinylidene Difluoride
RIPA	Radioimmunoprecipitation Assay Buffer
RNA	Ribonucleic Acid
ROS	Reactive Oxygen Species
rpm	Revolutions Per Minute
SAED	Selected Area Electron Diffraction
SDS PAGE	Sodium Dodecyl Sulphate Polyacrylamide Gel Electrophoresis
SEM	Standard Error of the Mean
siRNA	Small Interfering RNA
STAT	Signal Transducer and Activator of Transcription
TACE	TNF α Converting Enzyme
TBS	Tris Buffer Saline
TCGA	The Cancer Genome Atlas

TEM	Transmission Electron Microscopy
TEMED	Tetramethylethylenediamine
TGF-β	Transforming growth factor beta
TMB	3,3′,5,5′-Tetramethylbenzidine
TNBC	Triple Negative Breast Cancer
Tris	Trizma Base

List of Schemes

List of Figures

XAV939, 6 μM lapatinib + XAV939 and erlotinib, respectively. (e) Combination index and (f) dose-response curves obtained following combination treatment. Drug combinations with CIs < 1.0 were considered as synergistic. Results expressed as the mean ± SEM are based on at least three independent experiments. The statistical significance was assessed versus that of the untreated cells. The significance level was set at $p < 0.05$ (*), $p < 0.01$ (**), $p < 0.001$ (***) or $p < 0.0001$ (****)

Figure 3.1.4 Determination of viability of MDA-MB-468 spheroids by alamarBlue assay upon treatment with inhibitors for 72 h. (a), (b), (c) and (d) refer to treatment with lapatinib, XAV939, 6 μM lapatinib + XAV939 and erlotinib, respectively. (e) Combination index and (f) dose-response curves obtained following combination treatment. Drug combinations with CIs < 1.0 were considered as synergistic. Results expressed as the mean ± SEM are based on at least three independent experiments. The statistical significance was assessed versus that of the untreated cells. The significance level was set at $p < 0.05$ (*), $p < 0.01$ (**), $p < 0.001$ (***) or $p < 0.0001$ (****).

Figure 3.1.5 Determination of viability of MCF-7 monolayer cultures by alamarBlue assay upon treatment with inhibitors for 48 h. (a), (b), (c) and (d) refer to treatment with lapatinib, XAV939, 6 μM lapatinib + XAV939 and erlotinib, respectively. (e) Combination index and (f) dose-response curves obtained following combination treatment. Drug combinations with CIs < 1.0 were considered as synergistic. Results expressed as the mean ± SEM are based on at least three independent experiments. The statistical significance was assessed versus

that of the untreated cells. The significance level was set at $p < 0.05$ (*), $p < 0.01$ (**), $p < 0.001$ (***) or $p < 0.0001$ (****).

Figure 3.1.6 Determination of viability of MCF-7 spheroids by alamarBlue assay upon treatment with inhibitors for 72 h. (a), (b), (c) and (d) refer to treatment with lapatinib, XAV939, 30 μM lapatinib + XAV939 and erlotinib, respectively. (e) Combination index and (f) dose-response curves obtained following combination treatment. Drug combinations with CIs < 1.0 were considered as synergistic. Results expressed as the mean ± SEM are based on at least three independent experiments. The statistical significance was assessed versus that of the untreated cells. The significance level was set at $p < 0.05$ (*), $p < 0.01$ (**), $p < 0.001$ (***) or $p < 0.0001$ (****).

Figure 3.1.7 Live-dead cell visualization of MDA-MB-231 spheroids using calcein-AM/propidium iodide (PI) dual staining. Green fluorescence by calcein-AM refers to live cells, whereas red fluorescence by PI refers to dead cells. (a) Untreated spheroids and (b), (c) and (d) spheroids treated for 72 h with 30 μM lapatinib, 25 μM XAV939 and 30 μM lapatinib + 25 μM XAV939, respectively. Scale bar: 250 μM.

Figure 3.1.8 Z-stack projections of MDA-MB-231 spheroids.

Figure 3.1.9 Graphical representation of the percent normalized corrected total cell fluorescence (CTCF) values obtained from quantification of live/dead cell imaging of MDA-MB-231 spheroids as presented in Figure. 3.1.7.

Figure 3.1.10 Live-dead cell visualization of MCF-7 spheroids using calcein-AM/ propidium iodide (PI) dual staining by Z-stack projection.

Green fluorescence by calcein-AM refers to live cell whereas red fluorescence by PI refers to dead cell population. (a) Untreated spheroids, (b) spheroids treated for 72 h with 30 μM lapatinib + 25 μM XAV939. (c) 3D-cross section image of treated MCF-7 spheroids representing the dead cells inside the core and live cells on the periphery.

Figure 3.1.11 Graphical representation of the percent normalized corrected total cell fluorescence (CTCF) values obtained from quantification of live/dead cell imaging of MCF-7 spheroids as presented in Figure. 3.1.10.

Figure 3.1.12 Visualization of the effect of inhibitors and their combination on MDA-MB-231 spheroids using phase-contrast microscopy. Combination treatment results in visible disintegration of spheroids. Scale bar represents 250 μM.

Figure 3.1.13 Evaluation of cell cycle profile of MDA-MB-231 (a) monolayer cultures and (b) spheroids. A G0/G1 phase cell cycle arrest was observed in both monolayer culture and spheroids following treatment.

Figure 3.1.14 Graphical representation of changes in gene expression levels of MDA-MB-231 monolayer cultures following treatment with Lapatinib and XAV939 for 48 h quantified by qRT-PCR analysis. (a) represents the gene expression level of Cyclin-D1 and (b) represents the gene expression level of CDK-4. Results are expressed as mean relative gene expression level compared to (GAPDH) ± SEM of three independent experiments, with $p < 0.05$ (*), $p < 0.01$ (**), $p < 0.001$ (***), $p < 0.0001$ (****).

Figure 3.1.24 Graphical representation of changes in gene expression levels obtained from MDA-MB-231 monolayer cultures following inhibitor treatment quantified by qRT-PCR analysis.

Figure 3.1.25 Representative Western blots showing E-cadherin, N-cadherin and Vimentin levels in cellular extracts of MDA-MB-231 monolayer cultures. For monolayer cultures, cells were treated with inhibitors for 48 h, where the concentration of lapatinib is 6 μM and of XAV939 is 50 μM. β-actin serves as a loading control. Graphs represent the changes in the expression levels of E-cadherin, N-cadherin and Vimentin with respect to untreated samples following inhibitor treatment. The expression levels were deduced from the blots using ImageJ software.

Figure 3.1.26 Graphical representation of changes in gene expression levels obtained from MDA-MB-231 monolayer cultures following inhibitor treatment quantified by qRT-PCR analysis.

Figure 3.1.27 Graphical representation of changes in gene expression levels obtained from MDA-MB-231 monolayer cultures following inhibitor treatment quantified by qRT-PCR analysis.

Figure 3.1.28 Graphical representation of changes in gene expression levels obtained from MDA-MB-231 spheroids following inhibitor treatment quantified by qRT-PCR analysis.

Figure 3.1.29 Graphical representation of changes in gene expression levels obtained from MDA-MB-231 spheroids following inhibitor treatment quantified by qRT-PCR analysis.

Figure 3.1.30 Graphical representation of changes in gene expression levels obtained from MDA-MB-231 spheroids following inhibitor treatment quantified by qRT-PCR analysis.

Figure 3.1.31 Representative Western blots showing Vimentin levels in cellular extracts of MDA-MB-231 spheroids. Spheroids were treated using 30 μM lapatinib and 25 μM XAV939 for 72 h. β-actin serves as a loading control. Graphs represent the changes in the expression level Vimentin with respect to untreated samples following inhibitor treatment. The expression levels were deduced from the blots using ImageJ software.

Figure 3.1.32 Representative Western blots showing (a) E-cadherin and (b) N-cadherin levels in cellular extracts of MDA-MB-468 monolayer cultures. β-actin serves as a loading control. (c) The histogram of immunofluorescence flowcytometry detecting Vimentin of MDA-MB-468 monolayer cultures. Graphs represent the changes in the expression levels of E-cadherin, N-cadherin and Vimentin with respect to untreated samples following inhibitor treatment. The expression levels were deduced from the blots using ImageJ software.

Figure 3.1.33 Representative Western blots showing (a) E-cadherin and (b) N-cadherin and Vimentin levels in cellular extracts of MCF-7 monolayer cultures. β-actin serves as a loading control. Graphs represent the changes in the expression levels of E-cadherin, N-cadherin and Vimentin with respect to untreated samples following inhibitor treatment. The expression levels were deduced from the blots using ImageJ software.

Figure 3.1.34 Graphical representation of changes in gene expression levels obtained from MDA-MB-231 monolayer culture following inhibitor treatment quantified by qRT-PCR analysis.

Figure 3.1.35 Graphical representation of changes in gene expression levels obtained from MDA-MB-231 spheroids following inhibitor treatment quantified by qRT-PCR analysis.

Figure 3.1.36 (a) Scratch wound-healing assays of MDA-MB-231 monolayer cultures. (b) Graphical representation of changes in wound healing capacity following inhibitor treatment and their combination with respect to untreated samples.

Figure 3.1.37 (a) Boyden-chamber invasion assays of MDA-MB-231 monolayer cultures. (b) Graphical representation of changes in invasiveness following inhibitor treatment and their combination with respect to untreated samples.

Figure 3.1.38 Graphical representation of changes in gene expression levels obtained from MDA-MB-231 monolayer culture following inhibitor treatment quantified by qRT-PCR analysis.

Figure 3.1.39 Graphical representation of changes in gene expression levels obtained from MDA-MB-231 spheroids following inhibitor treatment quantified by qRT-PCR analysis.

Figure 3.1.40 Western blots showing EGFR/pEGFR, AKT/pAKT, MAPK/pMAPK, STAT-3/pSTAT-3, β-catenin/GSK-3β/pGSK-3β and β-actin levels in MDA-MB-231 cell extracts of monolayer cultures. For monolayer cultures, cells were treated with inhibitors for 48 h, where the concentration of lapatinib is 6 μM and of XAV939 is 50 μM. β-actin serves as a loading

control. Graphs represent the changes in the expression levels of pEGFR, pAKT, pMAPK, pSTAT-3 and pGSK-3β with respect to untreated samples following inhibitor treatment. The expression levels were deduced from the blots using ImageJ software.

Figure 3.1.41 Western blots showing EGFR/pEGFR, AKT/pAKT, MAPK/pMAPK, STAT-3/pSTAT-3, β-catenin/GSK-3β/pGSK-3β and β-actin levels in MDA-MB-231 cell extracts of spheroids. Spheroids were treated using 30 μM lapatinib and 25 μM XAV939 for 72 h. β-actin serves as a loading control. Graphs represent the changes in the expression levels of pEGFR, pAKT, pMAPK, pSTAT-3 and pGSK-3β with respect to untreated samples following inhibitor treatment. The expression levels were deduced from the blots using ImageJ software.

Figure 3.1.42 Confocal images of MDA-MB-231 monolayer cultures immune-stained with (a) anti-EGFR antibody visualized by Alexa Flour-488. Nuclei were stained with DAPI. Upper row refers to untreated samples and lower row refers to samples treated with lapatinib + XAV939 (6 μM LAP + 50 μM XAV) for 48 h. Scale bar, 20 μM.

Figure 3.1.43 Confocal images of MDA-MB-231 monolayer cultures immune-stained with (a) anti-AKT antibody visualized by Alexa Flour-488. Nuclei were stained with DAPI. Upper row refers to untreated samples and lower row refers to samples treated with lapatinib + XAV939 (6 μM LAP + 50 μM XAV) for 48 h. Scale bar, 20 μM.

by Alexa Flour-488. Nuclei were stained with DAPI. Scale bar represents 20 μM.

Figure 3.2.10 Confocal images of MDA-MB-468 monolayer cultures immune-stained with anti-SQSTM1/P62 antibody visualized by Alexa Flour-488. Actin cytoskeleton were stained with Alexa Flour-555 conjugated phalloidin. Nuclei were stained with DAPI. Scale bar represents 20 μM.

Figure 3.2.11 Confocal images of MDA-MB-231 monolayer cultures immune-stained with anti-β-Catenin antibody visualized by Alexa Flour-488. Actin cytoskeleton were stained with Alexa Flour-555 conjugated phalloidin. Nuclei were stained with DAPI. Scale bar represents 20 μM.

Figure 3.2.12 Confocal images of MDA-MB-468 monolayer cultures immune-stained with anti-β-Catenin antibody visualized by Alexa Flour-488. Actin cytoskeleton were stained with Alexa Flour-555 conjugated phalloidin. Nuclei were stained with DAPI. Scale bar represents 20 μM.

Figure 3.2.13 Graphical representation of changes in gene expression levels in MDA-MB-231 following treatment with inhibitor/siRNA, quantified by qRT-PCR analysis. Results are expressed as mean relative gene expression level compared to β-actin ± SEM of three independent experiments, with $p < 0.05$ (*), $p < 0.01$ (**), $p < 0.001$ (***) or $p < 0.0001$ (****).

Figure 3.2.14 Graphical representation of changes in gene expression levels in MDA-MB-468 following treatment with inhibitor/siRNA, quantified by qRT-PCR analysis. Results are expressed as mean relative gene expression level compared to β-actin ± SEM

of three independent experiments, with $p < 0.05$ (*), $p < 0.01$ (**), $p < 0.001$ (***) or $p < 0.0001$ (****).

Figure 3.2.21 Graphical representation of changes in gene expression levels in MDA-MB-231 following treatment with inhibitor/siRNA, quantified by qRT-PCR analysis. Results are expressed as mean relative gene expression level compared to β-actin ± SEM of three independent experiments, with $p < 0.05$ (*), $p < 0.01$ (**), $p < 0.001$ (***) or $p < 0.0001$ (****).

Figure 3.2.22 Graphical representation of changes in gene expression levels in MDA-MB-231 following treatment with inhibitor/siRNA, quantified by qRT-PCR analysis. Results are expressed as mean relative gene expression level compared to β-actin ± SEM of three independent experiments, with $p < 0.05$ (*), $p < 0.01$ (**), $p < 0.001$ (***) or $p < 0.0001$ (****).

Figure 3.2.23 (a) Representative Western blots showing cMYC protein expression level in MDA-MB-231 cell extracts. β-actin serves as a loading control. (b) Graphs depicts the alteration in the expression levels of cMYC with respect to untreated samples following inhibitor/siRNA treatment. The expression levels were deduced from the blots using ImageJ software.

Figure 3.2.24 (a) Representative Western blots showing cMYC protein expression level in MDA-MB-468 cell extracts. β-actin serves as a loading control. (b) Graphs depicts the alteration in the expression levels of cMYC with respect to untreated samples following inhibitor/siRNA treatment. The expression levels were deduced from the blots using ImageJ software.

Figure 3.2.25 Flow cytometric analysis of CD44/CD24 cell surface markers of MDA-MB-231 cells following treatment with inhibitors/siRNA for a period of 48 h. Cells were stained with FITC conjugated anti-CD44 antibody and APC conjugated anti-CD24 antibody. The obtained data were analyzed using CytExpert software.

Figure 3.2.26 Flow cytometric analysis of CD44/CD24 cell surface markers of MDA-MB-468 cells following treatment with inhibitors/siRNA for a period of 48 h. Cells were stained with FITC conjugated anti-CD44 antibody and APC conjugated anti-CD24 antibody. The obtained data were analyzed using CytExpert software.

Figure 3.2.27 Graphical representation of changes in gene expression levels in MDA-MB-231 following treatment with inhibitor/siRNA, quantified by qRT-PCR analysis. Results are expressed as mean relative gene expression level compared to β-actin ± SEM of three independent experiments, with $p < 0.05$ (*), $p < 0.01$ (**), $p < 0.001$ (***) or $p < 0.0001$ (****).

Figure 3.2.28 Graphical representation of changes in gene expression levels in MDA-MB-231 following treatment with inhibitor/siRNA, quantified by qRT-PCR analysis. Results are expressed as mean relative gene expression level compared to β-actin ± SEM of three independent experiments, with $p < 0.05$ (*), $p < 0.01$ (**), $p < 0.001$ (***) or $p < 0.0001$ (****).

Figure 3.2.29 Graphical representation of changes in gene expression levels in MDA-MB-231 following treatment with inhibitor/siRNA, quantified by qRT-PCR analysis. Results are expressed as mean relative gene expression level compared to β-actin ± SEM

of three independent experiments, with $p < 0.05$ (*), $p < 0.01$ (**), $p < 0.001$ (***) or $p < 0.0001$ (****).

Figure 3.2.30 Graphical representation of changes in gene expression levels in MDA-MB-231 following treatment with inhibitor/siRNA, quantified by qRT-PCR analysis. Results are expressed as mean relative gene expression level compared to β-actin ± SEM of three independent experiments, with $p < 0.05$ (*), $p < 0.01$ (**), $p < 0.001$ (***) or $p < 0.0001$ (****).

Figure 3.2.31 Graphical representation of changes in gene expression levels in MDA-MB-231 following treatment with inhibitor/siRNA, quantified by qRT-PCR analysis. Results are expressed as mean relative gene expression level compared to β-actin ± SEM of three independent experiments, with $p < 0.05$ (*), $p < 0.01$ (**), $p < 0.001$ (***) or $p < 0.0001$ (****).

Figure 3.2.32 Graphical representation of changes in gene expression levels in MDA-MB-231 following treatment with inhibitor/siRNA, quantified by qRT-PCR analysis. Results are expressed as mean relative gene expression level compared to β-actin ± SEM of three independent experiments, with $p < 0.05$ (*), $p < 0.01$ (**), $p < 0.001$ (***) or $p < 0.0001$ (****).

Figure 3.2.33 (a) Representative Western blots showing E-Cadherin levels in MDA-MB-231 cell extracts. β-actin serves as a loading control. (b) Graphs depicts the alteration in the expression levels of E-Cadherin with respect to untreated samples following inhibitor/siRNA treatment. The expression levels were deduced from the blots using ImageJ software.

Figure 3.2.34 (a) Representative Western blots showing E-Cadherin levels in MDA-MB-468 cell extracts. β-actin serves as a loading control. (b) Graphs depicts the alteration in the expression levels of E-Cadherin with respect to untreated samples following inhibitor/siRNA treatment. The expression levels were deduced from the blots using ImageJ software.

Figure 3.2.35 The histogram of immunofluorescence flowcytometry detecting Vimentin of MDA-MB-231 monolayer cultures.

Figure 3.2.36 The histogram of immunofluorescence flowcytometry detecting Vimentin of MDA-MB-468 monolayer cultures.

Figure 3.2.37 Confocal images of MDA-MB-231 monolayer cultures immune-stained with anti-Vimentin antibody visualized by Alexa Flour-488. Actin cytoskeleton were stained with Alexa Flour-555 conjugated phalloidin. Nuclei were stained with DAPI. Scale bar represents 20 μM.

Figure 3.2.38 Confocal images of MDA-MB-468 monolayer cultures immune-stained with anti-Vimentin antibody visualized by Alexa Flour-488. Actin cytoskeleton were stained with Alexa Flour-555 conjugated phalloidin. Nuclei were stained with DAPI. Scale bar represents 20 μM.

Figure 3.2.39 (a) Representative Western blots showing Twist1, Zeb1 and Snail levels in MDA-MB-231 cell extracts. β-actin serves as a loading control. Graphs depicts the alteration in the expression levels of (b) Twist1, (c) Zeb-1 and (d) Snail with respect to untreated samples following inhibitor/siRNA treatment. The

expression levels were deduced from the blots using ImageJ software.

Figure 3.2.40 (a) Representative Western blots showing Twist1 and Snail levels in MDA-MB-468 cell extracts. β-actin serves as a loading control. Graphs depicts the alteration in the expression levels of (b) Twist1 and (c) Snail with respect to untreated samples following inhibitor/siRNA treatment. The expression levels were deduced from the blots using ImageJ software.

Figure 3.2.41 (a) Representative Western blots showing Snail levels in MDA-MB-231 spheroids cell extracts. β-actin serves as a loading control. (b) Graphs depicts the alteration in the expression levels of Snail with respect to untreated samples following inhibitor/siRNA treatment. The expression levels were deduced from the blots using ImageJ software.

Figure 3.2.42 (a) Representative Western blots showing E-cadherin and Twist-1 levels in MDA-MB-468 spheroids extracts. β-actin serves as a loading control. Graphs depicts the alteration in the expression levels of (b) E-cadherin and (c) Twist-1 with respect to untreated samples following inhibitor/siRNA treatment. The expression levels were deduced from the blots using ImageJ software.

Figure 3.2.43 (a) Scratch wound-healing assays of MDA-MB-231 monolayer cultures. (b) Graphical representation of changes in wound healing capacity following inhibitor/siRNA treatment and their combination with respect to untreated samples.

Figure 3.2.44 (a) Scratch wound-healing assays of MDA-MB-468 monolayer cultures. (b) Graphical representation of changes in wound

Results expressed as the mean ± SEM are based on at least three independent experiments.

Figure 3.2.50 (a) Determination of viability of MDA-MB-231 monolayer cultures by alamarBlue assay upon treatment with increasing concentration of FH535 and 10 nM siRNA. (b) Table representing the obtained IC_{50} values. Results expressed as the mean ± SEM are based on at least three independent experiments.

Figure 3.2.51 (a) Combination index and (b) dose-response curves obtained following combination treatment with FH535 and siRNA in MDA-MB-231 monolayer culture.

Figure 3.2.52 Determination of viability of MDA-MB-468 monolayer cultures by alamarBlue assay upon treatment with inhibitor/siRNA for 48 h. (a) and (b) represents treatment with increasing concentration of FH535 and siRNA, respectively. Results expressed as the mean ± SEM are based on at least three independent experiments.

Figure 3.2.53 (a) Determination of viability of MDA-MB-468 monolayer cultures by alamarBlue assay upon treatment with increasing concentration of FH535 and 10 nM siRNA. (b) Table representing the obtained IC_{50} values. Results expressed as the mean ± SEM are based on at least three independent experiments.

Figure 3.2.54 (a) Combination index and (b) dose-response curves obtained following combination treatment with FH535 and siRNA in MDA-MB-468 monolayer culture.

Figure 3.2.55 Determination of viability of MDA-MB-231 spheroids by alamarBlue assay upon treatment with inhibitor/siRNA for 48 h. (a) and (b) represents treatment with increasing concentration of FH535 and siRNA, respectively. Results expressed as the mean ± SEM are based on at least three independent experiments.

Figure 3.2.56 (a) Determination of viability of MDA-MB-231 spheroids by alamarBlue assay upon treatment with increasing concentration of FH535 and 10 nM siRNA. (b) Table representing the obtained IC_{50} values. Results expressed as the mean ± SEM are based on at least three independent experiments.

Figure 3.2.57 (a) Combination index and (b) dose-response curves obtained following combination treatment with FH535 and siRNA in MDA-MB-231 spheroids.

Figure 3.2.58 Determination of viability of MDA-MB-468 spheroids by alamarBlue assay upon treatment with inhibitor/siRNA for 48 h. (a) and (b) represents treatment with increasing concentration of FH535 and siRNA, respectively. Results expressed as the mean ± SEM are based on at least three independent experiments.

Figure 3.2.59 (a) Determination of viability of MDA-MB-468 spheroids by alamarBlue assay upon treatment with increasing concentration of FH535 and 10 nM siRNA. (b) Table representing the obtained IC_{50} values. Results expressed as the mean ± SEM are based on at least three independent experiments.

by Alexa Flour-488. Actin cytoskeleton were stained with Alexa Flour-555 conjugated phalloidin. Nuclei were stained with DAPI. Scale bar represents 20 μM.

Figure 3.2.80 Confocal images of MDA-MB-468 monolayer cultures immune-stained with anti-phospho AKT antibody visualized by Alexa Flour-488. Nuclei were stained with DAPI. Scale bar represents 20 μM.

Figure 3.2.81 (a) Representative Western blots showing phospho-STAT-3, STAT-3, phospho-MAPK and MAPK levels in MDA-MB-231 monolayer culture. β-actin serves as a loading control. Graphs depicts the alteration in the expression levels of (b) phospho-STAT-3 and (c) phosphor-MAPK with respect to untreated samples following inhibitor/siRNA treatment. The expression levels were deduced from the blots using ImageJ software.

Figure 3.2.82 (a) Representative Western blots showing phospho-STAT-3, STAT-3, phospho-MAPK and MAPK levels in MDA-MB-468 monolayer culture. β-actin serves as a loading control. Graphs depicts the alteration in the expression levels of (b) phospho-STAT-3 and (c) phosphor-MAPK with respect to untreated samples following inhibitor/siRNA treatment. The expression levels were deduced from the blots using ImageJ software.

Figure 3.2.83 Representative Western blots showing LC3-I and LC3-II levels in MDA-MB-231 monolayer culture following treatment of (a) 24 h and (b) 48 h. β-actin serves as a loading control. Graphs depicts the normalized ratio of LC3-II to LC3-I expression obtained following treatment period of (c) 24 h and (d) 48 h

Z-stack projections of live dead cell imaging of MDA-MB-231 monolayer culture.

Figure 3.3.42 (a) Live-dead cell visualization of MDA-MB-468 monolayer culture using calcein-AM/propidium iodide (PI) dual staining. Green fluorescence by calcein-AM refers to live cells, whereas red fluorescence by PI refers to dead cells. Scale bar: 50 μm. (b) Z-stack projections of live dead cell imaging of MDA-MB-468 monolayer culture.

Figure 3.3.43 (a) Live-dead cell visualization of MCF-7 monolayer culture using calcein-AM/propidium iodide (PI) dual staining. Green fluorescence by calcein-AM refers to live cells, whereas red fluorescence by PI refers to dead cells. Scale bar: 50 μm. (b) Z-stack projections of live dead cell imaging of MCF-7 monolayer culture.

Figure 3.3.44 Imaging of Live and dead cell population. Live cells are denoted by green fluorescence, whereas dead cells are denoted by red fluorescence. MDA-MB-231 spheroids were treated for 72 h with nanocomposites. Scale bar represents 250 μM.

Figure 3.3.45 Imaging of Live and dead cell population. Live cells are denoted by green fluorescence, whereas dead cells are denoted by red fluorescence. MDA-MB-468 spheroids were treated for 72 h with nanocomposites. Scale bar represents 250 μM.

Figure 3.3.46 Imaging of Live and dead cell population. Live cells are denoted by green fluorescence, whereas dead cells are denoted by red fluorescence. MCF-7 spheroids were treated for 72 h with nanocomposites. Scale bar represents 250 μM.

relative gene expression standard compared to GAPDH ± SEM.

Figure 3.3.53 Alteration of gene expression in MDA-MB-468 following treatment with nanocomposites quantified by qRT-PCR. The results of three separate studies are represented as the mean relative gene expression standard compared to GAPDH ± SEM.

Figure 3.3.54 Alteration of gene expression in MDA-MB-231 following treatment with nanocomposites quantified by qRT-PCR. The results of three separate studies are represented as the mean relative gene expression standard compared to GAPDH ± SEM.

Figure 3.3.55 Alteration of gene expression in MDA-MB-468 following treatment with nanocomposites quantified by qRT-PCR. The results of three separate studies are represented as the mean relative gene expression standard compared to GAPDH ± SEM.

Figure 3.3.56 Alteration of gene expression in MDA-MB-231 following treatment with nanocomposites quantified by qRT-PCR. The results of three separate studies are represented as the mean relative gene expression standard compared to GAPDH ± SEM.

Figure 3.3.57 Alteration of gene expression in MDA-MB-468 following treatment with nanocomposites quantified by qRT-PCR. The results of three separate studies are represented as the mean

changes in the expression levels in (c) MDA-MB-231 and (d) MDA-MB-468.

List of Tables

Section 1

Introduction and Review of Literature

Introduction and Review of Literature

The spread of malignant cells from a primary tumor to distant areas, known as metastasis, is the most difficult aspect of cancer therapy and the leading cause of mortality in cancer patients. Jean Claude was the first to introduce the word "metastasis" as a hallmark of cancer in 1829. Metastasis in Greek means "displacement," with meta meaning "next" and stasis meaning "placement". It refers to the migration of malignant cells from the initial site of tumor to various places of the body that results in the production of additional tumors, which is the leading cause of cancer-related mortality [1]. Metastasis happens in a succession of separate phases known as a "metastatic cascade." The key molecular mechanism involved in the process of metastasis is epithelial to mesenchymal transition (EMT). EMT has been shown to have a pivotal role in cancer cell metastasis and treatment resistance in recent investigations [2]. EMT causes cells to lose cell-cell interactions and cell-extracellular matrix adhesion, resulting in the development of mesenchymal cell phenotypes. This in turn results in the formation of secondary tumors in the distant site of the body, thereby decreasing the life-expectancy of the patients.

1.1. Epithelial to Mesenchymal Transition: EMT is a complex molecular process by which epithelial cells lose their differentiated characteristics and instead gain mesenchymal features like increased motility, invasiveness and elevated resistance to apoptosis [3]. EMT plays a pivotal role in the morphogenesis of multicellular organisms, particularly during embryonic development and wound healing [4]. Inappropriate EMT induction may have, however, deleterious effects due to a compromised mechanical and physiological integrity of tissues, which in case of cancer may lead to metastasis. At the molecular level, cells undergoing EMT exhibit a decreased expression level of epithelial genes (i.e., E-cadherin, occludin,

ZO-1) and an increased expression level of mesenchymal genes (i.e., N-cadherin, vimentin, fibronectin) [5]. Loss of E-cadherin is considered to be a hallmark of EMT [6]. However, tumor cells exhibit multiple transitional states and express mixed epithelial and mesenchymal phenotype. These array of hybrid cells with partial EMT can move collectively as cluster, and are thought to be more aggressive than cells exhibiting complete EMT phenotype [7]. Mesenchymal-to-epithelial transition (MET) is the process of reversion of EMT and it is found to transform circulating cancer cells upon reaching a desirable metastatic niche to develop secondary tumors [8]. Research evidences suggests that the disruption of cell–cell adhesion and cellular polarity, remodeling of the cytoskeleton, and changes in cell–matrix adhesion are orchestrated by EMT, which helps in migration and invasion of cancer cells. Hypoxic condition in solid tumor, cytokines, growth factors released from tumor microenvironment, metabolic alteration, stroma crosstalk, innate and adaptive immune responses are known to induce EMT during cancer progression [9]. Moreover, the switch in gene expression from mesenchymal to epithelial phenotype is triggered by complex regulatory network. Transcriptional factors such as SNAI1 and SNAI2, ZEB1 and ZEB2, Twist1, and E12/E47 are also known to regulate the induction of EMT [10]. Additionally, non-coding RNAs (miRNAs and long non-coding RNAs), chromatin remodeling and epigenetic modifications, alternative splicing, post-translational regulation, protein stability, and subcellular localization are also involved in the process of EMT induction [11]. However, additional research into the involvement of EMT in metastasis, control, and reversal is required. Alternative ways of dispersion, colonization via a MET-independent pathway, and studies of circulating cancer cells in the blood, all support a more nuanced picture of EMT and MET's function in cancer metastasis. Although, EMT is a process associated with normal development, it is increasingly being recognized as one of the central mechanisms responsible for the induction of invasive and metastatic properties in solid tumors.

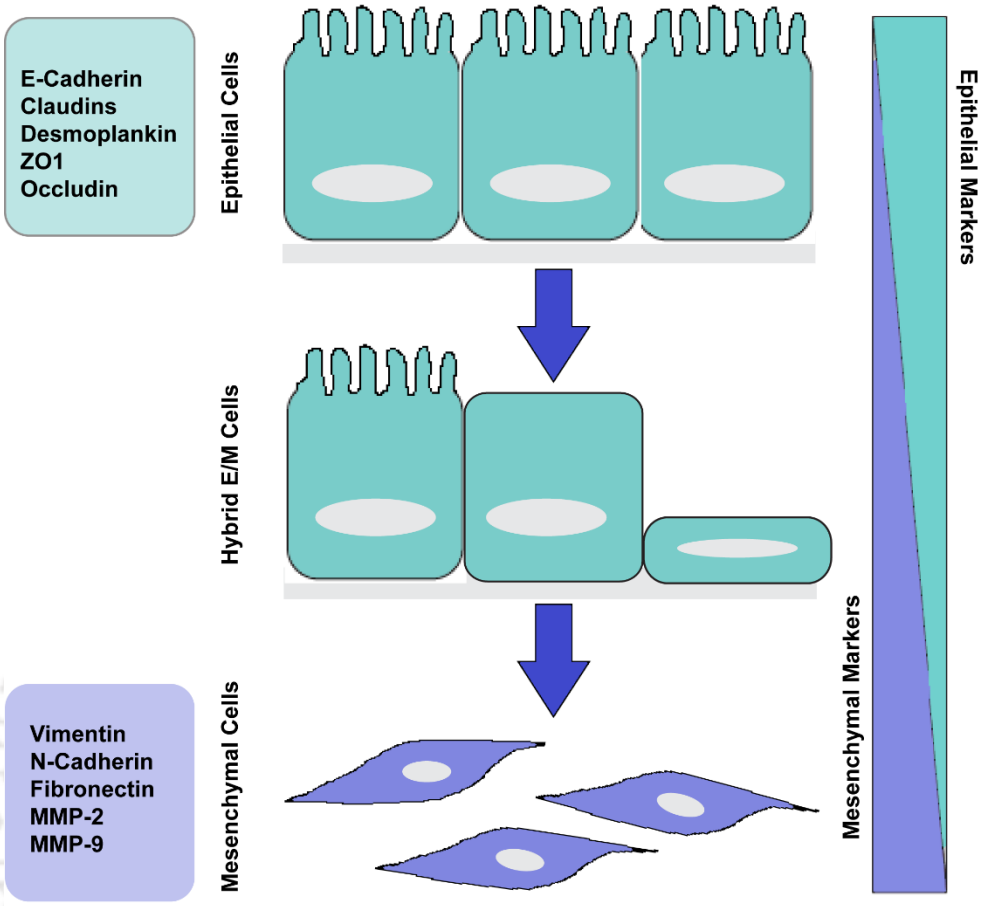

Scheme 1.1: The trajectory of differentiation change is pictorially graphed with epithelial cells on the top, hybrid E/M cells in the middle, and mesenchymal cells on the bottom hand of the arrow. The shift from epithelial to mesenchymal phenotype is marked by the loss of epithelial markers and the acquisition of mesenchymal markers (conceptualized and redrawn from Babaei *et al*. https://doi.org/10.1016/j.biopha.2020.110909).

1.2. EMT and Triple Negative Breast Cancer: Worldwide 2.3 million women were estimated to be diagnosed with breast cancer, which accounted in approximately 685 000 deaths in 2020. As of the end of 2020, 7.8 million women have been diagnosed with breast cancer in the previous five years, making it the most prevalent cancer in the world [12]. Out of all breast cancer cases, the triple negative

breast cancer (TNBC) is the most aggressive subtype, which represents 15 to 20% of all breast cancer. Typical characteristics of TNBC are the lack of expression of estrogen receptor (ER), progesterone receptor (PR), human epidermal growth factor receptor 2 (HER-2) [13]. Compared to other BC types, TNBC tumors are found to be aggressive, invasive, grade III, and lymph node-positive leading to high rate of morbidity and mortality [14]. As a group, patients with triple-negative tumors have a relatively poor outcome and cannot be treated with endocrine therapy or therapies targeted to HER-2. Analysis of epidemiological data reveals that TNBC is most common in premenopausal women under 40 years old, who account for roughly 15-20 percent of all breast cancer patients [15]. TNBC is highly aggressive, invasive and around 46% of TNBC patients are likely to develop distant metastasis. The prevalence of cells with mesenchymal features is one of TNBCs' well-known characteristics; where cells have undergone epithelial to mesenchymal transition (EMT). Following metastasis, the median survival time is only 13.3 months and recurrence rate after surgery is more than 25%. The mortality rate of TNBC patients within 3 months after recurrence is as high as 75% [16]. As TNBC is resistant to endocrine treatment or molecular targeted therapy, chemotherapy is the primary systemic treatment. However, post operational traditional adjuvant chemotherapy is found to be ineffective as the residual metastatic lesions eventually lead to tumor recurrence. TNBC is a diverse collection of malignancies; intrinsic subtype analysis revealed that around 80% of TNBC tumors are basal-like and claudin-deficient [17]. Similarly, the vast majority of TNBC cell lines have been classified as basal-like or mesenchymal-like. It is found that, EMT markers and $CD44^{High}$ /$CD24^{Low}$ expression are much greater in basal-like and mesenchymal-like TNBC subtypes, and are linked to poor prognosis [18]. As a result, targeting EMT for the development of new TNBC treatments is of tremendous interest.

1.3. EMT and Cancer Stem Cells: Cancer stem cells (CSCs) are defined by their ability to self-renew and possessing pluripotent properties [19]. These characteristics enable a small percentage of CSCs to produce multiple lineages of daughter cells, which then establish new cancers in primary or distant organs, resulting in tumor recurrence or metastasis. Because of the heterogeneity in the frequency and functionality of CSCs, their existence and roles have been questioned. CSCs can be detected using specific surface markers that differ between cancer types and even subgroups. During stress condition, CSCs divide into daughter progenitor cells, which operate as additional tumor-initiating cells, allowing the initial tumor cell population to remain heterogeneous or to initiate secondary metastases in a more suitable habitat [20]. There lies a strong co-relation between cancer stem cell and EMT as both plays a pivotal role in metastasis. Multiple evidence suggests that in addition to having a key role in metastasis, EMT is strongly linked to the activity of cancer stem cells. Recent reports revealed that EMT influences cancer cells to develop into cancer stem cells, which results in increased relapse, drug resistance, and metastasis in human malignancies [21]. Furthermore, inhibitors with the primary goal of inhibiting EMT also reduce stem cell-like features in addition to inhibiting EMT and metastasis. In addition, in breast cancer, EMT induction elevates the expression of stem cell gene profile like $CD44^{High}/CD24^{Low}$ [21]. Multiple pathways have been implicated in both the processes such as EGFR, Wnt/β-catenin, Hedgehog, Notch, and STAT3 [22]. Vijay et al. reported increased population of CSCs following induction of EMT in TNBC. They also discovered that inhibiting GSK3B, an EMT regulator, reduced the expression of mesenchymal cell markers and the $CD44^{High}/ CD24^{Low}$ cell population [23]. Transcription factors responsible for EMT plays a role in maintaining stem cells by inducing the expression of genes involving cancer stem cells. Traditional chemotherapy and radiation therapies are unsuccessful against CSCs since they are meant to target rapidly proliferating cells. The quiescent condition of CSCs,

limited population number, and dynamic CSC placement are the three obstacles of CSC targeting. CSCs' naturally quiescent nature permits them to evade therapy and stay in the host as a latent tumor cell reservoir [24]. The remaining CSCs can proliferate heterogeneous tumors over time, leading to tumor recurrence in patients [25]. Due to an increasing number of CSCs circulating in the system, studies have demonstrated that therapeutic reduction of tumors may result in an even more aggressive malignancy [26]. The CSC population generally makes up fewer than 5% of all cancer cells [27]. CSCs have been detected inside tumors, in tissues surrounding tumors (because to their extremely invasive nature), and in the vascular system [28]. CSCs are challenging to detect and target on account of their presence in multiple sites and small cell numbers. Furthermore, the status of the CSC is strongly influenced by signals from the surrounding microenvironment, which impact whether the CSC is self-renewing, differentiating, or regenerating from differentiated cells [29]. The latter occurrence, in particular, has been linked to treatment failures in many forms of human cancer [30]. Therefore, the development of successful CSC-targeted treatments will be aided by a better understanding of the bidirectional conversion between CSCs and differentiated cancer cells.

1.4. EMT and Multi Drug Resistance: Chemotherapy is one of the most successful cancer therapies; nevertheless, the development of multidrug resistance (MDR) has hampered its effectiveness. MDR is induced by long-term (dose- or time-dependent) chemotherapeutic drug treatment, resulting in cross-resistance to a wide range of structurally and mechanically diverse chemotherapeutic medicines [31]. MDR is caused by a number of mechanisms. (i) enhanced drug efflux via efflux pumps such P-glycoprotein (P-gp) encoded by ABCB1; (ii) reduced drug uptake via transporters; (iii) activation of drug-metabolizing enzymes including cytochrome P450 and glutathione S-transferase; (iv) activation of DNA repair

mechanisms; (v) apoptosis evasion [32]**.** Apart from metastasis, EMT is also known to regulate multidrug resistance (MDR). The link between EMT and MDR lies in a small population of cells known as cancer stem cells (CSCs), which are thought to be responsible for tumorigenesis [33]. CSCs confer MDR by excessive drug efflux conducted by multiple cell membrane transporter proteins, especially the ATP-binding cassette (ABC) transporter family of proteins [34]. The ABC genes are the biggest family of trans-membrane proteins, and they employ ATP hydrolysis energy to drive the transport of various substrates (drugs, drug metabolites, and endogenous metabolites) across biological membranes, which is essential for most aspects of cell life [35]. CSCs are also known to overexpress ABC transporters including ABCB1, ABCC1 and ABCG2. These transporters are known to have broad drug specificity and pump out diverse range of structurally and mechanically unrelated substances, lowering intracellular accumulation and as a result, decreasing biological efficacies [36]. Several clinically used chemotherapeutic agents, including microtubule-targeting taxanes (e.g., docetaxel and paclitaxel) and vinca alkaloids (vinblastine and vincristine), DNA-damaging anthracyclines (daunorubicin and doxorubicin), topoisomerase inhibitors (etoposide and topotecan), and tyrosine kinase inhibitors (dasatinib and gefitinib) are susceptible to ABC transporters [37]. As a result, developing techniques to target ABC transporters is a prerequisite in the treatment of cancer.

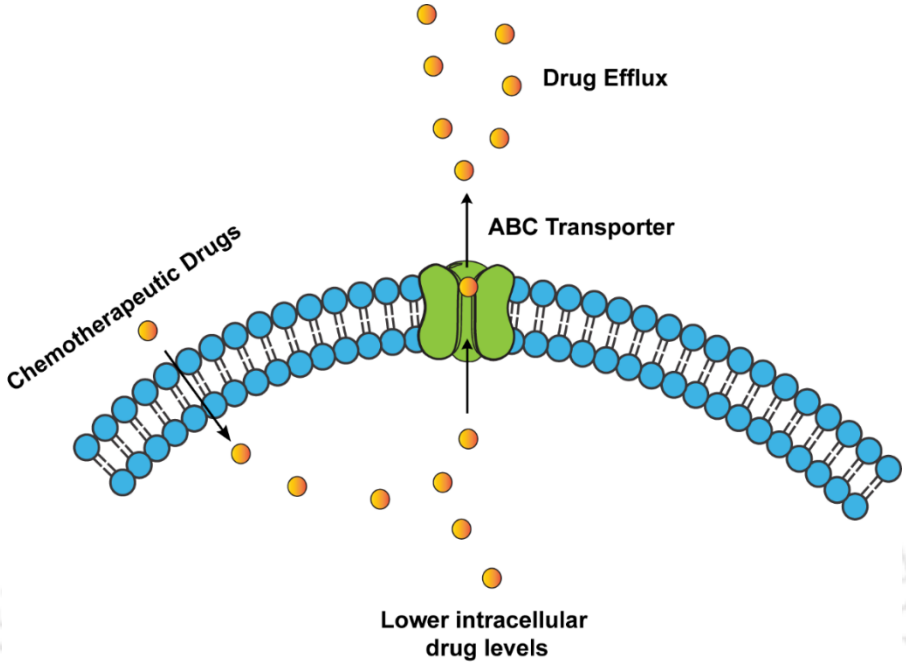

Scheme 1.2: Schematic representation of multi drug resistance in cancer cells contributed by ABC transporters.

1.5. EMT and Wnt Signaling Pathway: Numerous signaling pathways have been identified responsible for inducing and maintaining EMT and CSC characteristics. Among these signaling pathways, Wnt/β-catenin signaling has been reported to be a prominent contributor of EMT, stemness and CSC properties of TNBC [38]. The Wnt signaling pathway is important for differentiation, polarity, migration, invasion, adhesion, and survival during development [39]. These same cellular mechanisms are implicated in tumorigenesis and metastasis. Hence treatment methods to target Wnt pathway signaling components is highly warranted. Wnt signaling pathway dysregulation has been linked to a variety of malignancies, including those with a high prevalence and/or poor prognosis, such as colorectal, breast, ovarian, and prostate cancer [40]. Traditionally, this complex signaling

network has been divided into canonical (β-catenin dependent) and non-canonical (β-catenin independent) pathways. Binding of Wnt ligands to receptors generates a cascade of events leading to the disassembly of the Axin/APC/GSK3β destruction complex and the stabilization of β-catenin [41]. TCF/LEF-mediated activation of target genes involved in cell differentiation and proliferation occurs when β-catenin accumulates in the cytoplasm and is translocated to the nucleus. C-myc, CyclinD1, and Axin2 are all downstream targets of active canonical Wnt signaling [42]. With the cooperation of TCF/LEF, β-catenin binds to the promoter region of the target gene such as Snail and stimulates the transcription process [43]. Additionally, Snail can build a positive feedback loop with β-catenin by physically interacting with it, or indirectly increase the quantity of free β-catenin through the EMT process [44]. GSK-3β inactivation can boost Snail expression in two ways: first, it is phosphorylated by GSK-3β in the nucleus, and then it can be transported from the nucleus to the cytosol, where it can be phosphorylated by GSK-3β again before being degraded [45].

1.6. EMT and EGFR: Genetic and immunohistochemical analyses have shown that the epidermal growth factor receptor (EGFR) is frequently overexpressed in TNBC, often correlating with a poor prognosis [46]. Overexpression of the EGFR gene has been found in up to 78 percent of triple-negative breast tumors compared to non-triple-negative breast cancers, indicating that EGFR might be a therapeutic target for triple-negative breast cancer. It is well-known that anomalous activation of EGFR in cancer cells results in deregulated proliferation, EMT, invasion, metastasis and resistance to apoptosis. Intriguingly, EGFR inhibition has been shown to limit EMT and, as a result, cell migration and invasion abilities [47].

1.7. EMT and Autophagy: Autophagy is an evolutionary conserved biological process that targets cellular contents to the lysosomal compartment for degradation [48]. Through this mechanism cells turnover damaged organelles, pathogens and large protein aggregates to ensure of maintenance of cellular homeostasis [49]. This unique cellular degradation process serves as an important source of amino acids, nucleotides and fatty acids, particularly for cells unable to acquire sufficient nutrients from the extracellular milieu to sustain ATP production and biosynthesis [50]. Cells strategically activate autophagy to overcome intracellular or environmental stress, including hypoxia cellular ROS and drug effect [51]. However, autophagy plays a complex and highly context-dependent role in cancer progression, often termed as 'double-edged sword' effect [52]. The tumor-suppressive function of autophagy can be partly attributed to its ability to induce cell death via several mechanisms; however, a positive role in tumorigenesis and metastatic cascade has also been validated [53].

Although, it was perceived earlier that EMT and autophagy are too distant to associate, emerging evidence suggests the intricate relationship between these two critical processes of malignancy [54]. On one side, cells undergoing EMT exploits autophagy to acquire necessary resources and reduce cellular stress for survival during metastasis. On the other side, before the onset of EMT, autophagy acts as an onco-suppressive signal by selectively destabilizing crucial mediators of this metastatic process. Although sophisticated connectivity exists between EMT and autophagy, recent studies suggest SQSTM1 as the central regulator at the crossroad between EMT and autophagy [55].

1.8. EMT and SQSTM1: As SQSTM1 is enlisted at the crossroads of so many crucial cellular pathways, it is certain that dysregulation of SQSTM1 homeostasis is linked to multiple human diseases, including cancer [54]. Accumulation of

SQSTM1 is linked with an increase in pro-survival signal, EMT and cancer dissemination. A study by Li et al. reveals that SQSTM1 accumulation in epithelial cells is a necessary and sufficient condition to induce tumorigenesis and deterioration without other extra carcinogen stimuli [56]. Accumulation of SQSTM1 culminates into the stabilization of crucial oncogenic transcription factors, which leads to EMT [57]. EMT is a highly dynamic biological process that allows epithelial cells to transiently assume mesenchymal features by undergoing profound molecular and biochemical changes [58]. Although this process requires precise regulation of gene expression and initiation of specific signaling pathways, EMT is mainly regulated by the morphological reprogramming of cellular architecture, which is governed by alteration in the interaction attributes of the cells with the surrounding milieu and is supported by a profound restructuring of the cell cytoskeleton [59]. Amidst numerous signaling modulators, transcription factor Twist1 is a core regulator in both early embryonic morphogenesis and cancer development and metastasis [60]. It facilitates loss of E-Cadherin mediated cell-cell adhesion, facilitates EMT and promotes cell proliferation. Unlike other EMT factors such as Slug and Snail, it is structurally different and consists of basic helix–loop–helix (bHLH) protein. The findings by Qiang et al. provided evidence that SQSTM1 promotes EMT mainly by interacting with Twist1 protein. The group has demonstrated that SQSTM1 binds with Twist1 via its UBA domain and stabilizes it, which further increases cell proliferation and migration *in vitro* and *in vivo* [61]. One of the hallmarks of EMT is the functional loss of E-cadherin, a metastatic suppressor during tumor progression [24]. Transcription factor Snail is a prominent inducer of EMT and actively represses E-cadherin expression [62]. Bertrand and coworkers investigated the role of SQSTM1 in Snail regulation. They have found that robust Snail mRNA level was observed in SQSTM1 overexpressing MDCK and NBT-II cells concerning control cells following EMT induction by TGFβ. Also, treatment with SQSTM1 siRNA sharply decreased the

expression of Snail in the cells irrespective of TGFβ treatment [63]. These data indicate the modulation of transcription factor Snail by SQSTM1. TGFβ induced EMT is dependent on the Smad signaling pathway, which controls the activation of transcription factors. To elucidate the role of SQSTM1 in the activation of the Smad pathway, Bertrand et al. further investigated the expression of Smad4 during EMT. They observed that the overexpression of SQSTM1 stabilized Smad4 during TGFβ induced EMT. Whereas, treatment with SQSTM1 siRNA lowered the Smad4 expression irrespective of TGFβ treatment [63]. These findings suggest the role of SQSTM1 in stabilizing Smad4 during TGFβ induced EMT.

Additionally, the team provided evidence that SQSTM1 is accumulated during EMT, which leads to the downregulation of expression of the junctional proteins E-cadherin, occludin and claudin and up-regulation of N-cadherin expression. Studies by Li et al. demonstrated that SQSTM1 interacts with vimentin and enhances breast cancer metastasis [64]. SQSTM1 down-regulates the expression of these junctional proteins by increasing the expression of Snail. SQSTM1 regulates the transcription of Snail by acting on the Smad signaling pathway via its UBA domain. The interaction of SQSTM1 with Snail and Smad4 is dependent on the UBA domain and is not dependent on LIR domain [63]. Hence, suggesting the fact that SQSTM1 has a wide role in controlling the progression of EMT, thereby making it an attractive target for cancer therapy.

1.9. Crosstalk Between SQSTM1, Autophagy and EMT: Multiple crosstalks and feedback loops mediate the intricate interplay between autophagy and EMT. Numerous studies have demonstrated interactions between autophagy and EMT, although it does appear this is both context- and tissue-dependent [65]. SQSTM1 is one of the critical signaling modulator, responsible for maintaining the complicated relationship between them. SQSTM1 binds directly to LC3, resulting

in specific degradation by autophagy which makes SQSTM1 a valuable marker of autophagy and a key regulator of fundamental processes. SQSTM1 protein is rapidly and continuously degraded by autophagy and elevated SQSTM1 expression in the absence of significant changes in SQSTM1 mRNA is used as an indicator of autophagic impairment [66]. Thus, basal levels of autophagy are essential for normal tissue homeostasis. Selective degradation of the specific EMT proteins seems to be the primary molecular mechanism through which autophagy controls EMT. SQSTM1 fails to be customarily degraded by autophagy deficiency in the tumor, which causes the accumulation of SQSTM1. Elevated SQSTM1 expression corresponds to accumulation of degenerated protein aggregates, production of ROS, induction of endoplasmic reticulum (ER) stress and DNA damage. It was earlier discussed that SQSTM1, an autophagy adaptor protein, binds with EMT regulators to affect EMT progression. For example, SQSTM1 sustains a level of HDAC6 to promote EMT in prostate cancer cells [67]. SQSTM1 also interacts with TWIST1 to promote EMT by inhibiting its degradation [61]. Additionally, an elevated level of SQSTM1 by autophagic impairment leads to the stabilization of other EMT regulators such as SNAIL, TWIST, Smad4 and it has been shown to increase the transcriptional activity of NF-κβ to promote EMT by enhancing the nuclear translocation of p65 [57]. Mathew et al. showed that when cells with impairment in both apoptosis and autophagy are metabolically stressed, the accumulation of SQSTM1 leads to enhanced tumorigenicity through an as yet undefined mechanism involving increased aneuploidy. These observations place SQSTM1 as the 'missing link' between deficient autophagy and increased tumorigenesis through the control of genome instability [68]. Manipulation of autophagy and thus SQSTM1 has also been reported to prevent an EMT-like phenotype, halt the progression invasion and ultimately metastasis in a number of cancer cell lines and tissues, including breast, colorectal, pancreatic and ovarian cancers [69]. Although EMT doesn't regulate autophagy directly, several crucial

EMT related signaling pathways, including integrin, WNTs, NF-κβ, and TGF-β signaling pathways, play a crucial role in autophagy. Furthermore, increasing observations have pointed out that the interaction between cytoskeleton and mitochondria is also the critical regulatory mechanism in the process [70]. Complex web-like molecular connectivity exists in between autophagy and EMT, where SQSTM1 serves to fine-tune the balance between them.

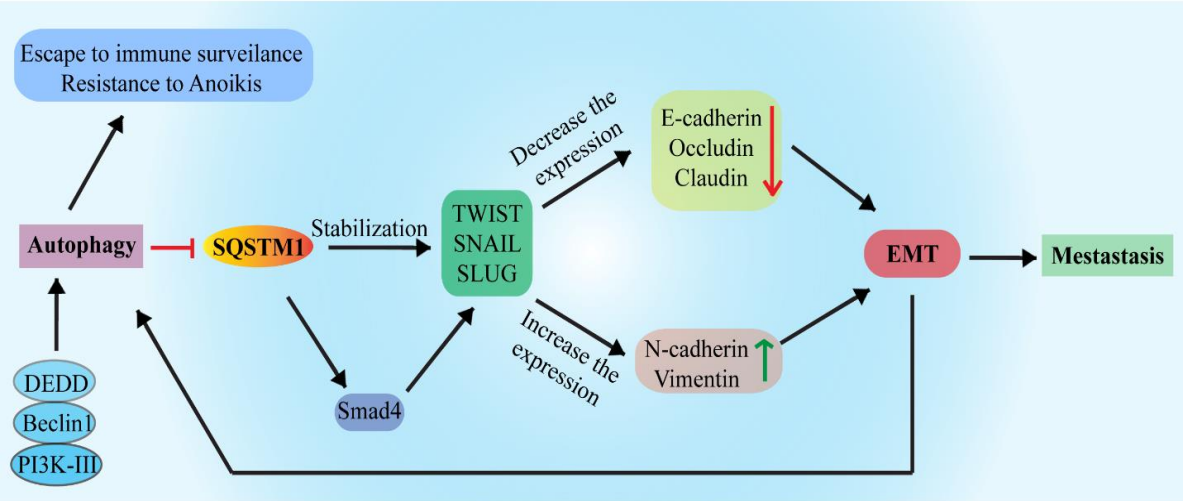

Scheme 1.3: Schematic representation of signaling pathways at the crossroad between autophagy and EMT. During cancer progression, TGFβ activates several pathways that facilitate EMT. SQSTM1 interact with crucial transcription factors responsible for EMT and further stabilizes them to prevent cellular degradation. SQSTM1 also helps Smad mediated upregulation of EMT transcription factors. Enhanced transcription factors concomitantly enhance the expression of mesenchymal markers N-cadherin, Vimentin and downregulate junctional proteins such as occludin, claudin, E-cadherin etc.

1.10. Nano-carrier Mediated Targeted Delivery of Drugs in TNBC: Since cancer cells divides and proliferate in accelerated rate, chemotherapeutic drugs are so built that it targets the rapidly dividing cancer cells. As a consequence, it also affects the healthy or non-cancerous cells that are growing faster. Henceforth,

along with the cancer cells, conventional cancer therapies also affect healthy cells, leaving behind undesired toxic side effect. This non-selective and non-targeted nature of chemotherapies could pose serious health issue. Besides, the development of the multi-drug resistance, some chemotherapeutic drugs have problems of poor stability, low water solubility and low efficiency. Therefore, to overcome these concerns, nano-based drug delivery system is being developed. Nanotechnology-based integrated nanomedicines have been documented to overcome the limitations of traditional treatment strategies and deliver the drugs successfully to the tumor sites [71]. The advantages of nanocomposites drug delivery system are improved loading capacity, specific targeted delivery, prolonged circulation time, bioavailability, and biocompatibility. In this regard, the use of biocompatible and biodegradable polymeric nanoparticles as drug delivery vehicles has attracted particular attention. Poly(d,l-lactic-co-glycolic acid) (PLGA) is one such FDA-approved polymer that has been widely investigated for various biomedical applications, particularly for cancer treatment. PLGA nanoparticles have distinguishing features such as sustained drug release ability, high encapsulation efficiency, stability, biodegradability, and biocompatibility [72]. To enable optical tracking and monitoring of the nanocarriers, fluorescent moieties may be attached to polymeric templates. The particles then discovered known as 'nanoclusters', which differ widely in physicochemical properties from their nanoparticle counterparts. Fluorescent NPs are evolving as a promising tool for theranostic purposes. Nanoclusters can be used to advance therapeutics by integrating multiple components into a single nanoplatform. A minimal number of atoms comprise the nanocluster, which typically measures less than 2 nm. Nanoclusters are considered over any fluorophores because they feature excellent photophysical properties [73]. In comparison to the single-metallic ones, bimetallic nanoclusters are often more beneficial in different ways, such as increased fluorescence and greater catalytic properties [74]. Although nanoclusters are

generally found to be nontoxic, some nanoclusters have been reported to exhibit cytotoxicity. The cytotoxic properties of nanoclusters can be observed due to their minute size, which aids in cellular ROS generation. During the process of nanocluster synthesis, several polymers are used as a template or stabilizer. D-penicillamine is one of such polymers used as a template for synthesizing metallic nanoclusters. D-penicillamine, a copper chelator, is an FDA-approved drug used to treat Wilson's disease, kidney stone, rheumatoid arthritis, and various heavy metal poisonings [75]. A combination of d-penicillamine and cupric sulfate produce dose-dependent reduction in cell viability in MCF-7 cells by producing hydrogen peroxide (H_2O_2) [76]. Therefore, using a suitable polymer with anticancer activity or polymer that is being converted to cytotoxic agent after being catalyzed by nanoclusters can be a novel strategy for cancer therapeutics. Furthermore, the selective targeting of the cancer cells could be accomplished by integrating distinct ligands in the carriers. Ligand-specific receptors specifically expressed or overexpressed in cancer cells help specifically bind the carrier, followed by its internalization. Transferrin, a plasma protein, is one of such promising ligands for selective targeting. It is essential for iron homeostasis and is extensively internalized in cancer cells due to increased iron needs during accelerated proliferation [77]. Transferrin receptors have a high affinity for diferric transferrin, and the resulting complex is internalized by receptor-mediated endocytosis [78]. As a result, using transferrin in a carrier could help with selective drug delivery in tumors.

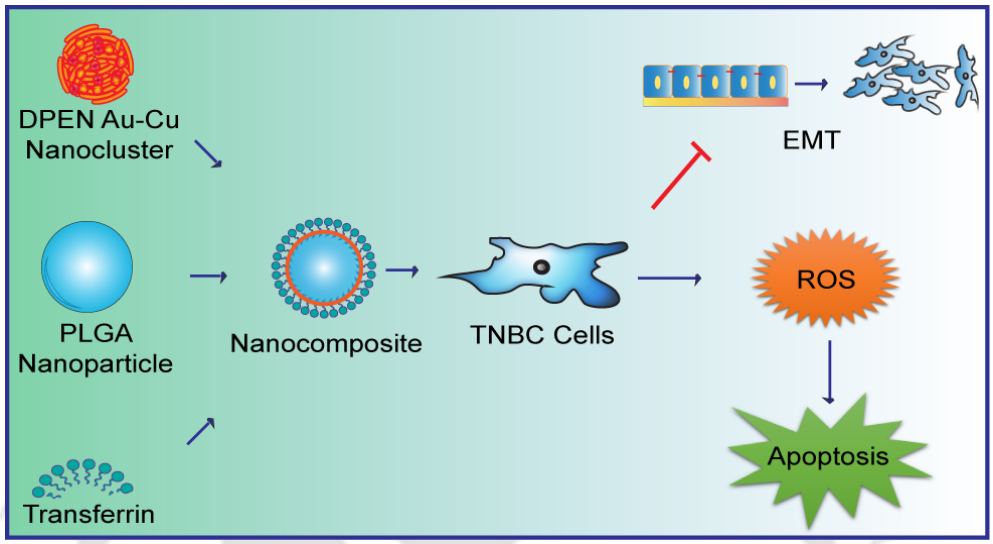

Scheme 1.4: Schematic representation of synthesis of nanocomposites to specifically target the TNBC cells and overall observable cellular events.

1.11. Key Features and Scope of Research: The fundamental understanding of molecular mechanism governing EMT and metastasis can offer substantial therapeutic leverage to effectively target the signaling pathways and achieve complete remission. The present research investigation is based on the following scopes as potential research areas.

- Identification of key molecular pathways regulating EMT and MDR characteristics in TNBC.
- Exploring the role of EGFR pathway in regulating EMT and MDR dynamics of TNBC.
- Exploring the role of Wnt/β-catenin pathway in promoting EMT and further metastasis in TNBC.

- Co-targeting pathways to inhibit EMT and MDR dynamics of TNBC.
- Understanding the role of autophagy adaptor protein in regulating EMT and metastasis.
- Identification of co-relation between Wnt signaling and adaptor protein SQSTM1/P62.
- Repurposing of FDA approved drugs for TNBC therapy.
- Nanocarrier mediated targeted delivery of drugs specifically targeting TNBC cells.

1.12. Objectives of the Current Thesis:

- Targeting signaling pathways to alter EMT and MDR dynamics of TNBC.
- Exploiting the interplay between EMT and autophagy to restrain metastatic TNBC.
- Targeting TNBC by nanocarrier mediated targeted delivery of novel drugs.

1.13. Salient Outcome of the Thesis Work:

- The current study is the first to use co-targeting of EGFR and Wnt/β-catenin signaling to influence the EMT and MDR dynamics in TNBC.
- Co-targeting these pathways incurred the phase transition from epithelial to mesenchymal transition (EMT) to mesenchymal to epithelial transition (MET).
- The inhibitor combination successfully downregulated the expression of ABC transporters ABCB1, ABCG2 and ABCC1 responsible for MDR.
- Similarly, co-targeting autophagy adaptor protein SQSTM1/P62 and Wnt/β-Catenin pathway induced mesenchymal to epithelial transition (MET) in TNBC

- Inhibition of SQSTM1/P62 and Wnt/β-Catenin signaling repressed mesenchymal differentiation and stemness of TNBC.
- Suppression of SQSTM1/P62 and Wnt/β-Catenin signaling decreased the migration and invasion potential of TNBC.
- Additionally, a novel therapeutic module has been fabricated by coating a non-toxic, biodegradable PLGA nanoparticle core with D-penicillamine templated Au-Cu bimetallic nanoclusters. Further, the resultant nanomaterials were coated with recombinant transferrin protein to specifically target transferrin receptor overexpressing TNBC cells.
- Application of the nanocomposites incurred the phase transition from epithelial to mesenchymal transition (EMT) to mesenchymal to epithelial transition (MET).
- The nanocomposites successfully downregulated the expression of ABC transporters ABCB1 and ABCC1 responsible for multidrug resistance (MDR).
- Regulation of EMT and MDR adroitly inhibited the migration capacity of TNBC cell line MDA-MB-231 and MDA-MB-468.

Section 2

Materials and Methods

Materials and Methods

2.1. Materials:

BD Biosciences- FITC Annexin V Apoptosis Detection Kit

Bio-rad Laboratories- cDNA synthesis kit, PCR Master mix, SYBR Green Master mix for qPCR

Borosil- Glasswares

Cell Signaling Technology- Antibodies used are listed below (**Table. 2.1**)

SL. No	Antibodies	Catalog No
1	EGFR	4267
2	pEGFR	3777
3	Akt	4691
4	pAkt	4060
5	MAPK	4695
6	pMAPK	4370
7	Stat-3	12640
8	pStat-3	9145
9	Claudin	13255
10	GSK-3β	12456
11	pGSK-3β	5558
12	E-cadherin	3195
13	N-Cadherin	13116
14	Vimentin	5741
15	Vimentin mAb (Alexa Fluor® 647 Conjugate)	9856

16	B-actin	D6A8
17	LC3A/B	12741
18	NF-κβ mAb (Alexa Fluor® 647 Conjugate)	8801
19	CD44 mAb (FITC Conjugate)	75122
20	CD24 mAB (PE Conjugate)	903785
21	Anti-Rat IgG (Alexa Fluor® 647 Conjugate)	4418
22	Anti-Rabbit IgG (Alexa Fluor® 647 Conjugate)	4414
23	Anti-Rabbit IgG (Alexa Fluor® 488 Conjugate)	4412
24	HIF-1α	36169
25	SAPK/JNK	8206
26	Phospho SAPK/JNK	8206

Table 2.1: List of antibodies purchased from Cell Signaling Technology.

Corning Inc. – Growth factor reduced matrigel matrix, Boyden chamber transwell inserts

Eppendorf - Cell culture plates

GE Healthcare- Agarose gel and SDS-PAGE running apparatus

Gibco- Antibiotic-Antimycotic solution

HiMedia India – Bovine serum albumin (BSA), Methanol, Ethanol, Cobalt chloride

Promega Corporation– DNase - I

Sigma-Aldrich (USA) – Agarose, Dulbecco's modified eagle's medium (DMEM), Ponceau S, Propidium iodide (PI), RIPA Buffer, Triton-X-100, Trizma base (Tris) , Tween -20, Tetra methyl ethylene diamine (TEMED), Tri reagent, Ammonium

persulphate (APS), Dimethylsulphoxide (DMSO), Sodium pyruvate, Sodium bicarbonate, Epidermal growth factor (EGF), Chemiluminescent reagent, 2',7'-dichlorofluorescein diacetate (DCFDA), DAPI, 3,3',5,5'-Tetramethylbenzidine (TMB), Hydorgen peroxide (H_2O_2), D-penicillamine, poly(vinyl alcohol) (PVA), Acetonitrile, Poly(lactic-co-glycolic acid) (PLGA), Copper sulfate (CuSO4), HAuCl4 (Au, 17 wt % in dilute HCl; 99.99%), Human transferrin, Phosphate-buffered saline (PBS), MISSION® esiRNA targeting human SQSTM1/P62, Universal Negative Control #1 scrambled siRNA, RNAse, Anti-β-catenin Antibody, Anti-VANGL2 Antibody, Anti-rabbit IgG HRP-linked Antibody, Anti-mouse IgG HRP-linked Antibody, PVDF membrane, Erlotinib, Lapatinib, XAV939, FH535, Rapamycin, Hydroxychloroquine.

Tarsons Products Pvt. Ltd - Plasticware

Thermo Fisher Scientific- Cell culture plates, DNA and Protein ladder, Trypan blue, Lipofectamine™ RNAiMAX Transfection Reagent, alamarBlue, Fetal bovine serum (FBS), Penicillin-streptomycin, JC-1 dye, Calcein-AM, SYBR Green Master Mix, Anti-SQSTM1/P62 Antibody, Anti-ZEB-1 Antibody, Anti-Twist-1 Antibody, Anti-SNAI1 Antibody

Integrated DNA Technologies (IDT)- Primers for all PCR reactions have been listed below (**Table. 2.2**):

Name	Primer Sequence
E-Cadherin	Fwd: 5'- TGAAGGTGACAGAGCCTCTGGAT -3' Rev: 5'- TGGGTGAATTCGGGCTTGTT -3'
Vimentin	Fwd: 5'- AGTCCACTGAGTACCGGAGAC -3' Rev: 5'- CATTTCACGCATCTGGCGTTC -3'
N-cadherin	Fwd: 5'- CCATCAAGCCTGTGGGAATC -3' Rev: 5'- GCAGATCGGACCGGATACTG -3'

Fibronectin	Fwd: 5'- GGTGACACTTATGAGCGTCCTAAA -3' Rev: 5'- AACATGTAACCACCAGTCTCATGTG -3'
EpCAM	Fwd: 5'- GCTGGCCGTAAACTGCTTTG -3' Rev: 5'- ACATTTGGCAGCCAGCTTTG -3'
Twist-1	Fwd: 5'- TGCATGCATTCTCAAGAGGT -3' Rev: 5'- CTATGGTTTTGCAGGCCAGT -3'
SNAI2	Fwd: 5'- ATGAGGAATCTGGCTGCTGT -3' Rev: 5'- CAGGAGAAAATGCCTTTGGA -3'
Ki-67	Fwd: 5'- AGAGCCTTAGCAATAGCAACG -3' Rev: 5'- GTCTCCCGCGATTCCTCTG -3'
MDM2	Fwd: 5'- ACCTCACAGATTCCAGCTTCG -3' Rev: 5'- TTTCATAGTATAAGTGTCTTTTT -3'
ABCB1	Fwd: 5'- GGGAGCTTAACACCCGACTTA -3' Rev: 5'- GCCAAAATCACAAGGGTTAGCTT -3'
ABCG2	Fwd: 5'- TGGCTTAGACTCAAGCACAGC -3' Rev: 5'- TCGTCCCTGCTTAGACATCC -3'
ABCC1	Fwd: 5'- CTGAGAAGGAGGCGCCCTG -3' Rev: 5'- GTGTCCGGATGGTGGACTG -3'
Caveolin-1	Fwd: 5'- AACACGTAGCTGCCCTTCAG -3' Rev: 5'- GGATGGGAACGGTGTAGAGAT -3'
Cyclin-D1	Fwd: 5'- CCGTCCATGCGGAAGATC -3' Rev: 5'- CCTCCTCCTCGCACTTCTGT -3'
CDK-4	Fwd: 5'- GGACATATCTGGACAAGGCACC -3' Rev: 5'- ACTGTTCCACCACTTGTCACCAG -3'
ALDH1A3	Fwd: 5'- ATCAACTGCTACAACGCCCT -3' Rev: 5'- TATTCGGCCAAAGCGTATTC -3'
MYC	Fwd: 5'- GCCACGTCTCCACACATCAG -3' Rev: 5'- TGGTGCATTTTCGGTTGTTG -3'

SQSTM1	Fwd: 5'- AGGCGCACTACCGCGAT -3' Rev: 5'- CGTCACTGGAAAAGGCAACC -3'
LEF1	Fwd: 5'- TGTTTATCCCATCACGGGTGG -3' Rev: 5'- CATGGAAGTGTCGCCTGACAG -3'
TCF7	Fwd: 5'- AACTGGCCCGCAAGGAAAG -3' Rev: 5'- CTCCGGGTAAGTACCGAATGC -3'
Transferrin receptor-1	Fwd: 5'- GGACGCGCTAGTGTTCTTCT -3' Rev: 5'- CATCTACTTGCCGAGCCAGG -3'
GAPDH	Fwd: 5'- GTCTCCTCTGACTTCAACAGCG -3' Rev: 5'- ACCACCCTGTTGCTGTAGCCAA -3'
β-actin	Fwd: 5'- CTGGAACGGTGAAGGTGACA -3' Rev: 5'- AAGGGACTTCCTGTAACAATGCA -3'

Table 2.2: List of primers used for all PCR reactions.

2.2. Cell Lines and Cell Culture Conditions:

Human breast cancer cell lines MCF-7, MDA-MB-231, MDA-MB-468 human cervical cancer cell line HeLa and human embryonic kidney cell line HEK-293 were purchased from the National Centre for Cell Science, Pune, India. The cells were cultured in Dulbecco's Modified Eagle's Medium-high glucose supplemented with L-glutamine, sodium pyruvate, 10% fetal bovine serum (FBS), Sodium bicarbonate, 100 units/ml penicillin and 100 µg/ml streptomycin at 37 °C in humidified air containing 5% CO_2.

2.3. Culture Condition for 3D Multicellular Tumor Spheroids: Spheroids of different cell lines were generated using a forced floating method [79, 80]. Briefly, cells were cultured as monolayers up to confluency, trypsinized and resuspended in DMEM. In the meantime, wells of 96-well plates were coated with agarose (1.5%

w/v) containing serum-free DMEM. Next, the cells were seeded at a density of 2×10^4 cells/well, after which the plates were centrifuged at 700 rcf for 10 min. Subsequently, the 96-well plates were incubated at 37 °C in a humidified atmosphere containing 5% CO_2 for 96 h. The resulting spheroids were visually monitored with a Nikon Eclipse Ti microscope. The spheroids generated after 96 h incubation were subsequently used for all experimental purpose.

2.4. Method Sections:

2.4.1. Methods Related to Targeting Signaling Pathways to Alter EMT and MDR Dynamics of TNBC.

2.4.1.1. EMT Induction: To induce EMT, cells were trypsinized, counted and seeded in appropriate numbers in 6-well plates or 60 mm dishes. Cell were allowed to attach for 24 h in complete media containing 10% serum. After attachment, cells were starved for 4 h in serum free media. Next, the serum free media was replaced with 0.5 % serum media supplemented with 20 nM EGF. After incubation of 30 min, cells were treated with inhibitors as desired.

2.4.1.2. Determination of Cell Viability: In order to understand the therapeutic potential of the inhibitors alone or in combination, the percent of viable cell was assessed following treatment. Cell viability was evaluated using an alamarBlue assay. Resazurin, the active ingredient of alamarBlue, is converted to its reduced form resorufin while entering into the living cells [81]. Following treatment for 48 h of monolayer cultures in 96-well plates, 10 µl alamarBlue was directly added to the wells and incubated for 2 h at 37 °C under 5% CO_2 humidified conditions. In case of spheroids, following treatment for 72 h, 20 µl alamarBlue was added and incubated for 4 h at 37 °C under 5% CO_2 in humidified conditions. After the respective incubations, absorbance was measured at 570 nm with a reference

of 600 nm using a microplate reader (Infinite M200 Pro, Tecan, Switzerland). Cell viability (%) was determined using the following formula:

$$\text{Cell Viability (\%)} = \frac{(abs570 - abs600)Sample}{(abs570 - abs600)Control} x100$$

2.4.1.3. Drug Combination Assays: The cell viability data was further processed and sigmoidal-dose response curves were plotted using GraphPad Prism software. Further, from the sigmoidal-dose response curves, inhibitory concentration-50 (IC_{50}) values were determined. For combination therapy, the concentration of one of the inhibitors was kept constant to IC_{25} while the concentration of another inhibitor was increased in a dose dependent manner. The combined effect of lapatinib and XAV939 was determined by analyzing the Chou and Talalay combination index (CI) using Calcusyn software (Biosoft) [82].

2.4.1.4. Determination of Cell Cycle Pattern: To analyze the effect of the drug combination on cell cycle progression, propidium iodide (PI) based flow cytometry analysis was performed. Cells were seeded at a density of 1×10^5 cells per 60 mm tissue culture petri-dish and allowed to attach for 12 h. Cells were synchronized prior to treatment by serum starvation with 0.5% serum for 24 h. Treatment with the inhibitors and their combination was performed for 48 h in complete media. Following treatment, cells were trypsinized, centrifuged at 650 rcf for 6 min and fixed by adding 70% chilled ethanol dropwise. Fixed cells were stored in -20 °C until further analysis as described by Riccardi et al. [83]. Briefly, cells were washed with chilled phosphate buffered saline (PBS) and incubated with RNAse for 1 h at 37 °C. Next, the cells were incubated with PI and stored in

the dark on ice until further analysis. The samples were analyzed using a BD FacsCalibur, and the collected data were analyzed using FCS Express software.

2.4.1.5. Detection of Reactive Oxygen Species: Cellular ROS generation following drug treatment was analyzed using 2′,7′-dichlorofluorescein diacetate (DCFDA) dye. DCFDA is a cell-permeant reagent, and in the presence of hydroxyl, peroxyl and other ROS activities within the cell, it is oxidized to 2′,7′-dichlorofluorescein (DCF), which gives a green fluorescence. For ROS detection, cells were incubated with 10 μM DCFDA for 30 min and afterwards treated with individual inhibitors and their combination for 6 h. Next, cells were trypsinized, washed with PBS thrice and resuspended in 500 μl PBS. Finally, cells were analyzed in FITC channel using CytoFLEX flow cytometer.

2.4.1.6. Detection of Mitochondrial Membrane Potential: Mitochondrial membrane potential was determined using JC-1 staining. The cyanine dye JC-1 (5,5′,6,6′-tetrachloro-1,1′,3,3′-tetraethylbenzimi-dazolylcarbocyanine iodide) forms red aggregates in polarized mitochondria, whereas it remains as a monomer in depolarized mitochondria [84]. Cells were treated with inhibitors and their combination for 48 h. After completion of the treatment, JC-1 dye (10 μM) was added to each cell culture well for 20 min. For positive control, cells were incubated with 50 μM Carbonyl cyanide 3-chlorophenylhydrazone (CCCP) for 30 min along with the JC-1 dye. After the incubation, the cells were trypsinized and washed with PBS extensively. Finally, cells were resuspended in 500 μl PBS and analyzed using CytoFLEX flow cytometer. Fluorescence intensities were collected in the red and green channels. Positive and negative controls were used to detect depolarized population and for fluorescence compensation.

2.4.1.7. Determination of Apoptotic Cell Population: Early apoptotic, apoptotic and necrotic cell populations were estimated using a FITC Annexin V Apoptosis Detection Kit. Cells were treated for a period of 48 h. Next, cells were trypsinized, washed with chilled PBS and processed according to the manufacturer's instructions. Fluorescence data was collected in green and red channel using CytoFLEX flow cytometer. Data analysis and fluorescence compensation were performed using CytExpert software.

2.4.1.8. Calcein-AM/ Propidium Iodide (PI) Dual Staining: To visualize the percentage of live and dead cells population following treatment, cells were stained with calcein-AM and PI. Calcein AM is a cell-permeant non-fluorescent dye which after entering inside live cells is converted to green-fluorescent calcein by acetoxymethyl ester hydrolysis by intracellular esterases [85]. Whereas, PI is a not permeant to live cells, and binds to DNA of dead cells by intercalating between the bases and gives red fluorescence [86]. For imaging live–dead cell populations, monolayer cultures were treated for 48 h, and spheroids were treated for 72 h. Cells were carefully rinsed with PBS thrice. Thereafter, Calcein AM/PI solution was added in the final concentrations of 2 μM and 4 μM followed by a 30 min incubation in dark. After incubation, the stained cells and spheroids were washed thrice with PBS and imaged using a Zeiss LSM 880 confocal microscope in conjunction with Z-stacking analysis.

2.4.1.9. RNA Isolation and Expression Study: Following treatment RNA was isolated from the cells using Tri reagent. From the obtained RNA, cDNA was synthesized using an iScript cDNA synthesis kit according to the manufacturer's instructions. Amplification of the cDNA of interest was performed using a SYBR Green Master Mix and a Rotor-Gene Q (Qiagen) real-time PCR cycler. The data

obtained were normalized to GAPDH (glyceraldehyde-3-phosphate dehydrogenase) or β-actin. Further, the normalized data were quantified using the delta-delta CT method [87]. The obtained quantitative RT-PCR (qRT-PCR) data were analyzed using LinReg PCR software.

2.4.1.10. Protein Expression Analysis by Western Blot: Following treatment, total protein was extracted from the cells using RIPA lysis buffer. Protein from each sample was quantified using BCA protein assay kit. Equal amount of protein from each sample were subjected to SDS-PAGE. From the resolved gel protein were subsequently transferred to PVDF membranes. Next, the membranes were blocked using blocking buffer (4% BSA in TBST) and incubated overnight with primary antibodies. Following which the blots were extensively washed using TBST. Further, blots were incubated with HRP conjugated secondary antibodies for a period of 2 h at room temperature. Following incubation, blots were rewashed extensively with TBST. Signals were developed using chemiluminescent reagent, and images were acquired using ChemiDoc (BioRad). The images were quantified using ImageJ software. Finally, the data obtained were normalized to GAPDH (glyceraldehyde-3-phosphate dehydrogenase) or β-actin and protein expression data were analyzed.

2.4.1.11. Determination of Migration Potential: Migration was assessed using a scratch wound-healing assay, where the migration rate of the cells towards the wound area (created using a scratch) was determined. Scratch wound-healing assays were performed using a protocol described by Wu et al. [88]. Briefly, cells were grown to 70–80% confluence in complete DMEM media. Next, the media were replaced by 0.5% serum media for 24 h. Confluent cell monolayers were scraped with a sterile pipette tip to create 'wounds'. The wounded monolayers

were washed with PBS to remove cell debris. Next, the cells were treated with inhibitors and their combination and incubated at 37 °C under humidified conditions and 5% CO_2 for a period of 24 h. Images of the 'wounds' before and after treatment were captured using a Nikon Eclipse Ti microscope and analyzed using ImageJ software.

2.4.1.12. Detection of Invasion Property: Matrigel invasion assay was performed to detect the alteration of invasiveness of cells. Invasion assays were performed using a method described by Chen et al. [89]. Briefly, the upper chamber of the transwell inserts were coated with diluted Matrigel (1 mg/ml in serum-free medium). The coated transwells were incubated at 37 °C overnight for solidification. In the upper chamber 2×10^5 cells were seeded in serum free medium whereas the lower chamber was filled with 750 µl of serum media containing 10% FBS. After incubation of 24 h, the upper side of the chamber was carefully wiped using a wet swab to remove the non-migrated cells and washed thrice with PBS. To fix the migrated cells, the lower part of the chamber was incubated in 4% formaldehyde at 37 °C for 15 min. Following fixation, cells were washed thrice with PBS and for visualization stained with DAPI (1 µM). Finally, cells were rewashed thrice in PBS and visualized using Zeiss LSM 880 confocal microscope. The fold change in fluorescence intensity of DAPI represents the alteration of invasion potential. DAPI only stains dsDNA, preventing non-specific staining of the membrane of transwells.

2.4.1.13. Statistical Analysis: All statistical analyses were performed using GraphPad Prism software. The experimental data are expressed as mean ± SEM. The one-way and two-way ANOVA test were used to assess possible correlations

between groups. A p-value < 0.05 was considered statistically significant where * p < 0.05, ** p < 0.001, *** p < 0.001, **** p < 0.0001, respectively.

2.4.2. Methods Related to Exploiting the Interplay Between EMT and Autophagy to Restrain Metastatic TNBC.

2.4.2.1. EMT Induction: To induce EMT, cells were trypsinized, counted and seeded in appropriate numbers in 6-well plates or 60 mm dishes. Cell were allowed to attach for 24 h in complete media containing 10% serum. After attachment, cells were starved with 0.5% serum media for 12 h. After serum starvation, media was replaced with 0.5 % serum media supplemented with 20 nM EGF. After incubation of 30 min, cells were treated as desired.

2.4.2.2. siRNA Transfection: For siRNA transfection, reverse transfection was carried out with Lipofectamine™ RNAiMAX Transfection Reagent according to the manufacturer's instructions. MISSION® esiRNA targeting human SQSTM1/P62 and Universal Negative Control #1 scrambled siRNA were purchased from Sigma-Aldrich, St. Louis, MI, USA. While performing reverse transfection for SQSTM1/P62, all the other cells were transfected with the negative control siRNA using the same transfection protocol.

2.4.2.3. Immunofluorescence Flow Cytometry: To perform immunofluorescence flow cytometry, following treatment, cells were washed with PBS, fixed with 4% formaldehyde and rewashed with excess PBS. Next, the cells were resuspended in 1X PBS. Cells were permeabilized by adding 100% chilled

methanol slowly to pre-chilled cells, while gently vortexing, to a final concentration of 90% methanol. Following fixation, cells were rewashed in excess PBS, to remove methanol. Next, cells were resuspended in 100 µl of diluted primary antibody, prepared in antibody dilution buffer and incubated for overnight at 4 °C. Cells were washed thrice in antibody dilution buffer and resuspend in 100 µl of diluted fluorochrome-conjugated secondary antibody. After 2 h of incubation at room temperature, cells were rewashed thrice with antibody dilution buffer and resuspended in 500 µl of antibody dilution buffer. Finally, the cells were analyzed using CytoFLEX flow cytometer.

2.4.2.4. Immunofluorescence Microscopy: For immunofluorescence analysis, following treatment, cells were washed thrice with PBS and fixed with 4% formaldehyde for 15 min at room temperature and rewashed. Next, the cells were immersed in blocking buffer for 2 h and subsequently incubated overnight at 4 °C with primary antibodies. After a second wash, the cells were incubated with a fluorochrome-conjugated secondary antibody for 2 h at room temperature in the dark. After rewashing, Alexa Fluor® 555 Phalloidin diluted in PBS was added and incubated with DAPI (1 µM) for 5 min. After a final wash, imaging was performed using a Zeiss LSM 880 confocal microscope.

2.4.2.5. Colony Formation Assay: The colony formation assay was performed as described by Crowley et al. [90]. Briefly, cells were seeded in 6-well plates and further treated with siRNA and inhibitors for 48 h. Following treatment, cells were washed with PBS, trypsinized and resuspended in DMEM media. The cells were counted and further resuspended in fresh medium at 400 cells/mL. 2 mL of cell suspension was added in 6 well culture plate and incubated for a period of 7 days at 37 °C. Every alternate 3 days the media was exchanged with fresh media.

Next, the colonies were washed with PBS, fixed with 100% methanol and stained with 0.5% crystal violet solution. The stained colonies were washed with excess water and dried for overnight. Using an inverted brightfield microscope, the colonies were then visualized and counted.

2.4.2.6. Western Blotting: RIPA lysis buffer (Sigma Aldrich) supplemented with protease inhibitor cocktail, sodium fluoride, sodium orthovanadate, phenylmethylsulfonyl fluoride (PMSF) and EDTA was used to extract the total protein from the cells following treatment. The obtained proteins were quantified using bicinchoninic acid (BCA) protein assays reagent, and an equal amount of protein from each sample were loaded for SDS-PAGE. The resolved proteins were subsequently transferred to PVDF membranes. The membranes were treated using blocking buffer (4% BSA in TBST) before being incubated with primary antibodies overnight in 4 °C. Next, the membranes were washed thoroughly using PBST and incubated with secondary antibody for 3 h at room temperature. The membranes were rewashed thoroughly, and further processed for development. Chemiluminescent reagent was used to produce the signals and ChemiDoc (BioRad) was used to record the images. The images were further analyzed using ImageJ software (Fiji). Anti-Akt, anti-phospho-Akt (Ser473), anti-p44/42 MAPK (Erk1/2), anti-phospho-p44/42 MAPK (Erk1/2) (Thr202/Tyr204), anti-Stat-3, anti-phospho-Stat-3 (Tyr705), anti-β-catenin, anti-E-cadherin, anti-N-cadherin and anti-Vimentin, anti-cMYC, anti-beclin-1, anti-ZEB1, anti-Twist1, anti-SNAI1 and anti-LC-3A/B antibodies were used to detect the desired protein expression.

2.4.2.6. Quantitative Real-Time PCR: Following treatment of 48 h, RNA was isolated from the cells using Trizol reagent. cDNA was generated from the acquired RNA using iScript cDNA synthesis kit as per the manufacturer

guidelines. The cDNA of interest was amplified using a PowerUpTM SYBR™ Green Master Mix and a Rotor-Gene Q (Qiagen) real-time PCR cycler. The obtained data were normalized to housekeeping gene β-actin and quantified using the delta-delta CT method. The LinReg PCR software was used to analyze the RT-PCR data.

2.4.3. Methods Related to Targeting TNBC by Nanocarrier Mediated Targeted Delivery of Novel Drugs.

2.4.3.1. EMT Induction: To mimic hypoxic conditions and induce EMT, TNBC cell line MDA-MB-231 and MDA-MB-468 and luminal cell MCF-7 were treated with $CoCl_2$ for 24h prior to each treatment. MDA-MB-231 was treated with 25 μM $CoCl_2$ whereas, MDA-MB-468 and MCF-7 were treated with 100 μM $CoCl_2$.

2.4.3.2. Synthesis of PLGA Nanoparticles: PLGA nanoparticles were synthesized using a slight modification of solvent evaporation technique as reported by Huang et al. [91]. Briefly, 50 mg PLGA was dissolved in 4 mL acetonitrile and poured dropwise in 60 mL 0.5% PVA solution. The resultant mixture was stirred at 600 rpm for 12 h. To remove the residual surfactant from the synthesized nanoparticles, the mixer was centrifuged for 15 min at 12 000 rcf and washed three times with deionized water.

2.4.3.3. Synthesis of Bimetallic D-Penicillamine–Au-Cu Nanoclusters: Bimetallic Au–Cu nanoclusters were synthesized as described by Chen et al. [77].

Briefly, 9 mL of 30 mM D-penicillamine solution was mixed with 500 μL of 10 mM $HAuCl_4$ solution and stirred vigorously for 10 min. Next, 500 μL of 5 mM $Cu(NO_3)_2$ solution containing 0.1 M nitric acid solution was added to the mixture. After stirring for 1 min, the color changed to milky white, which indicates the formation of d-penicillamine Au–Cu nanoclusters. To stabilize the solution, it was further mixed in the dark for 2 h at 600 rpm. To collect the nanoclusters, the mixer was centrifuged at 3000 rcf and thoroughly washed thrice using deionized water.

2.4.3.4. Synthesis of Nanocomposites: To synthesize the nanocomposites, at first, PLGA nanoparticles were coated with d-penicillamine Au–Cu nanocluster by mixing d-penicillamine Au–Cu nanocluster and PLGA for 6 h in dark at room temperature. Next, the solution was centrifuged at 3000 rcf for 15 min washed thrice with deionized water. The pellet was dispersed in 10 mL PBS containing 1 mg/mL transferrin and slowly stirred for 4 h in the dark. The synthesized nanocomposites were centrifuged at 3000 rcf for 15 min and washed thrice with deionized water by repeated centrifugation. Finally, the nanocomposites were redispersed in 5 mL deionized water.

2.4.3.5. Characterization of Nanocomposites: The zeta potential and hydrodynamic diameter of the nanoparticles and nanocomposites were measured using Zetasizer (Malvern). The nanoparticles and nanocomposites imaging were done by field emission scanning electron microscopy (FESEM) and transmission electron microscopy (TEM). For FESEM, the nanocomposites were drop-cast, dried overnight, and observed under a microscope (Sigma, Zeiss). For TEM imaging, 8 μL of nanocomposites was drop cast on TEM grid, dried by desiccation, and examined using TEM (JEOL, MA). Circular dichroism spectra were recorded using JASCO-815 spectrometer (Jasco, Japan).

2.4.3.6. UV–visible Spectroscopy and Luminescence Measurement: The absorbance profile of the synthesized nanocomposites was studied using UV–visible spectrophotometer (Carry-60 UV–vis, Agilent Technologies). The luminescence profile was measured using fluorescence spectrophotometer (FluoroMax-4, Horiba Scientific).

2.4.3.7. Atomic Absorption Spectroscopy (AAS) and Fourier Transform Infrared (FTIR) Spectroscopy: To determine the amount of Cu present in the nanocomposites, atomic absorption spectrophotometer was used (AA240, Varian Inc.). For FTIR analysis, nanocomposites were lyophilized and mixed with KBr. The produced pellets were analyzed in the range 4000–400 cm−1 using PerkinElmer Spectrum One machine.

2.4.3.8. Hydrogen Peroxide Detection: H_2O_2 detection was performed as follows: 1 mL 5 mM TMB (3,3',5,5'-Tetramethylbenzidine), and 1 mL H_2O_2 solution with different concentrations were added sequentially in 7.9 mL NaAc–HAc (pH 3.5) buffer. Similarly, for nanocomposites, H_2O_2 solution was replaced with nanocomposite. The mixture was incubated at 40 °C for 20 min then kept in an ice-water bath for 10 min to stop the reaction. Finally, the UV-vis spectroscopy of the resultant solution was scanned from 500 to 800 nm at room temperature, and the absorbance at 652 nm was used for quantitative analysis.

2.4.3.9. D-penicillamine estimation: For D-penicillamine estimation, different known concentrations of D-penicillamine was made for standard curve preparation. D-penicillamine exhibits distinct absorbance peak at 215 nm [92].

Finally, using UV-vis spectroscopy, absorbance at 215 nm was used for quantitative analysis.

2.4.3.10. Quantum Yield Measurements: The fluorescence quantum yield of as-synthesized nanoclusters and nanocomposite was determined relative to a reference sample -tyrosine. It was calculated by using the following formula-

$$QY = QY_{ref} \frac{\eta^2 IA_{ref}}{\eta_{ref}^2 AI_{ref}}$$

Where, QY_{ref} is the quantum yield of the reference compound, η is the refractive index of the solvent, I is the integrated fluorescence intensity, A is the absorbance at the excitation wavelength.

2.4.3.11. Western Blotting: To extract total protein, RIPA lysis buffer was used. Samples were quantified and equivalent amount was run on SDS-PAGE. Protein from the gel was transferred to the PVDF membrane, blocked using blocking buffer (4% BSA in TBST), and incubated with primary antibody for 12 h. Membranes were then washed with TBST, incubated with secondary antibody, and rewashed. After washing, signals were developed using chemiluminescent reagent, and to acquire image ChemiDoc (Bio-Rad) was used. ImageJ software was used for blot quantification. Anti-Akt, anti-phospho-Akt (Ser473), anti-p44/42 MAPK (Erk1/2), anti-phospho-p44/42 MAPK (Erk1/2) (Thr202/Tyr204), anti-Stat-3, anti-phospho-Stat-3 (Tyr705), anti-β-catenin and anti-HIF-1α antibodies were used to detect the desired protein expression.

2.4.3.12. Semiquantitative PCR and Quantitative Real-Time PCR: RNA was isolated from the samples using the Tri reagent, and cDNA was synthesized

using iScript cDNA synthesis kit. The gene of interest and the housekeeping gene were amplified using GoTaq Green Master Mix and Select Cycler II (Select BioProducts). To analyze the gene expression, amplified product was electrophoresed on 1% agarose gel. For real-time PCR, the amplification of gene of interest was done using SYBR Green Master Mix. For data analysis by ΔΔCt method, LinReg PCR software was used.

Section 3

Results and Discussion

3.1. Targeting Signaling Pathways to Alter EMT and MDR Dynamics of TNBC

Cellular Oncology 44, 405–422 (2021).

Results and Discussion

Abstract: Patients with advanced metastatic triple-negative breast cancer (TNBC) experience poor clinical outcomes due to a lack of effective targeted therapy. Epithelial to mesenchymal transition (EMT) is known to contribute to cancer progression, invasiveness and multidrug resistance (MDR). There is a strong correlation between various drug efflux mechanisms, cancer stem cells and tumor microenvironments, which in turn is synchronized by complex signaling crosstalk between EMT and MDR. Hence, it is hypothesized that combining these regulatory connections with targeted combinatorial therapies may be an effective approach to annihilate the progression/metastasis of TNBC.

AlamarBlue assays were used to depict TNBC cell viability, whereas flow cytometry was used to detect apoptotic cell populations, reactive-oxygen species (ROS) levels as well as mitochondrial depolarization. qRT-PCR, Western blotting and confocal microscopy were used to provide molecular-level information of the genes and proteins involved.

Initial analyses showed that targeting EGFR by either erlotinib (EGFR inhibitor) or lapatinib (EGFR/HER-2 inhibitor) alone was ineffective against TNBC. Interestingly, it was subsequently found that a low dose of lapatinib did act as a substrate rather than as an inhibitor facilitating EMT and MDR, leading to metastasis. Additional gene expression studies indicated that co-targeting the EGFR and Wnt/β-catenin pathways with lapatinib and XAV939 (a tankyrase inhibitor) promoted mesenchymal to epithelial transition (MET). Application of these inhibitors led to a 5.62-fold increase in the epithelial marker E-cadherin and

a 3.33-fold decrease in the stemness marker EpCAM, with concomitant 1.5-fold and 3.22-fold reductions in the ABC transporters ABCB1 and ABCG2, respectively. These co-targeting effects resulted in overcoming EMT and MDR, which in turn was highlighted by reduced levels of pEGFR, pAKT, pMAPK, pSTAT-3, pGSK-3β and β-catenin.

Experimental results indicate that the synergistic action of targeting both the EGFR and Wnt/β-catenin signaling pathways in TNBC cells may open up new avenues for combatting this disease

3.1.1 Results:

3.1.1.1. Co-targeting EGFR and Wnt/β-catenin Signaling Synergistically Inhibits TNBC Cell Survival: MDA-MB-231 cells were treated with lapatinib and XAV939 alone and in combination to determine their effect on cell viability. Using an alamarBlue assay on lapatinib treated monolayer cells, a significant dose-dependent decrease in cell viability was observed (**Figure. 3.1.1 a**). On the other hand, a higher dose of XAV939 was required to obtain cell death (**Figure. 3.1.1 b**). The combination of lapatinib with XAV939 was found to decrease TNBC cell viability in a dose-dependent manner at lower concentrations (**Figure. 3.1.1 c**). Combination index (CI) calculation revealed a CI value of < 1, indicating a dose-dependent synergistic interaction between lapatinib and XAV939 (**Figure. 3.1.1 e and f**). Erlotinib did not show any significant inhibitory effect in monolayer cultures (Fig. 3.1 d). Similar to the data reported by Bao et al. [93], it was found that only targeting EGFR in TNBC using erlotinib is ineffective (**Figure. 3.1.1 d**). Administration of the inhibitors in combination yielded higher anti-proliferative effects than when administered alone (**Figure. 3.1.1 a, b, and c**).

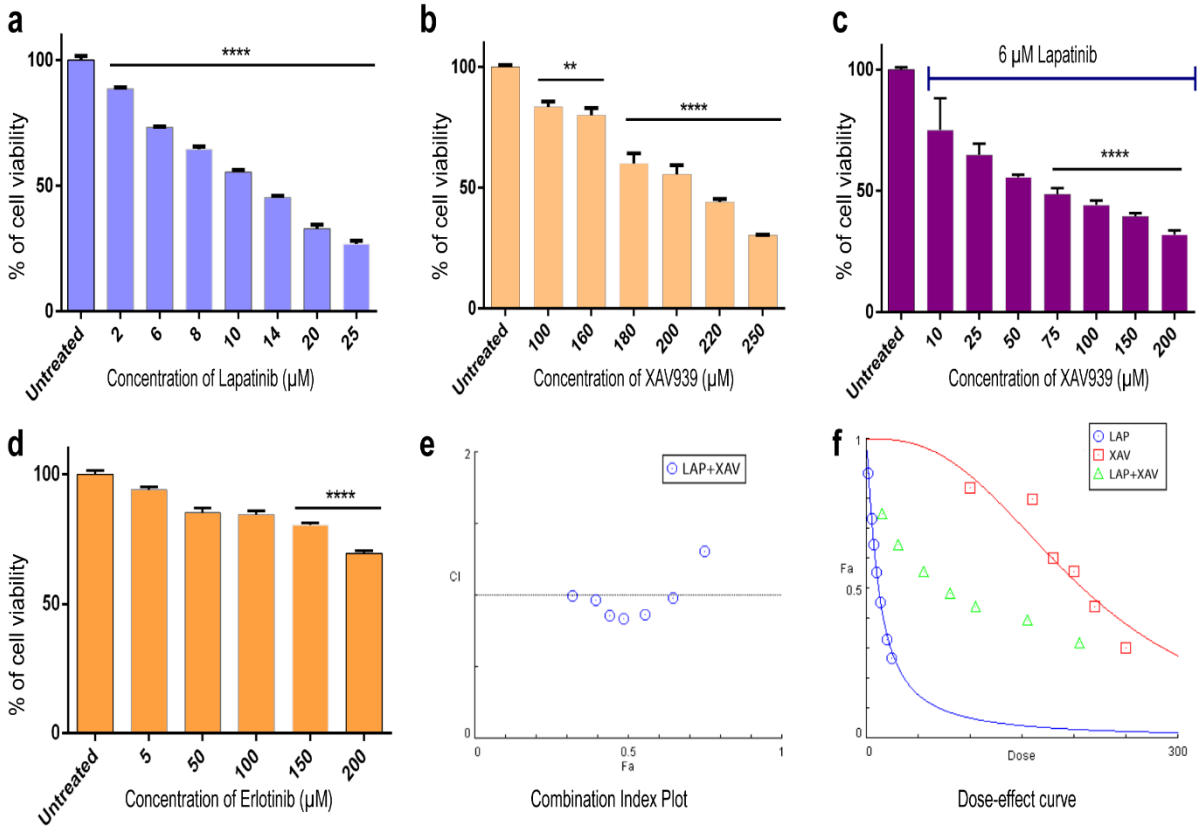

Figure 3.1.1: Determination of viability of MDA-MB-231 monolayer cultures by alamarBlue assay upon treatment with inhibitors for 48 h. (a), (b), (c) and (d) refer to treatment with lapatinib, XAV939, 6 μM lapatinib + XAV939 and erlotinib, respectively. (e) Combination index and (f) dose-response curves obtained following combination treatment. Drug combinations with CIs < 1.0 were considered as synergistic. Results expressed as the mean ± SEM are based on at least three independent experiments. The statistical significance was assessed versus that of the untreated cells. The significance level was set at $p < 0.05$ (*), $p < 0.01$ (**), $p < 0.001$ (***) or $p < 0.0001$ (****)

Similarly, alamarBlue assay was done to determine the effect of treatment with lapatinib and XAV939 in spheroids. A significant dose-dependent decrease in cell viability were observed following treatment with lapatinib (**Figure. 3.1.2 a**). Nonetheless, in comparison to monolayer culture, several-fold higher dose of lapatinib was required for the spheroids. Higher concentration of XAV939 was ineffective in case of spheroids (**Figure. 3.1.2 b**). Alike monolayer, the combination of lapatinib with XAV939 was found to decrease TNBC cell viability in a dose-dependent manner at lower concentrations (**Figure. 3.1.2 c**). The combination effect on spheroids was significant at a lower dose but, surprisingly, not effective at a higher dose (**Figure. 3.1.2 c**). Only EGFR targeting drug erlotinib was ineffective for spheroids (**Figure. 3.1.2 d**). Combination index (CI) calculation revealed a CI value of < 1, indicating a dose-dependent synergistic interaction between lapatinib and XAV939 (**Figure. 3.1.2 e and f**). When the inhibitors were administered together, they had a greater anti-proliferative impact than when they were administered separately. Significant correlations were also observed in other TNBC cells, i.e., MDA-MB-468 (**Figure. 3.1.3 and 3.1.4**) and luminal type MCF-7 cells (**Figure. 3.1.5 and 3.1.6**).

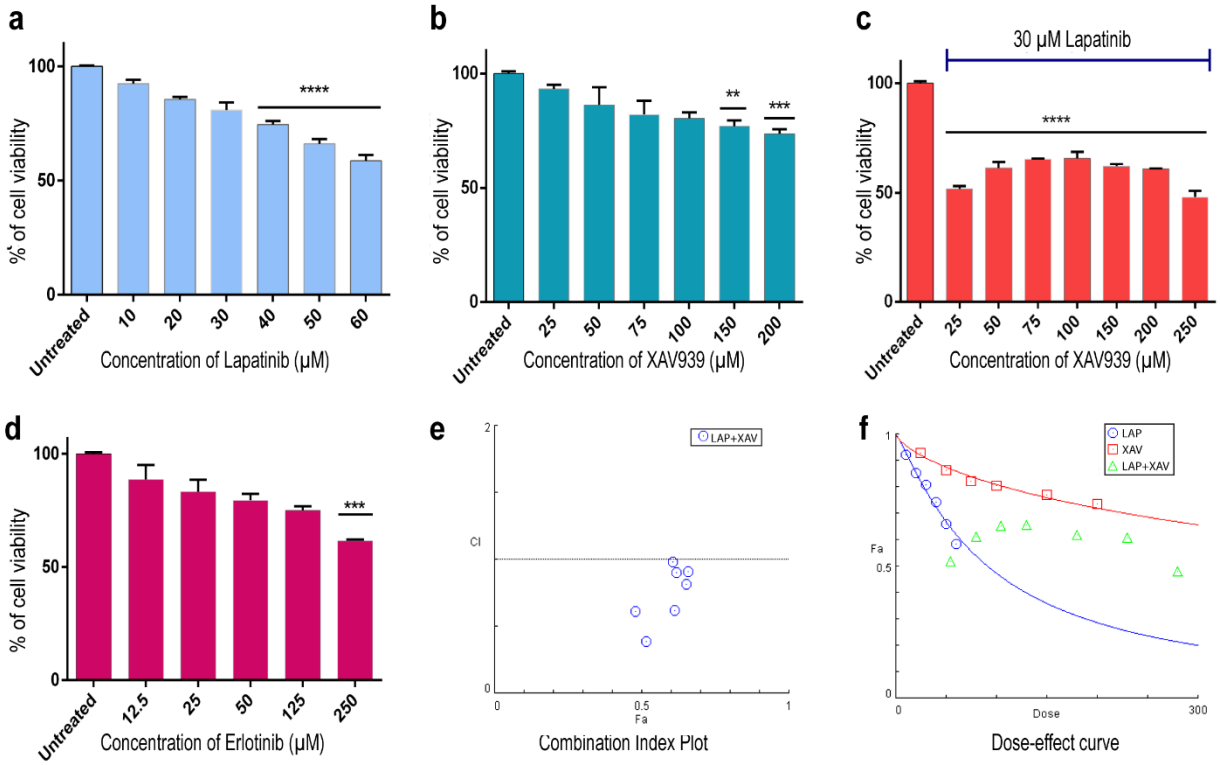

Figure 3.1.2: Determination of viability of MDA-MB-231 spheroids by alamarBlue assay upon treatment with inhibitors for 72 h. (a), (b), (c) and (d) refer to treatment with lapatinib, XAV939, 30 μM lapatinib + XAV939 and erlotinib, respectively. (e) Combination index and (f) dose-response curves obtained following combination treatment. Drug combinations with CIs < 1.0 were considered as synergistic. Results expressed as the mean ± SEM are based on at least three independent experiments. The statistical significance was assessed versus that of the untreated cells. The significance level was set at $p < 0.05$ (*), $p < 0.01$ (**), $p < 0.001$ (***) or $p < 0.0001$ (****)

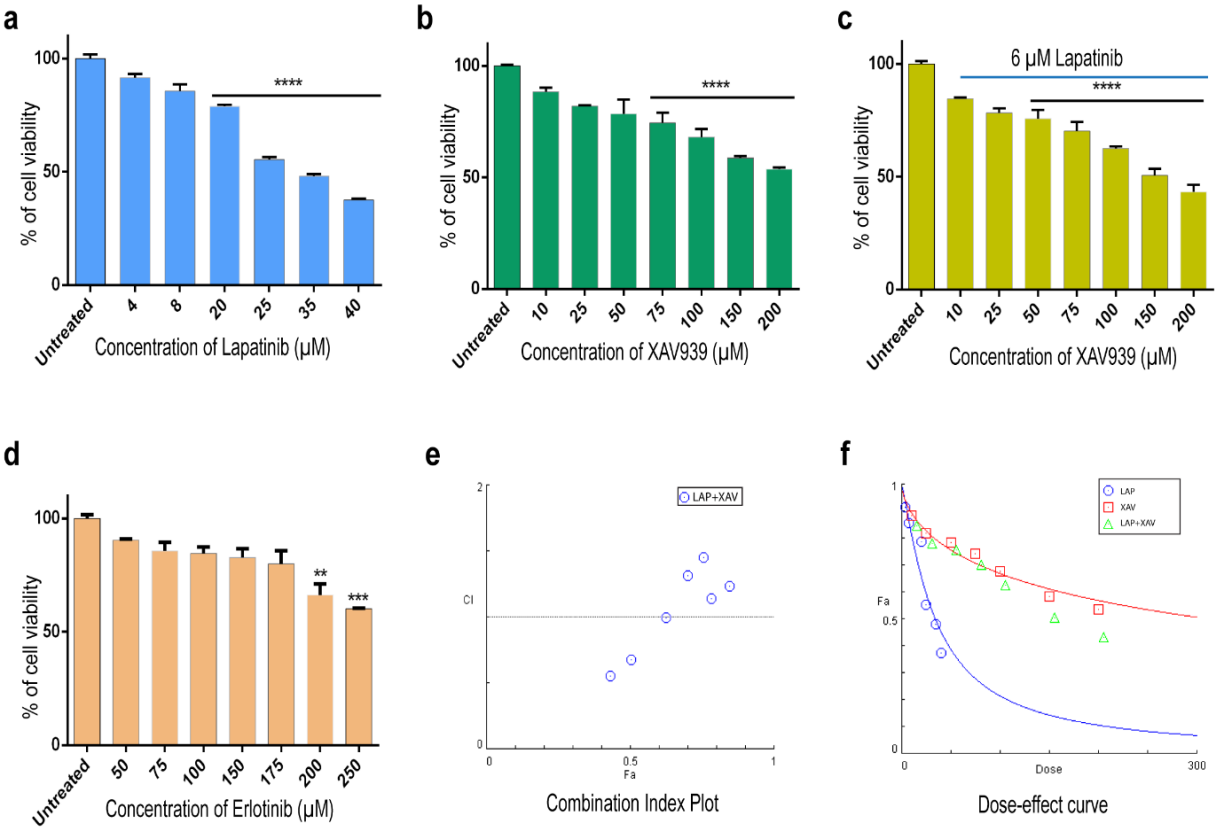

Figure 3.1.3: Determination of viability of MDA-MB-468 monolayer cultures by alamarBlue assay upon treatment with inhibitors for 48 h. (a), (b), (c) and (d) refer to treatment with lapatinib, XAV939, 6 μM lapatinib + XAV939 and erlotinib, respectively. (e) Combination index and (f) dose-response curves obtained following combination treatment. Drug combinations with CIs < 1.0 were considered as synergistic. Results expressed as the mean ± SEM are based on at least three independent experiments. The statistical significance was assessed versus that of the untreated cells. The significance level was set at $p < 0.05$ (*), $p < 0.01$ (**), $p < 0.001$ (***) or $p < 0.0001$ (****)

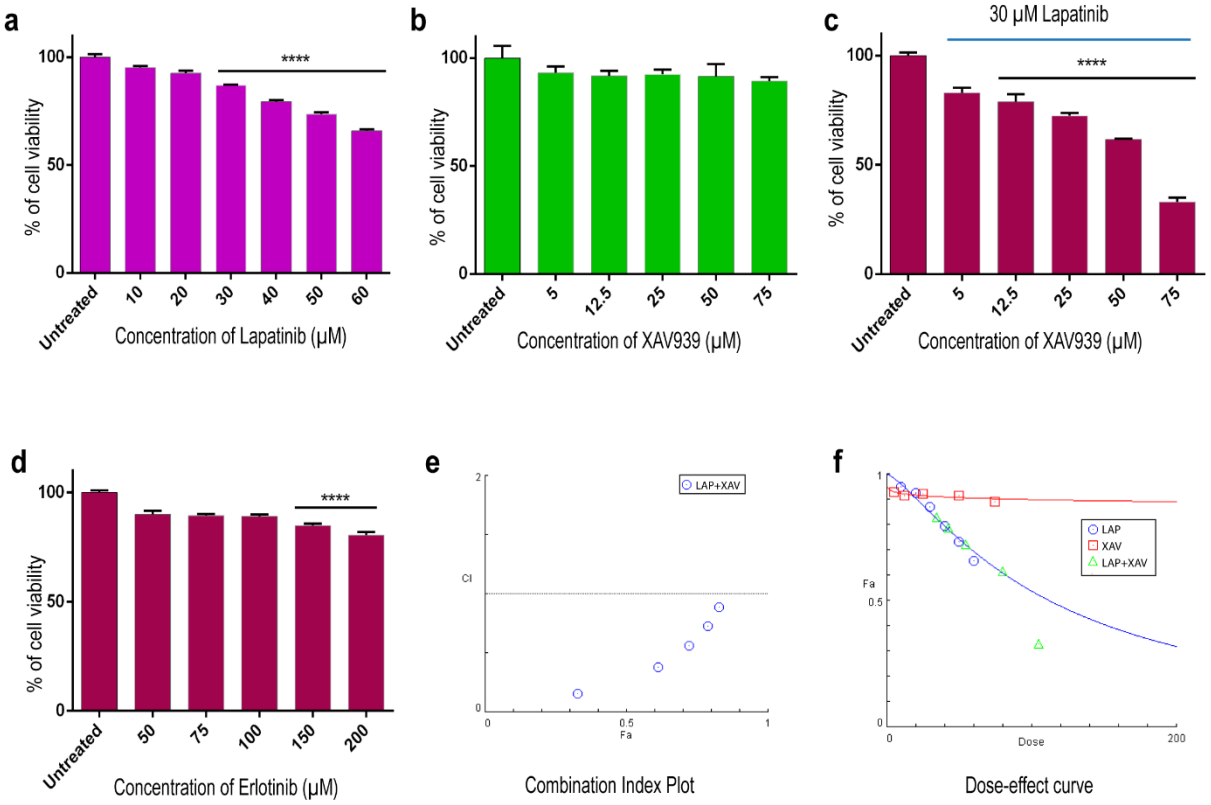

Figure 3.1.4: Determination of viability of MDA-MB-468 spheroids by alamarBlue assay upon treatment with inhibitors for 72 h. (a), (b), (c) and (d) refer to treatment with lapatinib, XAV939, 6 μM lapatinib + XAV939 and erlotinib, respectively. (e) Combination index and (f) dose-response curves obtained following combination treatment. Drug combinations with CIs < 1.0 were considered as synergistic. Results expressed as the mean ± SEM are based on at least three independent experiments. The statistical significance was assessed versus that of the untreated cells. The significance level was set at $p < 0.05$ (*), $p < 0.01$ (**), $p < 0.001$ (***) or $p < 0.0001$ (****).

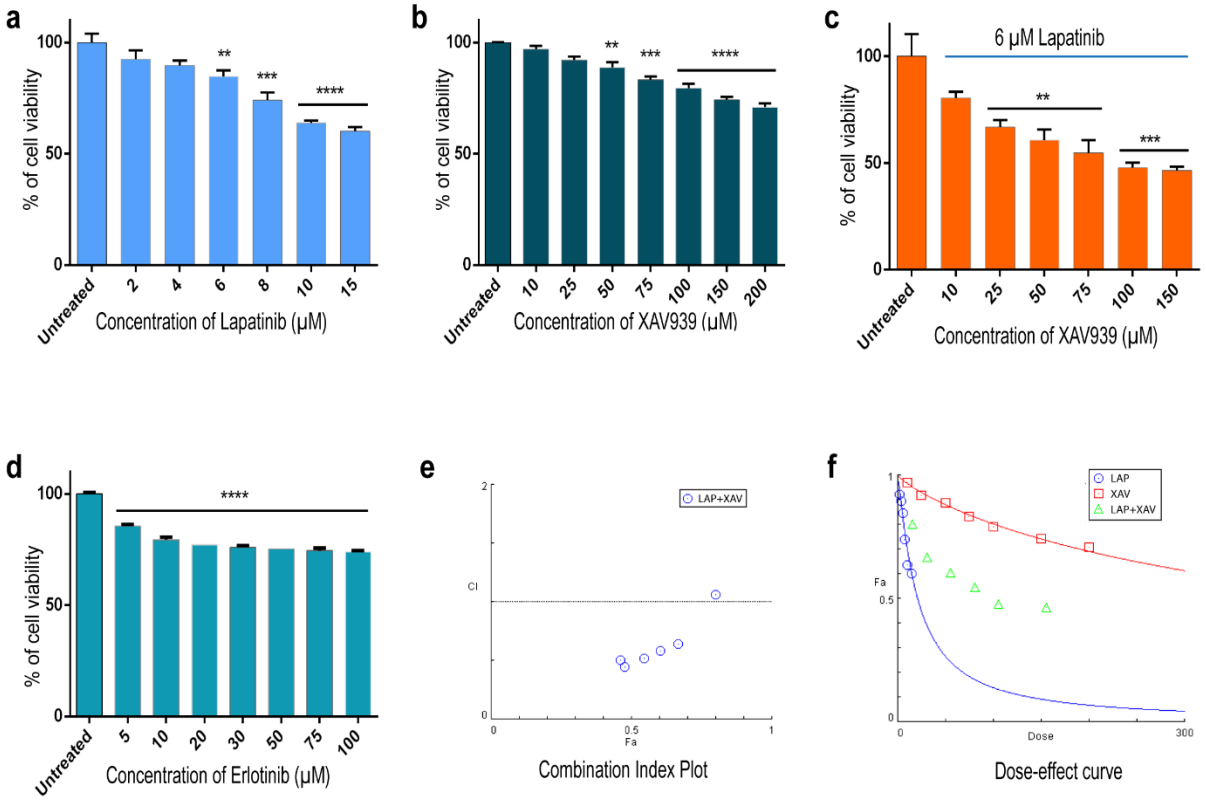

Figure 3.1.5: Determination of viability of MCF-7 monolayer cultures by alamarBlue assay upon treatment with inhibitors for 48 h. (a), (b), (c) and (d) refer to treatment with lapatinib, XAV939, 6 μM lapatinib + XAV939 and erlotinib, respectively. (e) Combination index and (f) dose-response curves obtained following combination treatment. Drug combinations with CIs < 1.0 were considered as synergistic. Results expressed as the mean ± SEM are based on at least three independent experiments. The statistical significance was assessed versus that of the untreated cells. The significance level was set at $p < 0.05$ (*), $p < 0.01$ (**), $p < 0.001$ (***) or $p < 0.0001$ (****)

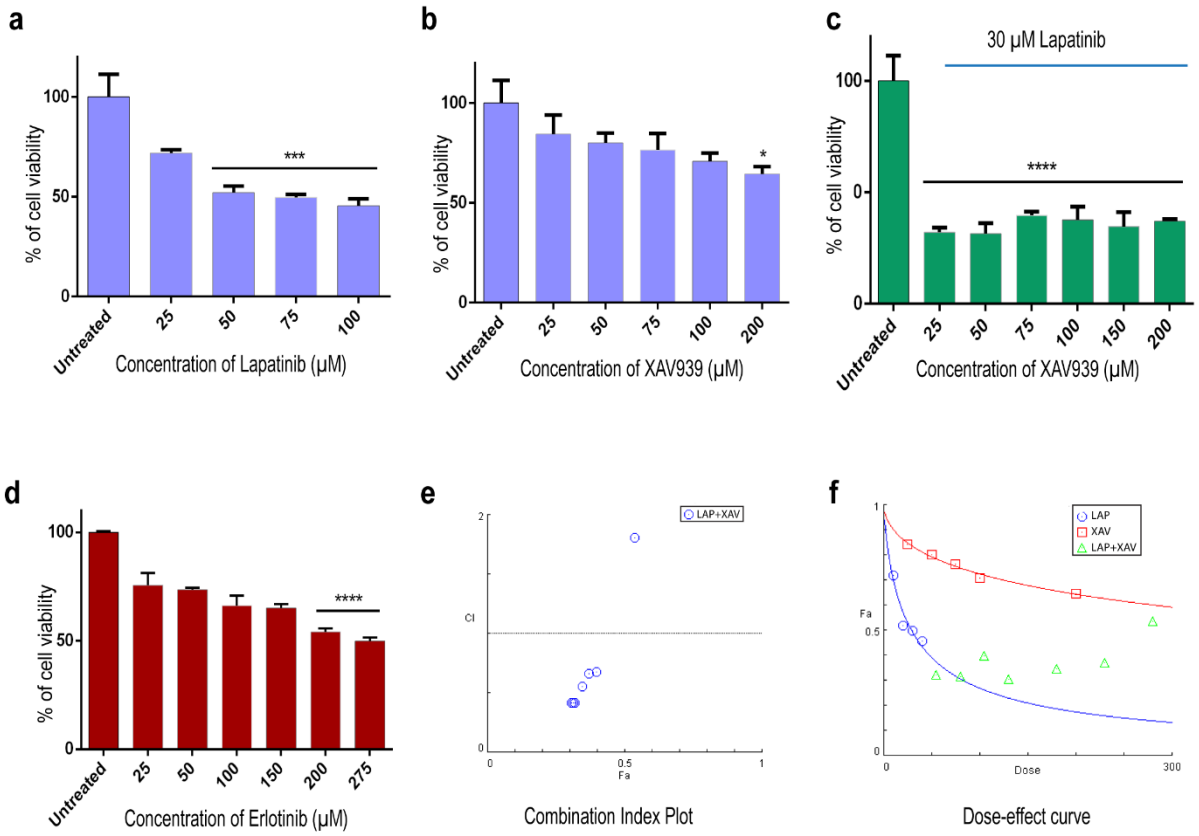

Figure 3.1.6: Determination of viability of MCF-7 spheroids by alamarBlue assay upon treatment with inhibitors for 72 h. (a), (b), (c) and (d) refer to treatment with lapatinib, XAV939, 30 μM lapatinib + XAV939 and erlotinib, respectively. (e) Combination index and (f) dose-response curves obtained following combination treatment. Drug combinations with CIs < 1.0 were considered as synergistic. Results expressed as the mean ± SEM are based on at least three independent experiments. The statistical significance was assessed versus that of the untreated cells. The significance level was set at $p < 0.05$ (*), $p < 0.01$ (**), $p < 0.001$ (***) or $p < 0.0001$ (****)

Live-dead cell imaging of spheroids following treatment provided a clear visualization of the effect of these inhibitors (**Figure. 3.1.7**). The 3D images of the spheroids acquired by z-stack projections are presented in **Figure. 3.1.8**. Fluorescence intensities of the spheroids presented in **Figure. 3.1.7** were quantified and are presented in **Table 3.1.1**. The percentages of live-dead cells were analyzed from the quantified fluorescence intensities and are graphically represented in **Figure. 3.1.9**.

Similar results were also obtained using z-stack projection of live-dead cell staining of MCF-7 spheroids (**Figure. 3.1.10**). Fluorescence intensities of the spheroids presented in **Figure. 3.1.10** were quantified and are presented in **Table 3.1.2**. The percentages of live-dead cells were analyzed from the quantified fluorescence intensities and are graphically represented in **Figure. 3.1.11**.

Moreover, it was found that the co-treatment markedly induced disintegration of the spheroids (**Figure. 3.1.12**). Taken together, these data indicate that modulation of EGFR and Wnt/β-catenin signaling synergistically inhibits TNBC cell survival.

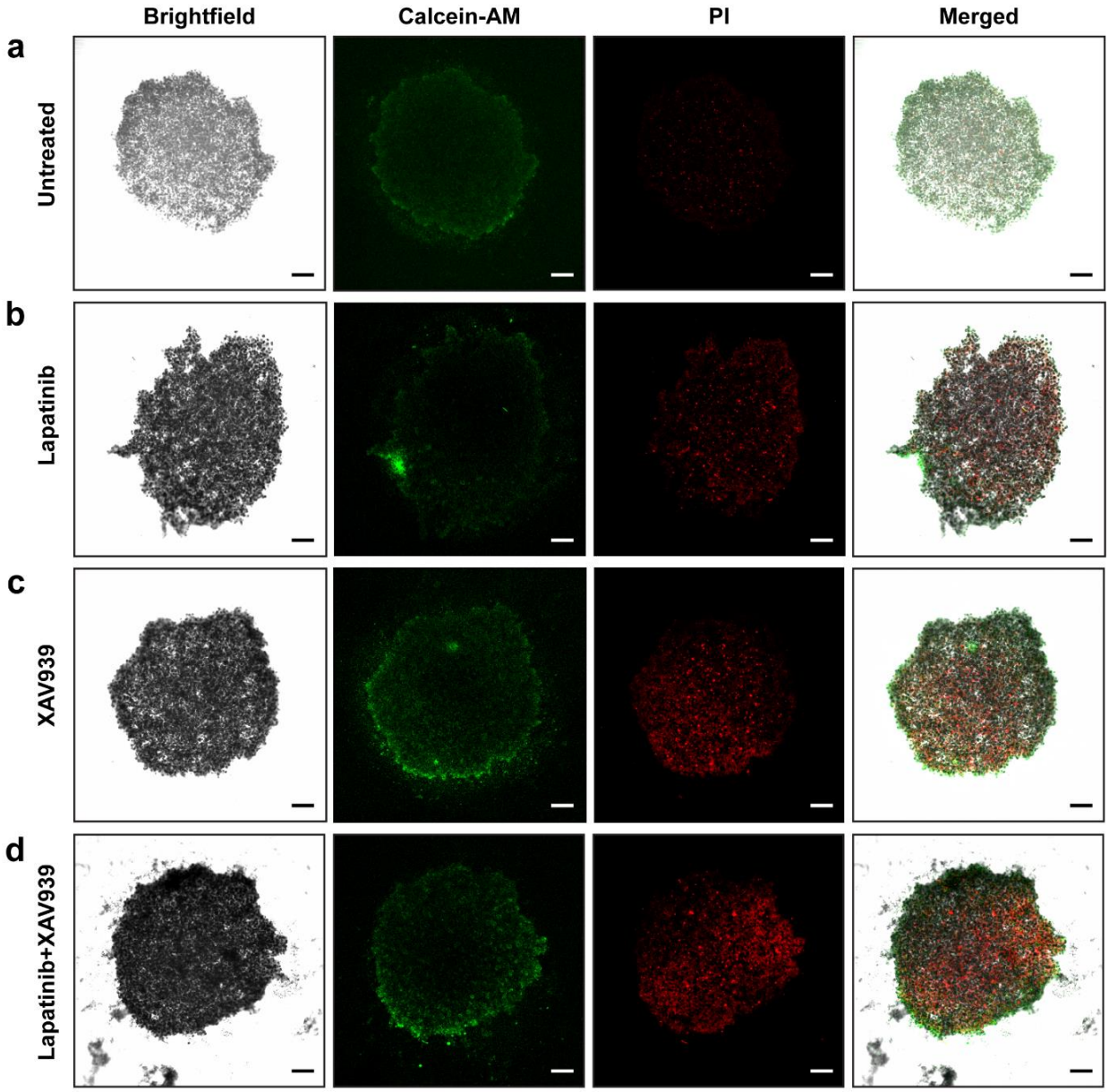

Figure 3.1.7: Live-dead cell visualization of MDA-MB-231 spheroids using calcein-AM/propidium iodide (PI) dual staining. Green fluorescence by calcein-AM refers to live cells, whereas red fluorescence by PI refers to dead cells. (a) Untreated spheroids and (b), (c) and (d) spheroids treated for 72 h with 30 μM lapatinib, 25 μM XAV939 and 30 μM lapatinib + 25 μM XAV939, respectively. Scale bar: 250 μM.

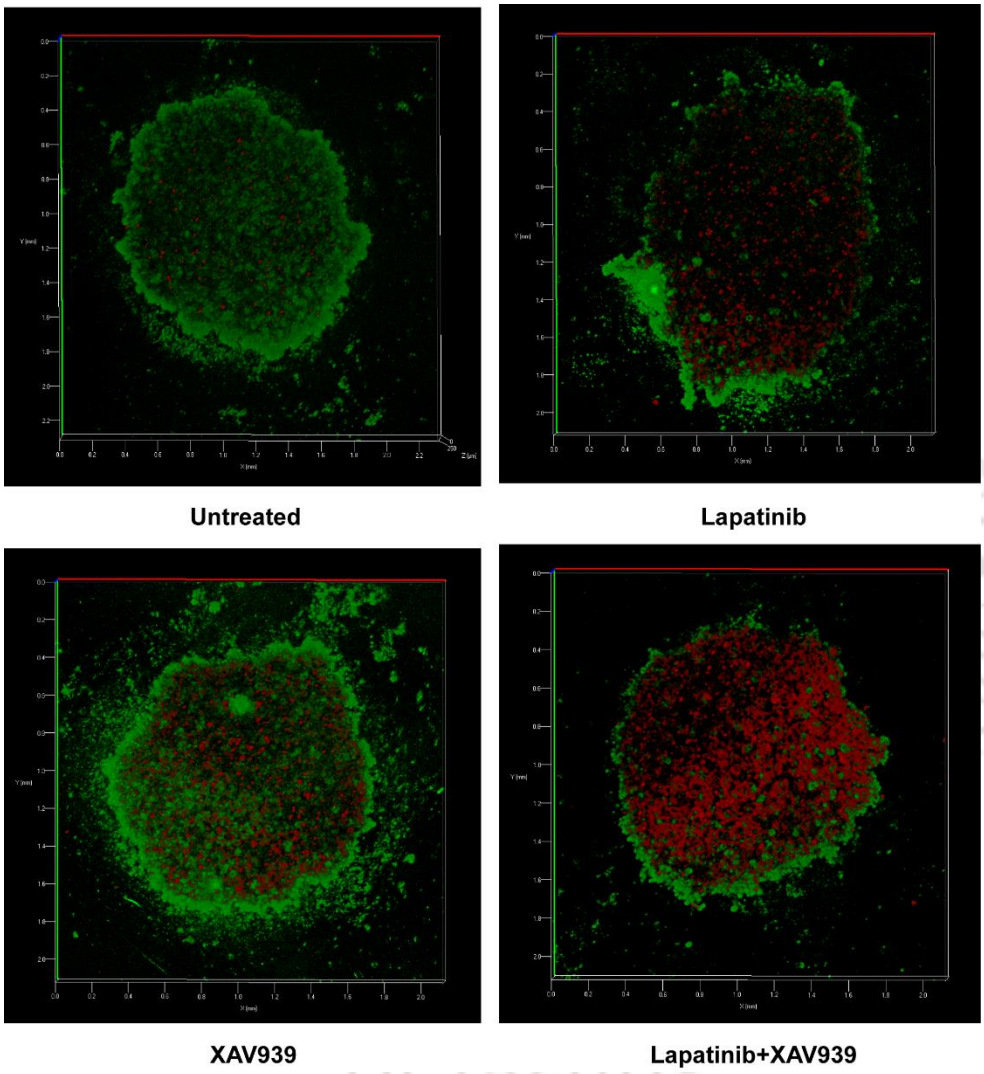

Figure 3.1.8: Z-stack projections of MDA-MB-231 spheroids.

	Corrected total cell fluorescence (CTCF)	
Sample	**Live**	**Dead**
Untreated	21.24	3.26
Lapatinib	9.91	8.09
XAV939	20.01	12.23
Lapatinib+XAV939	13.91	19.64

Table 3.1.1: Fluorescence intensity obtained from live/dead cell imaging of MDA-MB-231 spheroids as presented in **Figure. 3.1.7**.

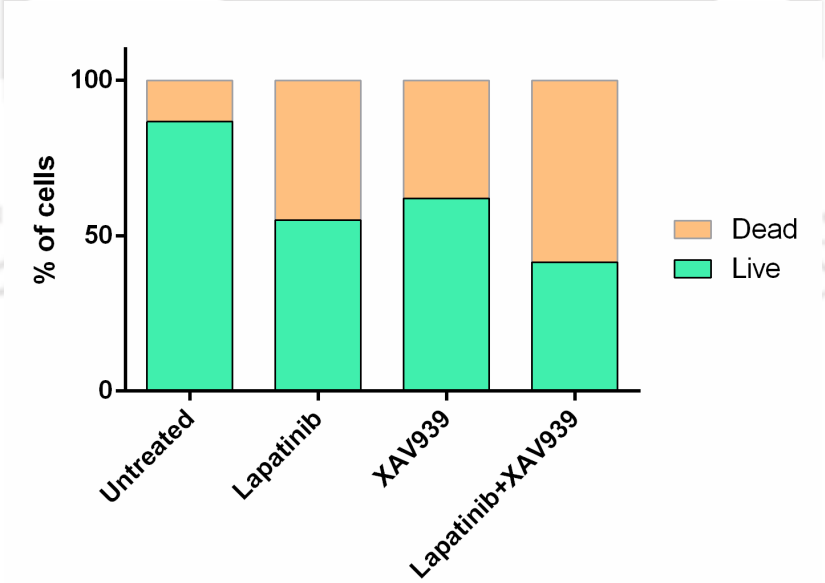

Figure 3.1.9: Graphical representation of the percent normalized corrected total cell fluorescence (CTCF) values obtained from quantification of live/dead cell imaging of MDA-MB-231 spheroids as presented in **Figure. 3.1.7**.

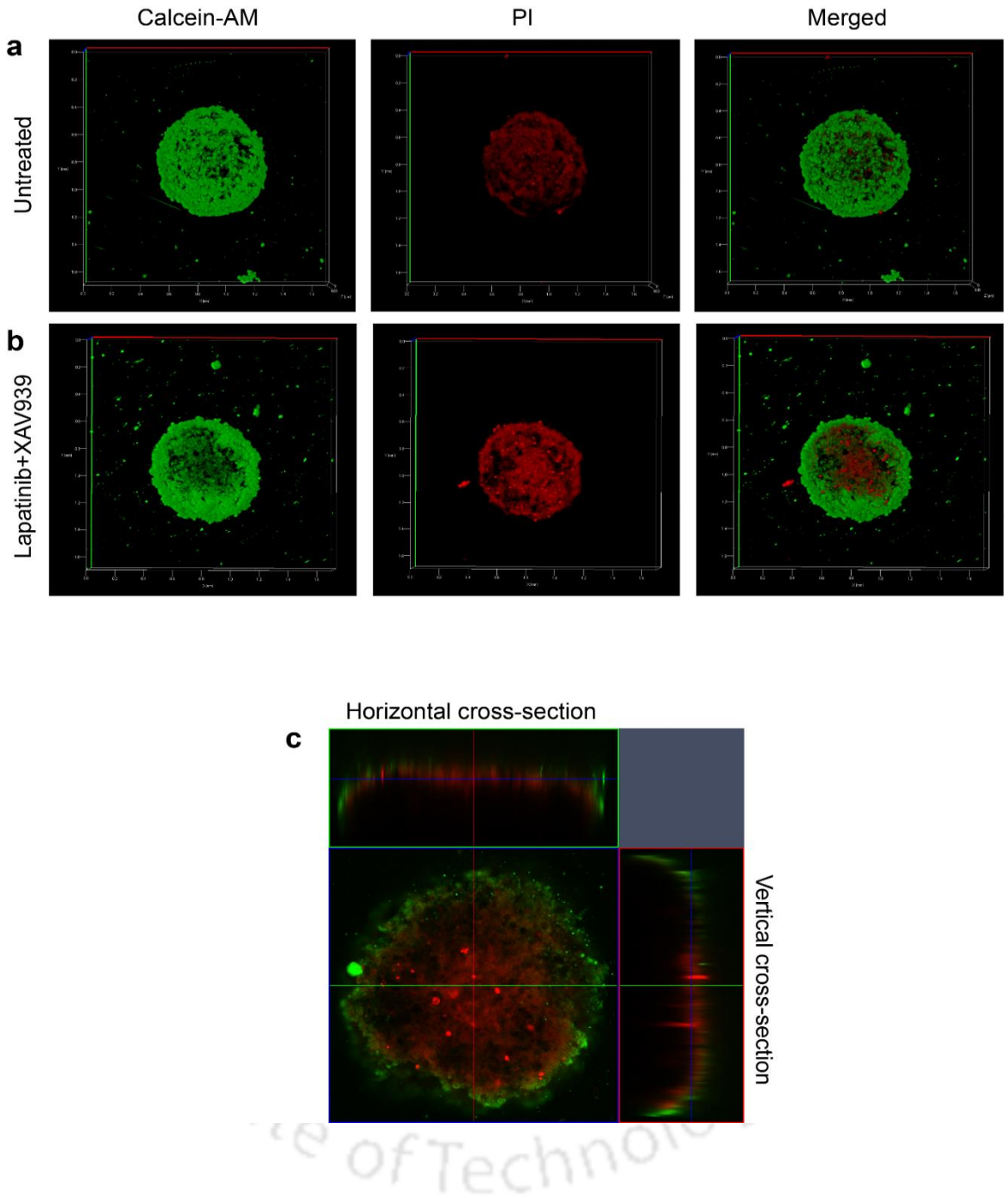

Figure 3.1.10: Live-dead cell visualization of MCF-7 spheroids using calcein-AM/ propidium iodide (PI) dual staining by Z-stack projection. Green fluorescence by calcein-AM refers to live cell whereas red fluorescence by PI refers to dead cell population. (a) Untreated spheroids, (b) spheroids treated for 72 h with 30 μM lapatinib + 25 μM XAV939. (c) 3D-cross section image of treated MCF-7 spheroids representing the dead cells inside the core and live cells on the periphery.

	Corrected total cell fluorescence (CTCF)	
Sample	**Live**	**Dead**
Untreated	35.75514	17.406
Lapatinib+XAV939	31.96878	28.169

Table 3.1.2: Fluorescence intensity obtained from live/dead cell imaging of MCF-7 spheroids as presented in **Figure. 3.1.10**.

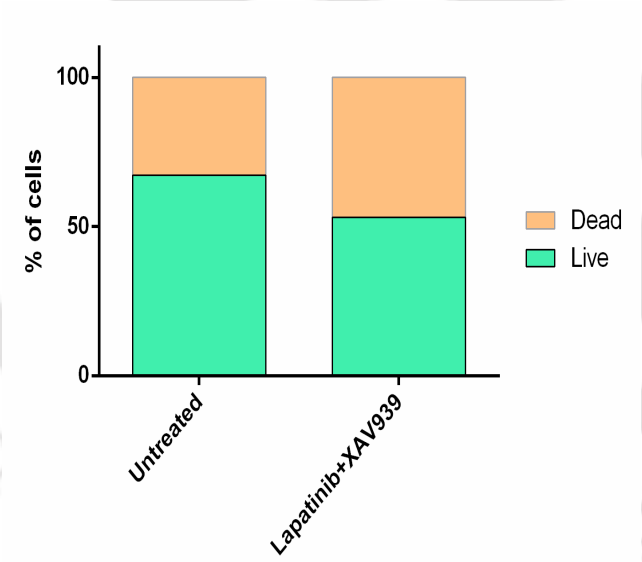

Figure 3.1.11: Graphical representation of the percent normalized corrected total cell fluorescence (CTCF) values obtained from quantification of live/dead cell imaging of MCF-7 spheroids as presented in **Figure. 3.1.10**.

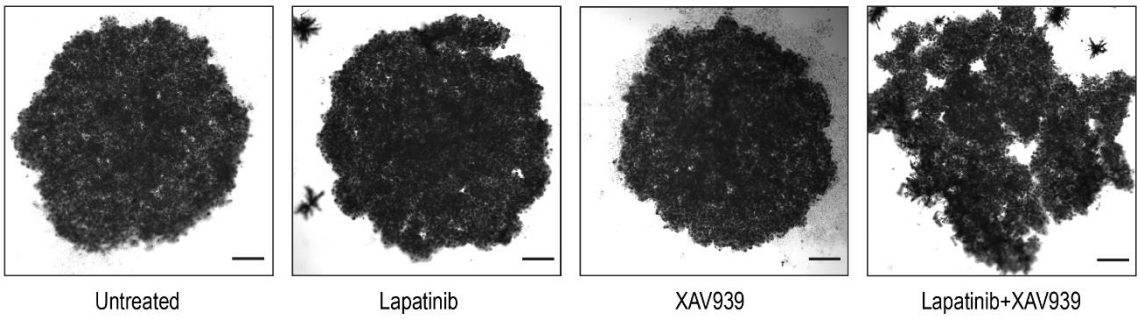

Figure 3.1.12: Visualization of the effect of inhibitors and their combination on MDA-MB-231 spheroids using phase-contrast microscopy. Combination treatment results in visible disintegration of spheroids. Scale bar represents 250 μM.

3.1.1.2. Inhibition of EGFR and Wnt/β-catenin Signaling Results in G0/G1 Cell Cycle Arrest: To better document the effect of EGFR and Wnt/β catenin inhibition on cell growth/survival, cell cycle progression was monitored following 48 h treatment in case of monolayer cultures and 72 h in case of spheroids. A G0/G1 phase cell cycle arrest was observed in both cases. The percentage of G0/G1 phase cells was increased to 16.53% in monolayers and 13% in spheroids (**Figure. 3.1.13 a and b**). Cyclin-D1 and cyclin-dependent kinase-4 (CDK-4) are regulatory proteins responsible for driving cell cycle progression from the G1 to S phase [94]. Thus, the expression levels of cyclin-D1 and CDK-4 were analyzed using qRT-PCR to better understand the mechanism of action of the inhibitors. The expression levels of cyclin-D1 and CDK-4 were found to be down-regulated by 3.57-fold and 3.33-fold, respectively (**Figure. 3.1.14 a and b**). Therefore, it was concluded that modulation of the EGFR and Wnt/β-catenin signaling pathway ablates cyclin-D1 and CDK-4, leading to G0/G1 cell cycle arrest.

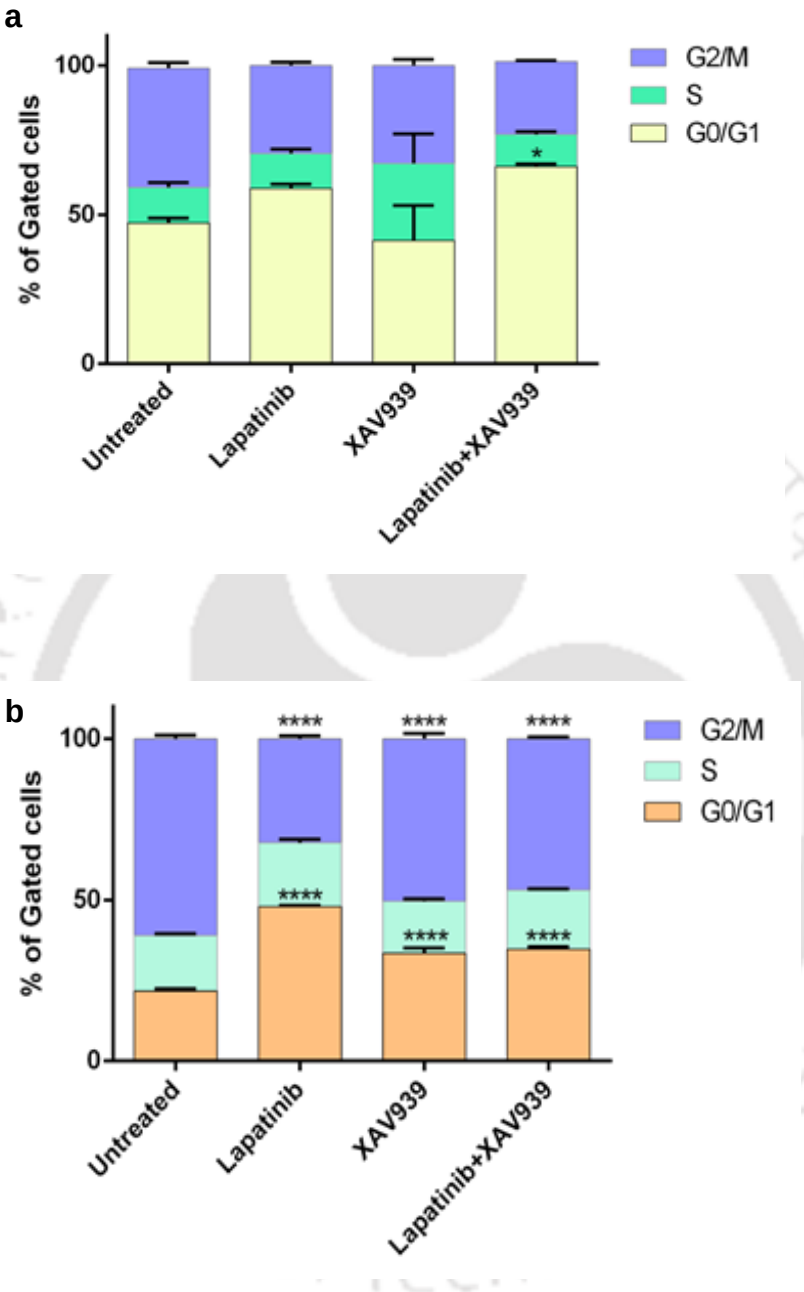

Figure 3.1.13: Evaluation of cell cycle profile of MDA-MB-231 (a) monolayer cultures and (b) spheroids. A G0/G1 phase cell cycle arrest was observed in both monolayer culture and spheroids following treatment.

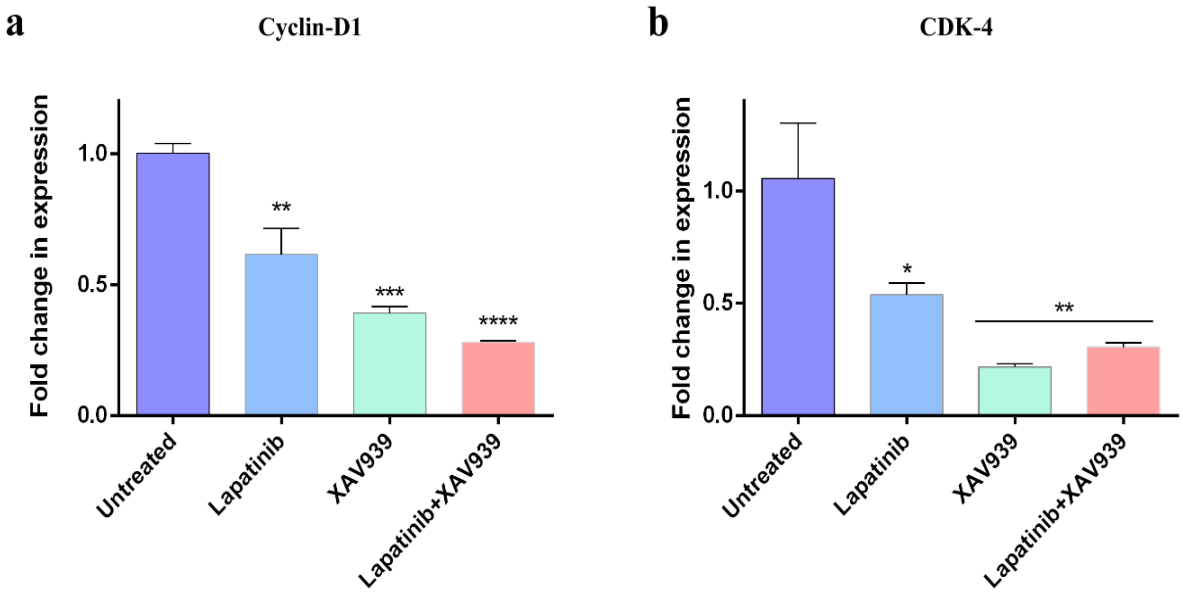

Figure 3.1.14: Graphical representation of changes in gene expression levels of MDA-MB-231 monolayer cultures following treatment with Lapatinib and XAV939 for 48 h quantified by qRT-PCR analysis. (a) represents the gene expression level of Cyclin-D1 and (b) represents the gene expression level of CDK-4. Results are expressed as mean relative gene expression level compared to (GAPDH) ± SEM of three independent experiments, with $p < 0.05$ (*), $p < 0.01$ (**), $p < 0.001$ (***), $p < 0.0001$ (****).

3.1.1.3. Suppression of EGFR and Wnt/β-catenin Signaling Generates ROS, Depolarizes Mitochondrial Membrane Potential and Induces Apoptosis: In an attempt to explicate the mechanism underlying cell death, the generation of ROS and mitochondrial membrane integrity were examined. Cellular ROS levels were detected using 2′,7′-dichlorodihydrofluorescein diacetate (DCFDA)-based flow cytometry [95]. The flow cytometric analyses showed that lapatinib and XAV939 in combination generated a 3.3-fold increase in ROS compared to the respective untreated controls (**Figure. 3.1.15 a**). The combined administration did, however, not increase ROS generation in spheroids (**Figure. 3.1.15 b**). Similar to MDA-MB-231, increase in ROS generation was also detected in MDA-MB-468 (**Figure. 3.1.16**) and MCF-7 (**Figure. 3.1.17**) monolayer culture and spheroids following treatment.

An elevated ROS level manifests its detrimental effect on the integrity of the mitochondrial membrane and its associated trans-membrane potential [96]. The effect of ROS accumulation on mitochondrial membrane integrity was assessed using JC-1-based flow cytometry. The cyanine dye JC-1 (5,5′,6,6′-tetrachloro-1,1′,3,3′-tetraethylbenzimi-dazolylcarbocyanine iodide) forms red aggregates in polarized mitochondria, whereas it remains as a monomer in depolarized mitochondria [84]. A prominent red fluorescence from healthy mitochondria and a ~ 37% increase in green fluorescence from treated cells was observed, suggesting mitochondrial membrane depolarization (**Figure. 3.1.18**). Increase in green fluorescence from treated cells was also observed in MDA-MB-468 (**Figure. 3.1.19**) and MCF-7 (**Figure. 3.1.20**).

Cells react rapidly to redox imbalance with a plethora of biological responses, including cell cycle-specific growth arrest, transcription-coupled repair of damaged DNA and apoptosis. Following the trail of ROS generation and mitochondrial membrane potential disruption, the percentage of apoptotic cells was examined after combination treatment. Using flow cytometry, it was detected that co-therapy increased apoptotic cell populations by approximately 41.19% and 20% in monolayer cultures and spheroids, respectively (**Figure. 3.1.21 a and b**).

Similar results were obtained with MDA-MB-468 and MCF-7 cells (**Figure. 3.1.22** and **Figure. 3.1.23**). The percentages of apoptotic cell populations following co-treatment are listed in **Table 3.1.3**.

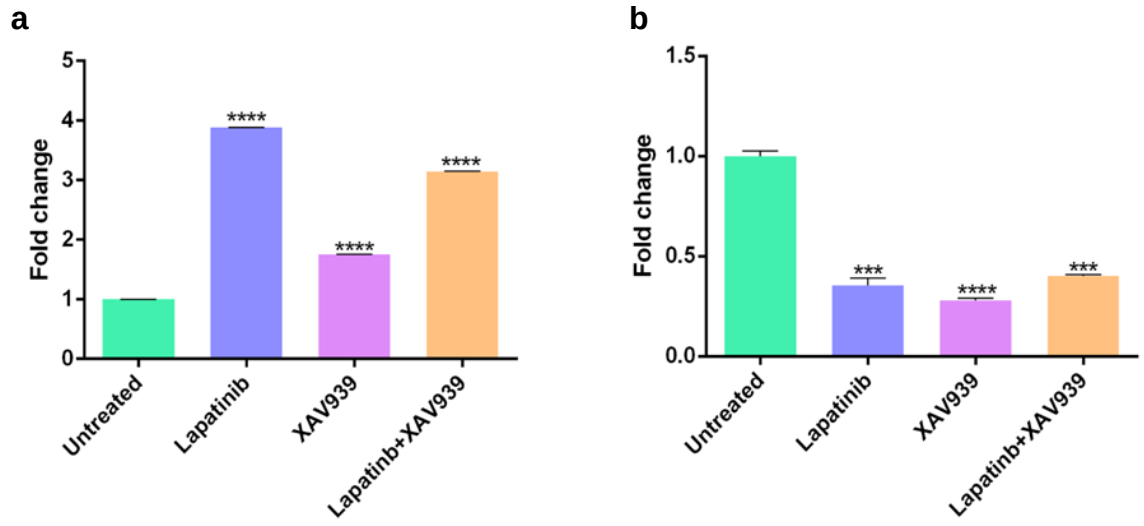

Figure 3.1.15: Cellular reactive oxygen species detection using a DCFDA-based flow cytometric assay in MDA-MB-231 (a) monolayer cultures and (b) spheroids

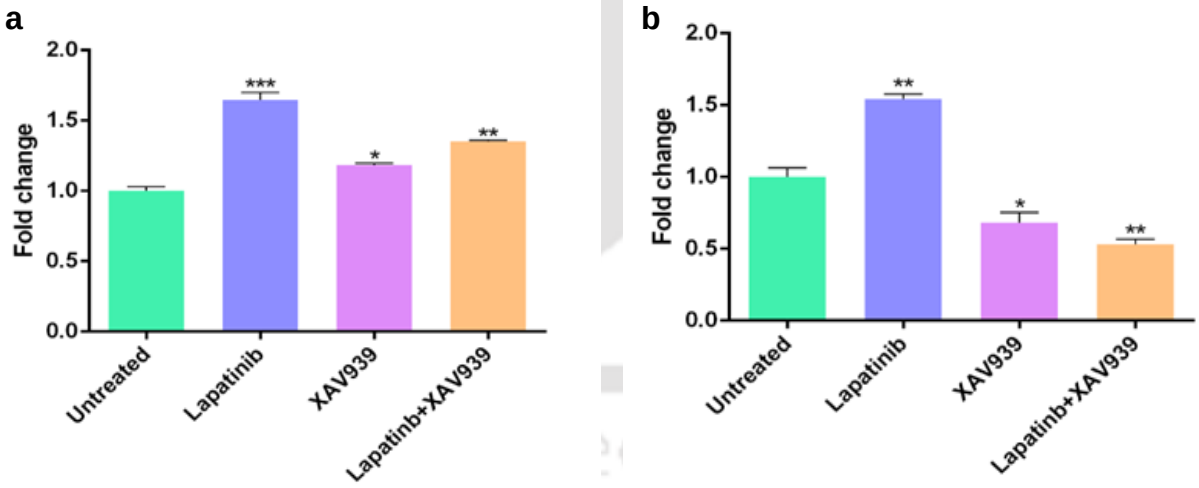

Figure 3.1.16: Cellular reactive oxygen species detection using a DCFDA-based flow cytometric assay in MDA-MB-468 (a) monolayer cultures and (b) spheroids

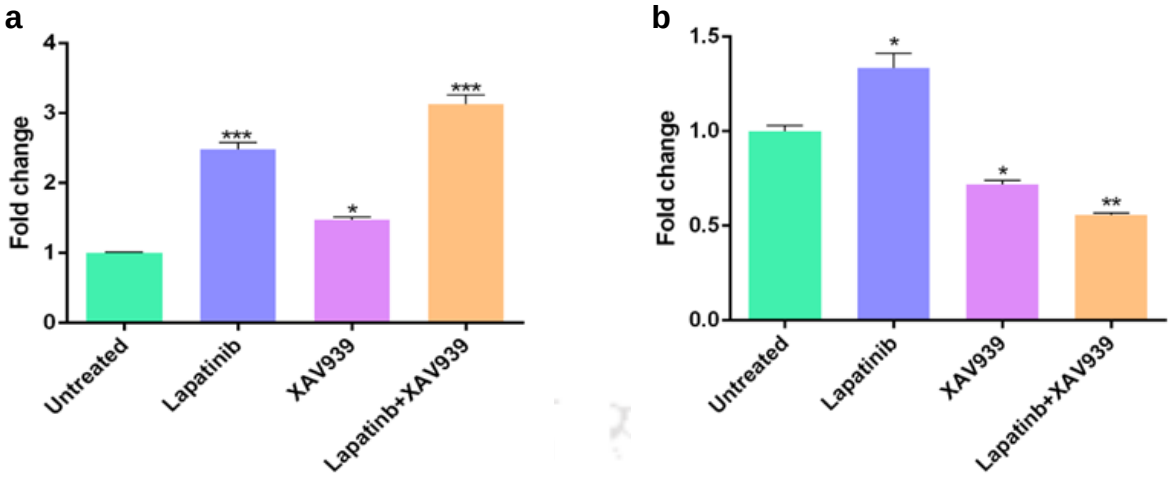

Figure 3.1.17: Cellular reactive oxygen species detection using a DCFDA-based flow cytometric assay in MCF-7 (a) monolayer cultures and (b) spheroids.

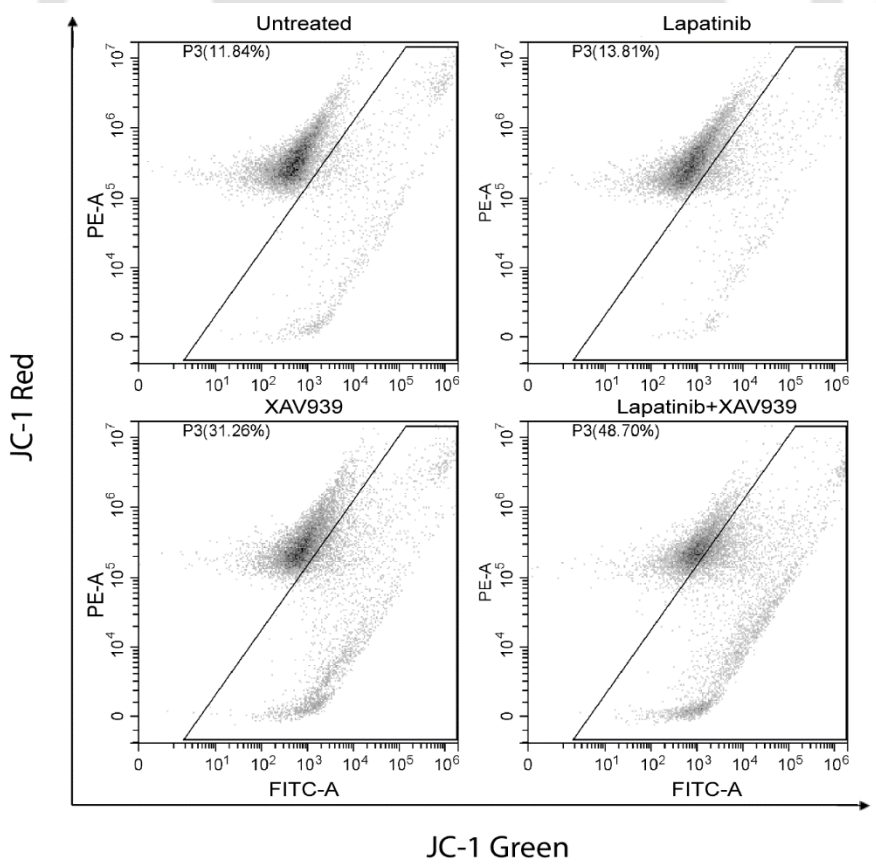

Figure 3.1.18: Mitochondrial membrane potential detection of MDA-MB-231 monolayer cells using JC-1 staining.

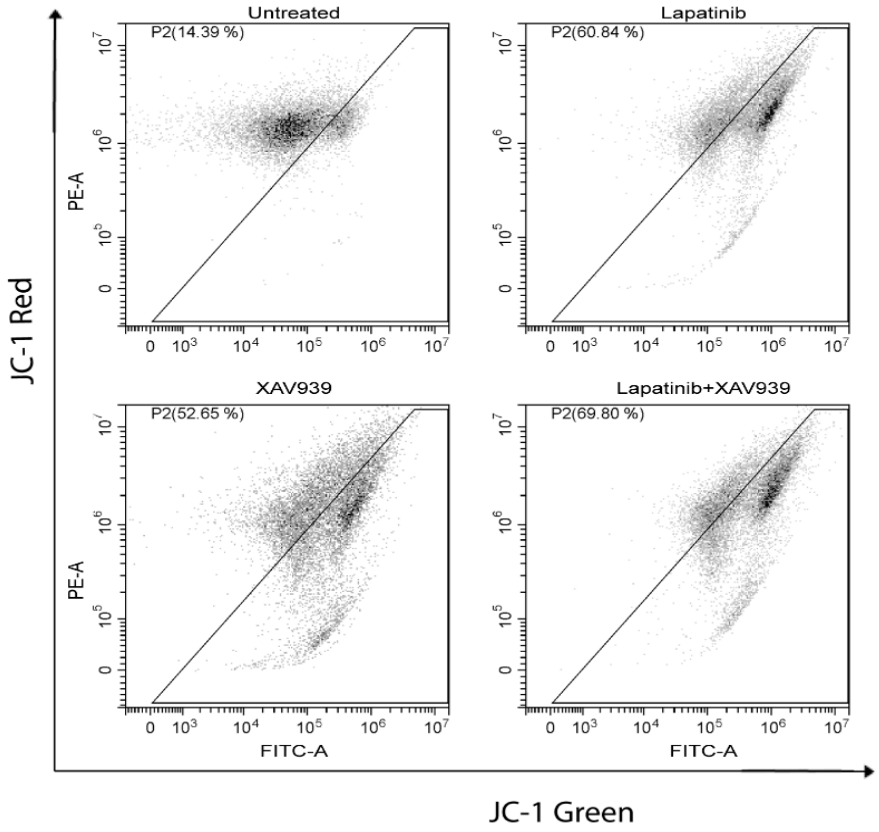

Figure 3.1.19: Mitochondrial membrane potential detection of MDA-MB-468 monolayer cells using JC-1 staining.

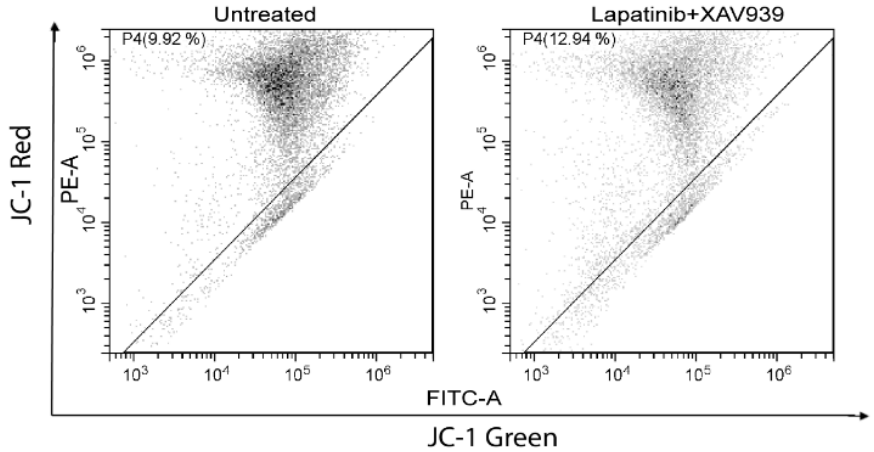

Figure 3.1.20: Mitochondrial membrane potential detection of MCF-7 monolayer cells using JC-1 staining

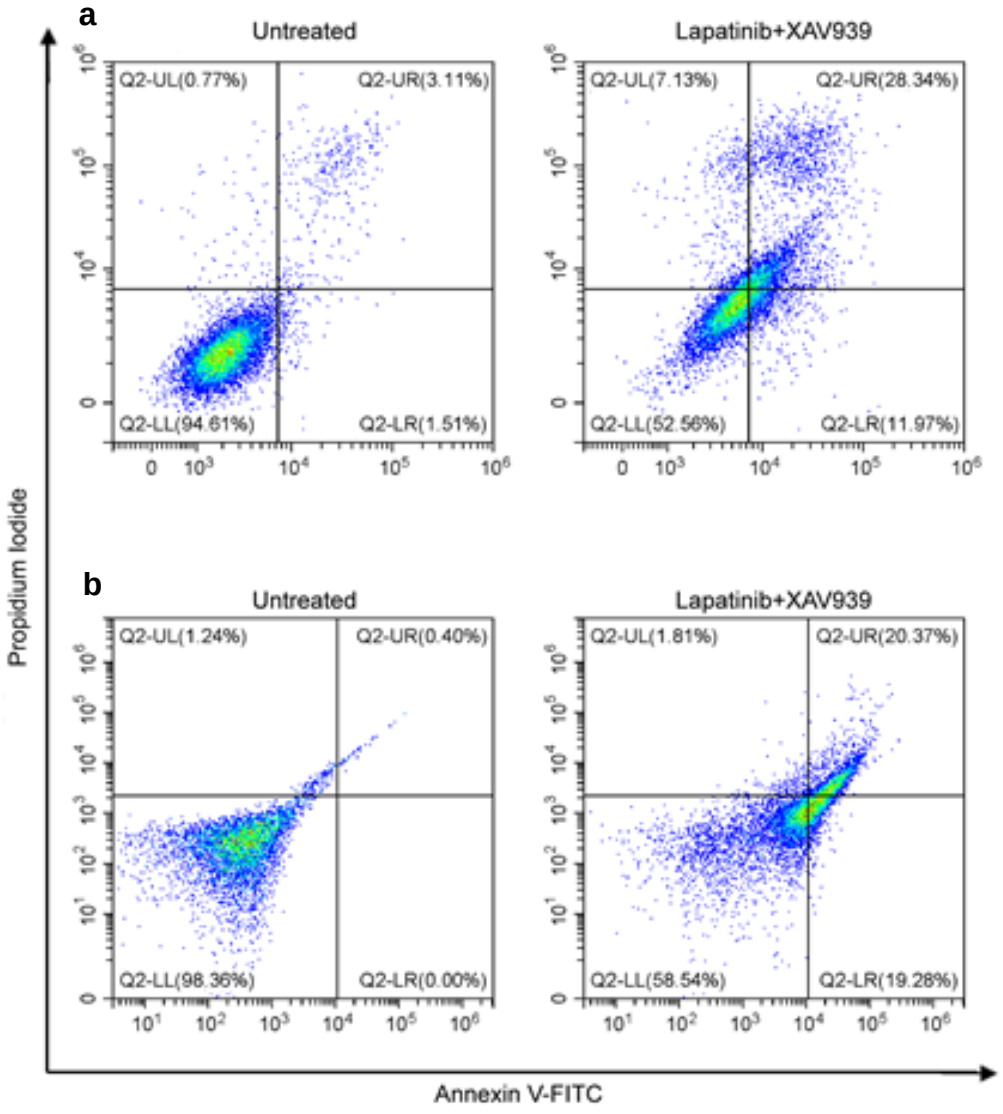

Figure 3.1.21: Flow cytometric analysis of apoptotic populations probed by annexin-V-FITC PI assay following treatment in MDA-MB-231 (a) monolayer cultures and (b) spheroids.

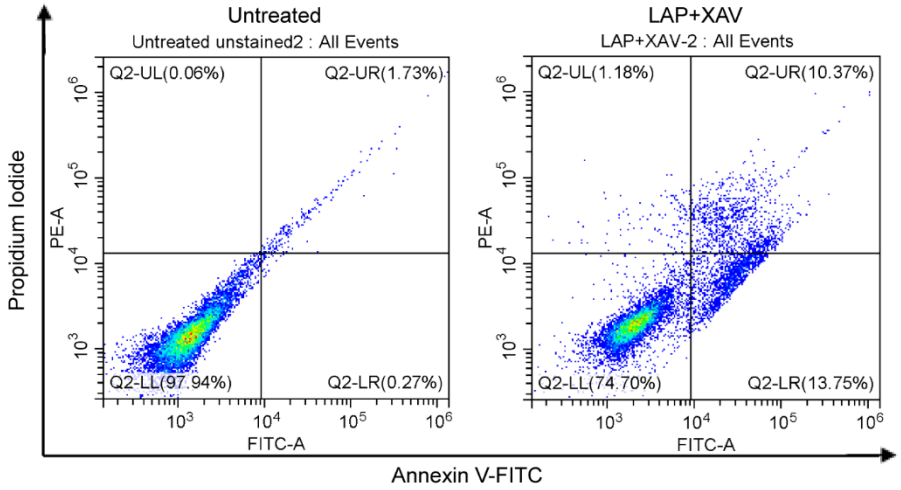

Figure 3.1.22: Flow cytometric analysis of apoptotic populations probed by annexin-V-FITC PI assay following treatment in MDA-MB-468.

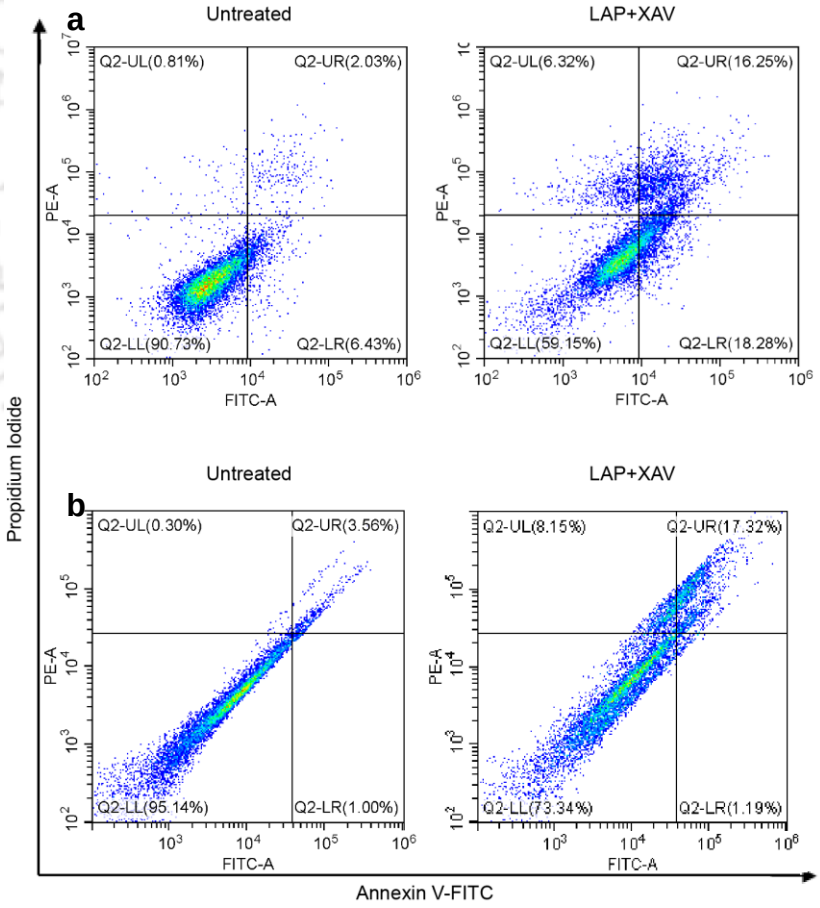

Figure 3.1.23: Flow cytometric analysis of apoptotic populations probed by annexin-V-FITC PI assay following treatment in MCF-7 (a) monolayer cultures and (b) spheroids.

% of apoptotic cells				
	Monolayer		**Spheroid**	
Cell Lines	**Untreated**	**Lapatinib+XAV939**	**Untreated**	**Lapatinib+XAV939**
MDA-MB-231	5.39	47.44	1.64	41.46
MDA-MB-468	2.06	25.348	1.71	23.95
MCF-7	9.27	40.85	4.8	27.06

Table 3.1.3: Tabular representation of increase in apoptotic cell population following treatment with Lapatinib+XAV939.

3.1.1.4. Inactivation of EGFR and Wnt/β-catenin Signaling Induces Mesenchymal-Epithelial Transition (MET): In the EMT process, tumor-associated epithelial cells obtain mesenchymal features with reduced cell-cell contacts and an increased motility, which play critical roles in invasion and metastasis. Both EGFR and Wnt/β-catenin signaling are crucial in EMT. Therefore, qRT-PCR was performed to evaluate changes in the expression of epithelial and mesenchymal markers under treated conditions. Loss of E-cadherin-mediated adhesion characterizes the transition from benign lesions to invasive, metastatic cancers [97]. Following combination treatment, E-cadherin was found to be upregulated by 5.7-fold. XAV939 alone upregulated E-cadherin expression by 2.5-fold, whereas lapatinib was found to be ineffective (**Figure. 3.1.24**). Vimentin and N-cadherin are major markers of EMT [98, 99]. Although co-therapy did not alter the vimentin and N-cadherin levels, lapatinib treatment increased their expression levels by 3.35-fold and 6.10-fold, respectively (**Figure. 3.1.24**). Significant changes in Fibronectin gene expression was not detected (**Figure. 3.1.24).** The expression level of key EMT-related proteins such as E-cadherin, N-cadherin and vimentin, was carried out using Western blot analysis. E-cadherin was found to be upregulated by 1.73-fold following combination treatment (**Figure. 3.1.25 a**), whereas, N-cadherin and vimentin were found to be downregulated by 3-fold and 2.18-fold, respectively (**Figure. 3.1.25 b**).

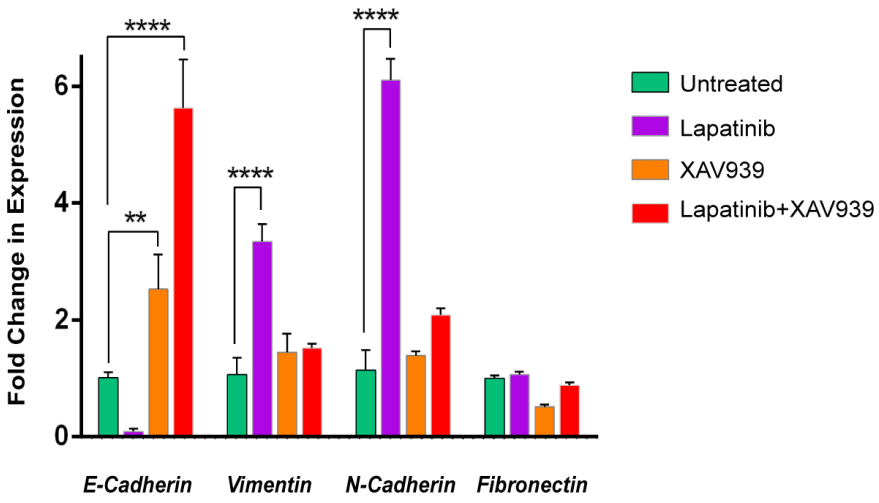

Figure 3.1.24: Graphical representation of changes in gene expression levels obtained from MDA-MB-231 monolayer cultures following inhibitor treatment quantified by qRT-PCR analysis.

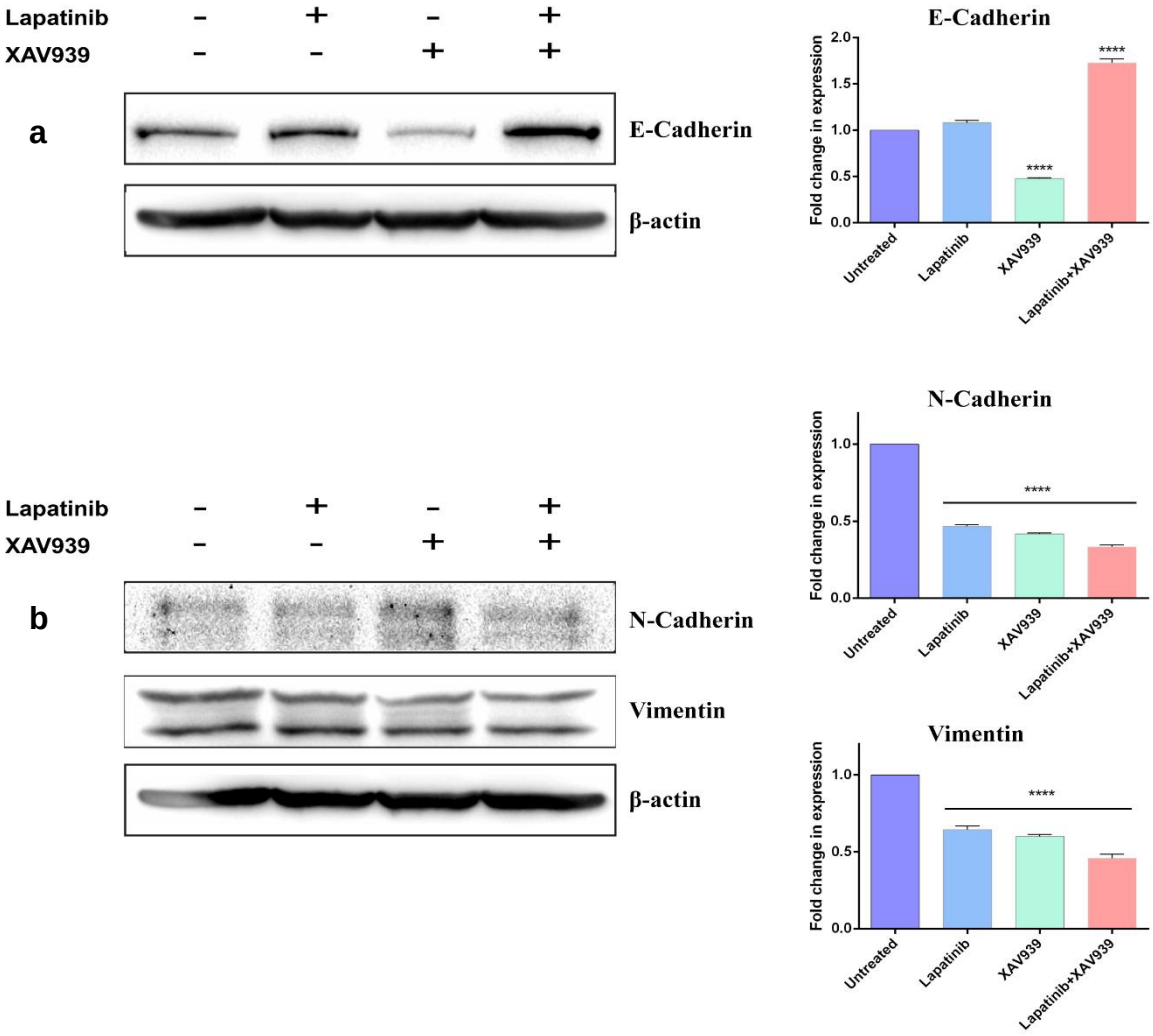

Figure 3.1.25: Representative Western blots showing E-cadherin, N-cadherin and Vimentin levels in cellular extracts of MDA-MB-231 monolayer cultures. For monolayer cultures, cells were treated with inhibitors for 48 h, where the concentration of lapatinib is 6 μM and of XAV939 is 50 μM. β-actin serves as a loading control. Graphs represent the changes in the expression levels of E-cadherin, N-cadherin and Vimentin with respect to untreated samples following inhibitor treatment. The expression levels were deduced from the blots using ImageJ software.

Besides EMT markers, some important proteins and transcription factors, such as Ki-67, Twist and SNAI2, are also implicated in the process of EMT. Although no significant alterations were observed for the transcription factors Twist and SNAI2, EpCAM and Ki-67 were found to be downregulated by 3.3-fold and 2.9-fold after combination therapy, respectively (**Figure. 3.1.26 and Figure. 3.1.27**).

The combination effect was also examined in tumor spheroids by qRT-PCR. Unlike in the monolayer cells, vimentin expression was low, and E-cadherin expression was only marginally elevated, even after 72 h of treatment (**Figure. 3.1.28**). However, other EMT markers such as N-cadherin and fibronectin were not found to be significantly altered after combination treatment (**Figure. 3.1.28**). While combination treatment led to decreased Twist1 expression, lapatinib alone increased its expression by two-fold. SNAI2 was upregulated under both treatment conditions (**Figure. 3.1.29**). Exogenous EpCAM expression in TNBC cells has been found to promote EMT, to induce a CSC-like phenotype and to enhance metastasis *in vitro* and *in vivo* [100]. It was found that after combination treatment, EpCAM was downregulated by 3.30-fold in monolayers but remained unaltered in spheroids (**Figure. 3.1.30**).

Expression analysis of key EMT related proteins were also carried out in spheroids. Remarkably, a 14.3-fold decrease in vimentin expression was observed in MDA-MB-231 spheroids following co-treatment (**Figure. 3.1.31**). Expression analysis of EMT-related proteins in two other cell lines, MDA-MB-468 and MCF-7, yielded similar EMT reversal results (**Figure. 3.1.32 and Figure. 3.1.33**). E-cadherin was, however, found to be downregulated in MCF-7 cells. The fold change in protein expression of EMT markers are presented in **Table. 3.1.4**.

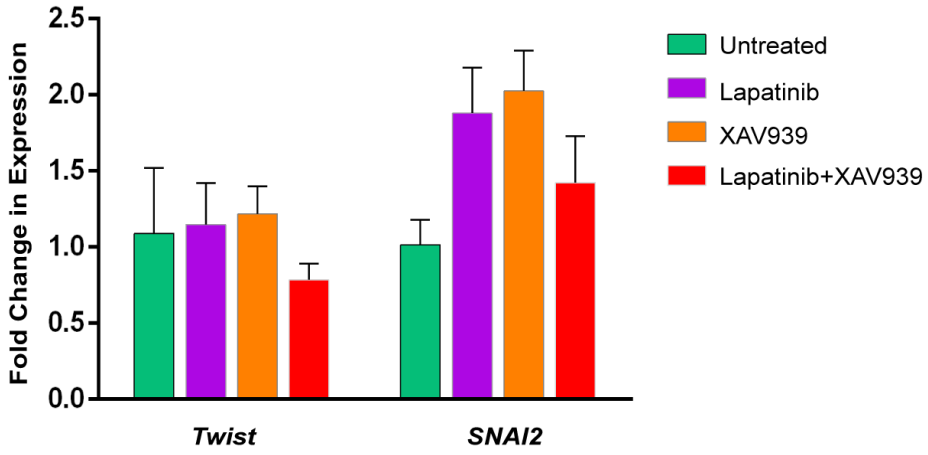

Figure 3.1.26: Graphical representation of changes in gene expression levels obtained from MDA-MB-231 monolayer cultures following inhibitor treatment quantified by qRT-PCR analysis.

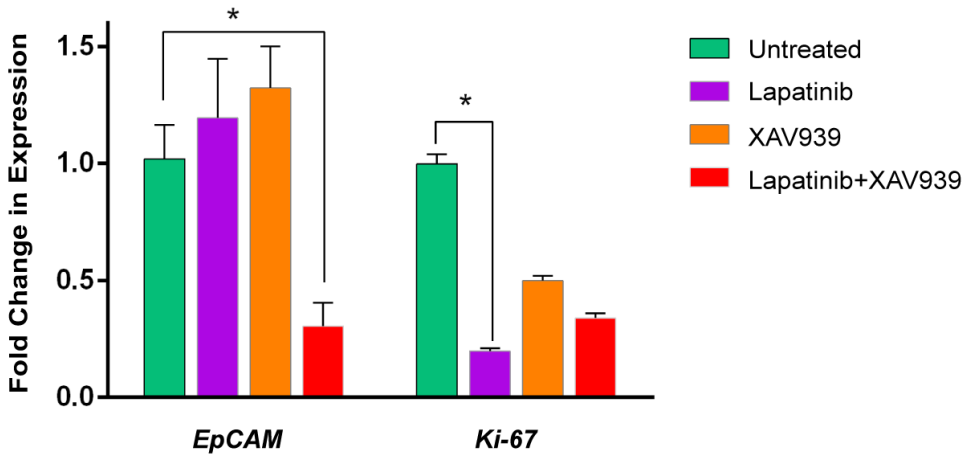

Figure 3.1.27: Graphical representation of changes in gene expression levels obtained from MDA-MB-231 monolayer cultures following inhibitor treatment quantified by qRT-PCR analysis.

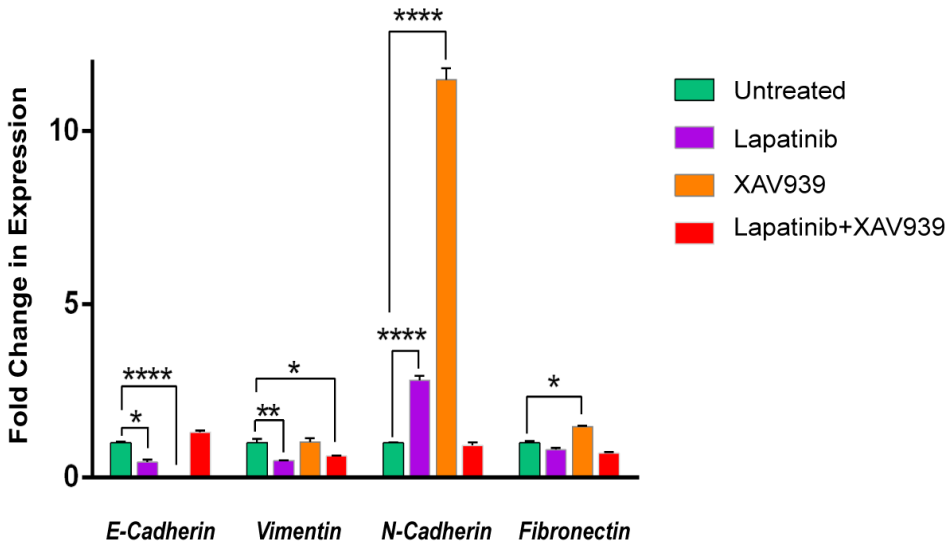

Figure 3.1.28: Graphical representation of changes in gene expression levels obtained from MDA-MB-231 spheroids following inhibitor treatment quantified by qRT-PCR analysis.

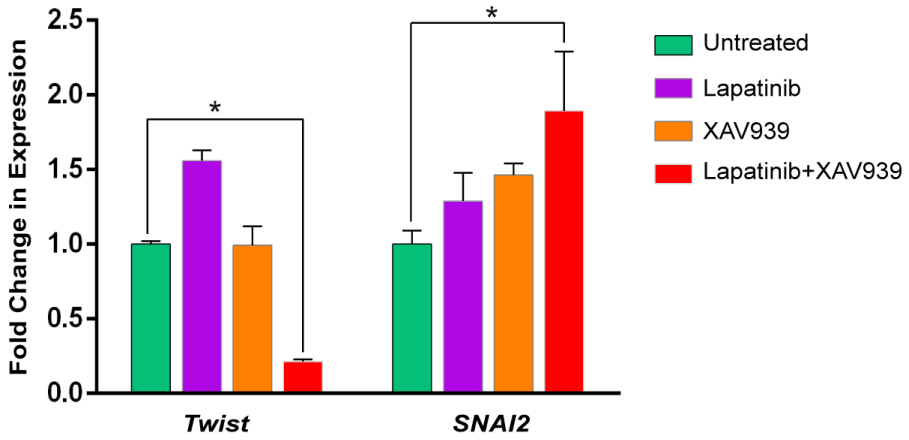

Figure 3.1.29: Graphical representation of changes in gene expression levels obtained from MDA-MB-231 spheroids following inhibitor treatment quantified by qRT-PCR analysis.

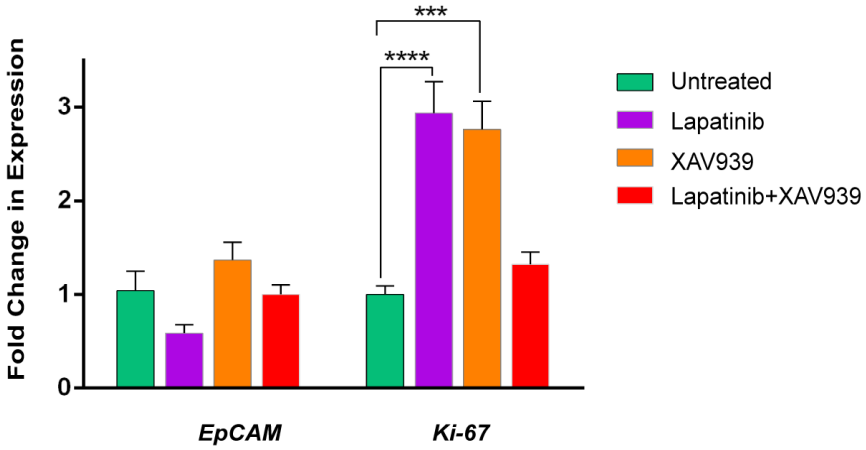

Figure 3.1.30: Graphical representation of changes in gene expression levels obtained from MDA-MB-231 spheroids following inhibitor treatment quantified by qRT-PCR analysis.

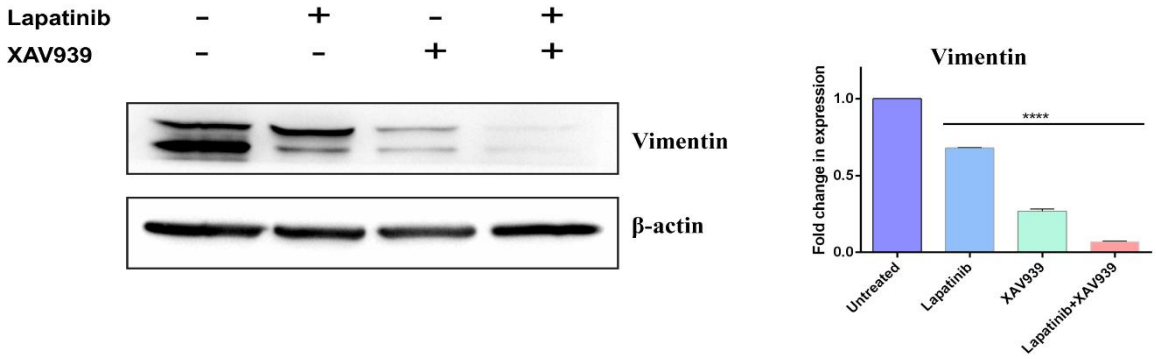

Figure 3.1.31: Representative Western blots showing Vimentin levels in cellular extracts of MDA-MB-231 spheroids. Spheroids were treated using 30 μM lapatinib and 25 μM XAV939 for 72 h. β-actin serves as a loading control. Graphs represent the changes in the expression level Vimentin with respect to untreated samples following inhibitor treatment. The expression levels were deduced from the blots using ImageJ software.

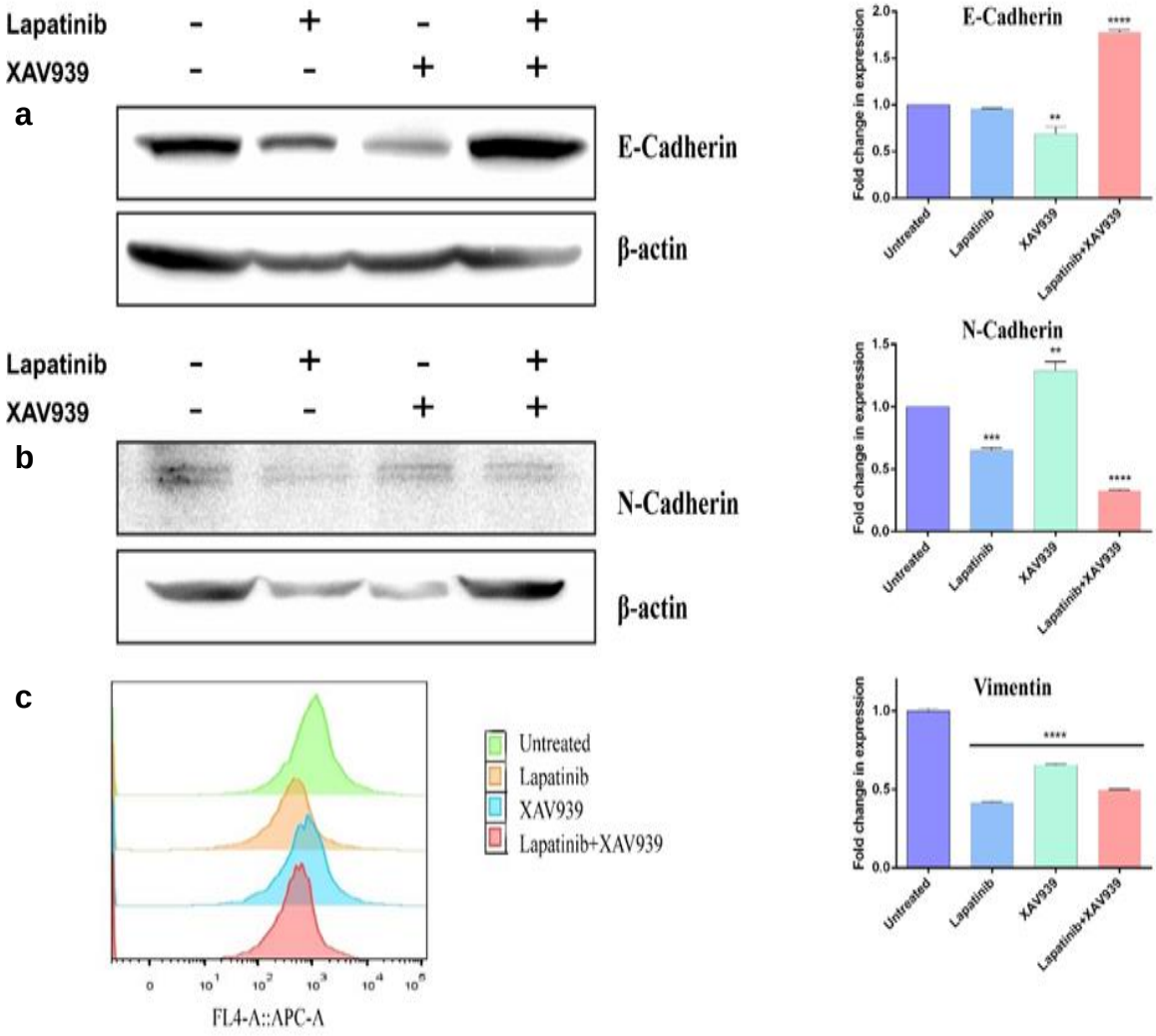

Figure 3.1.32: Representative Western blots showing (a) E-cadherin and (b) N-cadherin levels in cellular extracts of MDA-MB-468 monolayer cultures. β-actin serves as a loading control. (c) The histogram of immunofluorescence flowcytometry detecting Vimentin of MDA-MB-468 monolayer cultures. Graphs represent the changes in the expression levels of E-cadherin, N-cadherin and Vimentin with respect to untreated samples following inhibitor treatment. The expression levels were deduced from the blots using ImageJ software.

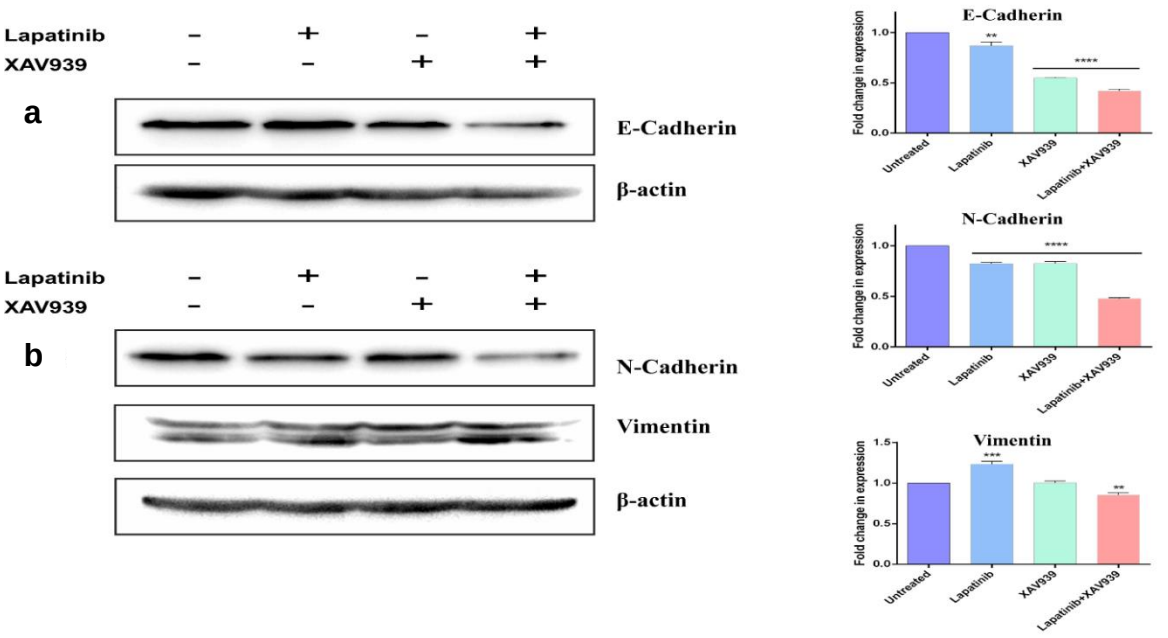

Figure 3.1.33: Representative Western blots showing (a) E-cadherin and (b) N-cadherin and Vimentin levels in cellular extracts of MCF-7 monolayer cultures. β-actin serves as a loading control. Graphs represent the changes in the expression levels of E-cadherin, N-cadherin and Vimentin with respect to untreated samples following inhibitor treatment. The expression levels were deduced from the blots using ImageJ software.

	Fold change in protein expression		
Protein	**MDA-MB-231**	**MDA-MB-468**	**MCF-7**
E-cadherin	1.73 ↑	1.78 ↑	2.38 ↓
N-cadherin	3 ↓	3.1 ↓	2.1 ↓
Vimentin	2.18 ↓	2 ↓	1.17 ↓

Table. 3.1.4: Tabular representation of fold change of EMT markers with respect to untreated control cells following treatment with Lapatinib+XAV939.

MDM2 plays a critical role in controlling p53 and, thus, apoptosis. MDM2 acts as a cellular antagonist of p53 [101]. It has also been reported that MDM2 increases drug resistance through inducing EMT independent of p53 [102]. Co-targeting EGFR and Wnt/β-catenin led to a decreased MDM2 level both in monolayers (1.26-fold) and tumor spheroids (4.16-fold), which incurred cell death following co-treatment (**Figure. 3.1.34 and Figure. 3.1.35**). It is well-known that caveolin-1 overexpression is correlated with migration, metastasis and drug resistance [103]. Co-treatment reduced the caveolin-1 expression level by 1.72-fold and 1.50-fold in monolayers and spheroids, respectively (**Figure. 3.1.34 and Figure. 3.1.35**). Together, these findings indicate that combined treatment with EGFR and Wnt/β catenin signaling inhibitors induces MET and concomitant reductions in the metastatic and invasive potentials of TNBC cells.

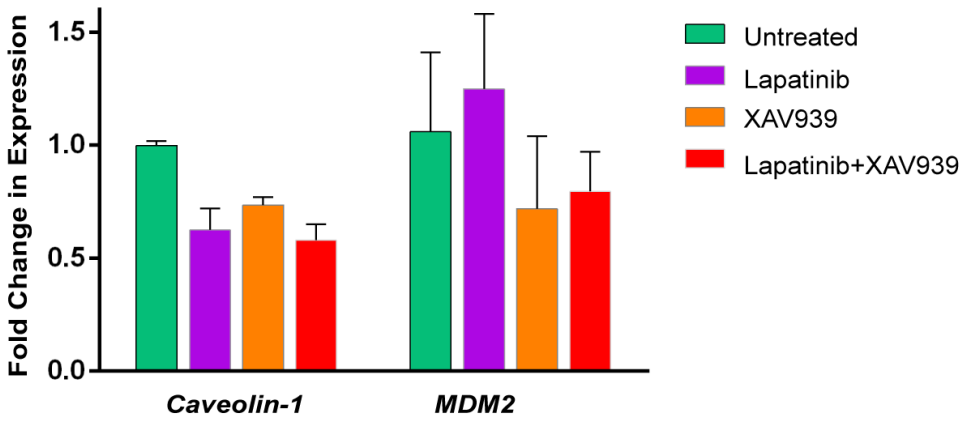

Figure 3.1.34: Graphical representation of changes in gene expression levels obtained from MDA-MB-231 monolayer culture following inhibitor treatment quantified by qRT-PCR analysis.

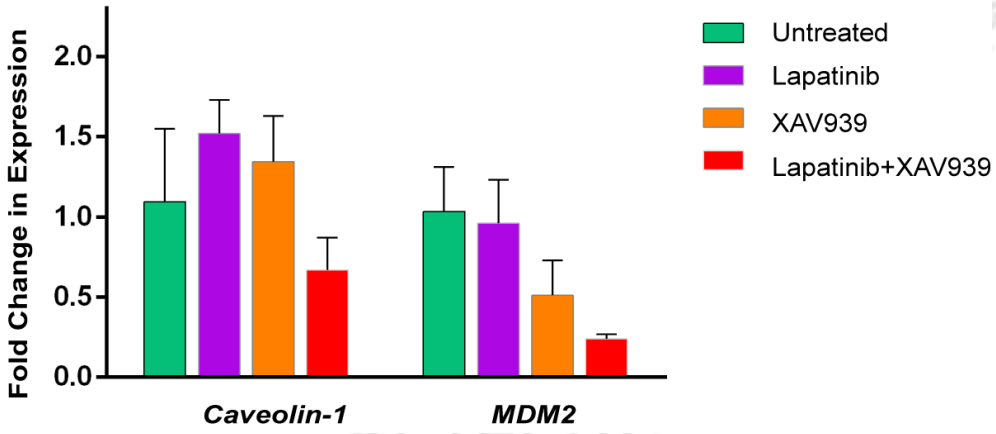

Figure 3.1.35: Graphical representation of changes in gene expression levels obtained from MDA-MB-231 spheroids following inhibitor treatment quantified by qRT-PCR analysis.

3.1.1.5. Co-targeting EGFR and Wnt/β-catenin Signaling Decreases TNBC Cell Migration and Invasion: During the process of EMT, epithelial cells reverse their morphology into mesenchymal cells and gain increased abilities for migration and invasion, which could result in metastasis. Since both EGFR and Wnt/β-catenin signaling are implicated in the migration and invasion of TNBC cells, the combined effect of lapatinib and XAV939 was investigated on the migration and invasion of MDA-MB-231 cells. Migration was assessed using a scratch wound-healing assay, where the migration rate of the cells towards the wound area (created using a scratch) was determined. Cells incubated with lapatinib, XAV939 and in combination showed slower wound healing abilities than the untreated cells. The rate of cell migration was found to be lowest in the combination treatment (**Figure. 3.1.36**). In addition, a Boyden chamber-based assay, in which cells invade a layer of matrigel on top of a membrane, was used to monitor the invasive capacity of MDA-MB-231 cells. After 24 h, a 3-fold reduction in invasion capacity was observed in cells treated with the combination of inhibitors compared to untreated cells (**Figure. 3.1.37**). Of note, the effect on migration and invasion was stronger upon co-treatment compared to treatment with each single agent, confirming the synergistic effect of the inhibitors (**Figure. 3.1.36 b and Figure. 3.1.37 b**). These data indicate that co-inhibition of EGFR and Wnt/β-catenin signaling reduces the migration and invasion capacities of TNBC cells.

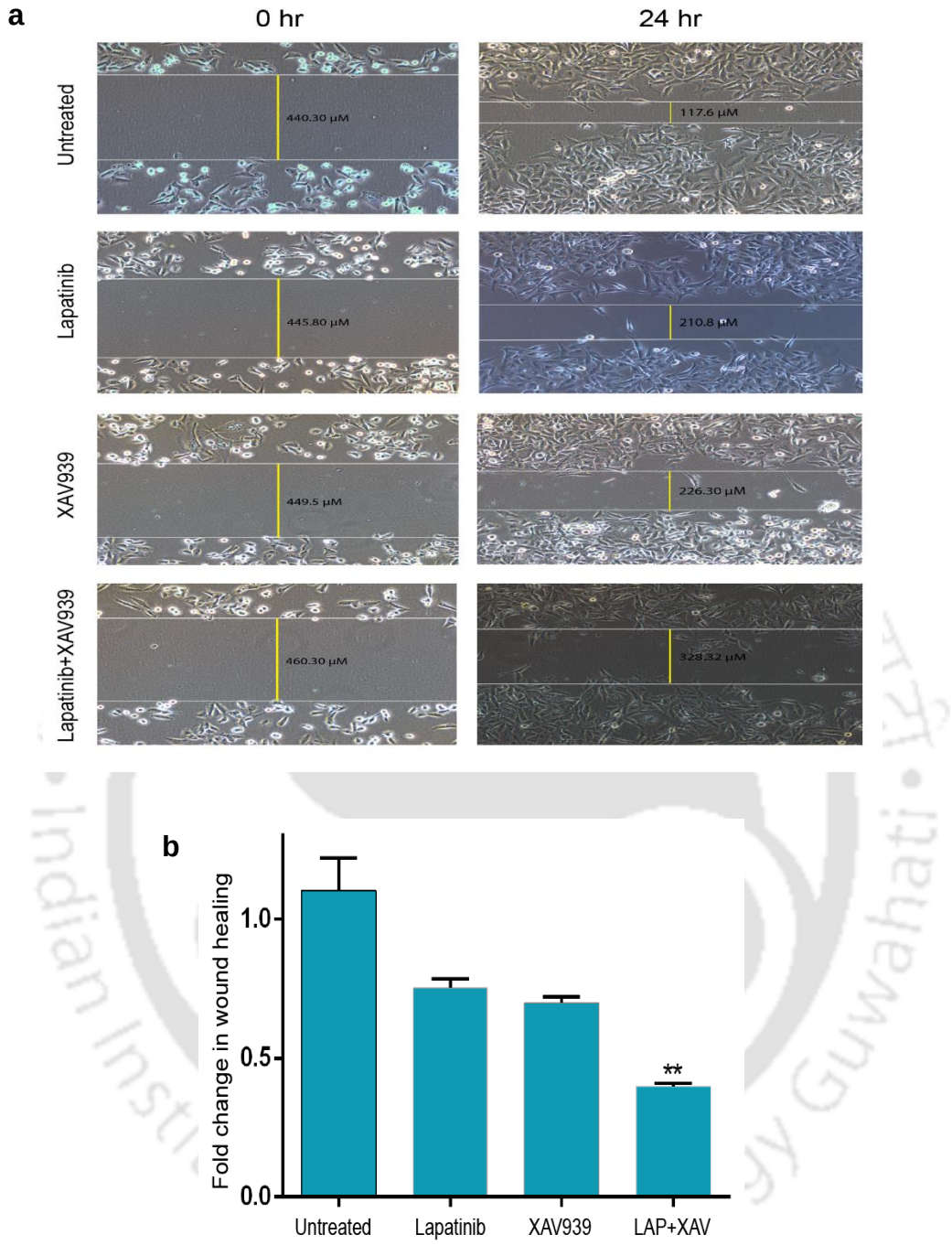

Figure 3.1.36: (a) Scratch wound-healing assays of MDA-MB-231 monolayer cultures. (b) Graphical representation of changes in wound healing capacity following inhibitor treatment and their combination with respect to untreated samples.

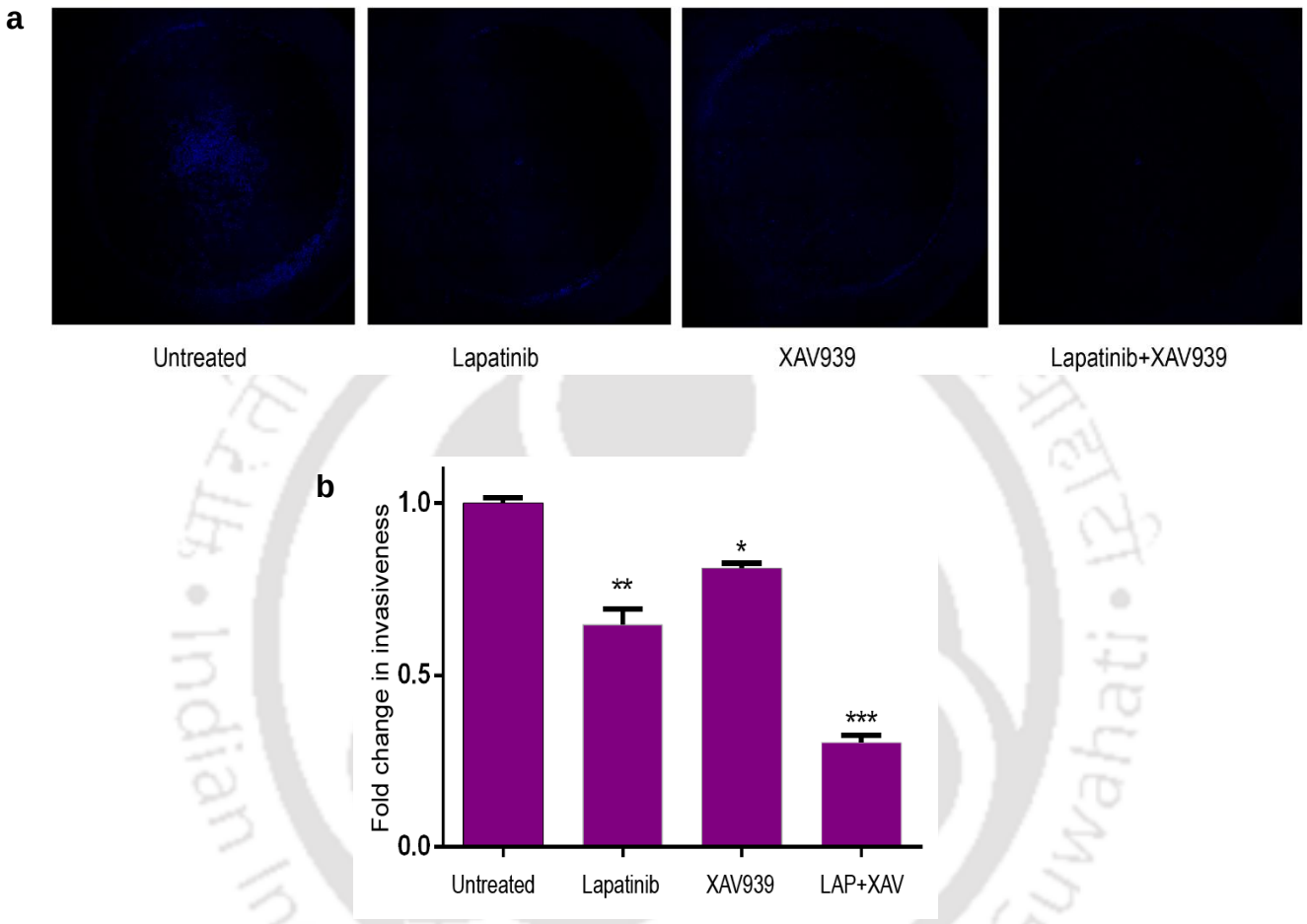

Figure 3.1.37: (a) Boyden-chamber invasion assays of MDA-MB-231 monolayer cultures. (b) Graphical representation of changes in invasiveness following inhibitor treatment and their combination with respect to untreated samples.

3.1.1.6. Suppression of EGFR and Wnt/β-catenin Signaling Alters the Expression of ABC Transporters in TNBC Cells: Drug efflux transport systems have extensively been studied owing to the phenomenon of MDR, in which cancer cells become cross-resistant to multiple cytotoxic anticancer drugs. MDR often results from the overexpression of ABC transporters [104]. Thus, gene expression analysis was done to investigate the alterations in the expression of ABC subfamily B member 1 (ABCB1; also called P-glycoprotein), ABC subfamily C member 1 (ABCC1; also called MDR-associated protein 1), ABC subfamily G member 2 (ABCG2; also called breast cancer resistance protein), all known to be involved in MDR, by qRT-PCR. In **Figure. 3.1.38** and **Figure. 3.1.39** the expression levels of the ABC transporters in MDA-MB-231 monolayer cultures and spheroids are depicted. The combination treatment led to decreased ABCB1 expression in both monolayers and spheroids. However, lapatinib treatment alone increased ABCB1 expression by 1.5-fold and 5.87-fold in monolayers and spheroids, respectively. After combination treatment, the expression of ABCG2 was found to be reduced significantly in monolayers, but to be slightly increased in spheroids. Although co-treatment did not alter ABCC1 expression, a higher expression was observed in XAV939 treated spheroids. Together, these data indicate that downregulation of EGFR and Wnt/β-catenin signaling alters the expression of major MDR-associated genes in TNBC cells.

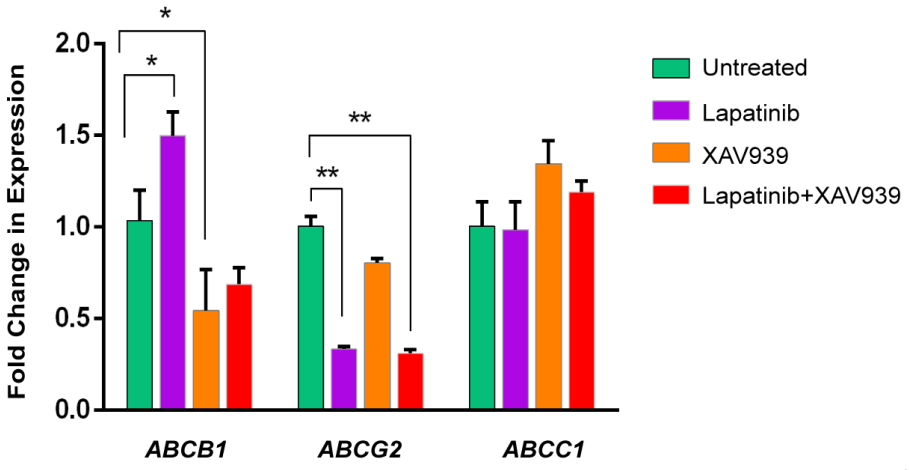

Figure 3.1.38: Graphical representation of changes in gene expression levels obtained from MDA-MB-231 monolayer culture following inhibitor treatment quantified by qRT-PCR analysis.

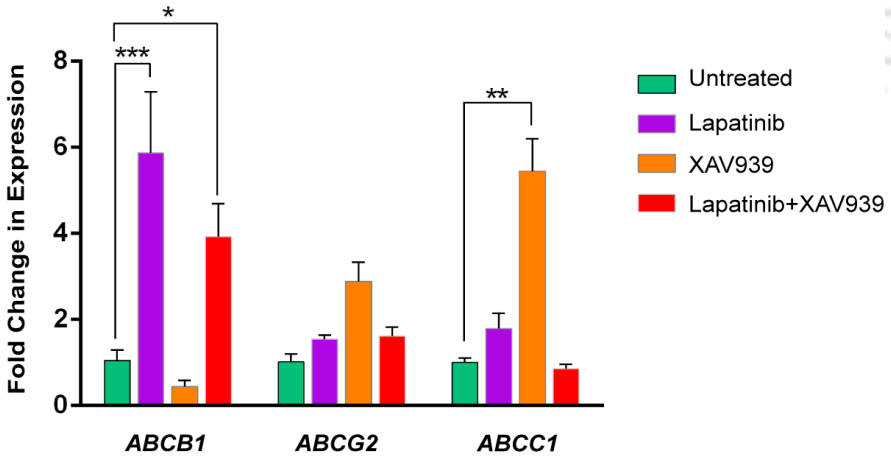

Figure 3.1.39: Graphical representation of changes in gene expression levels obtained from MDA-MB-231 spheroids following inhibitor treatment quantified by qRT-PCR analysis.

3.1.1.7. Alteration of EGFR and Wnt/β-catenin Signaling Downregulates Pro-survival Signals and Reveals Extensive Crosstalk and Downstream Convergence: The effect of the inhibitors on the expression of pro-survival proteins was evaluated by Western blot analysis (**Figure. 3.1.40**). EGF-treated MDA-MB-231 cells were incubated with varying concentrations of the inhibitors. Individual treatment with lapatinib or XAV939 reduced the pEGFR levels drastically, inferring possible crosstalk. Co-administration of lapatinib and XAV939 also reduced the phosphorylated receptor level (1.88-fold). At the indicated concentrations, each inhibitor was found to be insufficient to alter the level of pMAPK. Their combination, however, reduced the pMAPK level significantly. The activated form of AKT (pAKT) was found to be reduced more efficiently by XAV939 than by lapatinib, whereas the combination effectively diminished its level (3.125-fold). Like pMAPK, the inhibitor(s) alone could only marginally alter the level of β-catenin, but markedly (2.17-fold) when administered in combination. The PI3K-AKT signaling pathway is known to phosphorylate GSK-3β at Ser9, which leads to inactivation of GSK-3β and augmentation of β-catenin-TCF/LEF-1 transcriptional activity [105]. The expression of pGSK-3β was reduced significantly after combination treatment. Lapatinib alone reduced the p-GSK-3β level only marginally, whereas XAV939 had a better effect (2.22-fold). This finding is consistent with the previous results of the reduced pAKT level. pSTAT-3, another kinase with an interplaying role between the EGFR and Wnt/β-catenin signaling pathways, was also found to be downregulated (2.32-fold) after combination treatment.

Next, protein expression studies were carried out in spheroids to understand the effect of the inhibitors on cellular signaling. Treatment with individual inhibitors and their combination showed almost similar effects in spheroids compared to monolayers (**Figure. 3.1.41**). However, unlike in monolayers, XAV939 failed to show a significant effect on the pEGFR level in spheroids. The combination treatment was also not effective in altering the pSTAT-3 level.

Following EGF binding, EGFR is incorporated into clathrin-coated pits for further degradation in lysosomes [106]. Although endosomal EGF-EGFR complexes may retain cell signaling ability, lapatinib renders them inactive [106]. To understand whether co-treatment in the presence of EGF alters the surface expression of EGFR, immunofluorescence microscopic analyses were performed. Immunocytochemistry revealed that co-treatment did not alter EGFR surface expression (**Figure. 3.1.42**). Similarly, AKT distribution was found to be unaltered (**Figure. 3.1.43**). In line with the above Western blot results, cytosolic β-catenin was found to be significantly reduced (**Figure. 3.1.44**). The fold change of fluorescence intensity of immunocytochemistry images was quantified and is graphically presented in **Figure. 3.1.45**.

Altogether, experimental findings indicate crosstalk between the EGFR and Wnt/β-catenin pathways and their convergence to downstream signaling. Although a single inhibitor alone could influence the targets by blocking the phosphorylation of RTKs, the effects were only feebly percolated to its downstream effectors and unable to affect cell functions regulated by the targeted pathway. Therefore, blocking more than one pathway simultaneously may alter the effector functions (**Figure. 3.1.40** and **Figure. 3.1.41**).

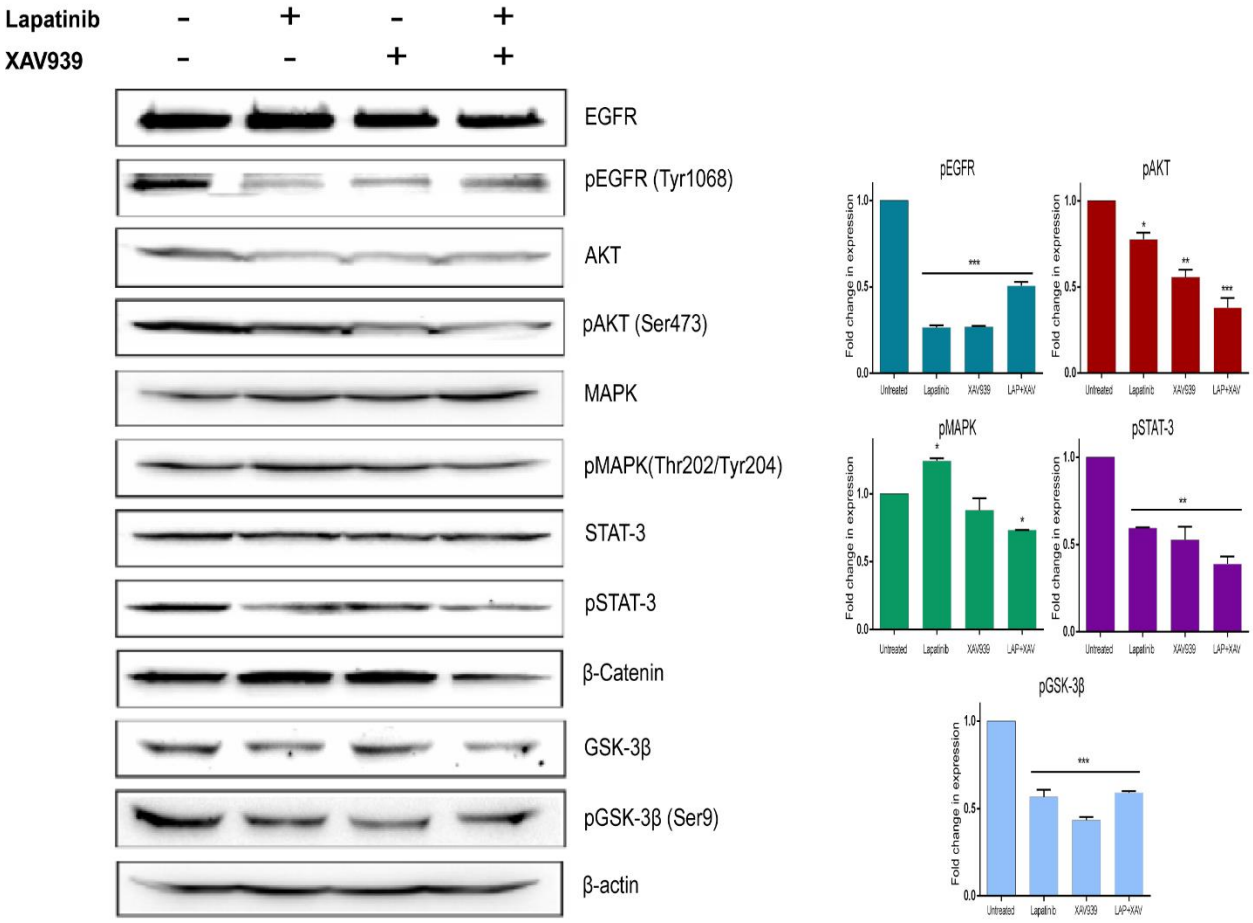

Figure 3.1.40: Western blots showing EGFR/pEGFR, AKT/pAKT, MAPK/pMAPK, STAT-3/pSTAT-3, β-catenin/GSK-3β/pGSK-3β and β-actin levels in MDA-MB-231 cell extracts of monolayer cultures. For monolayer cultures, cells were treated with inhibitors for 48 h, where the concentration of lapatinib is 6 μM and of XAV939 is 50 μM. β-actin serves as a loading control. Graphs represent the changes in the expression levels of pEGFR, pAKT, pMAPK, pSTAT-3 and pGSK-3β with respect to untreated samples following inhibitor treatment. The expression levels were deduced from the blots using ImageJ software.

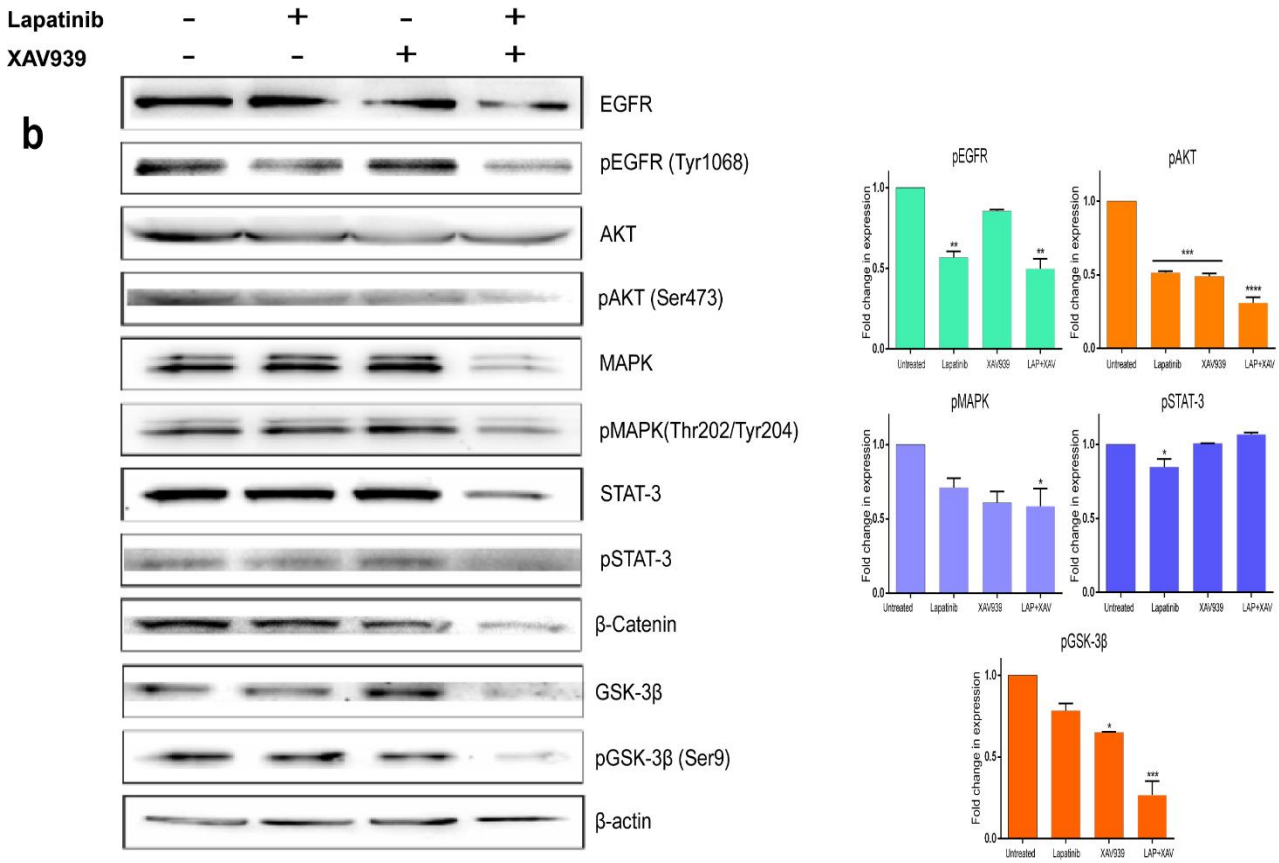

Figure 3.1.41: Western blots showing EGFR/pEGFR, AKT/pAKT, MAPK/pMAPK, STAT-3/pSTAT-3, β-catenin/GSK-3β/pGSK-3β and β-actin levels in MDA-MB-231 cell extracts of spheroids. Spheroids were treated using 30 μM lapatinib and 25 μM XAV939 for 72 h. β-actin serves as a loading control. Graphs represent the changes in the expression levels of pEGFR, pAKT, pMAPK, pSTAT-3 and pGSK-3β with respect to untreated samples following inhibitor treatment. The expression levels were deduced from the blots using ImageJ software.

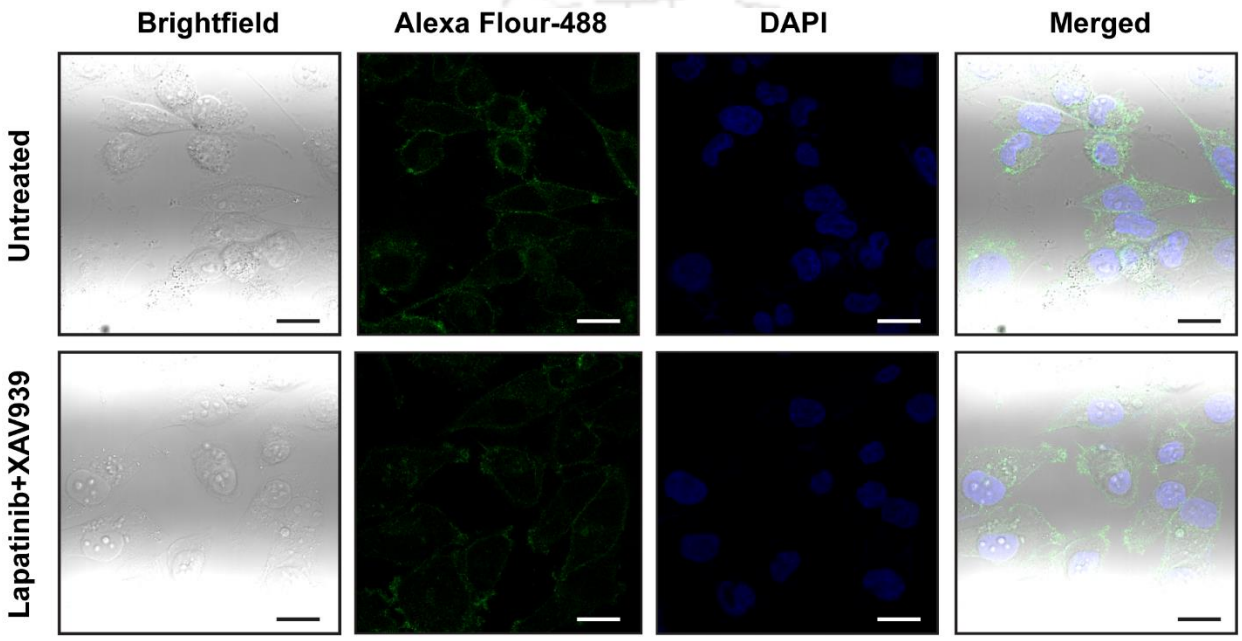

Figure 3.1.42: Confocal images of MDA-MB-231 monolayer cultures immune-stained with (a) anti-EGFR antibody visualized by Alexa Flour-488. Nuclei were stained with DAPI. Upper row refers to untreated samples and lower row refers to samples treated with lapatinib + XAV939 (6 μM LAP + 50 μM XAV) for 48 h. Scale bar, 20 μM.

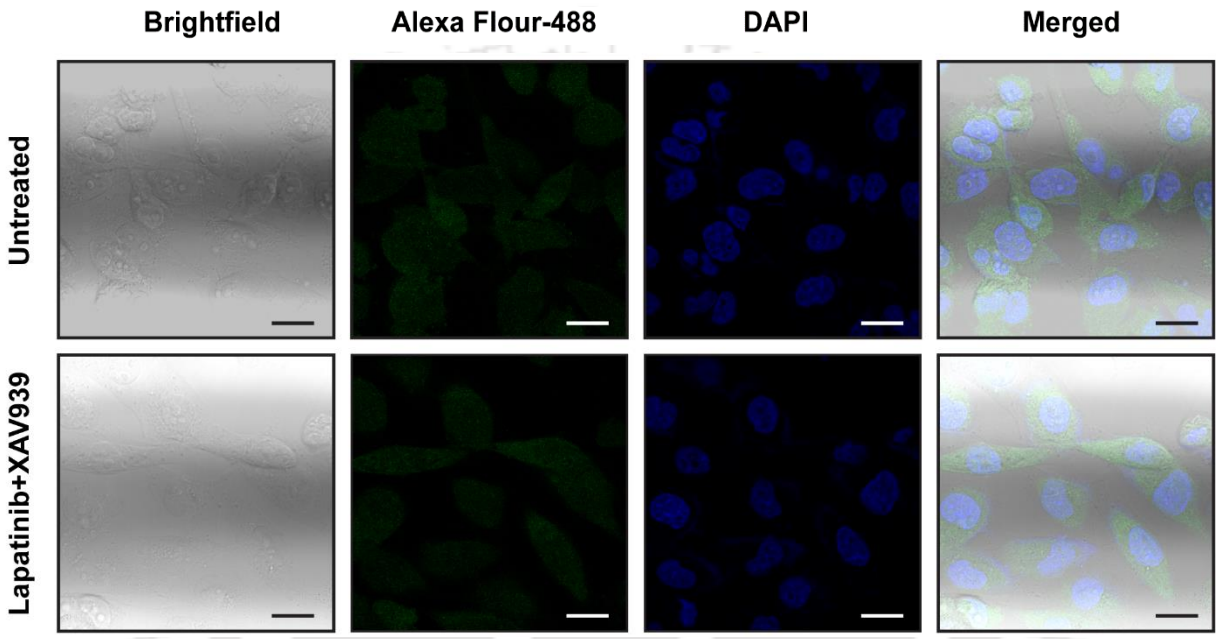

Figure 3.1.43: Confocal images of MDA-MB-231 monolayer cultures immune-stained with (a) anti-AKT antibody visualized by Alexa Flour-488. Nuclei were stained with DAPI. Upper row refers to untreated samples and lower row refers to samples treated with lapatinib + XAV939 (6 μM LAP + 50 μM XAV) for 48 h. Scale bar, 20 μM.

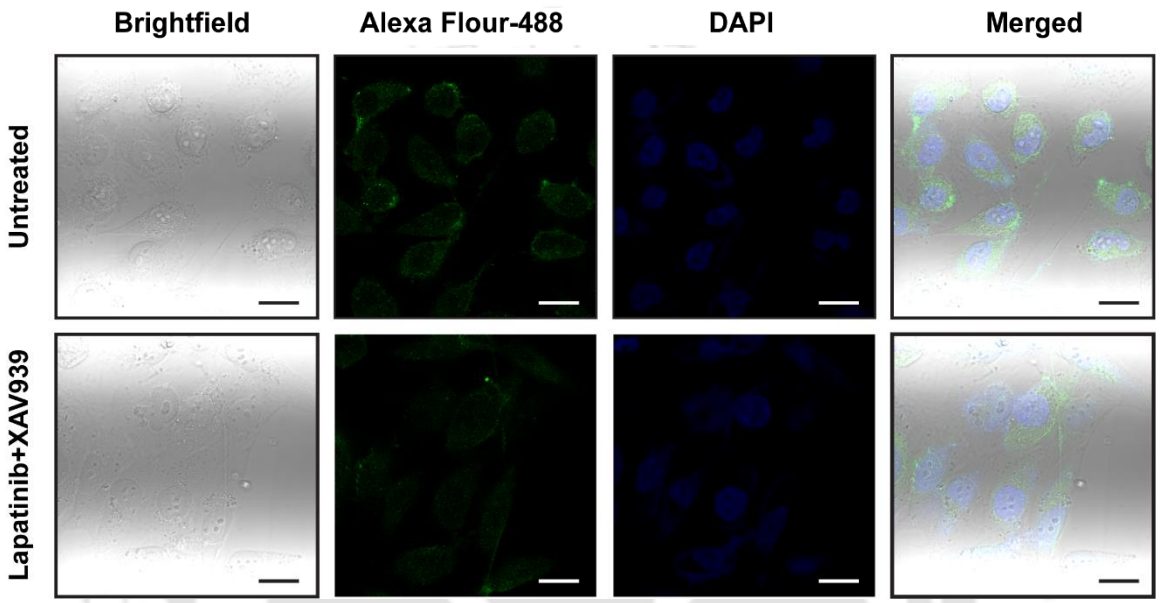

Figure 3.1.44: Confocal images of MDA-MB-231 monolayer cultures immune-stained with (a) anti-β-catenin antibody visualized by Alexa Flour-488. Nuclei were stained with DAPI. Upper row refers to untreated samples and lower row refers to samples treated with lapatinib + XAV939 (6 μM LAP + 50 μM XAV) for 48 h. Scale bar, 20 μM.

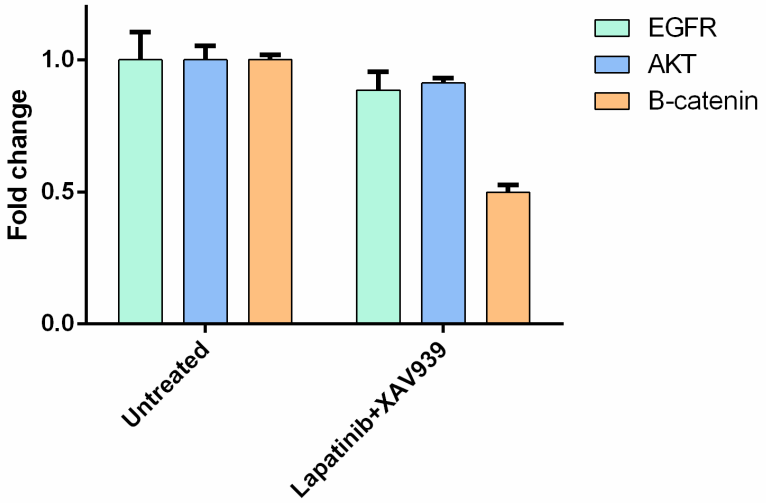

Figure 3.1.45: Graphical representation of the fold change normalized corrected total cell fluorescence (CTCF) values obtained from quantification of immunofluorescence images as presented in Figure 3.38-3.40.

3.1.2 Discussion: In TNBC, several signaling pathways have been found to be responsible for inducing EMT and maintaining CSC properties. Multiple crosstalks, feedback loops, and their essential roles in maintaining normal cellular developmental processes make it almost impossible to effectively target them and halt EMT progression. It is, therefore, quite perceptible that crosstalk between signaling pathways has to be obliterated in order to block EMT. To avert possible severe side effects arising from high concentrations of drugs in plasma, a combination of small molecule inhibitors at low concentrations was examined. Two inhibitors in particular were studied, lapatinib, an FDA approved drug for metastatic breast cancer [107] and XAV939, an inhibitor that is being tested at the preclinical stage [108]. It should be noted that although a few FDA-approved drugs do affect Wnt signaling, albeit nonspecifically, inhibitors explicitly targeting the Wnt/β-catenin pathway have only recently entered clinical trials [109]. It was observed that the combination effect on spheroids was significant at lower doses, but less effective at higher doses. This is possibly due to the complex ECM structure in spheroids that alters endosmosis. Cell-ECM and cell-cell interactions increase cell density and, thereby, may form a physical barrier that limits the penetration of compounds to cells, also known as limited mass transport effect [110]. At lower concentrations of the drug, endosmosis was possibly favored over higher concentrations. Also, increased interstitial fluid pressure (IFP) and hypoxic conditions in spheroids may attribute to the drug uptake process above a certain threshold [111].

Cyclin-D1 and CDK-4 partly mediate G1 to S-phase cell cycle progression by phosphorylation and inactivation of the retinoblastoma (Rb) protein, with a subsequent release of E2F transcription factors [94]. Tetsu et al. reported that β-catenin regulates the expression of Cyclin-D1 in colon carcinoma cells and that abnormal β-catenin expression levels may, therefore contribute to neoplastic transformation by causing Cyclin-D1 accumulation [112]. Cyclin-D1 is also known

to be a downstream target of HER-2 and EGFR [113]. Evidently, modulation of EGFR and Wnt/β-catenin signaling resulted in reduced expression of Cyclin-D1 and CDK-4, leading to G0/G1 cell cycle arrest. Similar to experimental findings, Masamha et al. reported that Cyclin-D1 degradation in ovarian cancer cells is sufficient to induce G0/G1 cell cycle arrest despite the constitutive expression of Cyclin-E2 [114]. The sub-G1 population, indicating cell shrinkage and DNA fragmentation, is considered to be a apoptotic cell population [115].

The effectiveness of traditional cancer chemotherapy is mostly based on the generation of ROS and, consequently, on increased oxidative stress that exceeds the reduction capacity of the cancerous tissues, ultimately leading to apoptosis or necrosis [116]. DCFDA based ROS analysis revealed that lapatinib alone led to accumulation of more ROS than the combination of inhibitors, which might be attributed to the activation of multiple death signaling cascades following combination therapy. In line with the obtained results, Arid et al. reported that lapatinib may act as a potent inducer of ROS in inflammatory breast cancer (IBC) cells [117]. The cellular ROS levels were, however, found to be decreased following single or combined treatment of tumor spheroids. Increased ROS levels cause mitochondrial membrane hyper-polarization, which leads to the collapse of mitochondrial membrane potential (ΔΨm), mitochondrial translocation of Bax and Bad, cytochrome-c release and, ultimately, apoptosis [118]. JC-1 staining data revealed an increase in depolarized mitochondria, confirming ROS-mediated mitochondrial membrane damage after combination treatment. The cytotoxicity of an anticancer drug depends heavily on its ability to initiate apoptosis in the targeted cells. In this regard, lapatinib and XAV939 have both been reported to induce caspase-dependent apoptosis [119, 120]. Liu et al. reported an almost 40% increase in apoptosis of MDA-MB-231 cells after 72 h treatment with 10 μM lapatinib [121]. The observed 41.19% increase in apoptotic cell population after co-

administration of lapatinib and XAV939 for 48 h at low concentrations substantiates the efficacy of the proposed treatment.

Considering the involvement of EGFR and Wnt/β-catenin signaling in inducing EMT and metastasis in TNBC, the effect of the inhibitor combination on EMT was evaluated. MDA-MB-231 cells are known to have an EMT-induced mesenchymal phenotype [122]. Following combination treatment, downregulation of vimentin, N-cadherin, fibronectin, Ki-67, SNAI2, Twist and EpCAM, and upregulation of E-cadherin indicate a reversal of the EMT process, i.e., MET, which contributes to reduced motility, invasiveness and drug resistance. Strikingly, only lapatinib treatment induced the cells to express high levels of mesenchymal markers and reduced levels of epithelial markers. Previously Hsiao et al. also reported that lapatinib induced increased migratory and metastatic properties in MDA-MB-231 cells [123]. According to their findings, lapatinib induces IL-6 expression triggered through the MAPK pathway. Elevated expression of IL-6 is indeed known to contribute to enhanced cancer aggressiveness [124]. The here observed increased level of pMAPK after lapatinib treatment correlates with these studies and decodes the probable cause of the enhanced EMT markers. However, contrasting lapatinib results were obtained in spheroids with upregulated levels of E-cadherin and reduced levels of vimentin, N-cadherin and EpCAM. A plausible explanation for this phenomenon may be linked to the drug efflux transport system.

The major obstacle of successful chemotherapy treatment is multidrug resistance (MDR), predominantly due to overexpression of ATP-binding cassette (ABC) transporters [104]. Although ABCB1 and ABCG2 were found to be significantly reduced upon combination treatment, lapatinib alone increased the expression of ABCB1 significantly in both monolayers and spheroids. ABCG2 was, however, found to be reduced in monolayers and to be increased in spheroids. The drug efflux functions of ABCB1 and ABCG2 are linked to ATP hydrolysis, which

is stimulated in the presence of the substrates. Polli et al. found that lapatinib acts both as a substrate and an inhibitor of ABCB1 and ABCG2 (IC_{50} values of 3.9 and 0.025 μmol/L, respectively) [125]. It was evident that lapatinib acted as a substrate for these two transporters at lower concentrations and as an inhibitor at higher concentrations. Based on higher IC_{50} values, lapatinib acted as a substrate for ABCB1 in both cases, thereby increasing its expression. On the contrary, based on the lower IC_{50} value of ABCG2, lapatinib acts as an inhibitor at the indicated dosages. Hypoxia-inducible factor 1α (HIF1α) is also known to induce the expression of ABCG2 [126], which may be attributed to the increased expression of ABCG2 observed in spheroids. Another possible mechanism is Twist1-mediated elevation of (ABC) transporters. Previously, Li et al. reported Twist1-mediated upregulation of EMT and MDR in breast cancer [127]. The mechanism for the here observed increased expression of ABCC1 by XAV939, however, remains to be resolved. It is hypothesized that the contrasting result obtained for lapatinib on monolayers and spheroid models regarding EMT regulation may be due to dose differences, resulting in differential activities of ABC transporters. At a 6-fold higher dose of lapatinib in the spheroids, these transporters are inhibited, leading to decreased expression of EMT markers. Although MDM2 and caveolin-1 are known to be involved in multiple cellular processes, they are also implicated in instigating EMT and drug resistance. Lapatinib and XAV939 combination therapy reduced their accumulation both in monolayers and spheroids. Therefore, experimental data indicate multiple connections between EMT and ABC transporters mediated by MDR.

Overall, the obtained results suggest that, in addition to other mechanisms that might be at play, inhibition of EMT contributes to inhibition of the migratory and invasive properties of mesenchymal-like TNBC cells. In line with this, Vijay et al. observed a decreased migration of TNBC cells after targeting EMT by inhibition of GSK-3β [23]. As a result, specific parts of the EGFR and Wnt/β-catenin pathways

were studied as in order to determine their involvement as primary mediators of pro-survival/anti-apoptotic/pro-migration/drug resistance signaling. After incubation with lapatinib, XAV939 and their combination, the pEGFR level was found to be reduced significantly. The effect of the combination was found to be profound in spheroids. Reduction of the pEGFR level by XAV939 suggested Wnt-mediated transactivation of EGFR, probably by MMP-mediated release of soluble EGFR ligand [128]. The unaltered level of β-catenin after administration of XAV939 alone indicated that this inhibitor could only exert its profound effect at high concentrations. Consistent with the report by Tian et al., where XAV939 decreased the expression of β-catenin, it was found that application of both inhibitors markedly downregulated β-catenin expression. This indicates a high responsiveness of the new therapeutic approach [120]. Concomitant reversal of EMT following decreases in pEGFR and β-catenin levels implies the importance of these pathways in TNBC aggressiveness.

Stimulation of EGFR activates pro-oncogenic MAPK, STAT-3 and AKT, which have been found to be highly dysregulated in metastatic TNBC [129-131]. The Wnt/β-catenin pathway shares a bidirectional positive feedback loop with MAPK, STAT3 and AKT, primarily through GSK3β [132-134]. Cell survival signals inactivate GSK3β through phosphorylation and, thereby, stabilize β-catenin [135]. Earlier studies have confirmed a role of MAPK, STAT-3 and AKT in EMT [131, 132, 136-138]. The observed decline in expression of pMAPK, pSTAT-3, pAKT and pGSK3β, vital downstream components of the EGFR and Wnt signaling pathways, after incubation with the inhibitors, signifies the complexity and web-like connectivity between the examined receptors and mark the inhibition of EMT and growth signals. These findings are clear indicators of synergistic anti-cancer cell survival actions of the combination treatment through downstream signaling.

3.1.3 Conclusion: Aberrant activation of EMT and associated cancer stem cell-like phenotypes are the major causes of resistance to therapy in TNBC. In the pursuit of effective therapy, co-treatment module using lapatinib and XAV939 was used, which target the EGFR and Wnt/β-catenin pathways, two pivotal signaling pathways underlying EMT. Concurrent with reversal of the EMT phenotype by co-treatment, expression of genes responsible for cancer stemness and MDR were also curbed. Additionally, inhibition of EMT resulted in reduced migration and invasion of TNBC cells. Nonetheless, the proposed combination therapy was able to circumvent most of the complexities by targeting multiple signaling nodes and preventing downstream crosstalk. Overall, experimental results underscore a potential combined application of EGFR and Wnt/β-catenin inhibitors in the targeted therapy of TNBC.

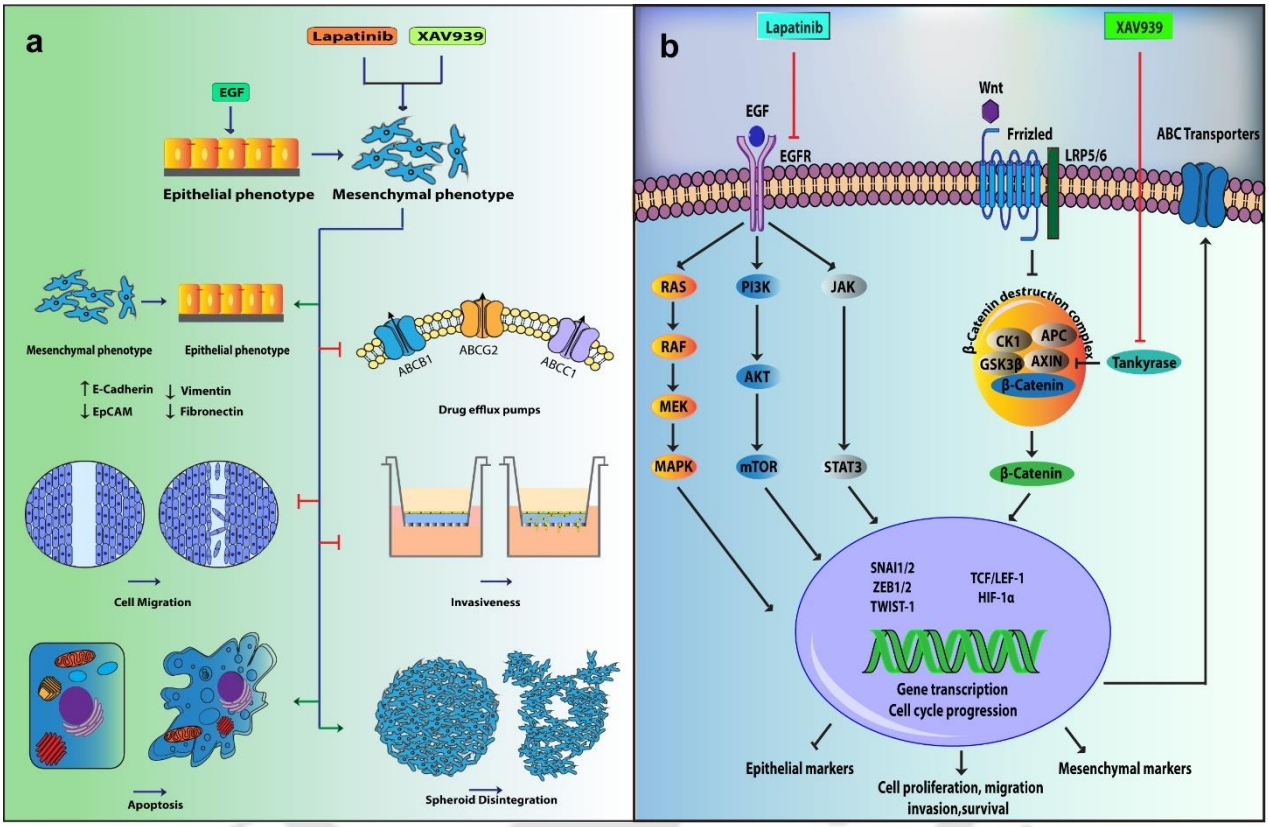

Scheme 3.1: Schematic illustration of (a) overall observable cellular events and (b) details of intracellular signaling upon lapatinib-XAV939 co-treatment regulating EMT and MDR dynamics

3.2. Exploiting the Interplay Between EMT and Autophagy to Restrain Metastatic TNBC

(Manuscript communicated)

Results and Discussion

Abstract: In continuation to the previous section-1, to impede the aggressiveness of TNBC, the components of autophagy and Wnt signaling pathway were modulated. The prevalence of cells with mesenchymal features is one of TNBCs' well-known characteristics; where cells have undergone epithelial to mesenchymal transition (EMT) and are found to be poorly differentiated, which in turn gives rise to cancer stem cells (CSCs). Wnt/β-catenin signaling has been reported to be a prominent contributor of EMT, stemness and CSC properties of TNBC. Nuclear accumulation of β-catenin promotes EMT, cell motility, invasion, colony formation, stem cell like properties and chemoresistance. Similarly, the Wnt/PCP pathway regulate cancer cell motility and invasion and promotes further cancer progression. Recognizing the centrality of both canonical and non-canonical Wnt signaling in the molecular pathogenesis of TNBC via EMT and MDR, it is postulated that modulating these pathways might be a method for achieving dramatic therapeutic results in TNBC. An intriguing correlation between Wnt signaling and SQSTM1/P62 is that SQSTM1/P62 cooperates with the components of non-canonical Wnt/PCP signaling pathway and helps in EMT and oncogenesis. SQSTM1 is a multifunctional stress-inducible scaffold protein involved in diverse cellular processes. However, SQSTM1 is critically involved at the interface of autophagy and EMT; all crucial events in the control of cell growth and cancer. Surprisingly, SQSTM1 is not crucial for organism survival in mammals. This signifies modulation of SQSTM1 expression may turn out to be a potential

therapeutic target in cancer dissemination. Therefore, an effective combination therapy module was devised to target Wnt/β-catenin signaling (FH535) and SQSTM1 (siRNA), simultaneously. The effect of an inhibitor (FH535) with combination of siRNA against SQSTM1 was investigated in TNBC cells to explore molecular alterations of EMT and MDR markers. Following combination therapy, cytotoxicity tests on TNBC cells revealed a significant dose-dependent reduction in cell viability and a synergistic interaction between inhibitors. The migration and invasion assay revealed downregulations of the metastatic property. Gene and protein expression analysis revealed down-regulation of key EMT regulators. The findings show the possibility of inhibiting EMT and MDR by co-targeting Wnt/β-catenin and SQSTM1 signaling pathway components for improved effectiveness in TNBC therapy.

3.2.1 Results:

3.2.1.1 SQSTM1/P62 and Wnt/β-Catenin are Elevated in TNBC Tumors and Their Higher Expression is Associated with Poor Prognosis: To address the role of SQSTM1/P62 and Wnt/β-Catenin signaling in TNBC, the messenger RNA expression in large dataset of TNBC from public databases were examined. 'Breast cancer gene-expression miner' (bc-GenExMiner) was used to analyze the mRNA expression difference between non-TNBC and TNBC tumors from the Cancer Genome Atlas (TCGA) database [139]. As shown in **Figure. 3.2.1 a**, the mRNA of SQSTM1/P62 is slightly increased with respect to non-TNBC tumor. However, β-Catenin is highly expressed in TNBC tumors with respect to non-TNBC tumors (**Figure. 3.2.1 b**). Similarly, Bee swarm plot of SQSTM1/P62 and β-Catenin mRNA expression in invasive breast tumors obtained from the Genotype-Tissue Expression (GTEx) and TCGA database displays significant elevation with respect to healthy tissue (**Figure. 3.2.2 a** and **b)**. Furthermore, the protein expression of SQSTM1/P62 and β-Catenin in breast cancer tissues from the Clinical Proteomic Tumor Analysis Consortium (CPTAC) database was analyzed using UALCAN portal [140]. Alike the mRNA expression, the protein expression of both SQSTM1/P62 and β-Catenin are elevated in TNBC samples (**Figure. 3.2.3 a** and **b)**. In addition, the role of elevated expression of SQSTM1/P62 and β-Catenin on the clinical outcome of the TNBC patients was investigated. From the TCGA/GTEx database, 1085 tumor samples and 112 normal samples were analyzed using Gene Expression Profiling Interactive Analysis 2 (GEPIA 2) portal [141]. From the plots

it is observed that higher expression of SQSTM1/P62 and β-Catenin leads to reduced overall survival of the patients (**Figure. 3.2.4 a** and **b)**.

Expression analysis based on cancer stages revealed increase in SQSTM1/P62 expression with progression to terminal stages (**Figure. 3.2.5)**. However, β-Catenin is found to decrease with the progression of cancer stages (**Figure. 3.2.6)**. Altogether, elevated expression of SQSTM1/P62 and Wnt/β-Catenin leads to TNBC progression and shorter survival.

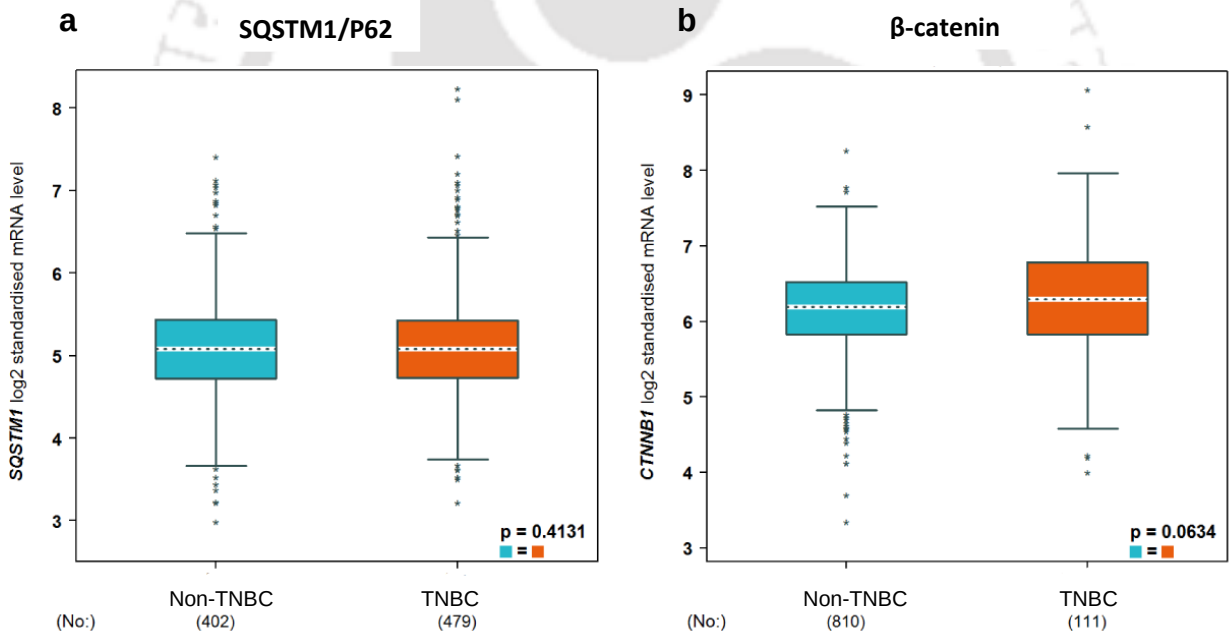

Figure. 3.2.1: (a) Box and whisker plot of SQSTM1/P62 mRNA expression in Non-TNBC and TNBC tumors. (b) Box and whisker plot of β-catenin (CTNNB1) mRNA expression in Non-TNBC and TNBC tumors. The datasets are obtained from Cancer Genome Atlas (TCGA) and GTEx database.

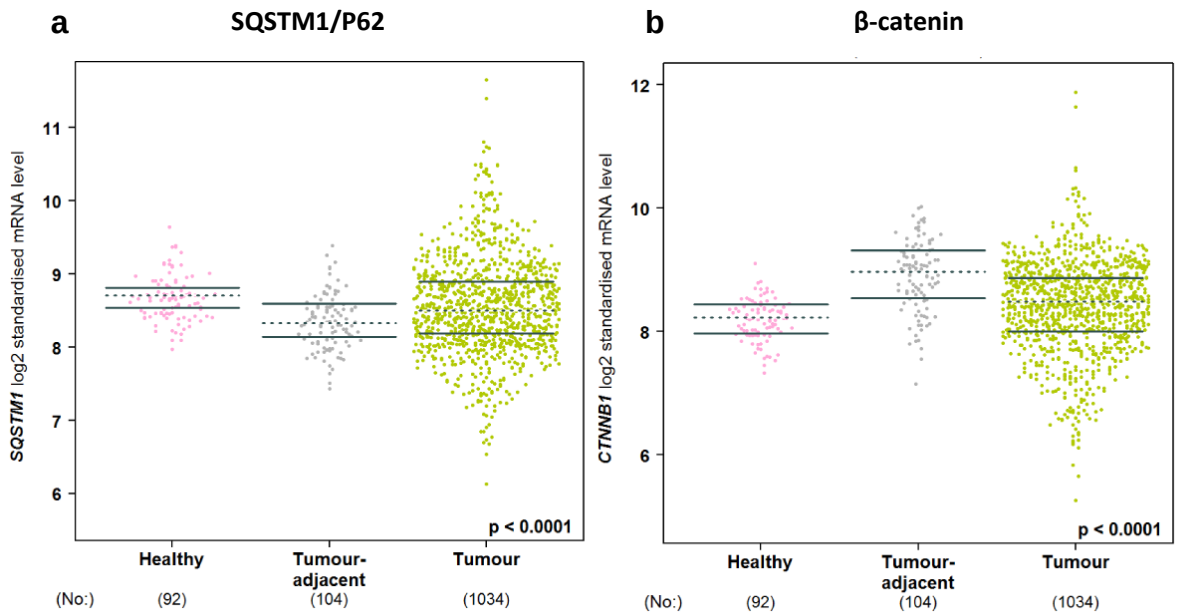

Figure. 3.2.2: (a) Bee swarm plot of SQSTM1/P62 mRNA expression in healthy and invasive tumors (b) Bee swarm plot of β-catenin (CTNNB1) mRNA expression in healthy and invasive tumors. The datasets are obtained from Cancer Genome Atlas (TCGA) database.

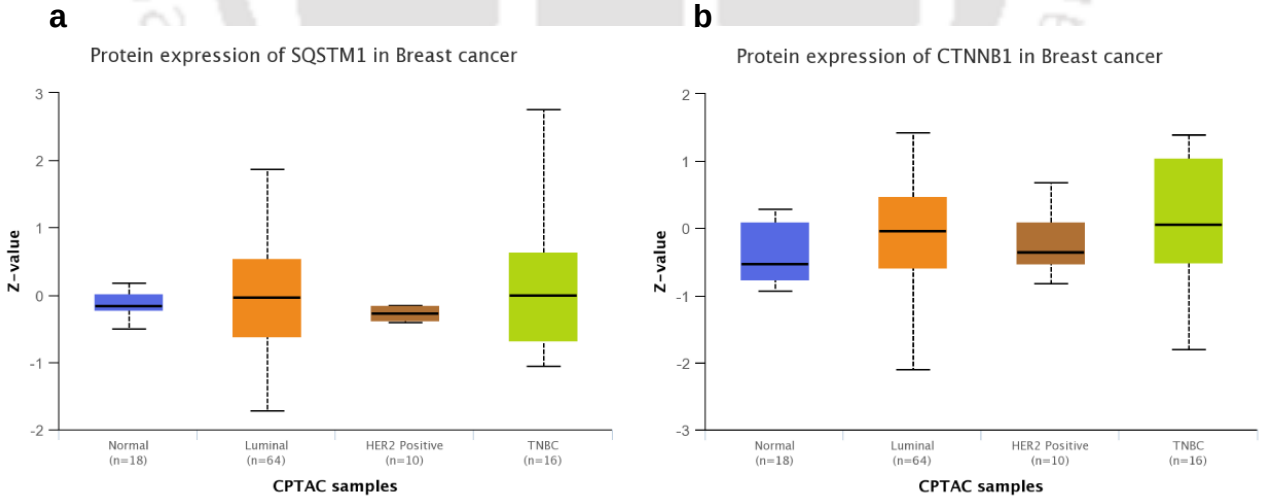

Figure. 3.2.3: Protein expression data of (a) SQSTM1/P62 and (b) β-Catenin (CTNNB1) in normal, luminal, HER-2 positive and TNBC breast cancer tissues obtained from the Clinical Proteomic Tumor Analysis Consortium (CPTAC) database.

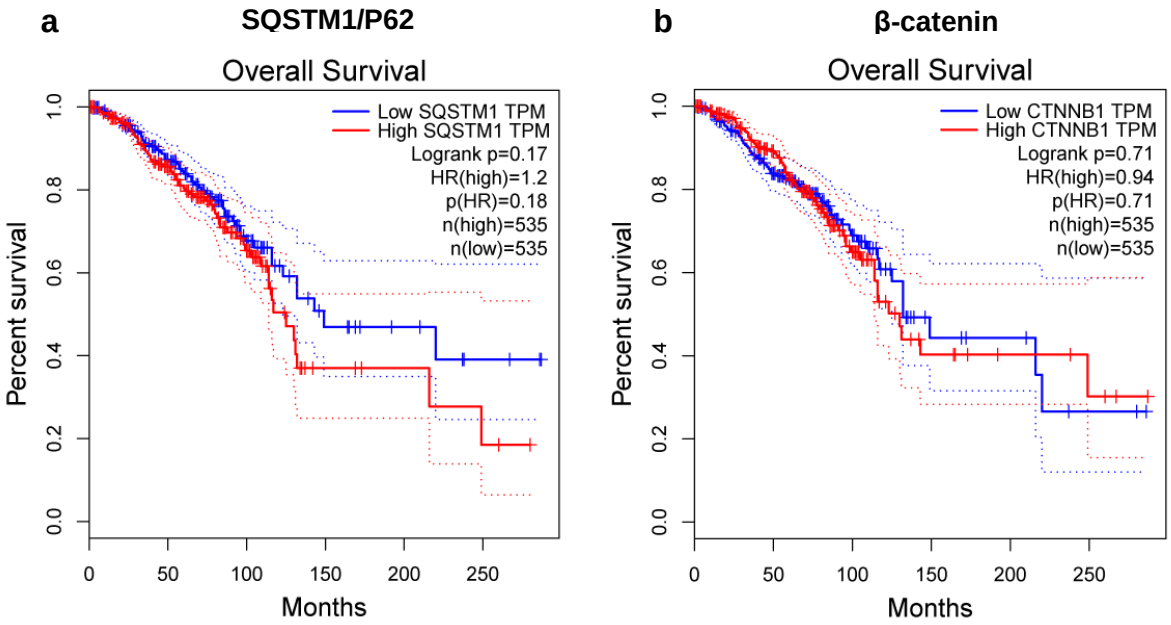

Figure. 3.2.4: (a) Kaplan-meier survival analysis of SQSTM1/P62 expression of TNBC patients. (b) Kaplan-meier survival analysis of β-catenin/CTNNB1 expression of TNBC patients. From the TCGA/GTEx database, 1085 tumor samples and 112 normal samples were analyzed using Gene Expression Profiling Interactive Analysis 2 (GEPIA 2) portal.

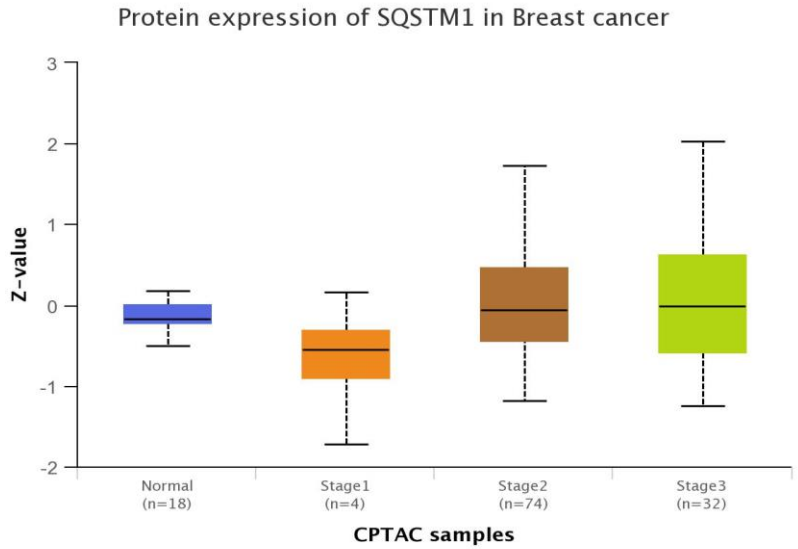

Figure. 3.2.5: Protein expression analysis of SQSTM1/P62 based on breast cancer stage obtained from cancer tissues. Data obtained from the Clinical Proteomic Tumor Analysis Consortium (CPTAC) database.

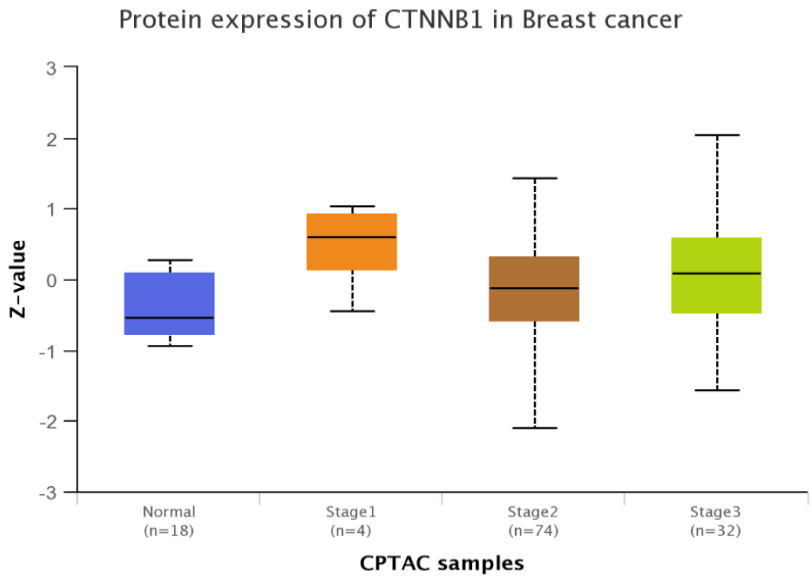

Figure. 3.2.6: Protein expression analysis of β-catenin/CTNNB1 based on breast cancer stage obtained from cancer tissues. Data obtained from the Clinical Proteomic Tumor Analysis Consortium (CPTAC) database.

3.2.1.2 SQSTM1/P62 and Wnt/β-Catenin are Important Mediator of Stem Like Properties of TNBC: To assess the role of SQSTM1/P62 and Wnt/β-Catenin signaling in promoting TNBC stem like properties, siRNA was used to mediate suppression of SQSTM1/P62 and FH535 to inhibit Wnt/β-Catenin signaling. The efficiencies of SQSTM1/P62 depletion was assessed by Western blotting. As shown in **Figure. 3.2.7** and **Figure. 3.2.8**, SQSTM1/P62 was effectively depleted by siRNA. Similarly, the effect of FH535 on Wnt/β-Catenin signaling was analyzed. β-Catenin was effectively downregulated by FH535 (**Figure. 3.2.7** and **Figure. 3.2.8)**. Additionally, immunocytochemistry of SQSTM1/P62 (**Figure. 3.2.9** and **Figure. 3.2.10)** and β-Catenin (**Figure. 3.2.11** and **Figure. 3.2.12)** was performed in both cell lines. In addition to Western blot analysis and immunocytochemistry, gene expression analysis of downstream transcription factors cMYC, TCF and LEF were performed (**Figure. 3.2.13** and **Figure. 3.2.14)**. TCF was found to be downregulated by 1.76-fold. However, no significant alteration was detected in cMYC and LEF expression upon co-treatment. Treatment with FH535 increased the cMYC and LEF expression (**Figure. 3.2.13** and **Figure. 3.2.14**). Further, colony formation assay and spheroid formation assay of SQSTM1/P62 and Wnt/β-Catenin signaling inhibited cells were performed. Knockdown of SQSTM1/P62 and inhibition of Wnt/β-Catenin pathway reduced the colony formation ability of the TNBC cells (**Figure. 3.2.15** and **Figure. 3.2.16**). The effect on colony formation was profound in case of co-treatment. Moreover, the sphere formation ability was dramatically decreased upon SQSTM1/P62 and Wnt/β-Catenin depletion (**Figure. 3.2.17** and **Figure. 3.2.18**). In addition, qRT PCR was performed to detect the change in gene expression of stemness marker ALDH1A3 and EpCAM, and genes maintaining stemness. ALDH1A3 was slightly increased in MDA-MB-231 and decreased in

MDA-MB-468 following treatment with FH535 (**Figure. 3.2.19** and **Figure. 3.2.20**). EpCAM was downregulated in MDA-MB-231 and elevated in MDA-MB-468 by co-treatment (**Figure. 3.2.19** and **Figure. 3.2.20**). Ki-67 and MDM2 are reported to play important role in maintaining the cancer stem cell niche [142, 143]. Knockdown of SQSTM1/P62 and inhibition of Wnt/β-Catenin effectively decreased the expression of Ki-67 in both TNBC cell lines (**Figure. 3.2.21** and **Figure. 3.2.22**). The co-treatment resulted in diminished expression of Ki-67. Suppression of SQSTM1/P62 diminished the expression of MDM2 in MDA-MB-231 and MDA-MB-468 (**Figure. 3.2.21** and **Figure. 3.2.22**). Comparatively, inhibition of Wnt/β-Catenin was less effective in suppressing MDM2. cMYC expression is reported to be positively correlated with self-renewal, chemoresistance and stemness properties of TNBC [144]. Protein expression analysis was carried out to detect the role of SQSTM1/P62 and β-Catenin in maintaining stemness of TNBC. As shown in **Figure. 3.2.23**, depletion of SQSTM1/P62 reduced the cMYC expression in MDA-MB-231 by 2.83-fold. In MDA-MB-468, Wnt/β-Catenin inhibition reduced the cMYC expression by 1.33-fold (**Figure. 3.2.24**). To identify cancer stem cells (CSCs) from the main tumor population, cell surface proteins like CD44 and CD24 are utilized [145]. Immuno flow cytometry assay revealed a decrease in CD44 population and increase in CD24 population following co-treatment (**Figure. 3.2.25 and Figure. 3.2.26)**.

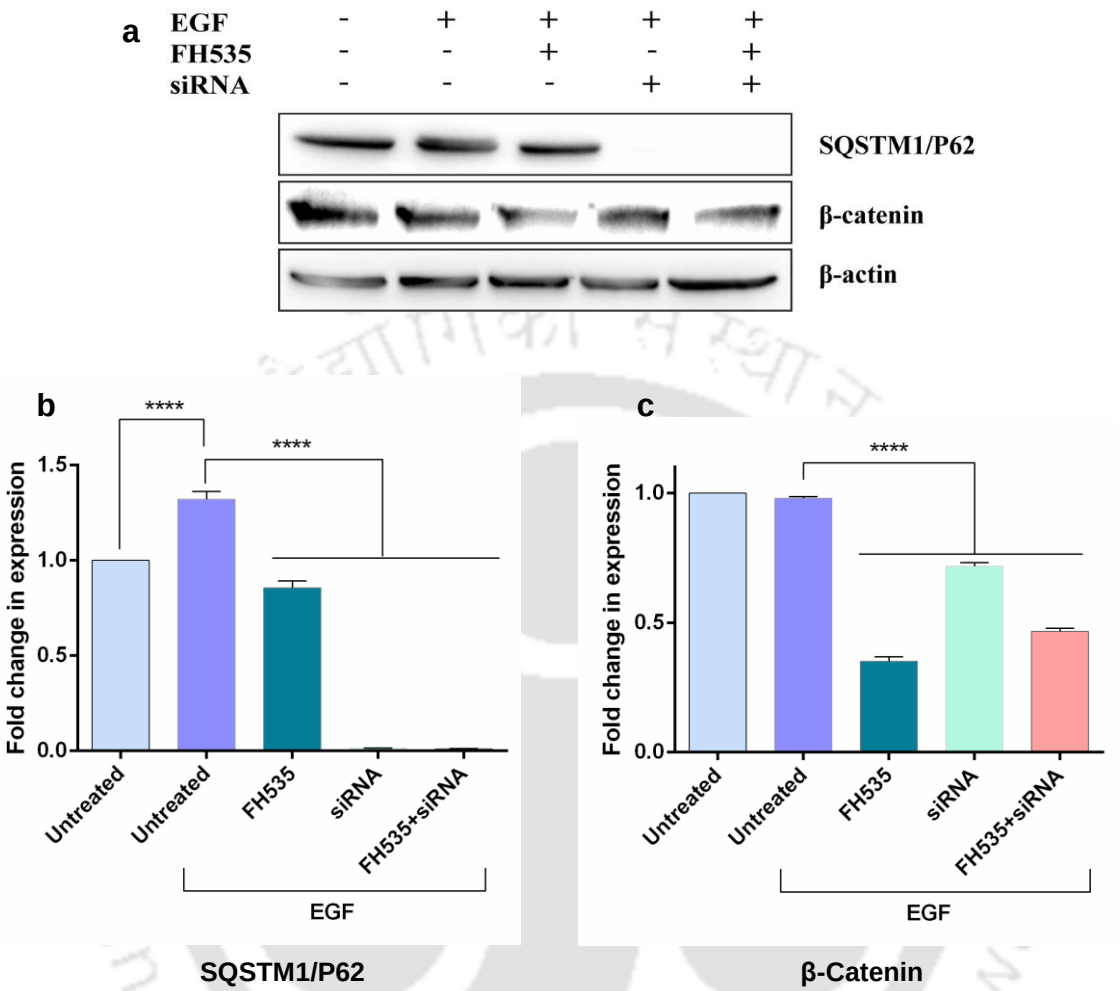

Figure. 3.2.7: (a) Representative Western blots showing SQSTM1/P62 and β-catenin levels in MDA-MB-231 cell extracts. β-actin serves as a loading control. Graphs depicts the alteration in the expression levels of (b) SQSTM1/P62 and (c) β-catenin with respect to untreated samples following inhibitor/siRNA treatment. The expression levels were deduced from the blots using ImageJ software.

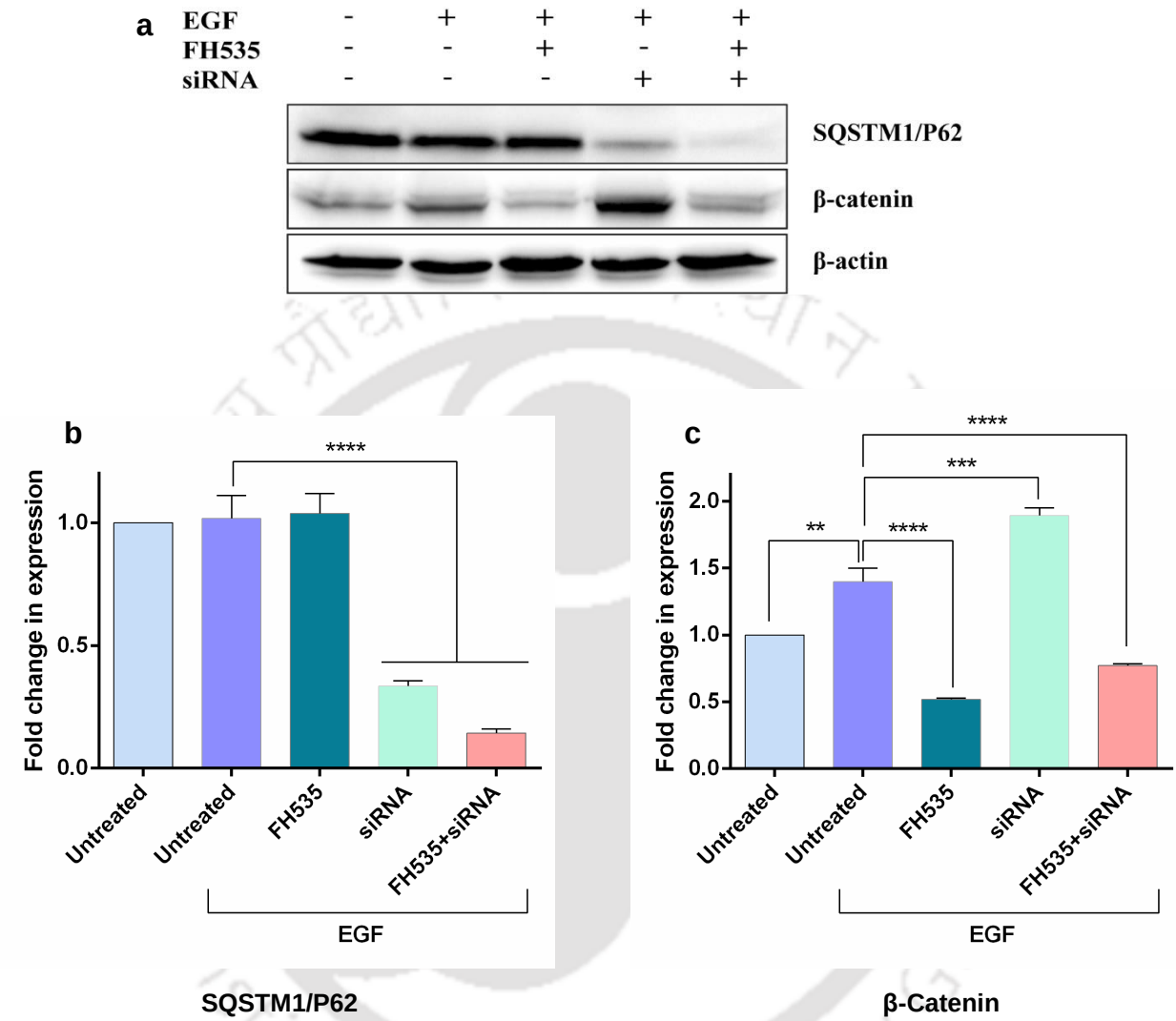

Figure. 3.2.8: (a) Representative Western blots showing SQSTM1/P62 and β-catenin levels in MDA-MB-468 cell extracts. β-actin serves as a loading control. Graphs depicts the alteration in the expression levels of (b) SQSTM1/P62 and (c) β-catenin with respect to untreated samples following inhibitor/siRNA treatment. The expression levels were deduced from the blots using ImageJ software.

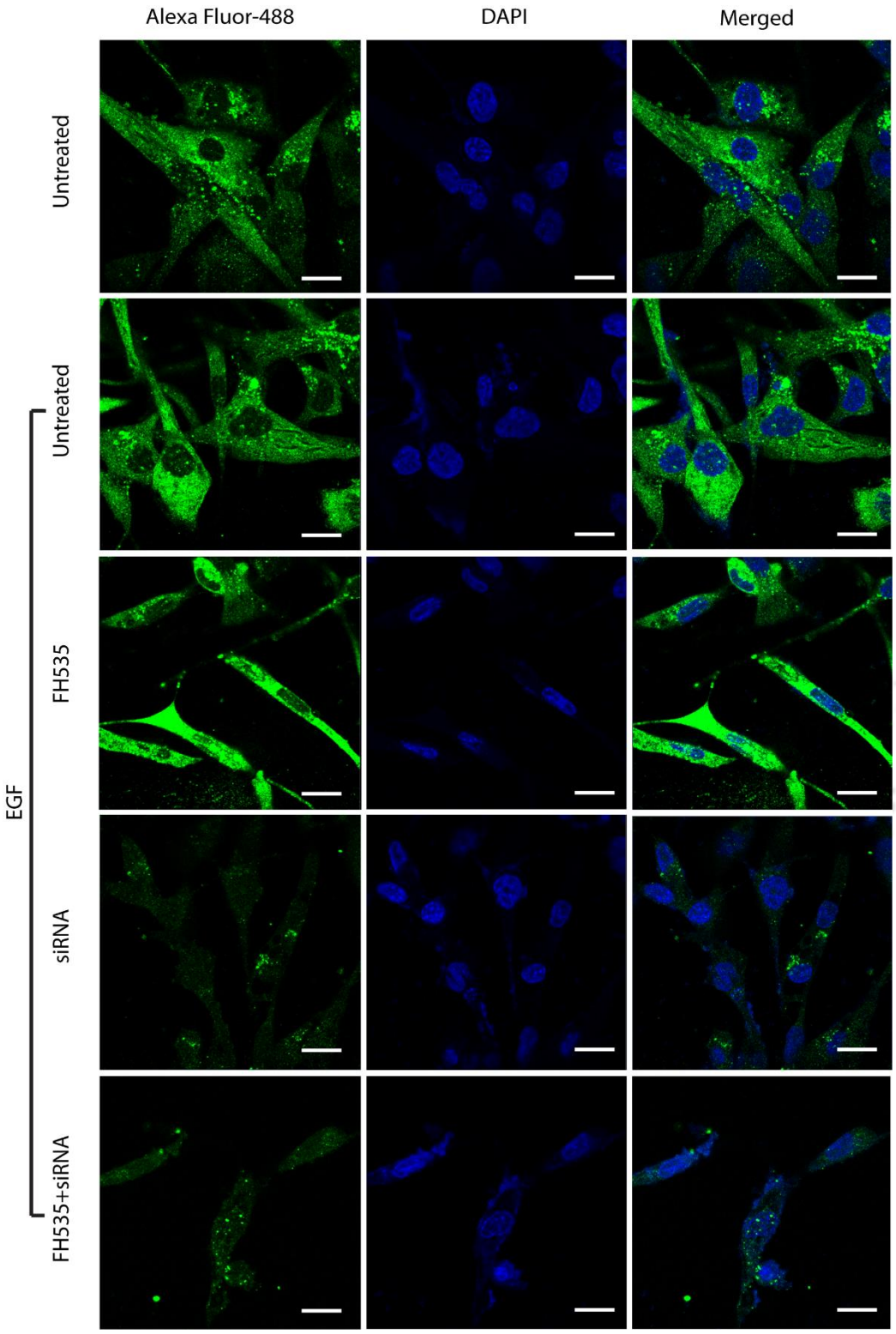

Figure. 3.2.9: Confocal images of MDA-MB-231 monolayer cultures immune-stained with anti-SQSTM1/P62 antibody visualized by Alexa Flour-488. Nuclei were stained with DAPI. Scale bar represents 20 μM.

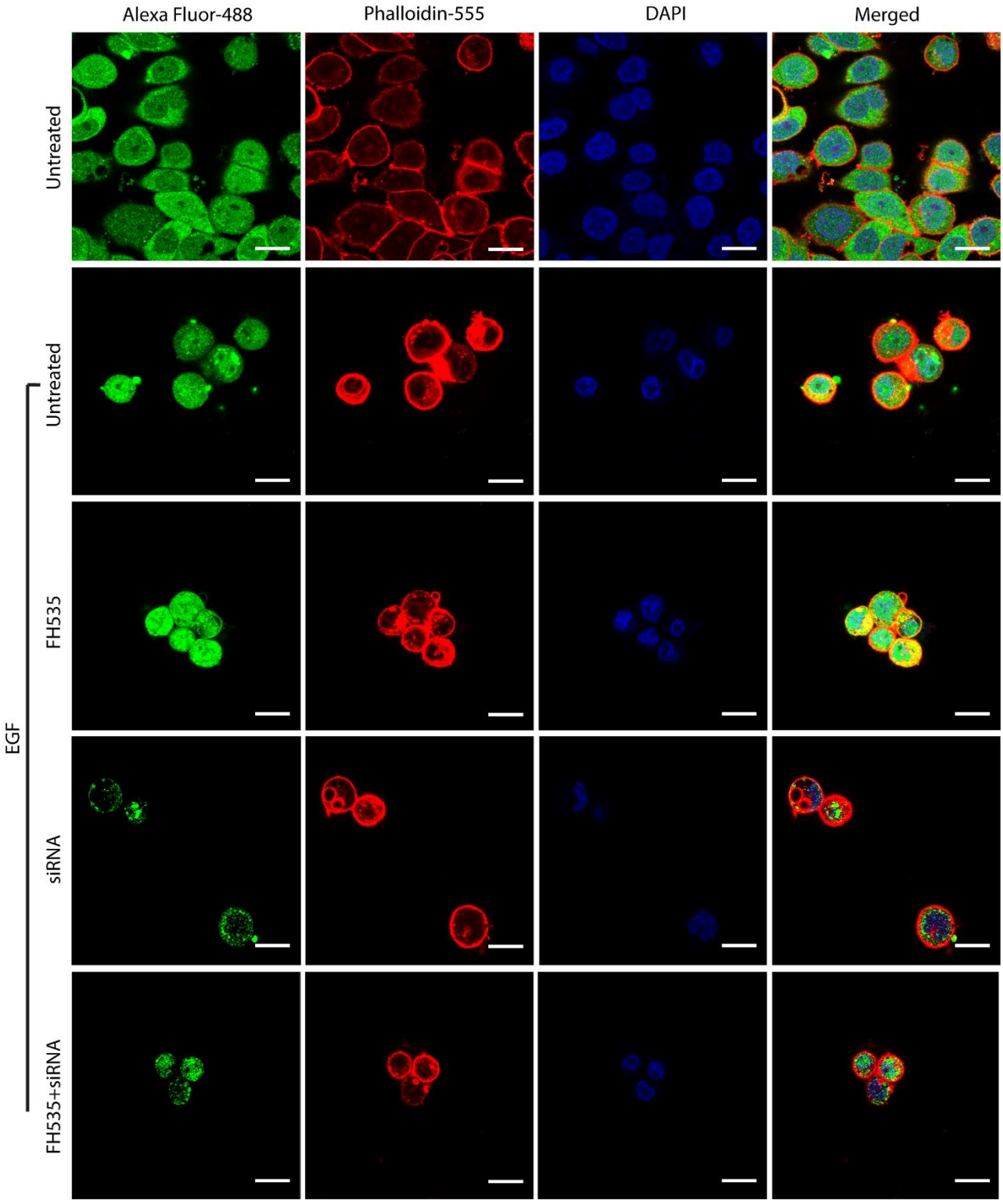

Figure. 3.2.10: Confocal images of MDA-MB-468 monolayer cultures immune-stained with anti-SQSTM1/P62 antibody visualized by Alexa Flour-488. Actin cytoskeleton were stained with Alexa Flour-555 conjugated phalloidin. Nuclei were stained with DAPI. Scale bar represents 20 μM.

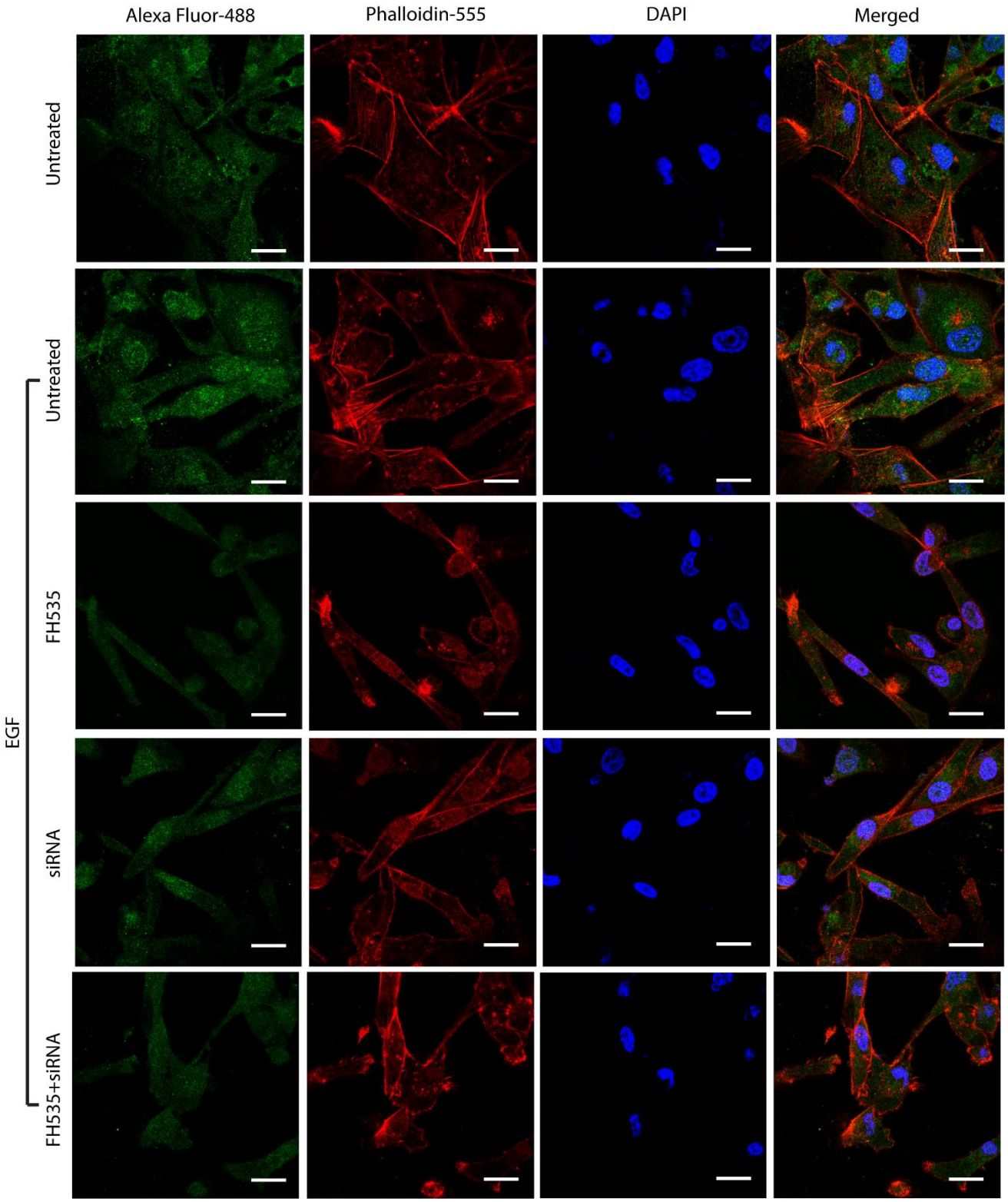

Figure. 3.2.11: Confocal images of MDA-MB-231 monolayer cultures immune-stained with anti-β-Catenin antibody visualized by Alexa Flour-488. Actin cytoskeleton were stained with Alexa Flour-555 conjugated phalloidin. Nuclei were stained with DAPI. Scale bar represents 20 μM.

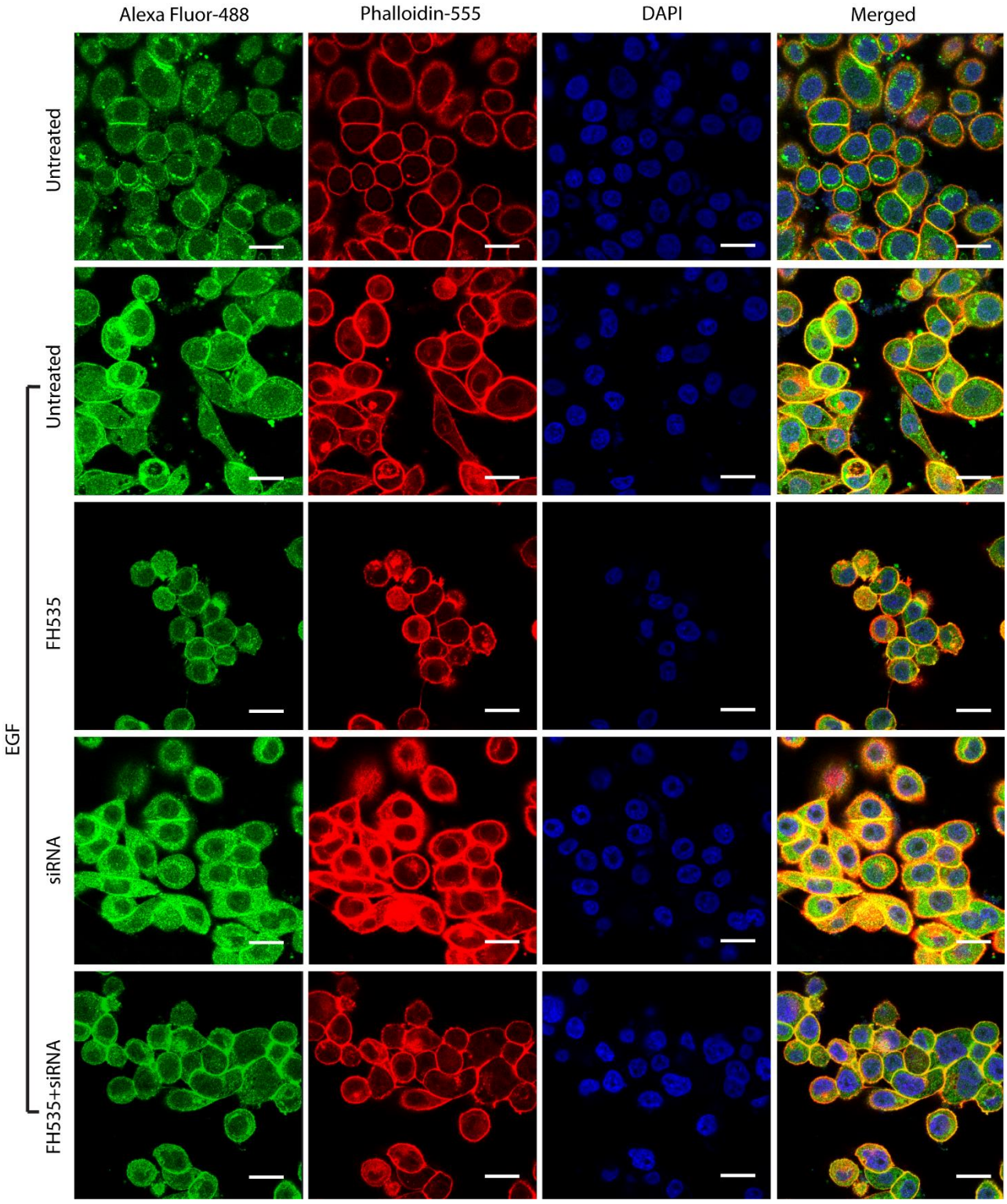

Figure. 3.2.12: Confocal images of MDA-MB-468 monolayer cultures immune-stained with anti-β-Catenin antibody visualized by Alexa Flour-488. Actin cytoskeleton were stained with Alexa Flour-555 conjugated phalloidin. Nuclei were stained with DAPI. Scale bar represents 20 μM.

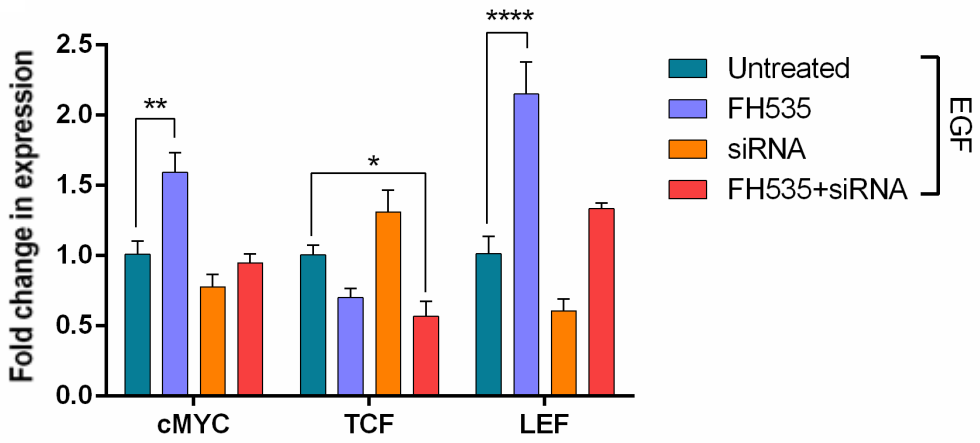

Figure. 3.2.13: Graphical representation of changes in gene expression levels in MDA-MB-231 following treatment with inhibitor/siRNA, quantified by qRT-PCR analysis. Results are expressed as mean relative gene expression level compared to β-actin ± SEM of three independent experiments, with $p < 0.05$ (*), $p < 0.01$ (**), $p < 0.001$ (***) or $p < 0.0001$ (****).

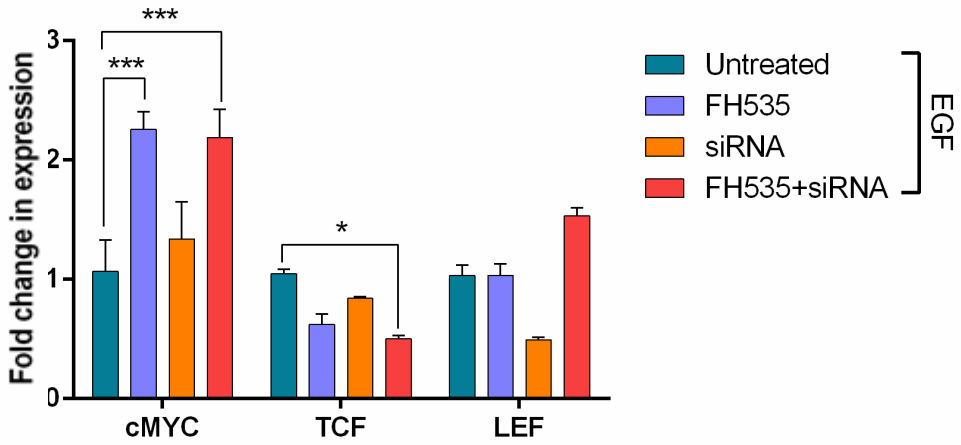

Figure. 3.2.14: Graphical representation of changes in gene expression levels in MDA-MB-468 following treatment with inhibitor/siRNA, quantified by qRT-PCR analysis. Results are expressed as mean relative gene expression level compared to β-actin ± SEM of three independent experiments, with $p < 0.05$ (*), $p < 0.01$ (**), $p < 0.001$ (***) or $p < 0.0001$ (****).

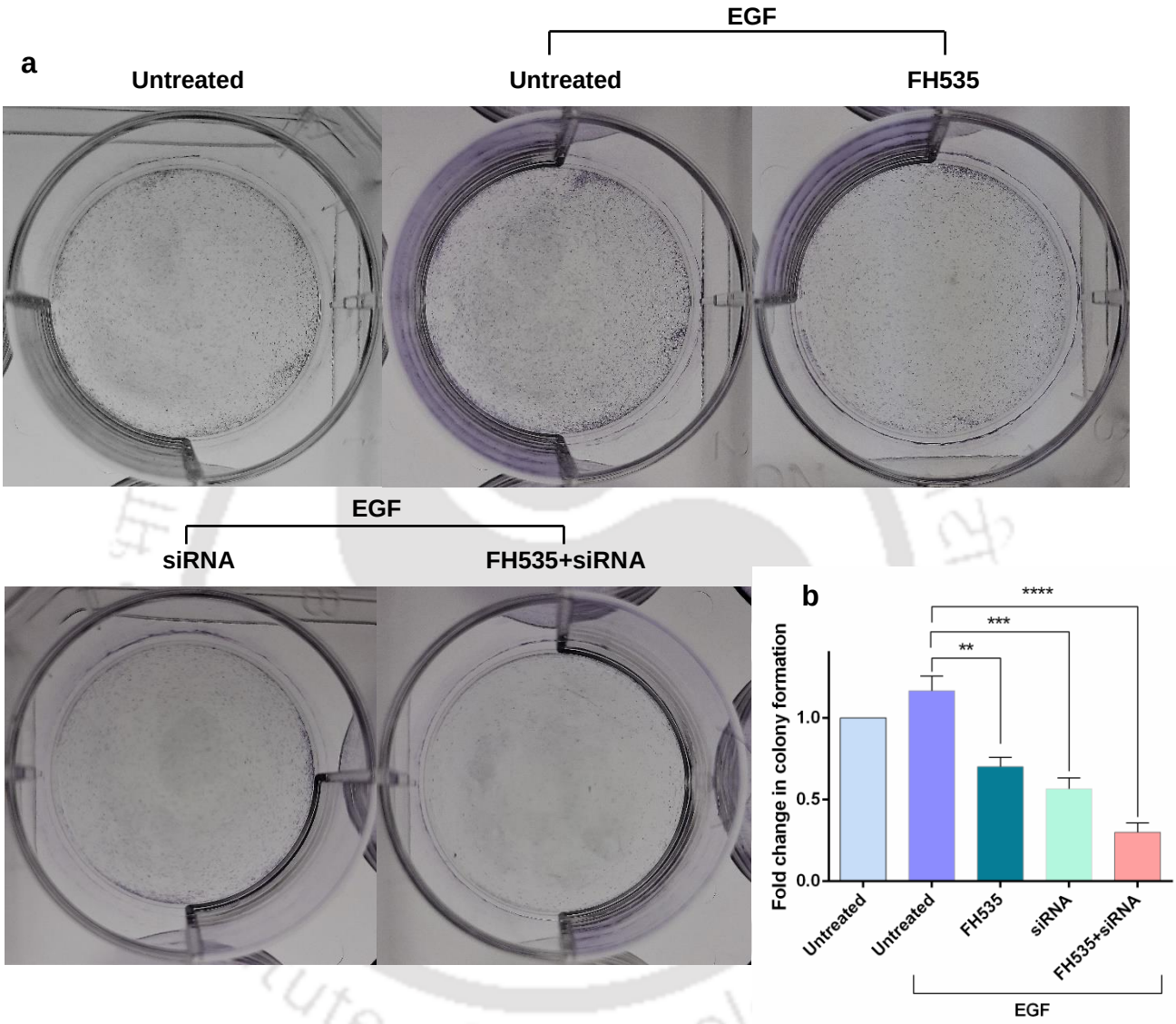

Figure. 3.2.15: (a) Alteration in colony forming ability of MDA-MB-231 cells following treatment with FH535 and siRNA. (b) Graphical representation of fold change in colony forming ability following co-treatment.

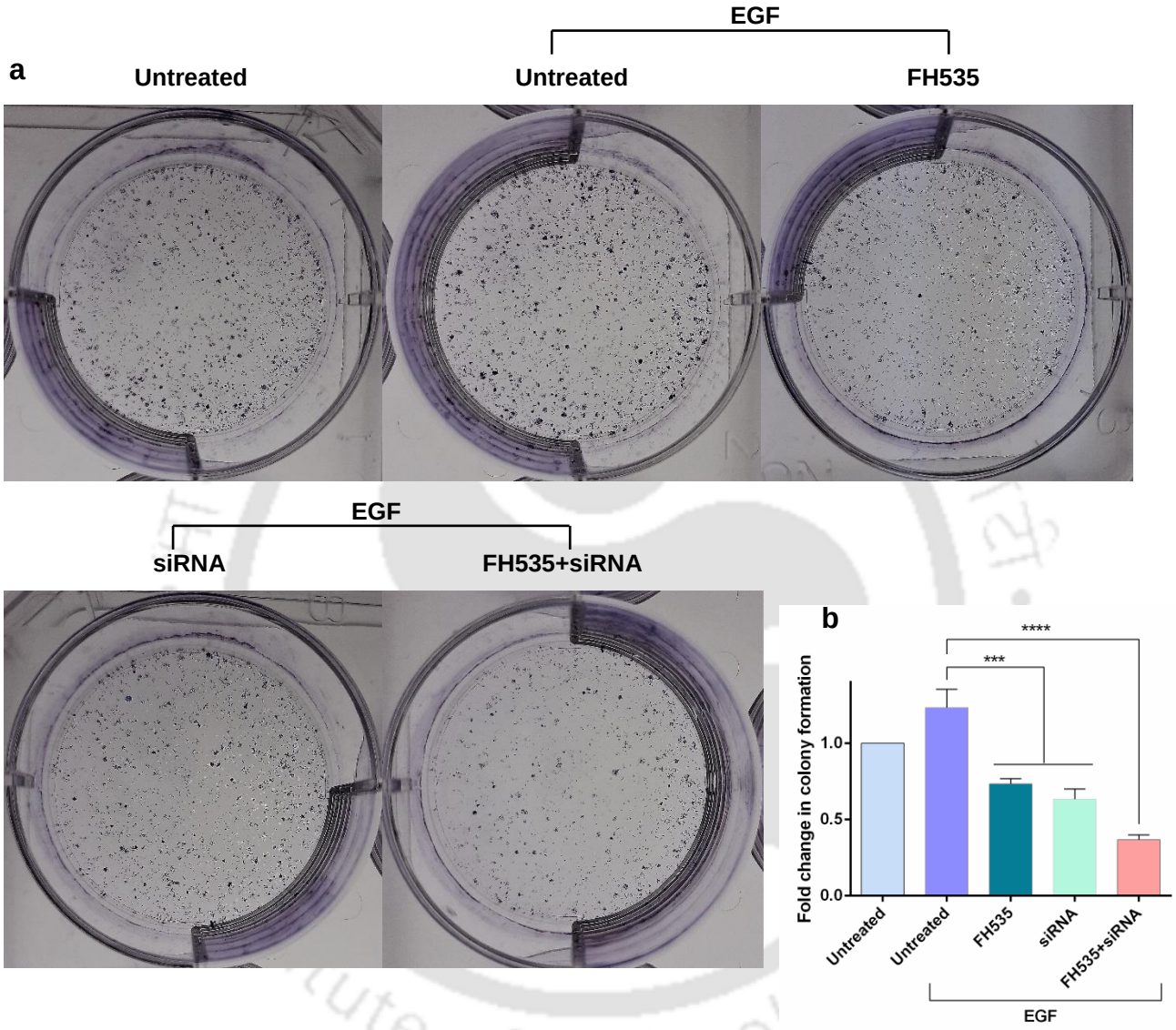

Figure. 3.2.16: (a) Alteration in colony forming ability of MDA-MB-468 cells following treatment with FH535 and siRNA. (b) Graphical representation of fold change in colony forming ability following co-treatment.

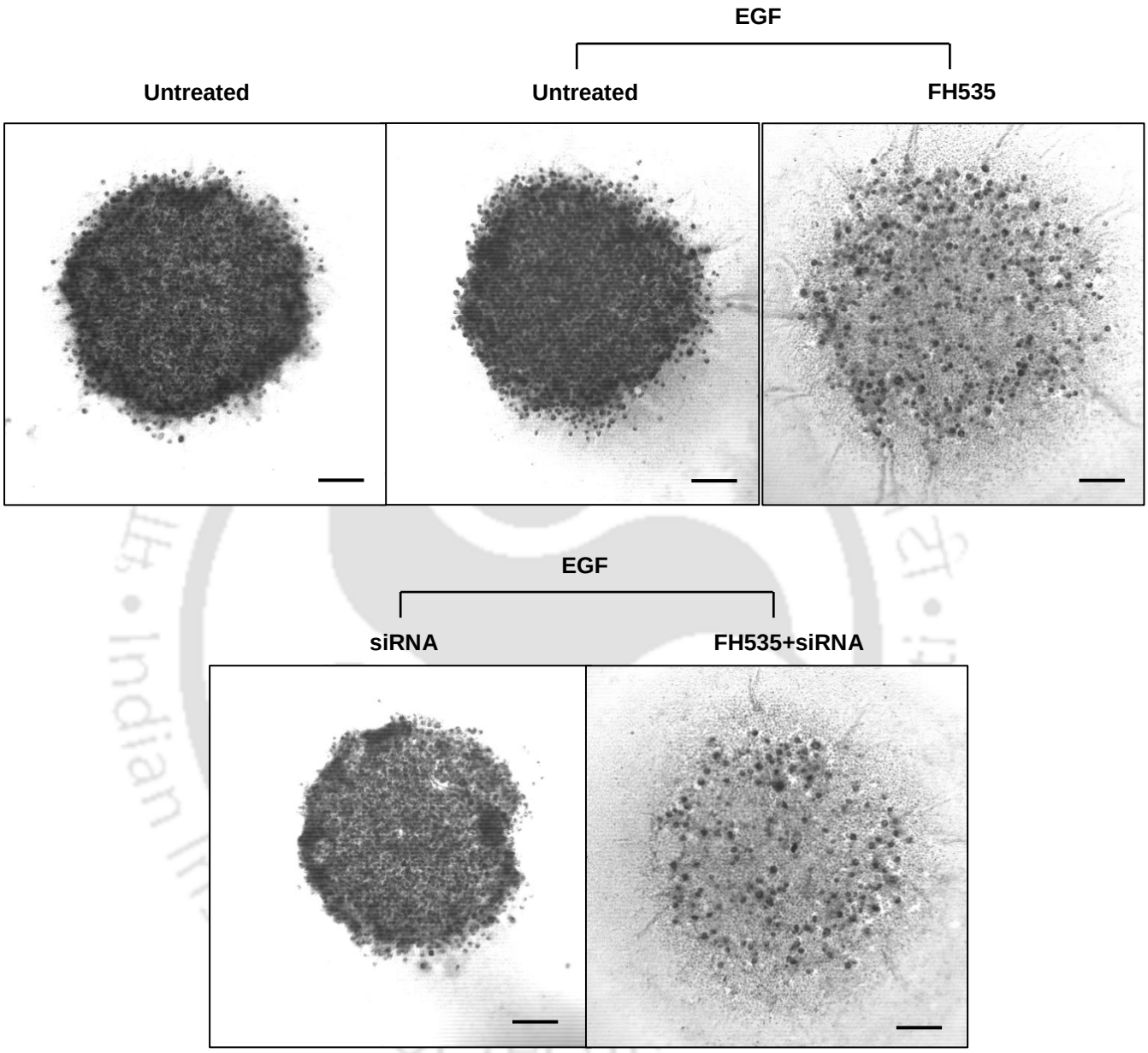

Figure. 3.2.17: Sphere formation assay of MDA-MB-231 cells to detect the alteration of stemness properties following treatment with inhibitor/siRNA. Scale bar represents 200 μM.

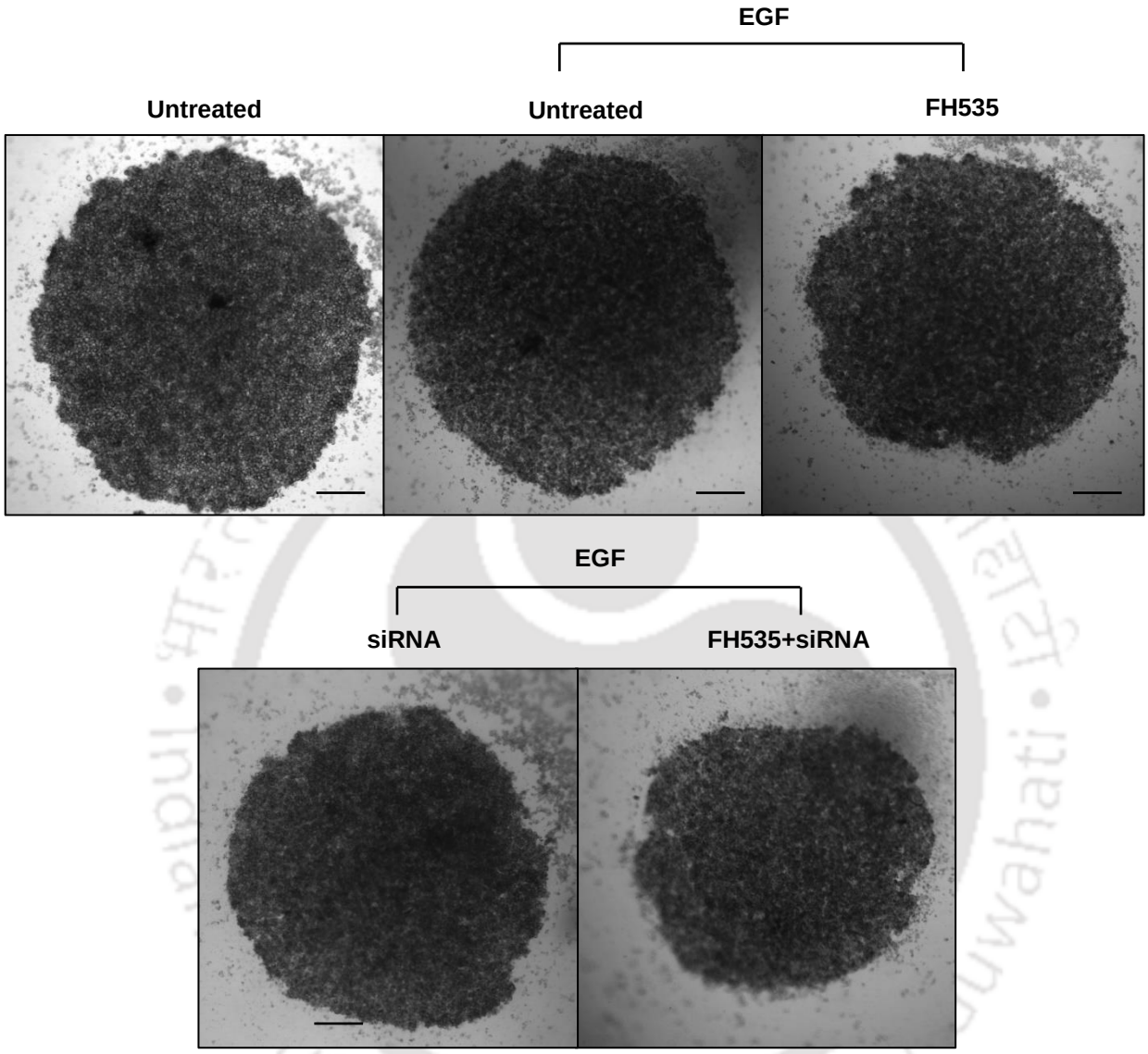

Figure. 3.2.18: Sphere formation assay of MDA-MB-468 cells to detect the alteration of stemness properties following treatment with inhibitor/siRNA. Scale bar represents 200 μM.

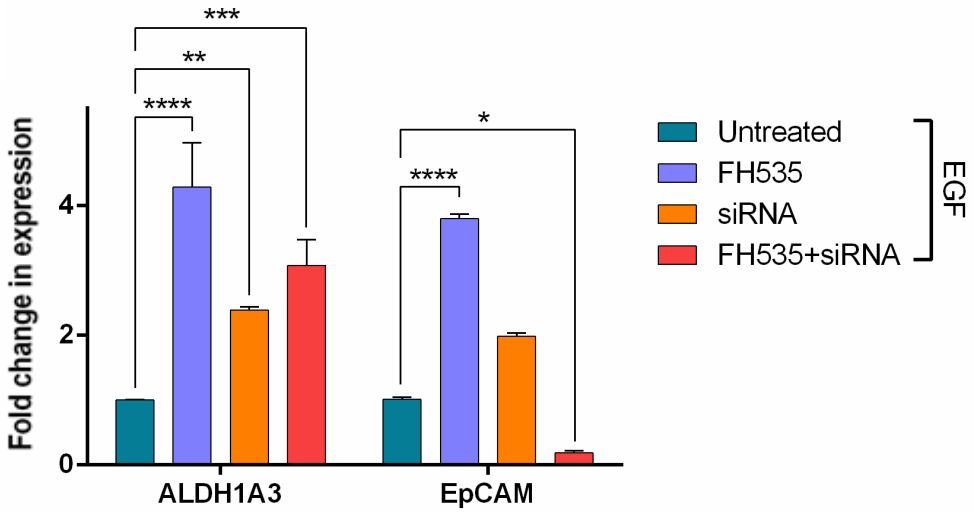

Figure. 3.2.19: Graphical representation of changes in gene expression levels in MDA-MB-231 following treatment with inhibitor/siRNA, quantified by qRT-PCR analysis. Results are expressed as mean relative gene expression level compared to β-actin ± SEM of three independent experiments, with $p < 0.05$ (*), $p < 0.01$ (**), $p < 0.001$ (***) or $p < 0.0001$ (****).

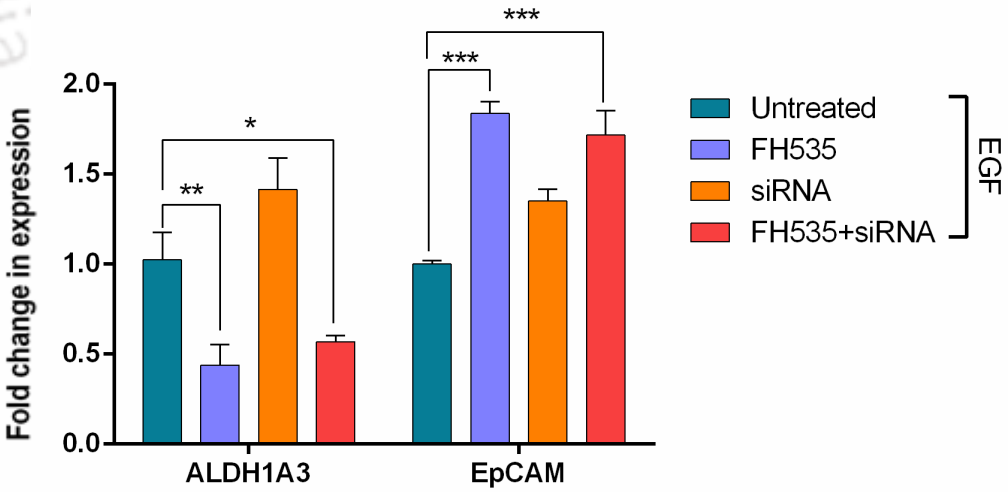

Figure. 3.2.20: Graphical representation of changes in gene expression levels in MDA-MB-468 following treatment with inhibitor/siRNA, quantified by qRT-PCR analysis. Results are expressed as mean relative gene expression level compared to β-actin ± SEM of three independent experiments, with $p < 0.05$ (*), $p < 0.01$ (**), $p < 0.001$ (***) or $p < 0.0001$ (****).

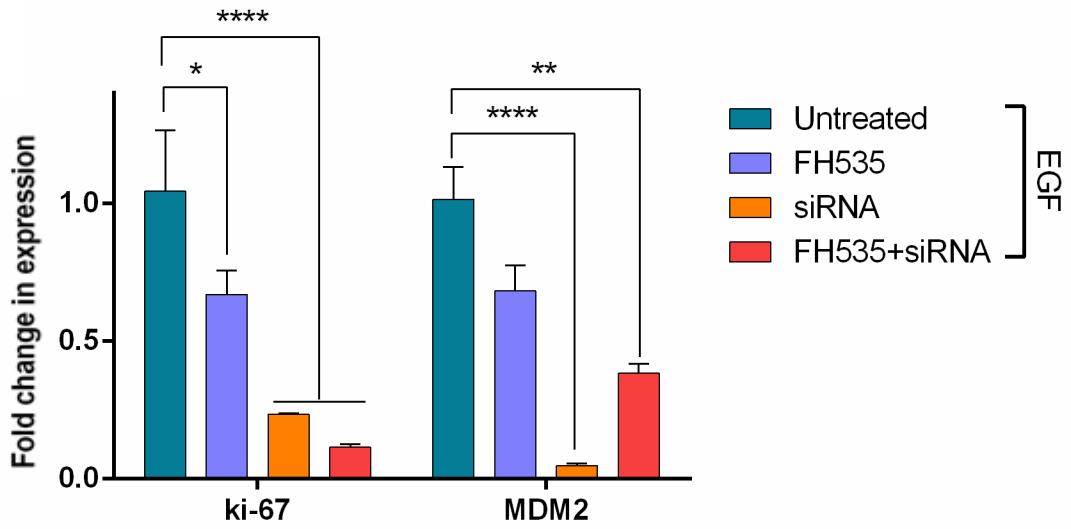

Figure. 3.2.21: Graphical representation of changes in gene expression levels in MDA-MB-231 following treatment with inhibitor/siRNA, quantified by qRT-PCR analysis. Results are expressed as mean relative gene expression level compared to β-actin ± SEM of three independent experiments, with $p < 0.05$ (*), $p < 0.01$ (**), $p < 0.001$ (***) or $p < 0.0001$ (****).

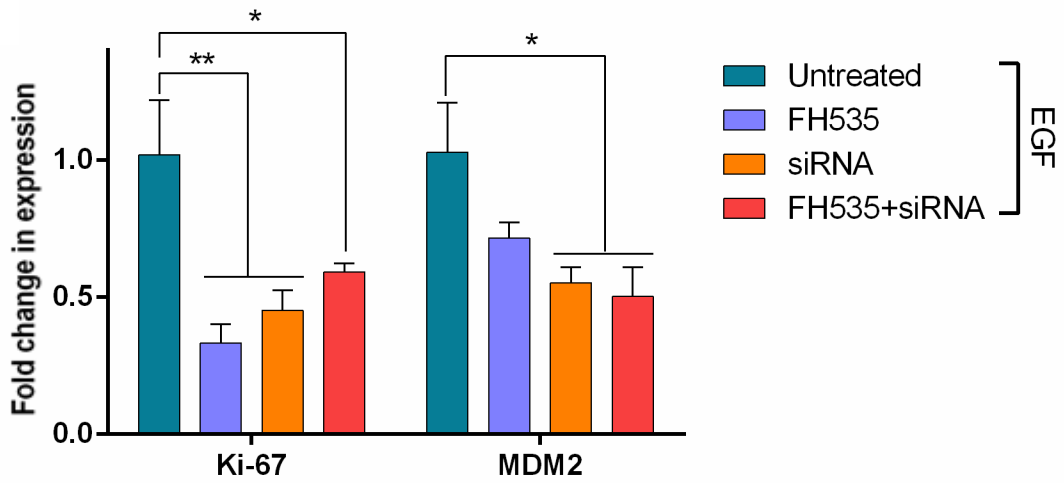

Figure. 3.2.22: Graphical representation of changes in gene expression levels in MDA-MB-231 following treatment with inhibitor/siRNA, quantified by qRT-PCR analysis. Results are expressed as mean relative gene expression level compared to β-actin ± SEM of three independent experiments, with $p < 0.05$ (*), $p < 0.01$ (**), $p < 0.001$ (***) or $p < 0.0001$ (****).

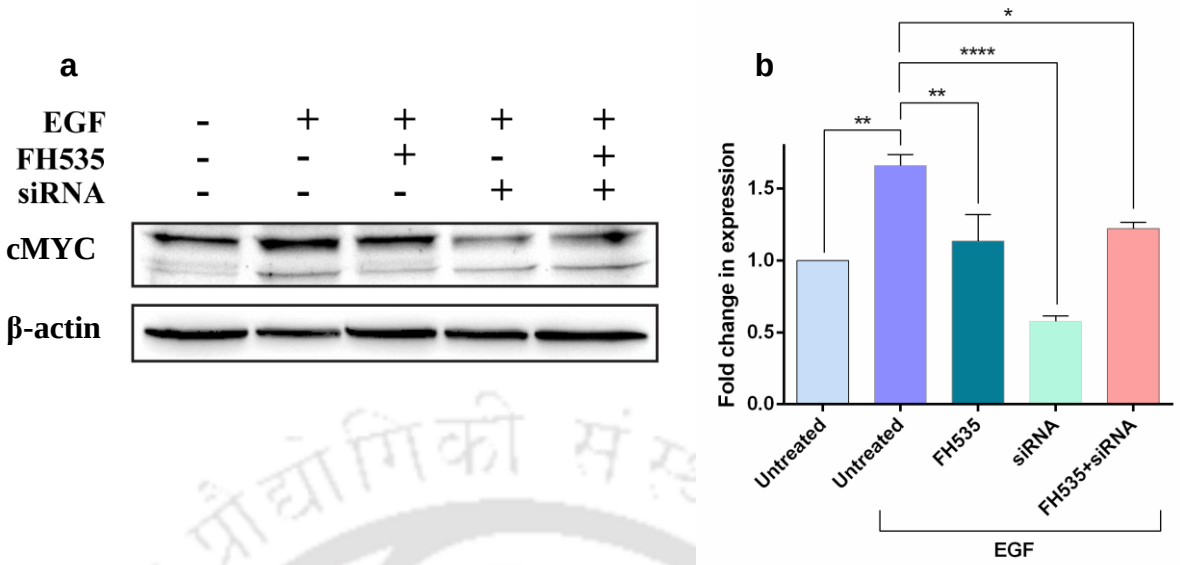

Figure. 3.2.23: (a) Representative Western blots showing cMYC protein expression level in MDA-MB-231 cell extracts. β-actin serves as a loading control. (b) Graphs depicts the alteration in the expression levels of cMYC with respect to untreated samples following inhibitor/siRNA treatment. The expression levels were deduced from the blots using ImageJ software.

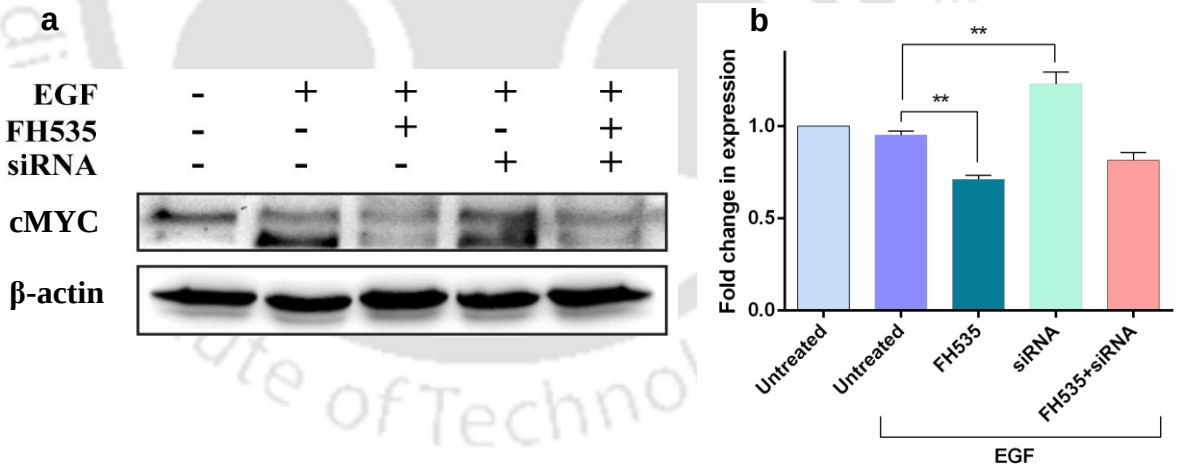

Figure. 3.2.24: (a) Representative Western blots showing cMYC protein expression level in MDA-MB-468 cell extracts. β-actin serves as a loading control. (b) Graphs depicts the alteration in the expression levels of cMYC with respect to untreated samples following inhibitor/siRNA treatment. The expression levels were deduced from the blots using ImageJ software.

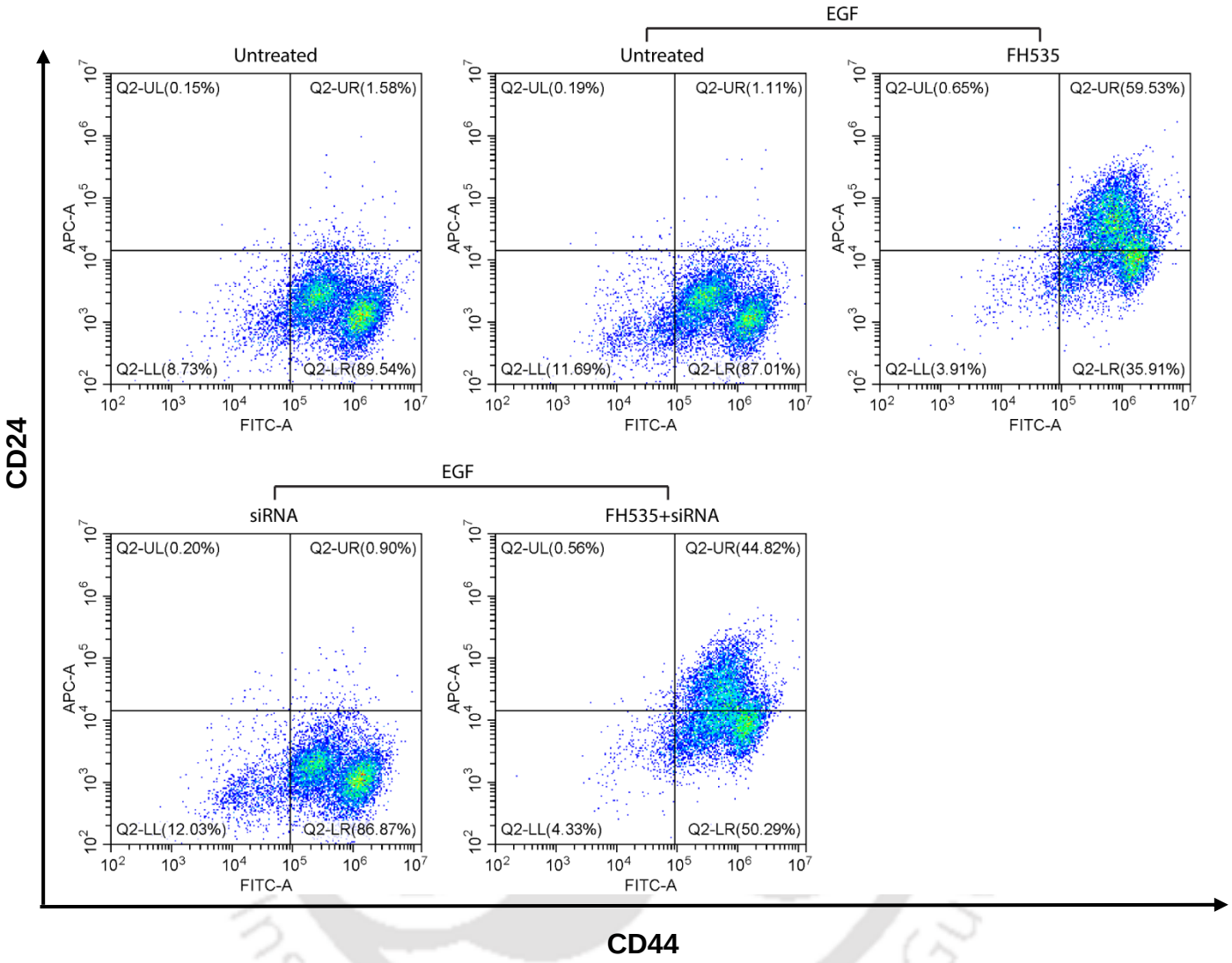

Figure. 3.2.25: Flow cytometric analysis of CD44/CD24 cell surface markers of MDA-MB-231 cells following treatment with inhibitors/siRNA for a period of 48 h. Cells were stained with FITC conjugated anti-CD44 antibody and APC conjugated anti-CD24 antibody. The obtained data were analyzed using CytExpert software.

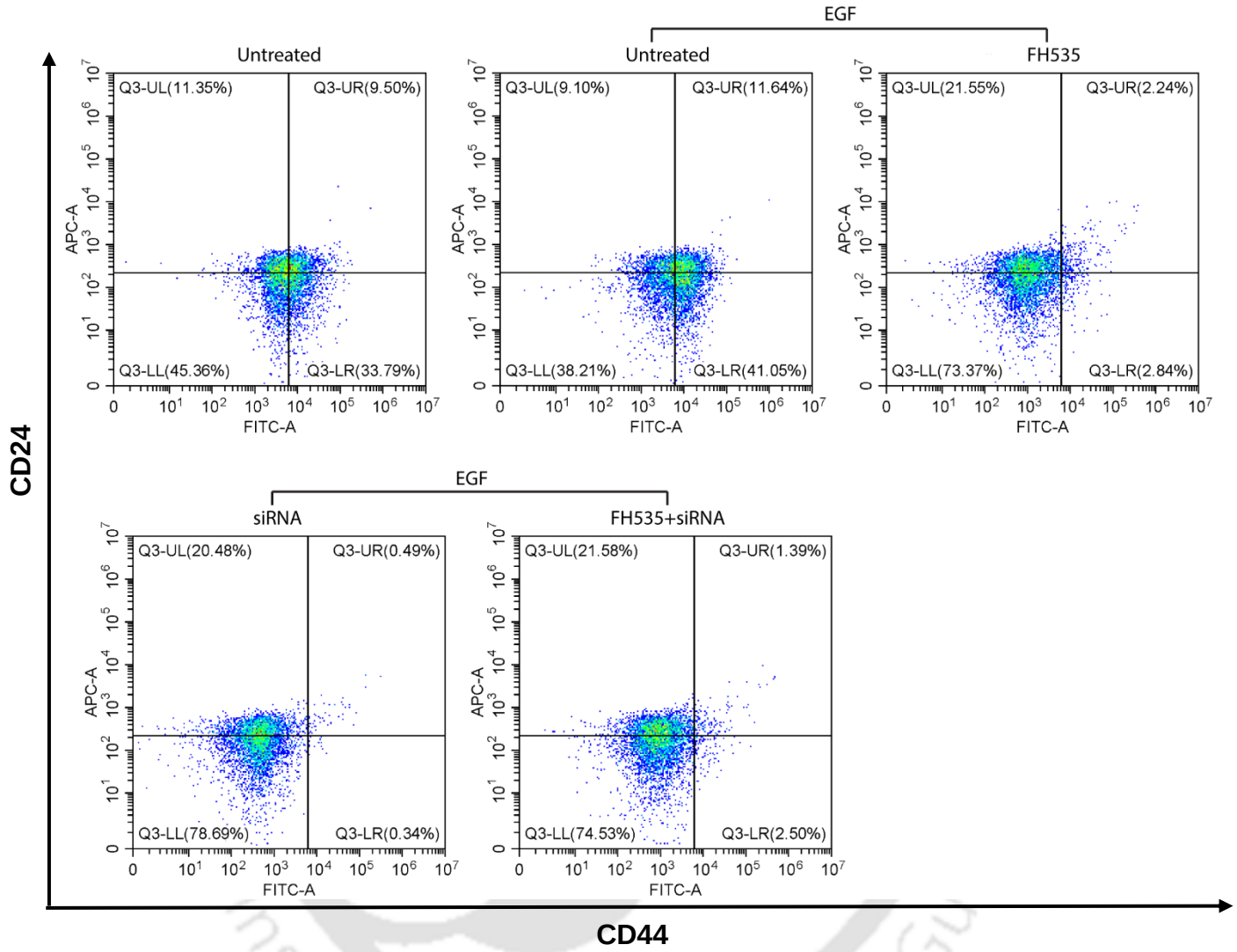

Figure. 3.2.26: Flow cytometric analysis of CD44/CD24 cell surface markers of MDA-MB-468 cells following treatment with inhibitors/siRNA for a period of 48 h. Cells were stained with FITC conjugated anti-CD44 antibody and APC conjugated anti-CD24 antibody. The obtained data were analyzed using CytExpert software.

3.2.1.3 Co-targeting SQSTM1/P62 and Wnt/β-Catenin Signaling Induces Mesenchymal to Epithelial Transition (MET) in TNBC: In the EMT process, tumor-associated epithelial cells obtain mesenchymal features with reduced cell-cell contacts and an increased motility, which play critical roles in invasion and metastasis. Given that suppression of SQSTM1/P62 and Wnt/β-Catenin independently and together resulted in diminished stemness of TNBC, it was then examined whether knockdown of SQSTM1/P62 and inhibition of Wnt/β-Catenin would affect the metastatic property of TNBC i.e., inhibit the epithelial to mesenchymal transition (EMT).

Therefore, qRT-PCR was performed to analyze the alteration of gene expression following co-targeting SQSTM1/P62 and Wnt/β-Catenin signaling. Loss of E-cadherin-mediated adhesion characterizes the transition from benign lesions to invasive, metastatic cancers [97]. On the other hand, Vimentin, N-Cadherin and Fibronectin are highly expressed in mesenchymal cells and are positively correlated with increased metastasis [146]. Following co-targeting signaling pathways E-cadherin was upregulated by several folds in both TNBC cell lines MDA-MB-231 and MDA-MB-468 (**Figure. 3.2.27** and **Figure. 3.2.28**). Mesenchymal marker Vimentin and N-cadherin were downregulated by several folds in both the cell lines (**Figure. 3.2.27** and **Figure. 3.2.28**). It can be observed that knockdown of SQSTM1/P62 alone was highly effective in diminishing the expression of vimentin. Both knockdown of SQSTM1/P62 and inhibition of Wnt/β-Catenin contributed to the depletion of N-Cadherin in MDA-MB-468 (**Figure. 3.2.27** and **Figure. 3.2.28**). Blocking Wnt/β-Catenin signaling was more effective in reducing the expression of Fibronectin over knockdown of SQSTM1/P62 (**Figure. 3.2.29** and **Figure. 3.2.30**).

Caveolin-1 plays a positive regulatory effect on TNBC invasion and metastasis [147]. Similar to other EMT factors, it was also downregulated following co-modulation of the pathways (**Figure. 3.2.29** and **Figure. 3.2.30**). Nonetheless, co-treatment reduced the expression of mesenchymal markers effectively.

EMT is orchestrated by a restricted number of transcription factors mainly the three Snail, Twist, and Zeb families, which are able to promote the repression of epithelial features and induction of mesenchymal features [148]. Hence, suppression of SQSTM1/P62 and Wnt/β-Catenin reduced the expression of Twist1 and Snail by 2.2-fold and 3.05-fold (**Figure. 3.2.31** and **Figure. 3.2.32**). It can be noticed that SQSTM1/P62 knockdown was more effective in downregulating Twist1 in comparision to the combination treatment.

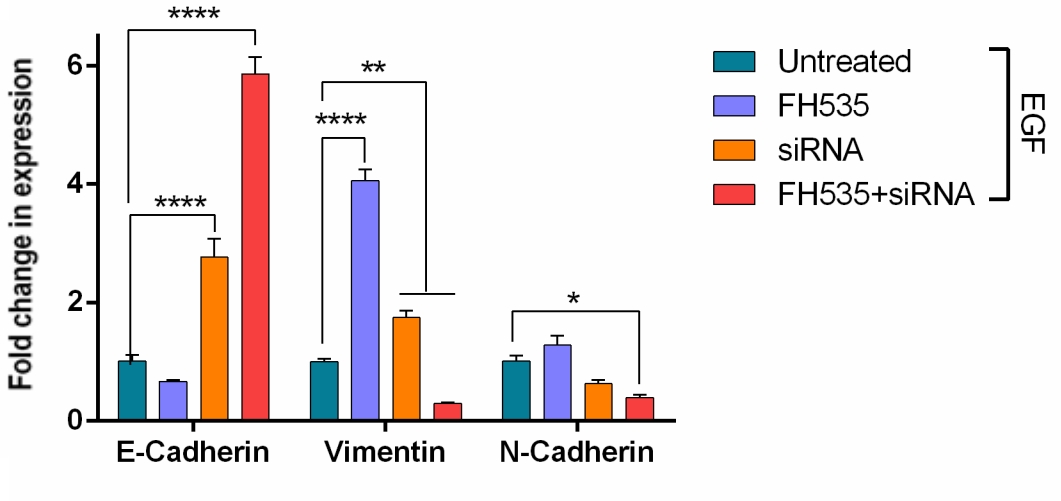

Figure. 3.2.27: Graphical representation of changes in gene expression levels in MDA-MB-231 following treatment with inhibitor/siRNA, quantified by qRT-PCR analysis. Results are expressed as mean relative gene expression level compared to β-actin ± SEM of three independent experiments, with $p < 0.05$ (*), $p < 0.01$ (**), $p < 0.001$ (***) or $p < 0.0001$ (****).

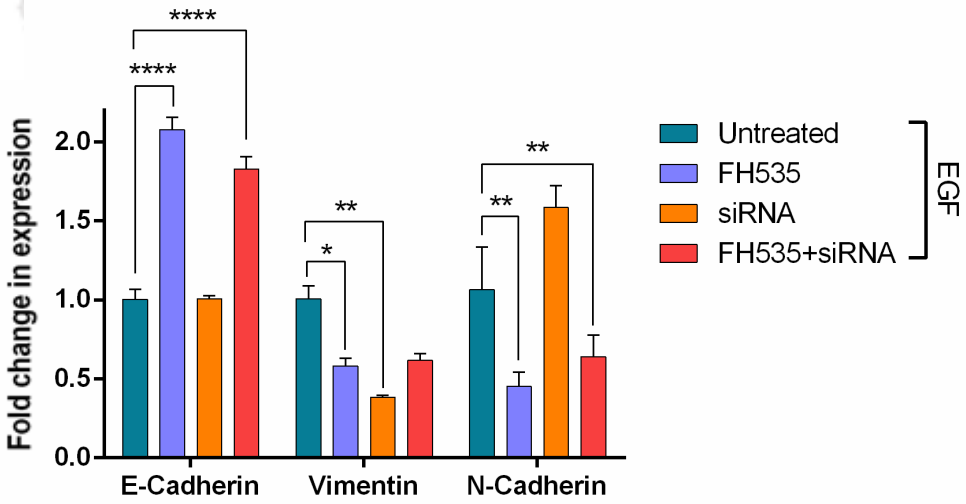

Figure. 3.2.28: Graphical representation of changes in gene expression levels in MDA-MB-231 following treatment with inhibitor/siRNA, quantified by qRT-PCR analysis. Results are expressed as mean relative gene expression level compared to β-actin ± SEM of three independent experiments, with $p < 0.05$ (*), $p < 0.01$ (**), $p < 0.001$ (***) or $p < 0.0001$ (****).

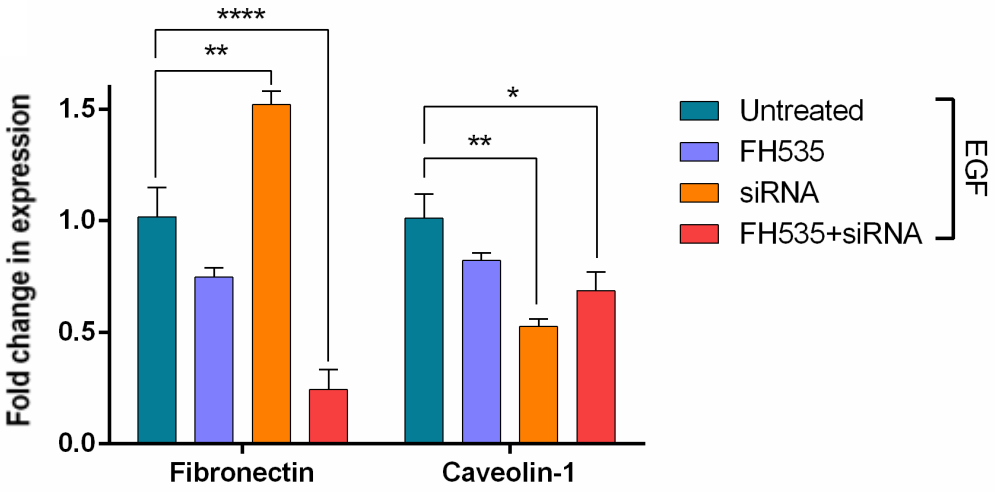

Figure. 3.2.29: Graphical representation of changes in gene expression levels in MDA-MB-231 following treatment with inhibitor/siRNA, quantified by qRT-PCR analysis. Results are expressed as mean relative gene expression level compared to β-actin ± SEM of three independent experiments, with $p < 0.05$ (*), $p < 0.01$ (**), $p < 0.001$ (***) or $p < 0.0001$ (****).

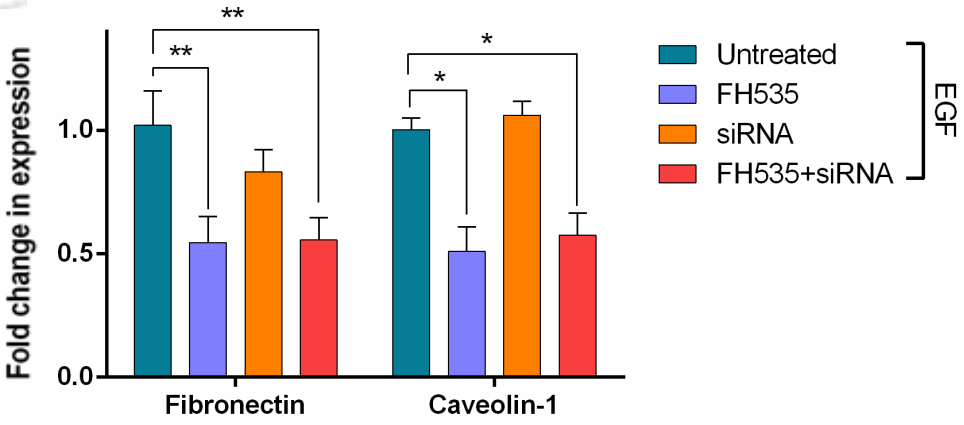

Figure. 3.2.30: Graphical representation of changes in gene expression levels in MDA-MB-231 following treatment with inhibitor/siRNA, quantified by qRT-PCR analysis. Results are expressed as mean relative gene expression level compared to β-actin ± SEM of three independent experiments, with $p < 0.05$ (*), $p < 0.01$ (**), $p < 0.001$ (***) or $p < 0.0001$ (****).

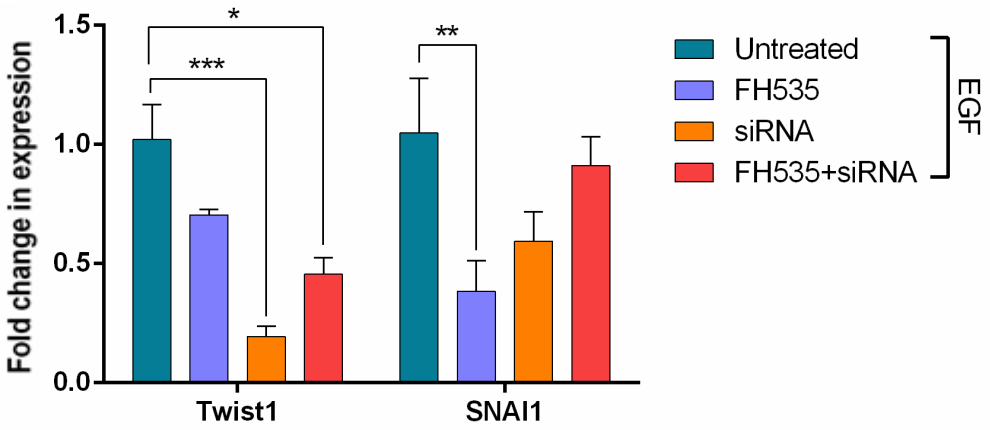

Figure. 3.2.31: Graphical representation of changes in gene expression levels in MDA-MB-231 following treatment with inhibitor/siRNA, quantified by qRT-PCR analysis. Results are expressed as mean relative gene expression level compared to β-actin ± SEM of three independent experiments, with $p < 0.05$ (*), $p < 0.01$ (**), $p < 0.001$ (***) or $p < 0.0001$ (****).

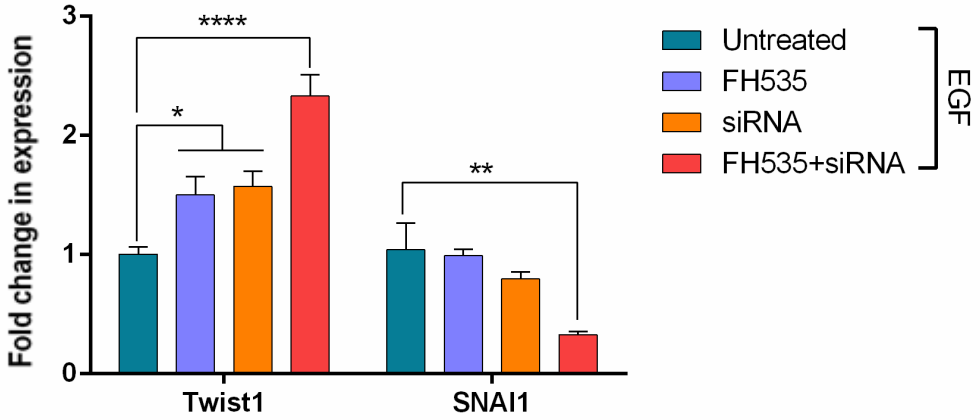

Figure. 3.2.32: Graphical representation of changes in gene expression levels in MDA-MB-231 following treatment with inhibitor/siRNA, quantified by qRT-PCR analysis. Results are expressed as mean relative gene expression level compared to β-actin ± SEM of three independent experiments, with $p < 0.05$ (*), $p < 0.01$ (**), $p < 0.001$ (***) or $p < 0.0001$ (****).

Furthermore, protein expression analysis was performed by Western blot. As shown in **Figure. 3.2.33** and **Figure. 3.2.34**, E-cadherin expression was significantly induced by knockdown of SQSTM1/P62 in both TNBC cell line MDA-MB-231 and MDA-MB-468. However, treatment with FH535 resulted in decrease in E-cadherin expression. Additionally, it also contributed to reduced E-cadherin expression in case of co-treatment (**Figure. 3.2.33** and **Figure. 3.2.34**). Moreover, mesenchymal marker vimentin was effectively depleted following knockdown of SQSTM1/P62 in both the cell lines (**Figure. 3.2.35** and **Figure. 3.2.36**). The similar effect was also observed in case of β-Catenin down-regulation. Similar to individual treatment, co-treatment effectively downregulated vimentin expression (**Figure. 3.2.35** and **Figure. 3.2.36**). Further, immunocytochemistry of MDA-MB-231 and MDA-MB-468 depicted the decrease in vimentin expression by co-treatment (**Figure. 3.2.37** and **Figure. 3.2.38)**.

Next, the alteration of expression level of transcription factors contributing to EMT was examined. The expression of Twist1 was diminished following co-treatment in both TNBC cell line MDA-MB-231 and MDA-MB-468 (**Figure. 3.2.39** and **Figure. 3.2.40**). Although, Knockdown of SQSTM1/P62 contributed to reduction of Twist1, the effect of inhibition of Wnt/β-Catenin signaling was more profound in MDA-MB-468 (**Figure. 3.2.39** and **Figure. 3.2.40**). Additionally, in MDA-MB-231, SQSTM1/P62 knockdown resulted in the reduction in ZEB1 expression (**Figure. 3.2.39**). Alteration of SQSTM1/P62 and Wnt/β-Catenin signaling had no effect on the expression of Snail in MDA-MB-231(**Figure. 3.2.39**). However, in MDA-MB-468 the Snail was effectively reduced by co-targeting (**Figure. 3.2.40**).

Besides analyzing the changes of protein expression in monolayer culture, the effect of combination was also examined in tumor spheroids which mimics the solid tumors. Unlike the monolayer culture, knockdown of SQSTM1/P62 reduced the expression of Snail in MDA-MB-231 3D spheroids (**Figure. 3.2.41**). Although,

Wnt/β-Catenin signaling inhibition increased the expression of E-cadherin in MDA-MB-468, the co-treatment was unable to increase it's expression (**Figure. 3.2.42**). The expression of Twist1 was almost found to be unaltered (**Figure. 3.2.42**).

Together, these findings indicate that co-targeting SQSTM1/P62 and Wnt/β-Catenin signaling induces MET and concomitant reductions in the metastatic potentials of TNBC cells.

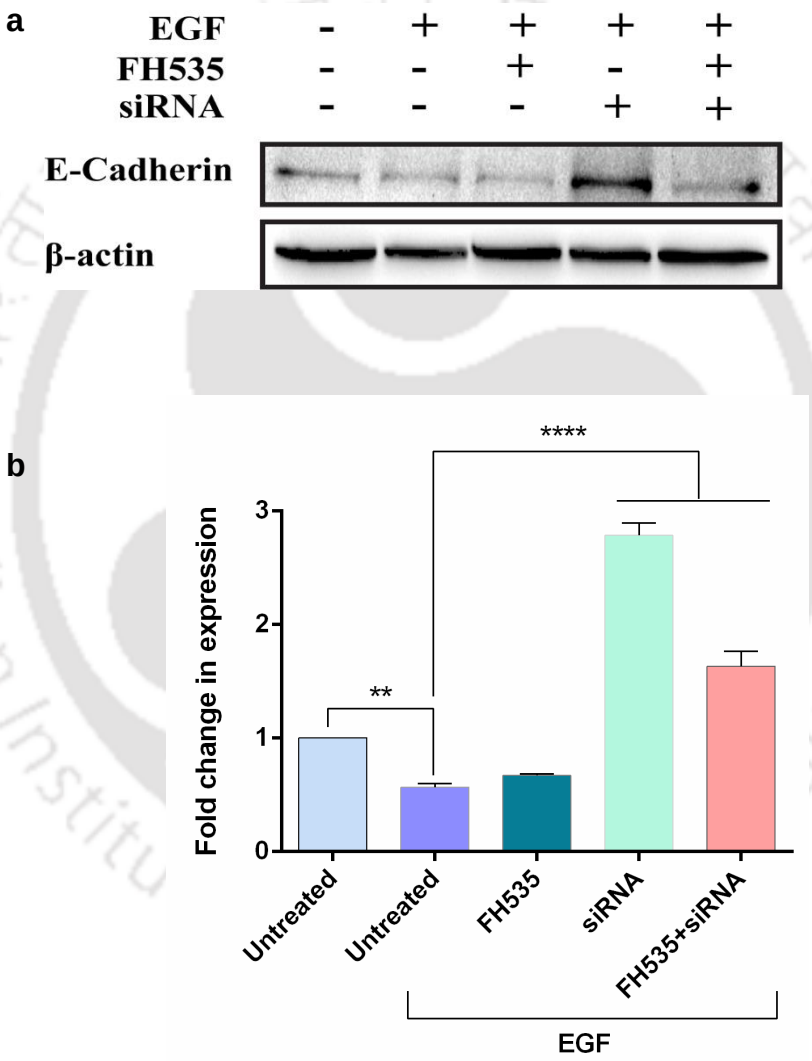

Figure. 3.2.33: (a) Representative Western blots showing E-Cadherin levels in MDA-MB-231 cell extracts. β-actin serves as a loading control. (b) Graphs depicts the alteration in the expression levels of E-Cadherin with respect to untreated samples following inhibitor/siRNA treatment. The expression levels were deduced from the blots using ImageJ software.

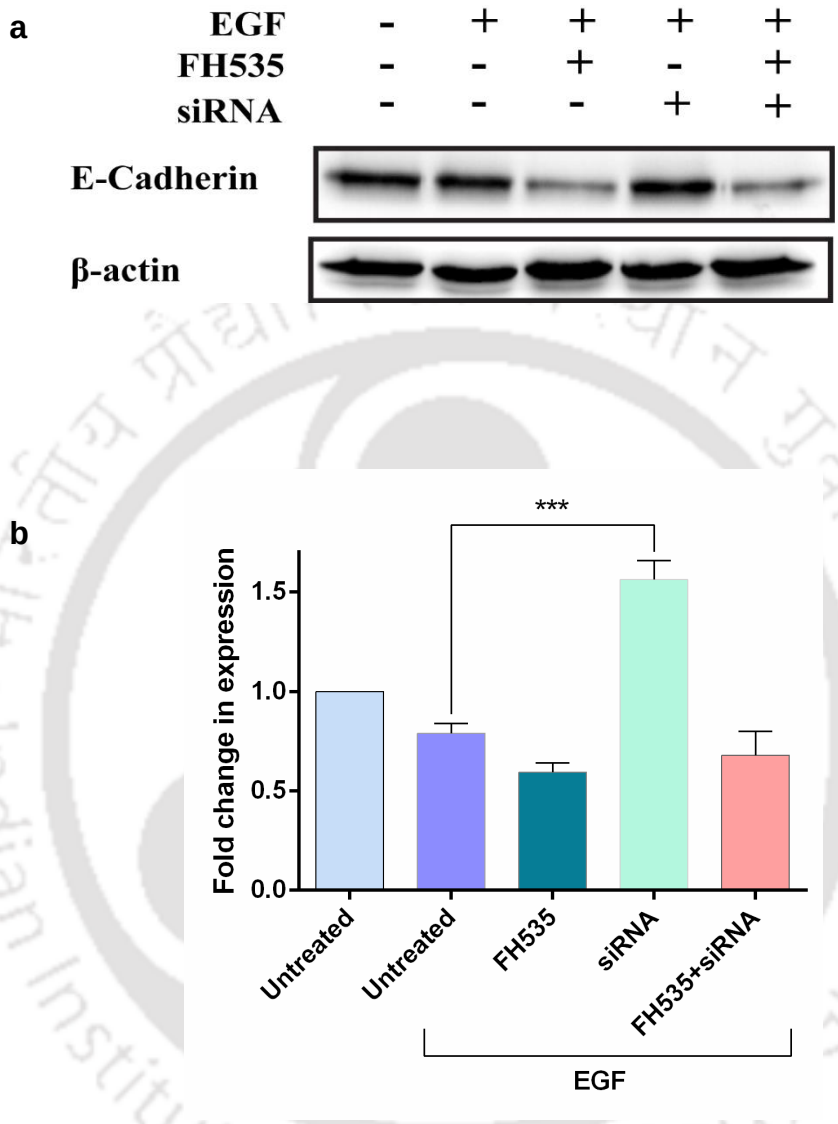

Figure. 3.2.34: (a) Representative Western blots showing E-Cadherin levels in MDA-MB-468 cell extracts. β-actin serves as a loading control. (b) Graphs depicts the alteration in the expression levels of E-Cadherin with respect to untreated samples following inhibitor/siRNA treatment. The expression levels were deduced from the blots using ImageJ software.

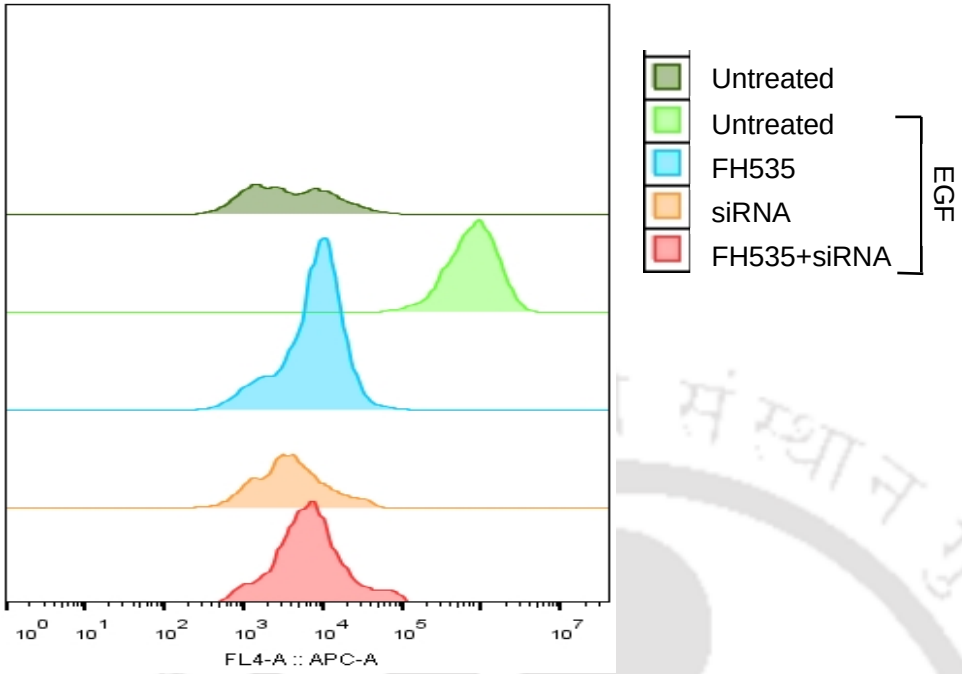

Figure. 3.2.35: The histogram of immunofluorescence flowcytometry detecting Vimentin of MDA-MB-231 monolayer cultures.

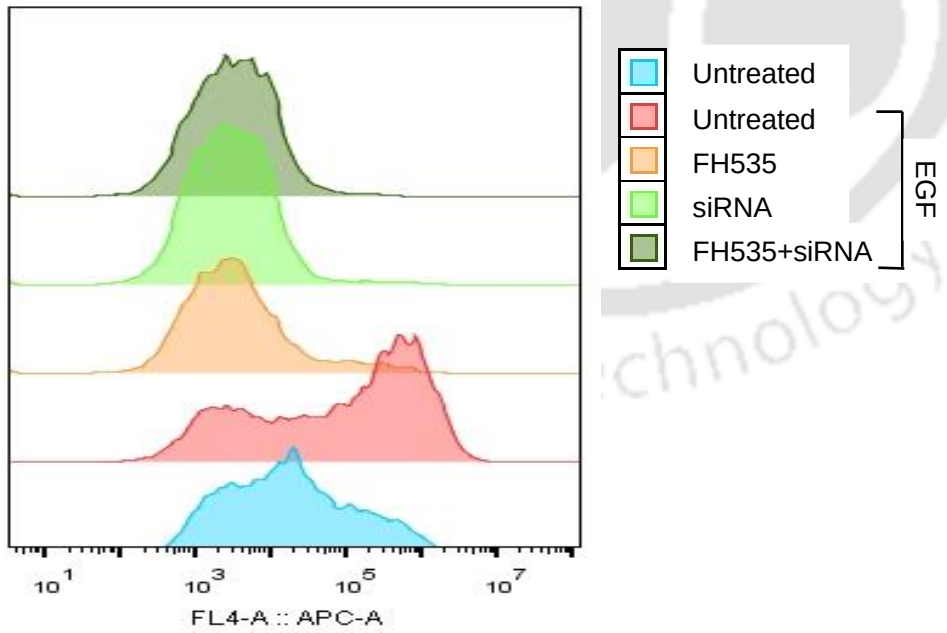

Figure. 3.2.36: The histogram of immunofluorescence flowcytometry detecting Vimentin of MDA-MB-468 monolayer cultures.

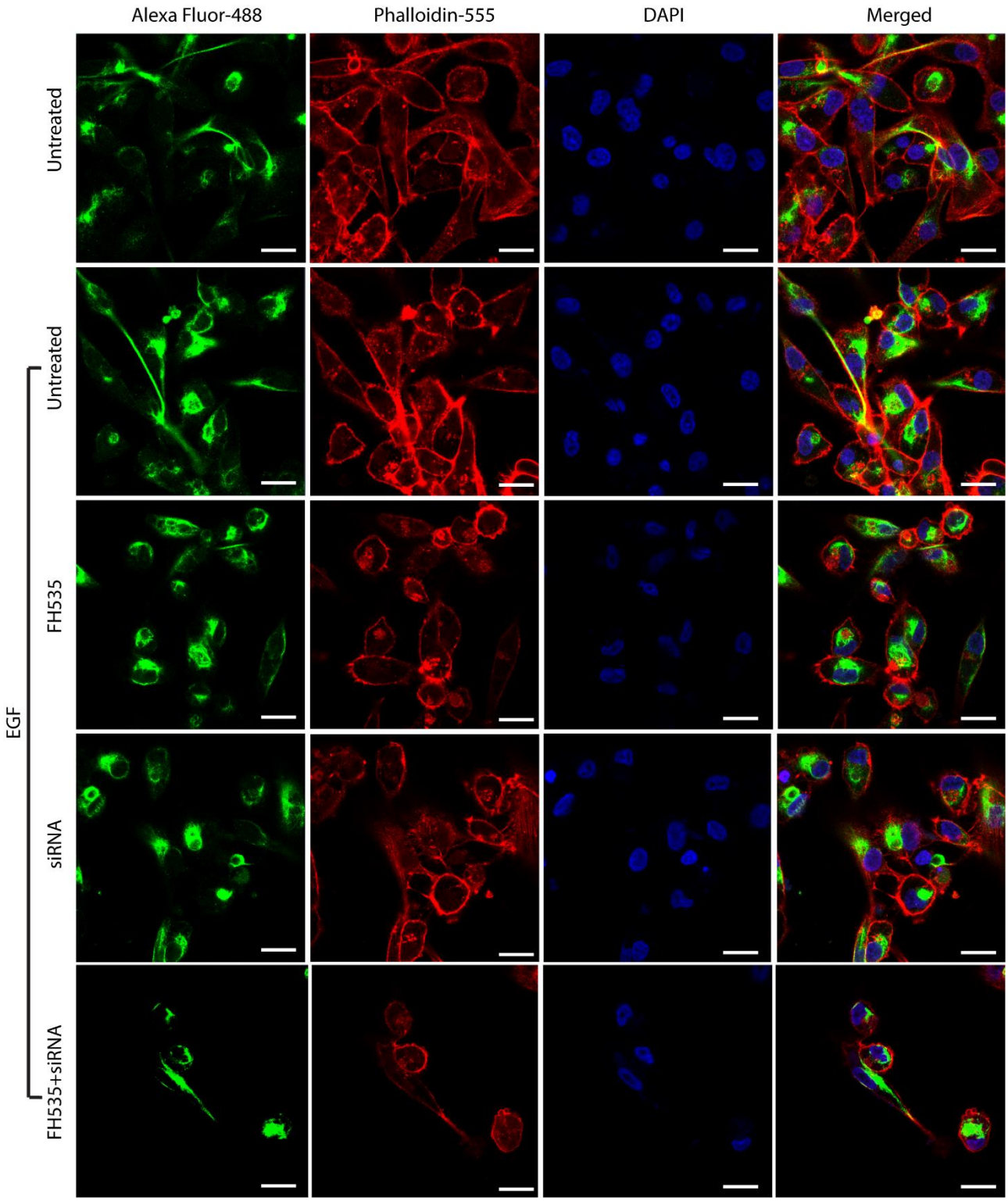

Figure. 3.2.37: Confocal images of MDA-MB-231 monolayer cultures immune-stained with anti-Vimentin antibody visualized by Alexa Flour-488. Actin cytoskeleton were stained with Alexa Flour-555 conjugated phalloidin. Nuclei were stained with DAPI. Scale bar represents 20 μM.

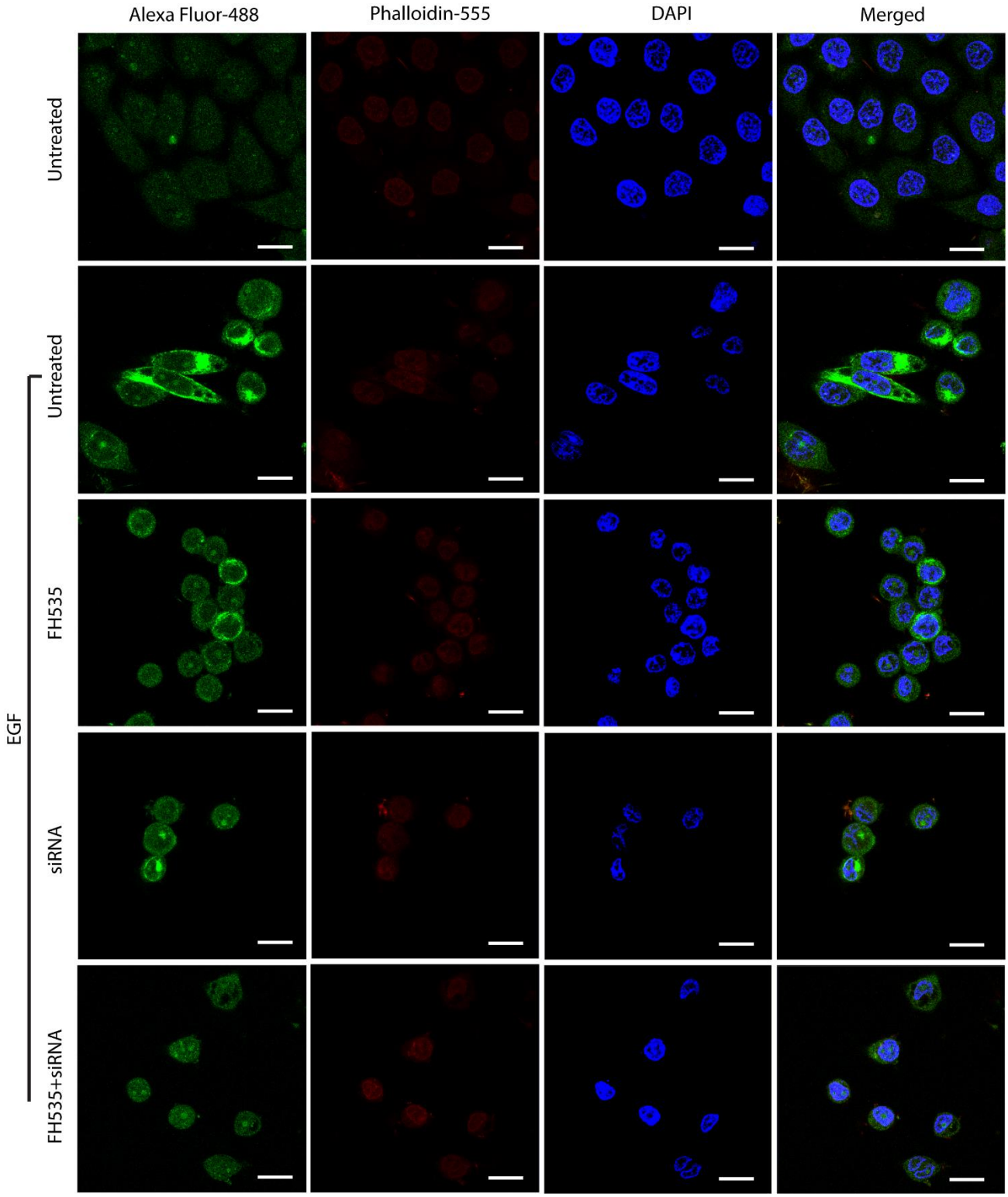

Figure. 3.2.38: Confocal images of MDA-MB-468 monolayer cultures immune-stained with anti-Vimentin antibody visualized by Alexa Flour-488. Actin cytoskeleton were stained with Alexa Flour-555 conjugated phalloidin. Nuclei were stained with DAPI. Scale bar represents 20 μM.

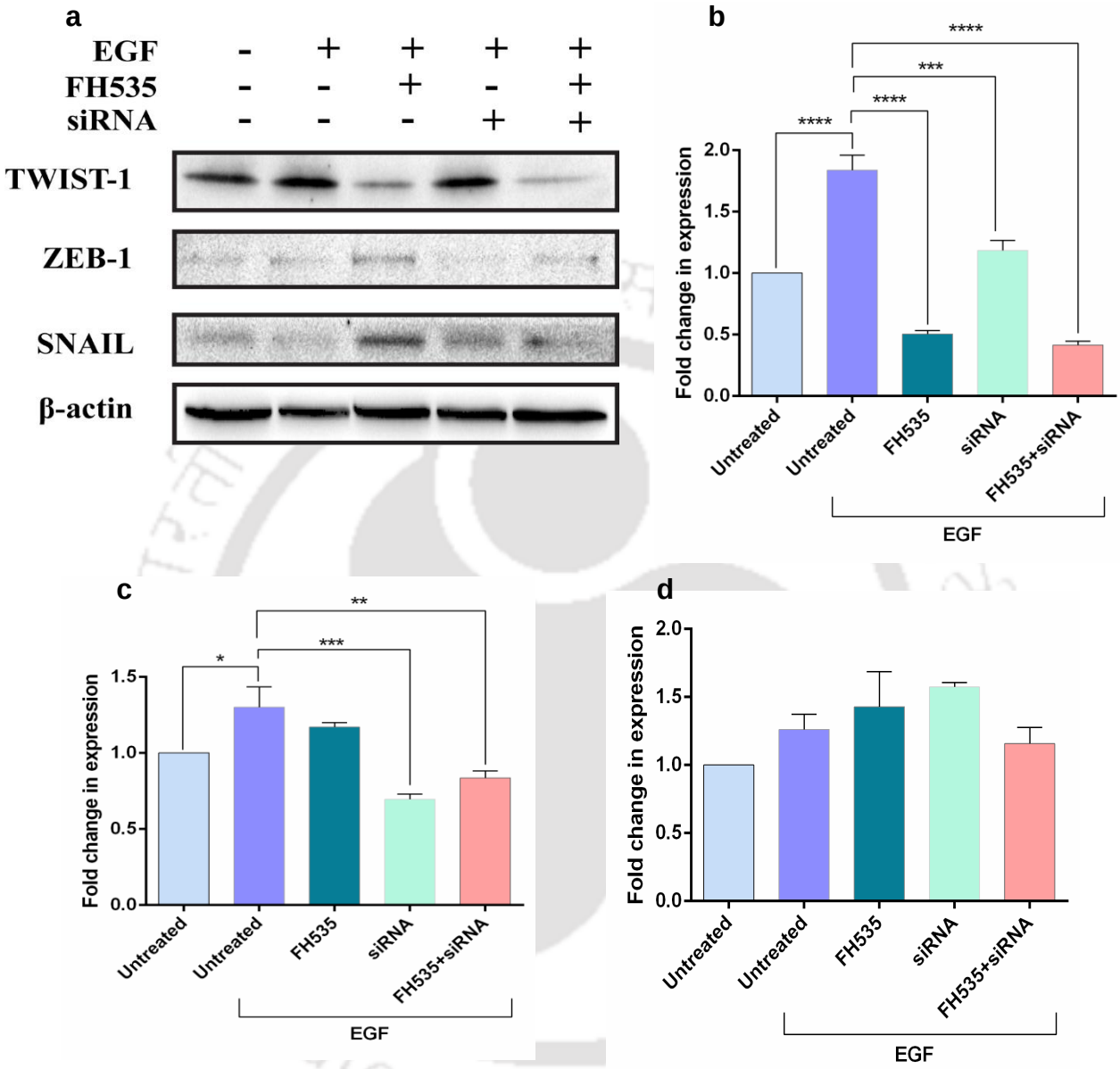

Figure. 3.2.39: (a) Representative Western blots showing Twist1, Zeb1 and Snail levels in MDA-MB-231 cell extracts. β-actin serves as a loading control. Graphs depicts the alteration in the expression levels of (b) Twist1, (c) Zeb-1 and (d) Snail with respect to untreated samples following inhibitor/siRNA treatment. The expression levels were deduced from the blots using ImageJ software.

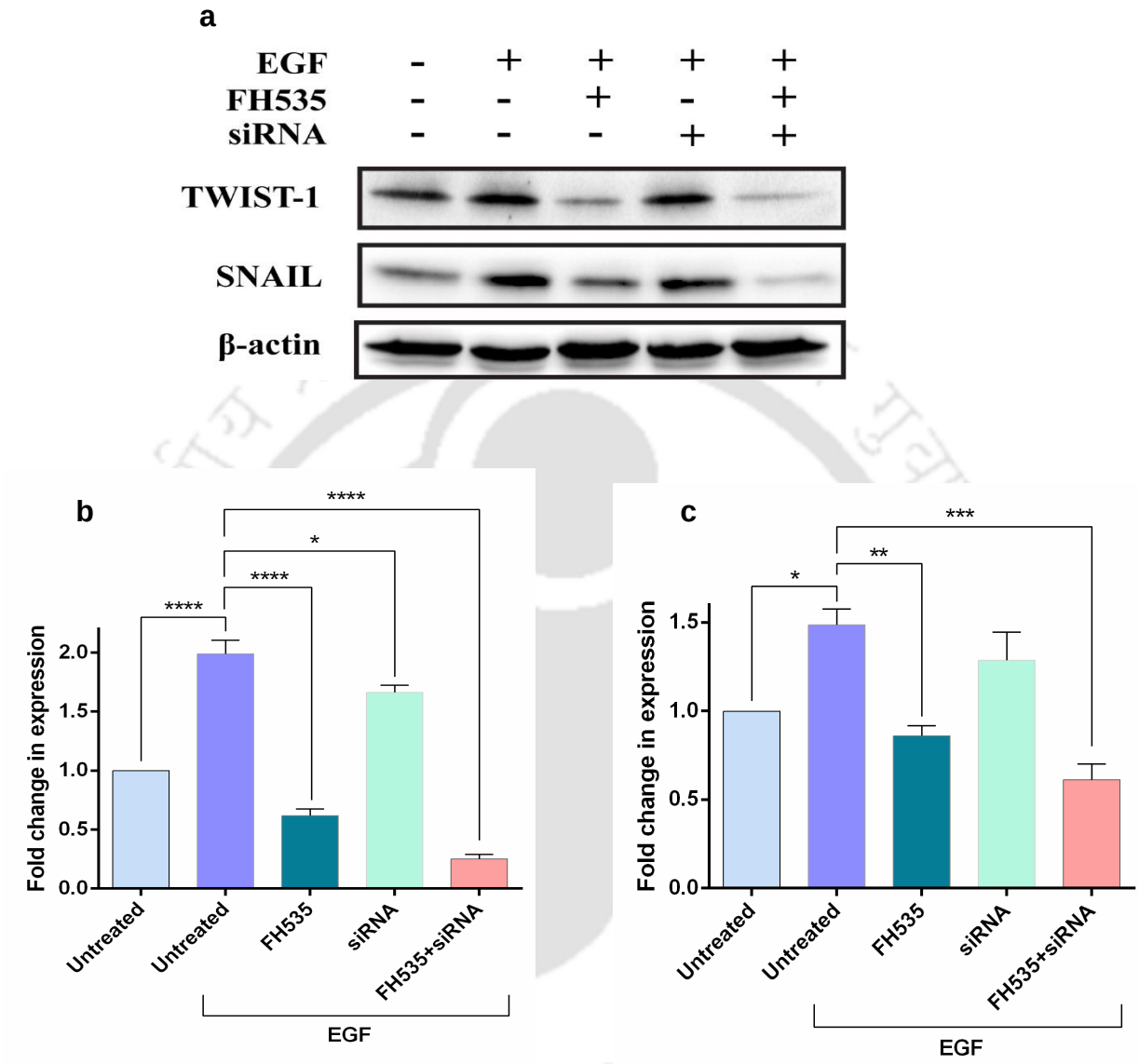

Figure. 3.2.40: (a) Representative Western blots showing Twist1 and Snail levels in MDA-MB-468 cell extracts. β-actin serves as a loading control. Graphs depicts the alteration in the expression levels of (b) Twist1 and (c) Snail with respect to untreated samples following inhibitor/siRNA treatment. The expression levels were deduced from the blots using ImageJ software.

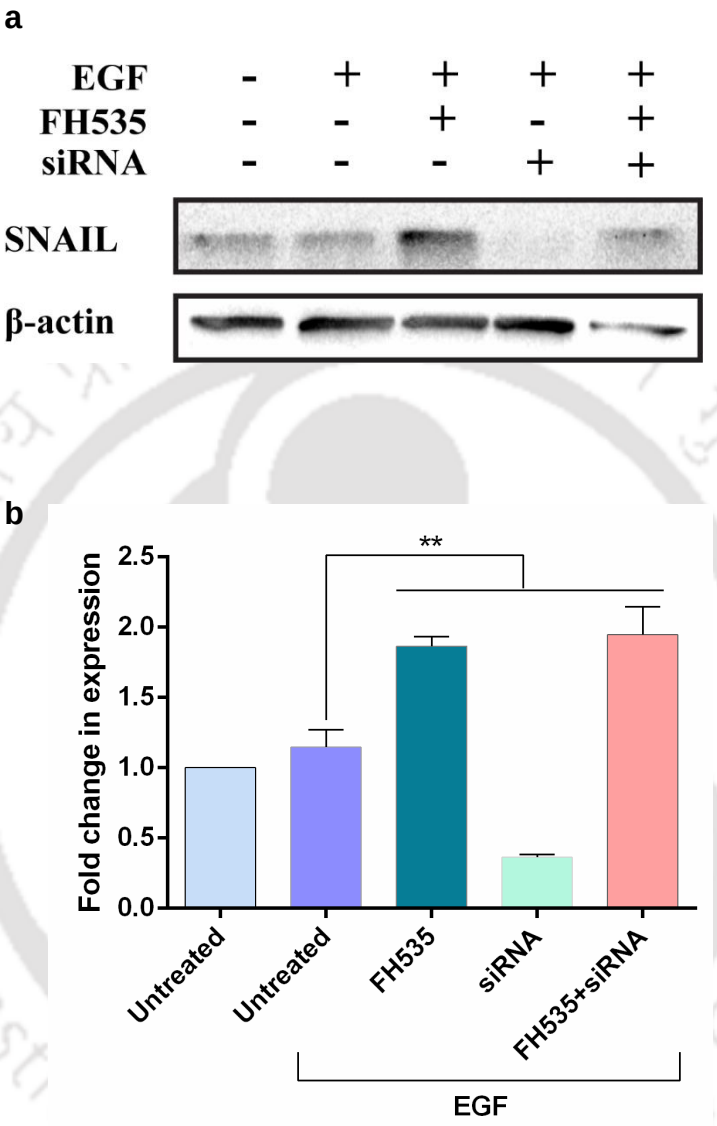

Figure. 3.2.41: (a) Representative Western blots showing Snail levels in MDA-MB-231 spheroids cell extracts. β-actin serves as a loading control. (b) Graphs depicts the alteration in the expression levels of Snail with respect to untreated samples following inhibitor/siRNA treatment. The expression levels were deduced from the blots using ImageJ software.

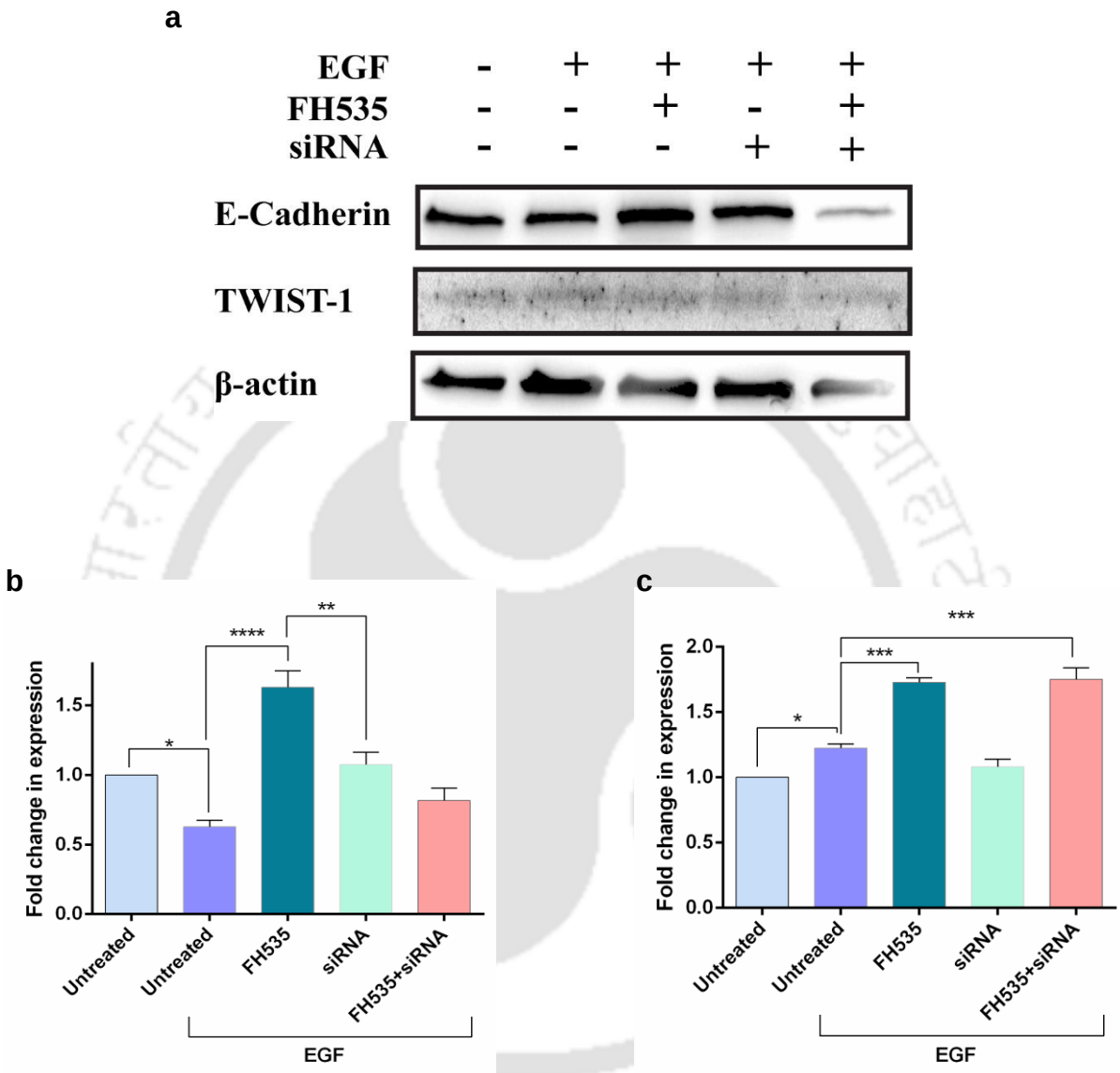

Figure. 3.2.42: (a) Representative Western blots showing E-cadherin and Twist-1 levels in MDA-MB-468 spheroids extracts. β-actin serves as a loading control. Graphs depicts the alteration in the expression levels of (b) E-cadherin and (c) Twist-1 with respect to untreated samples following inhibitor/siRNA treatment. The expression levels were deduced from the blots using ImageJ software.

3.2.1.4. Suppression of SQSTM1/P62 and Wnt/β-Catenin Signaling Decreases the Migration and Invasion Potential of TNBC: During the process of EMT, epithelial cells reverse their morphology into mesenchymal cells and gain increased abilities for migration and invasion, which ultimately results in metastasis [149]. Since increased expression of SQSTM1/P62 and Wnt/β-Catenin are implicated in the migration and invasion of TNBC cells, the combined effect of suppression of SQSTM1/P62 and Wnt/β-Catenin signaling on the migration and invasion of MDA-MB-231 cells was then investigated. Migration was assessed using a scratch wound-healing assay, where the migration rate of the cells towards the wound area (created using a scratch) was determined. The cells incubated with FH535, siRNA for SQSTM1/P62 and in combination showed slower wound healing abilities than the untreated cells (**Figure. 3.2.43 and Figure. 3.2.44**). The rate of cell migration was found to be lower in SQSTM1/P62 knockdown cells compared to Wnt/β-Catenin inhibited cells and lowest in the combination treatment (**Figure. 3.2.43 and Figure. 3.2.44**). In addition, a Boyden chamber-based assay, in which cells invade a layer of Matrigel on top of a membrane, was used to monitor the invasive capacity of MDA-MB-231 and MDA-MB-468 cells. After 24 h, a 5.22 and 3.68-fold reduction in invasion capacity was observed in cells treated with the combination of FH535 and siRNA compared to untreated cells (**Figure. 3.2.45 and Figure. 3.2.46**). Of note, the effect on migration and invasion was stronger upon co-treatment compared to treatment with each single agent, confirming the synergistic effect of the suppression of SQSTM1/P62 and Wnt/β-Catenin signaling (**Figure. 3.2.45 and Figure. 3.2.46**). These data indicate that co-inhibition of SQSTM1/P62 and Wnt/β-Catenin signaling reduces the migration and invasion capacities of TNBC cells.

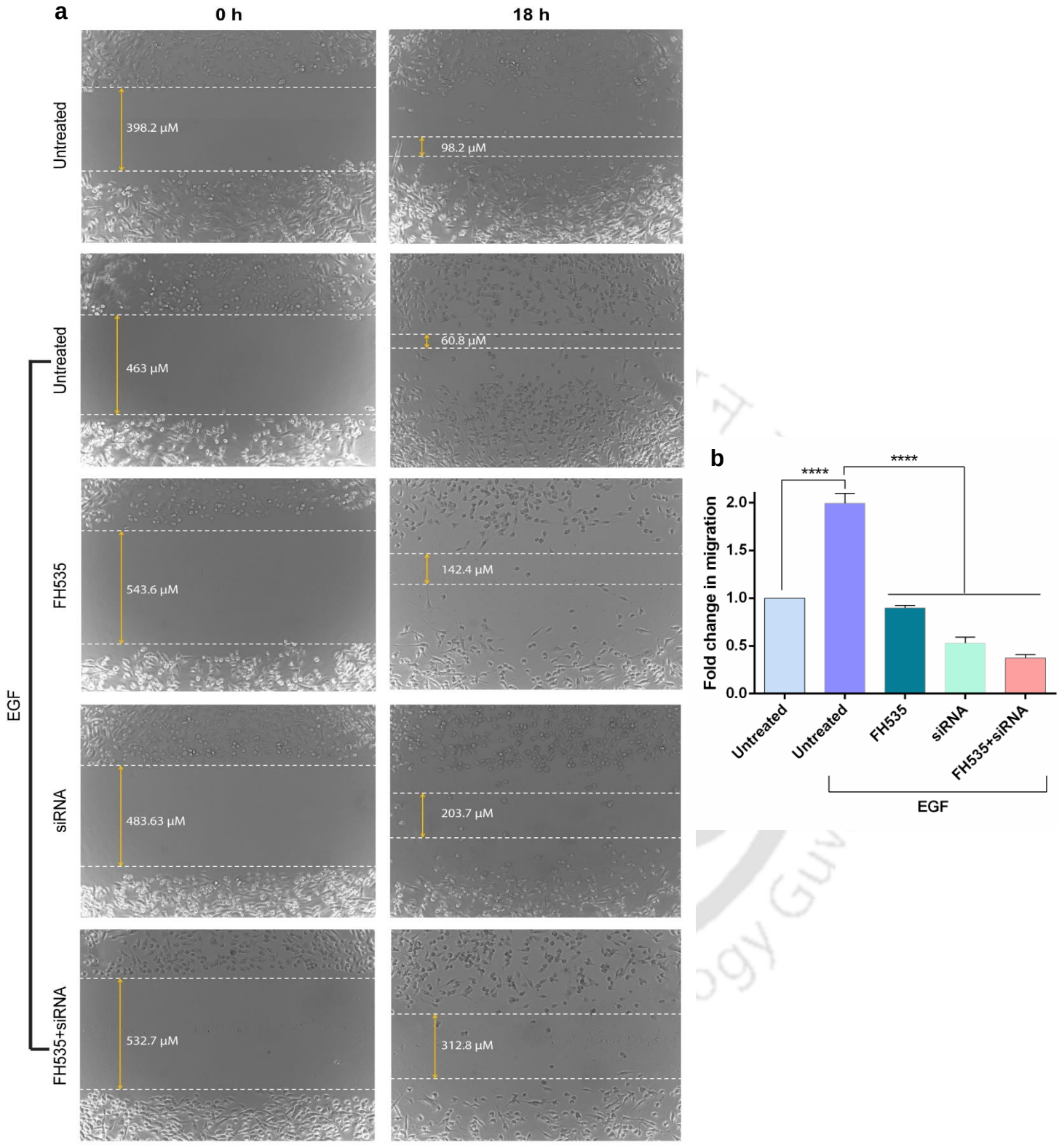

Figure. 3.2.43: (a) Scratch wound-healing assays of MDA-MB-231 monolayer cultures. (b) Graphical representation of changes in wound healing capacity following inhibitor/siRNA treatment and their combination with respect to untreated samples.

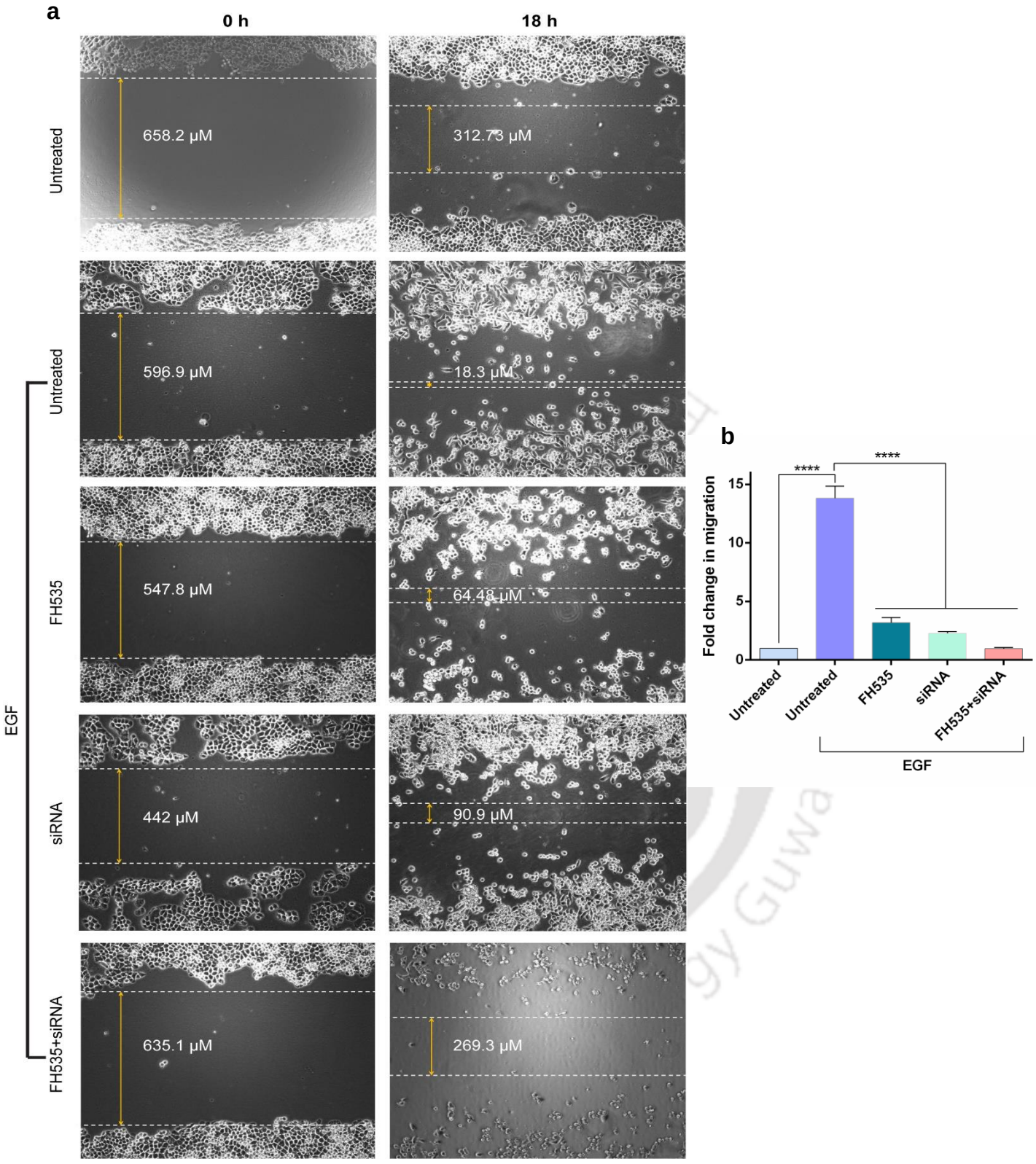

Figure. 3.2.44: (a) Scratch wound-healing assays of MDA-MB-468 monolayer cultures. (b) Graphical representation of changes in wound healing capacity following inhibitor/siRNA treatment and their combination with respect to untreated samples.

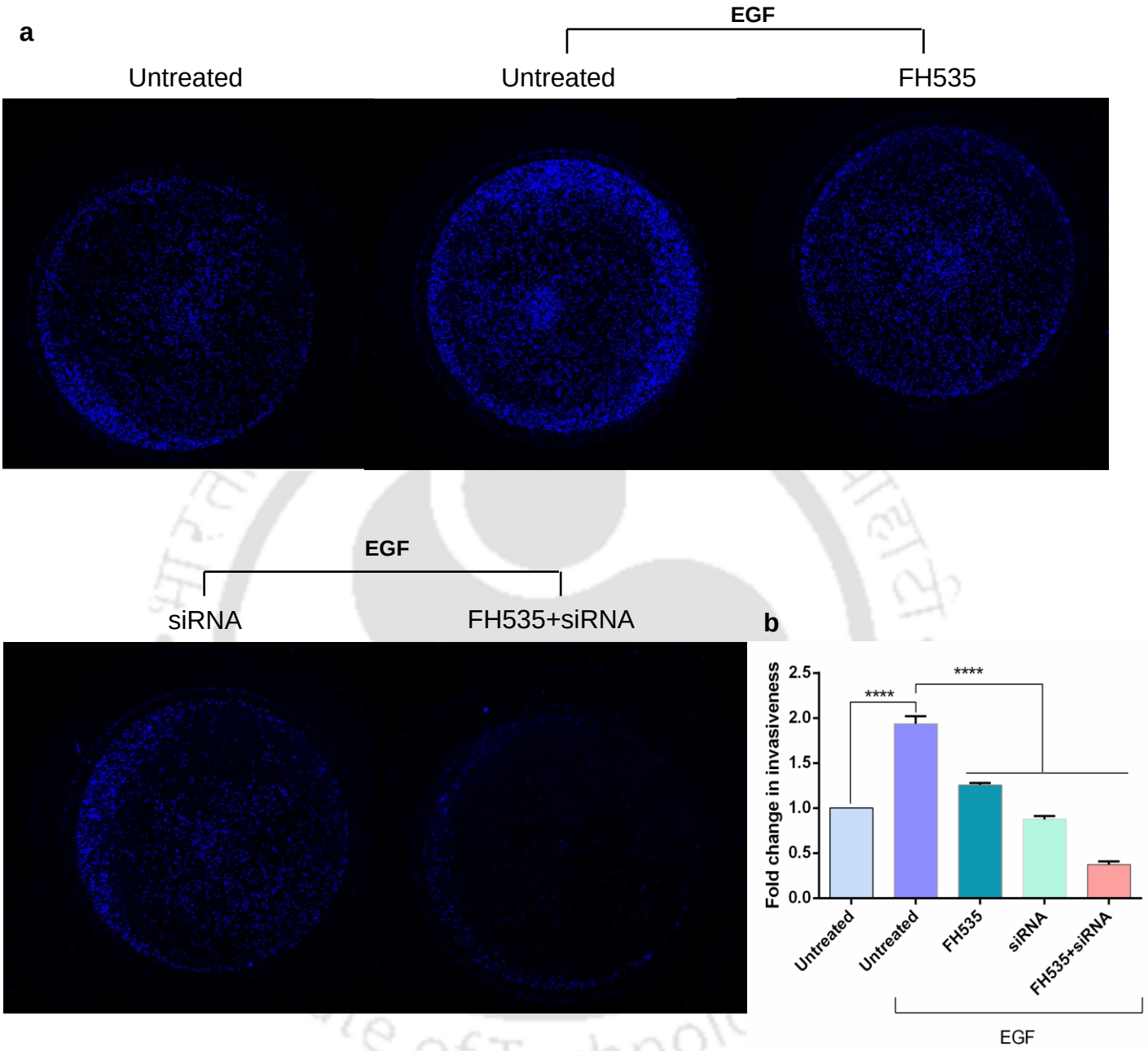

Figure. 3.2.45: (a) Boyden-chamber invasion assays of MDA-MB-231 monolayer cultures. (b) Graphical representation of changes in invasiveness following inhibitor/siRNA treatment and their combination with respect to untreated samples.

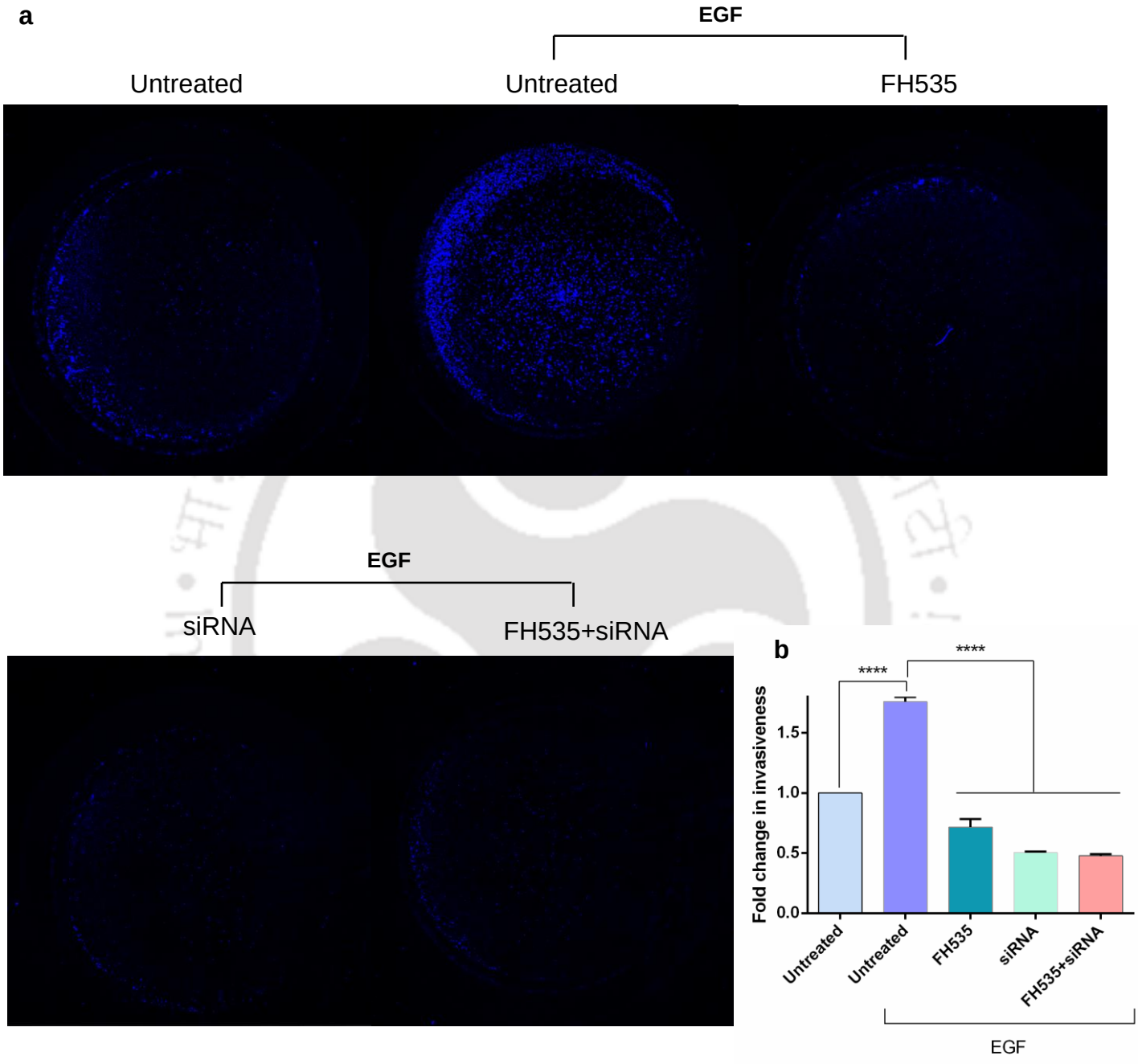

Figure. 3.2.46: (a) Boyden-chamber invasion assays of MDA-MB-468 monolayer cultures. (b) Graphical representation of changes in invasiveness following inhibitor/siRNA treatment and their combination with respect to untreated samples.

3.2.1.5. Inactivation of SQSTM1/P62 and Wnt/β-Catenin Signaling Alters the Expression of ABC Transporters.: Drug efflux transport systems have extensively been studied owing to the phenomenon of MDR, in which cancer cells become cross-resistant to multiple cytotoxic anticancer drugs [150]. MDR often results from the overexpression of ABC transporters [151]. This prompted to study alterations in the expression of ABC subfamily B member 1 (ABCB1; also called P-glycoprotein), ABC subfamily C member 1 (ABCC1; also called MDR-associated protein 1), ABC subfamily G member 2 (ABCG2; also called breast cancer resistance protein), which are known to be involved in MDR, by qRT-PCR. In **Figure. 3.2.47** and **Figure. 3.2.48** the expression levels of the ABC transporters in MDA-MB-231 and MDA-MB-468 are depicted. It was found that combination treatment led to decreased ABCB1 expression in both MDA-MB-231 and MDA-MB-468. However, FH535 treatment alone increased ABCB1 expression by 2.22-fold and 1.33-fold in MDA-MB-231 and MDA-MB-468, respectively. After combination treatment, the expression of ABCG2 was found to be reduced significantly in MDA-MB-468, but was slightly increased in MDA-MB-231. In fact, FH535 treatment increased ABCG2 expression in MDA-MB-231 by 3.67-fold. Although co-treatment marginally increased the ABCC1 expression in MDA-MB-231, it was decreased in MDA-MB-468. Indeed, knockdown of SQSTM1/P62 diminished the expression of ABCC1 in MDA-MB-231. Altogether, these data indicate that inactivation of SQSTM1/P62 and Wnt/β-Catenin signaling alters the expression of major MDR-associated genes in TNBC cells.

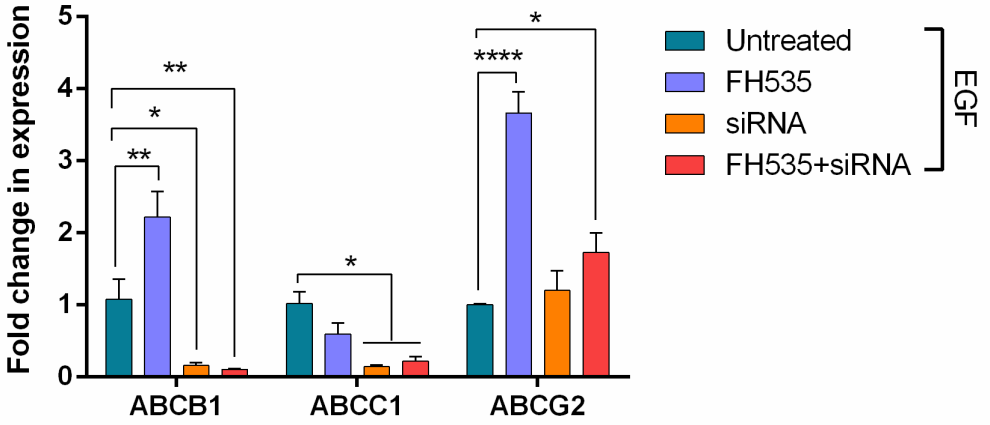

Figure. 3.2.47: Graphical representation of changes in gene expression levels in MDA-MB-231 following treatment with inhibitor/siRNA, quantified by qRT-PCR analysis. Results are expressed as mean relative gene expression level compared to β-actin ± SEM of three independent experiments, with $p < 0.05$ (*), $p < 0.01$ (**), $p < 0.001$ (***) or $p < 0.0001$ (****).

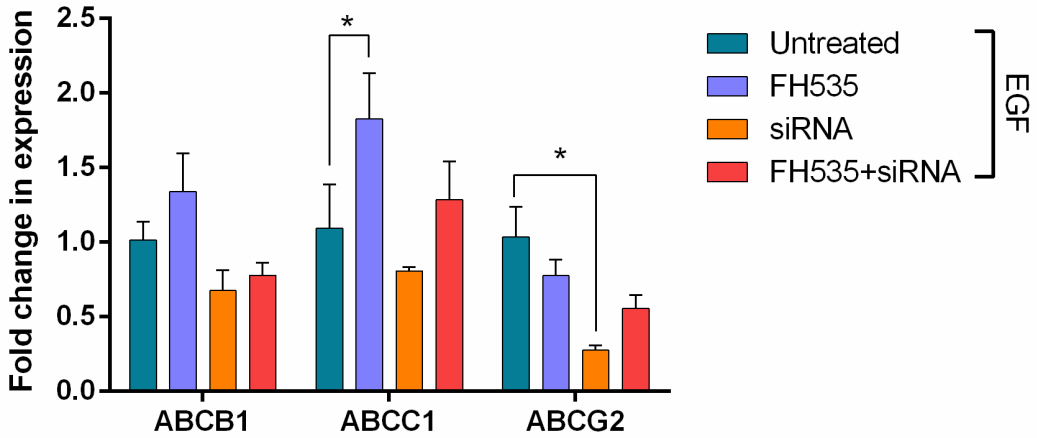

Figure. 3.2.48: Graphical representation of changes in gene expression levels in MDA-MB-468 following treatment with inhibitor/siRNA, quantified by qRT-PCR analysis. Results are expressed as mean relative gene expression level compared to β-actin ± SEM of three independent experiments, with $p < 0.05$ (*), $p < 0.01$ (**), $p < 0.001$ (***) or $p < 0.0001$ (****).

3.2.1.6 Co-targeting SQSTM1/P62 and Wnt/β-Catenin Signaling Synergistically Inhibits TNBC Cell Survival: To discern the effect of inhibition of SQSTM1/P62 and Wnt/β-Catenin signaling on cell survival, alamarBlue based cell viability assay was performed. A dose-dependent decrease in cell viability following treatment with Wnt/β-Catenin inhibitor FH535 in both the TNBC cell lines MDA-MB-231 and MDA-MB-468 was observed (**Figure. 3.2.49** and **Figure. 3.2.51**). A several-fold higher dose of FH535 was required for the spheroids (**Figure. 3.2.55** and **Figure. 3.2.58)**. On the other hand, any effect on cell viability following knockdown of SQSTM1/P62 was observed (**Figure. 3.2.49** and **Figure. 3.2.52**). Even transfection of higher concentration of siRNA had no effect on cell viability both in monolayer cultures and spheroids (**Figure. 3.2.55** and **Figure. 3.2.58**). Surprisingly, the combination of FH535 with siRNA was found to decrease cell viability significantly in a dose-dependent manner at lower concentrations in both monolayers and spheroids (**Figure. 3.2.50, Figure. 3.2.53, Figure. 3.2.56** and **Figure. 3.2.59**). Combination index (CI) calculation revealed a CI value of <1 in both the cases, indicating a dose-dependent synergistic interaction between SQSTM1/P62 and Wnt/β-Catenin signaling inhibition (**Figure. 3.2.51** and **Figure. 3.2.54**). Administration of the inhibitor and siRNA in combination yielded higher anti-proliferative effects than when administered alone. In case of spheroids, a relatable finding was observed as well (**Figure. 3.2.57** and **Figure. 3.2.60**).

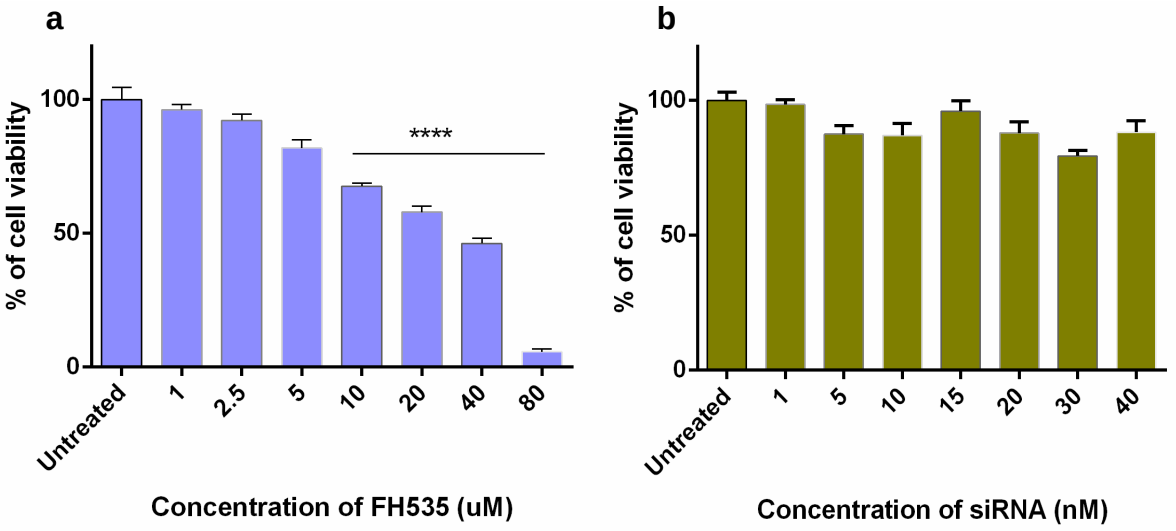

Figure. 3.2.49: Determination of viability of MDA-MB-231 monolayer cultures by alamarBlue assay upon treatment with inhibitor/siRNA for 48 h. (a) and (b) represents treatment with increasing concentration of FH535 and siRNA, respectively. Results expressed as the mean ± SEM are based on at least three independent experiments.

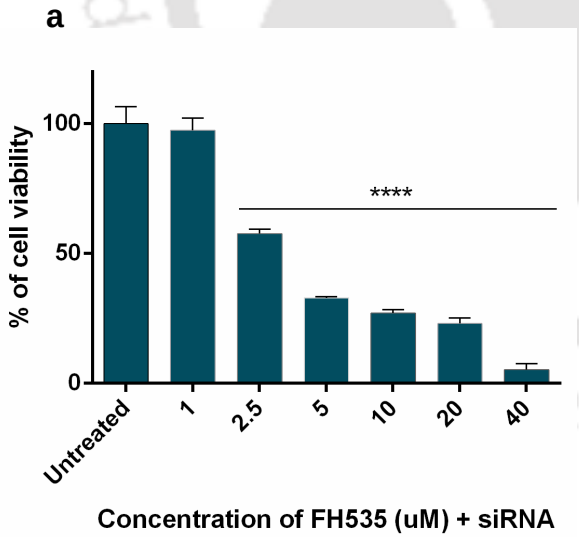

b

Inhibitor	IC_{50} (μM)
FH535	29.37
siRNA	-
FH535 + 10 nM siRNA	3.2

Figure. 3.2.50: (a) Determination of viability of MDA-MB-231 monolayer cultures by alamarBlue assay upon treatment with increasing concentration of FH535 and 10 nM siRNA. (b) Table representing the obtained IC_{50} values. Results expressed as the mean ± SEM are based on at least three independent experiments.

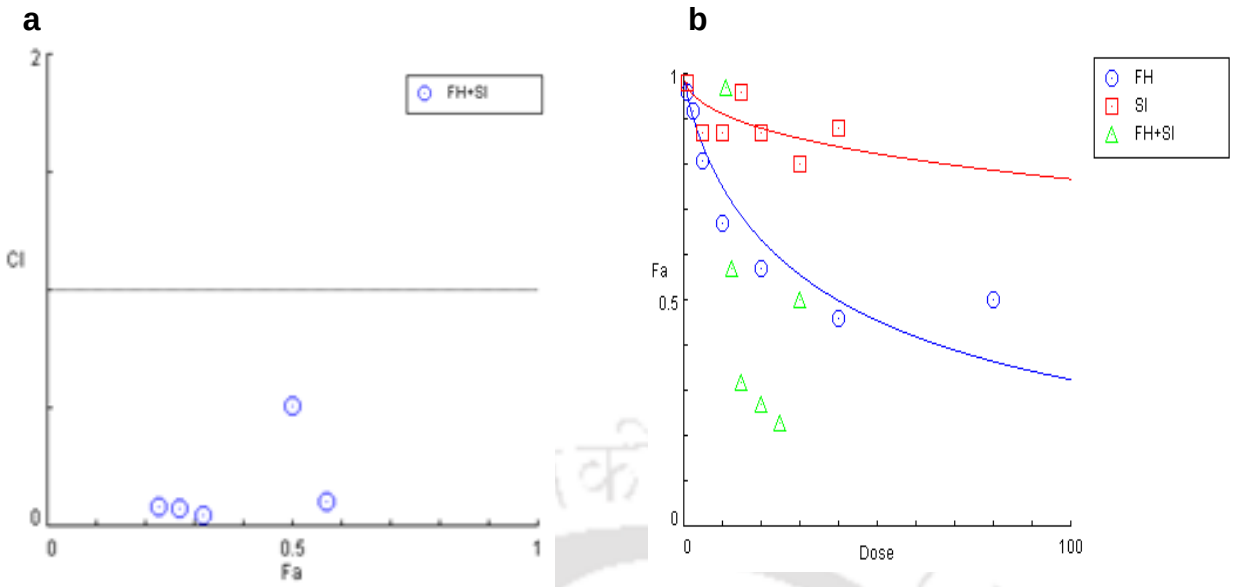

Figure. 3.2.51: (a) Combination index and (b) dose-response curves obtained following combination treatment with FH535 and siRNA in MDA-MB-231 monolayer culture.

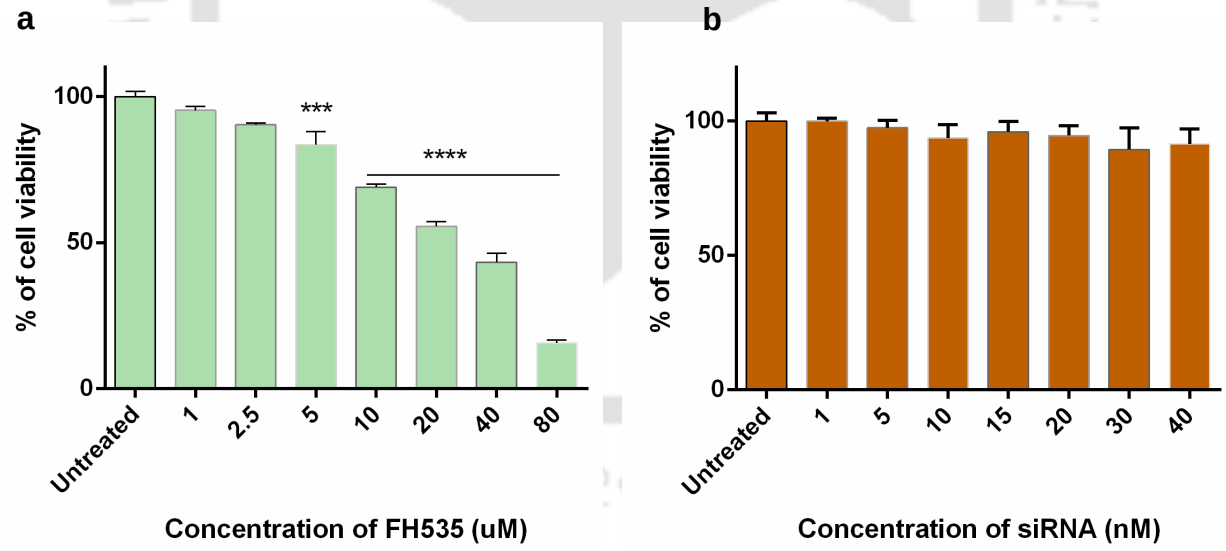

Figure. 3.2.52: Determination of viability of MDA-MB-468 monolayer cultures by alamarBlue assay upon treatment with inhibitor/siRNA for 48 h. (a) and (b) represents treatment with increasing concentration of FH535 and siRNA, respectively. Results expressed as the mean ± SEM are based on at least three independent experiments.

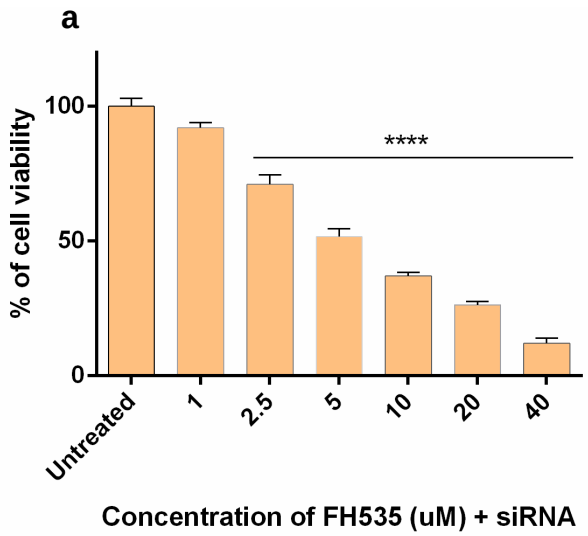

b

Inhibitor	IC_{50} (µM)
FH535	32.57
siRNA	-
FH535 + 10 nM siRNA	5

Figure. 3.2.53: (a) Determination of viability of MDA-MB-468 monolayer cultures by alamarBlue assay upon treatment with increasing concentration of FH535 and 10 nM siRNA. (b) Table representing the obtained IC_{50} values. Results expressed as the mean ± SEM are based on at least three independent experiments.

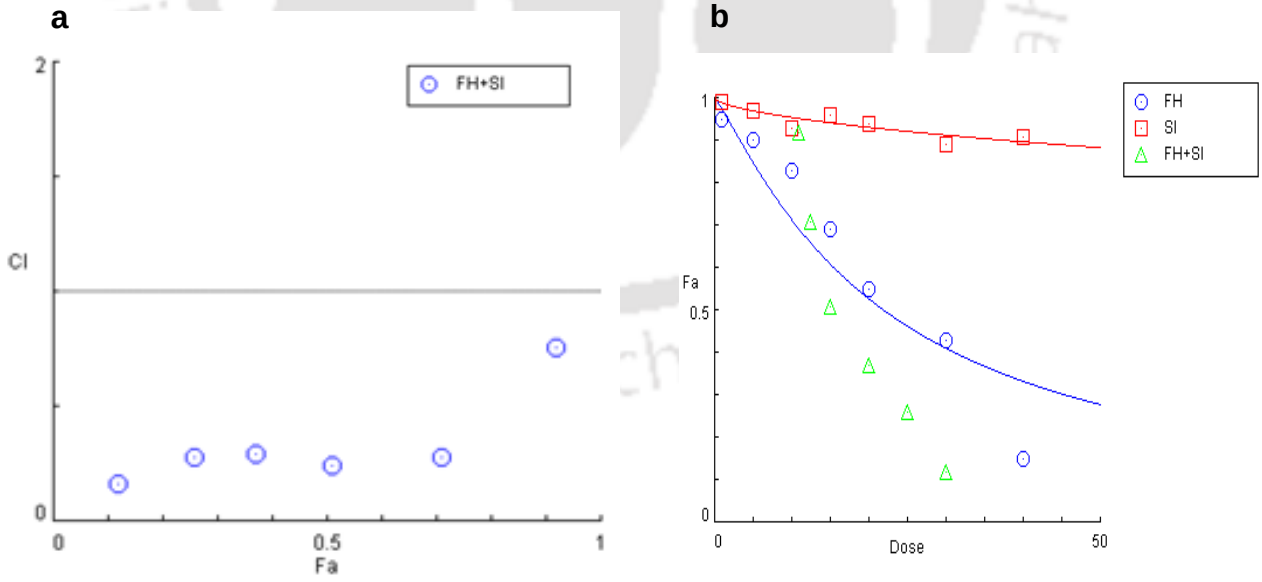

Figure. 3.2.54: (a) Combination index and (b) dose-response curves obtained following combination treatment with FH535 and siRNA in MDA-MB-468 monolayer culture.

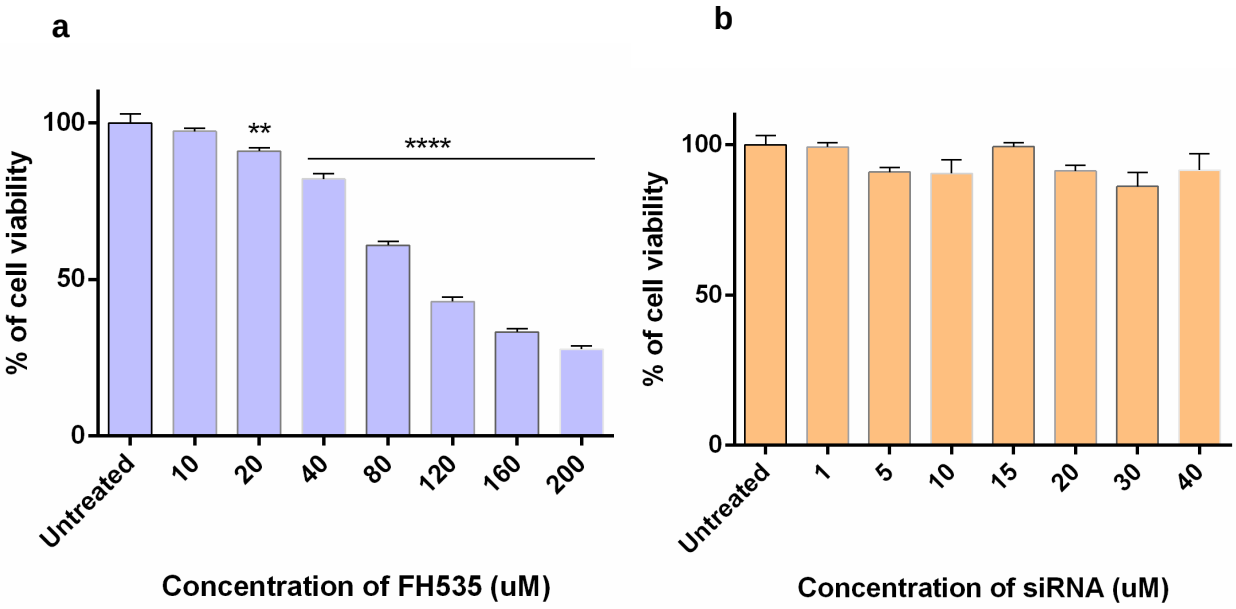

Figure. 3.2.55: Determination of viability of MDA-MB-231 spheroids by alamarBlue assay upon treatment with inhibitor/siRNA for 48 h. (a) and (b) represents treatment with increasing concentration of FH535 and siRNA, respectively. Results expressed as the mean ± SEM are based on at least three independent experiments.

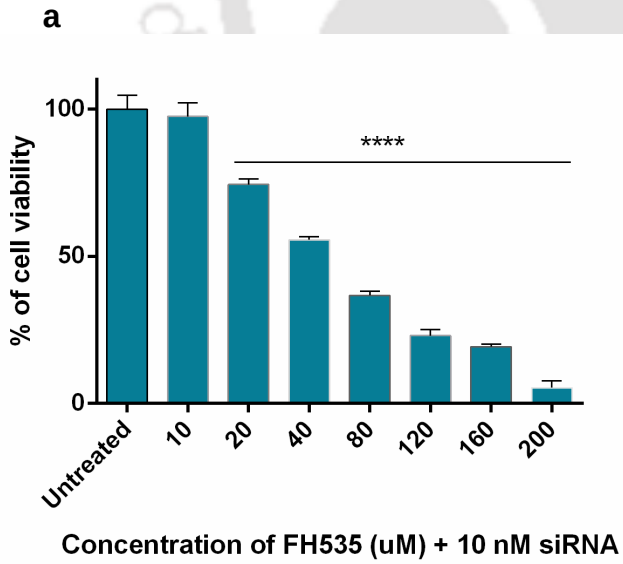

b

Inhibitor	IC_{50} (μM)
FH535	96
siRNA	-
FH535 + 10 nM siRNA	52.6

Figure. 3.2.56: (a) Determination of viability of MDA-MB-231 spheroids by alamarBlue assay upon treatment with increasing concentration of FH535 and 10 nM siRNA. (b) Table representing the obtained IC_{50} values. Results expressed as the mean ± SEM are based on at least three independent experiments.

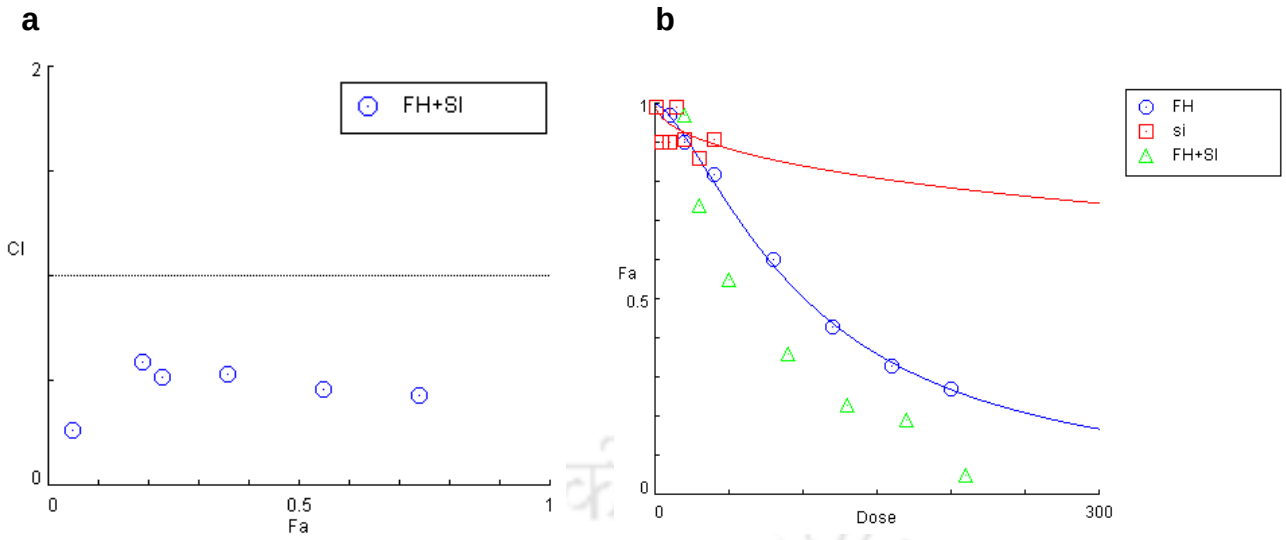

Figure. 3.2.57: (a) Combination index and (b) dose-response curves obtained following combination treatment with FH535 and siRNA in MDA-MB-231 spheroids.

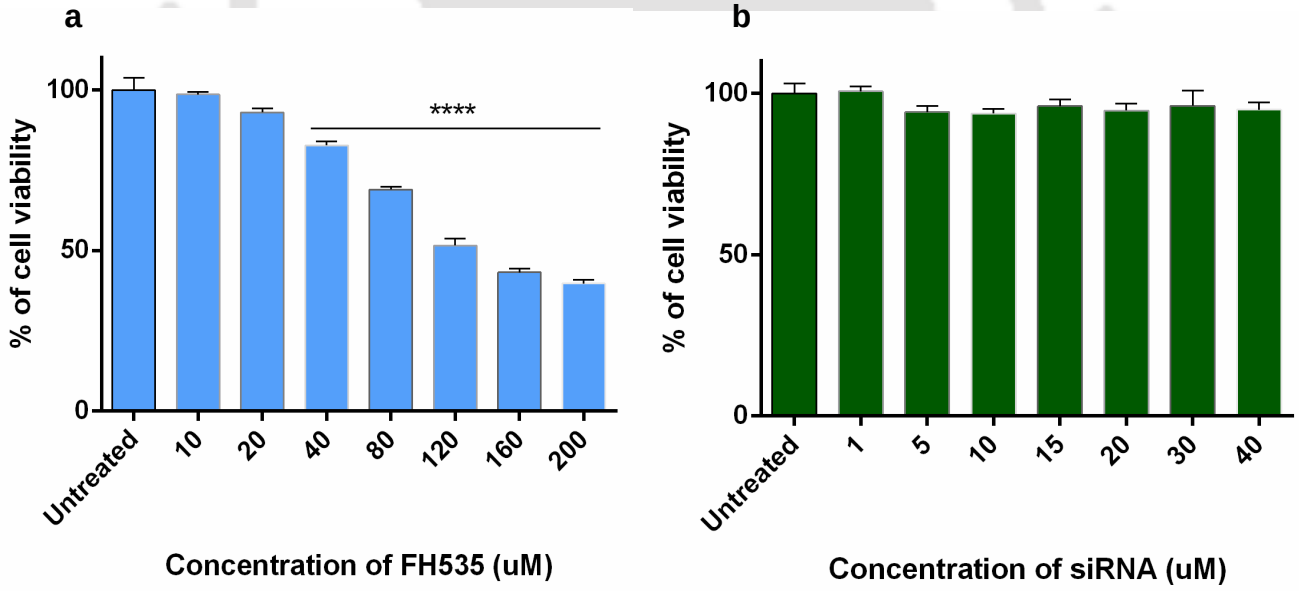

Figure. 3.2.58: Determination of viability of MDA-MB-468 spheroids by alamarBlue assay upon treatment with inhibitor/siRNA for 48 h. (a) and (b) represents treatment with increasing concentration of FH535 and siRNA, respectively. Results expressed as the mean ± SEM are based on at least three independent experiments.

a

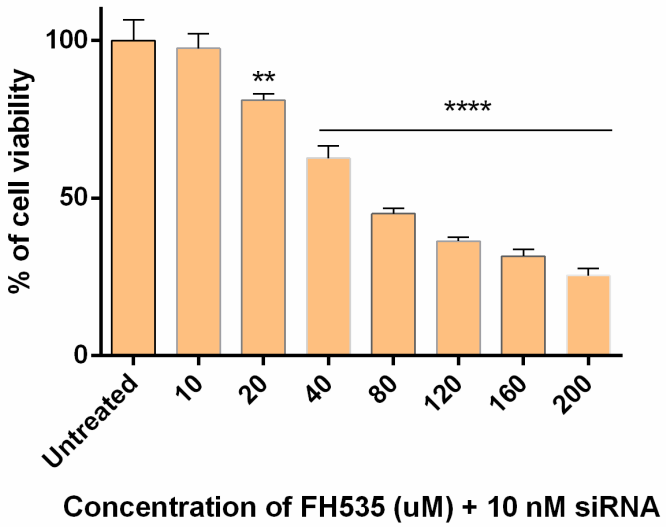

b

Inhibitor	IC_{50} (μM)
FH535	112.76
siRNA	-
FH535 + 10 nM siRNA	63.43

Figure. 3.2.59: (a) Determination of viability of MDA-MB-468 spheroids by alamarBlue assay upon treatment with increasing concentration of FH535 and 10 nM siRNA. (b) Table representing the obtained IC_{50} values. Results expressed as the mean ± SEM are based on at least three independent experiments.

a

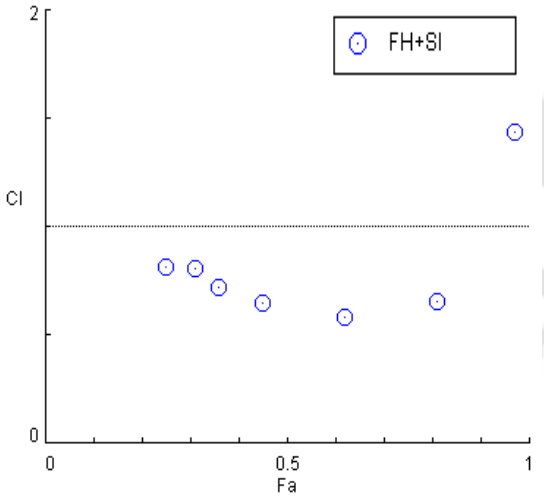

b

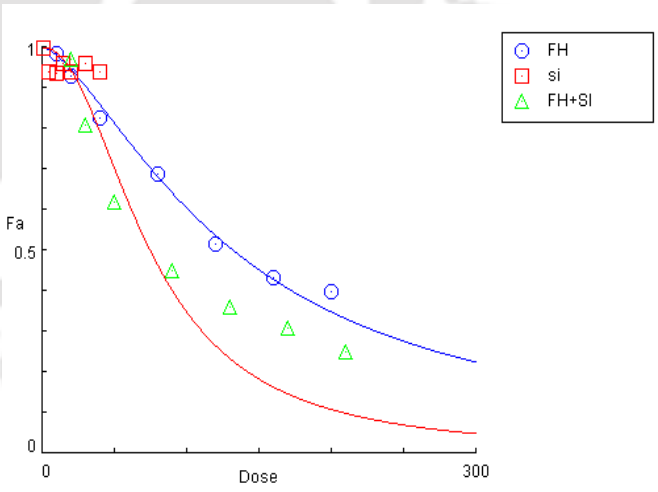

Figure. 3.2.60: (a) Combination index and (b) dose-response curves obtained following combination treatment with FH535 and siRNA in MDA-MB-231 spheroids.

Live-dead cell imaging of spheroids following treatment provided a clear visualization of the effect of the signaling modulation (**Figure. 3.2.61** and **Figure. 3.2.62**). Taken together, these data indicate that attenuation of SQSTM1/P62 and Wnt/β-Catenin signaling synergistically inhibits TNBC cell survival.

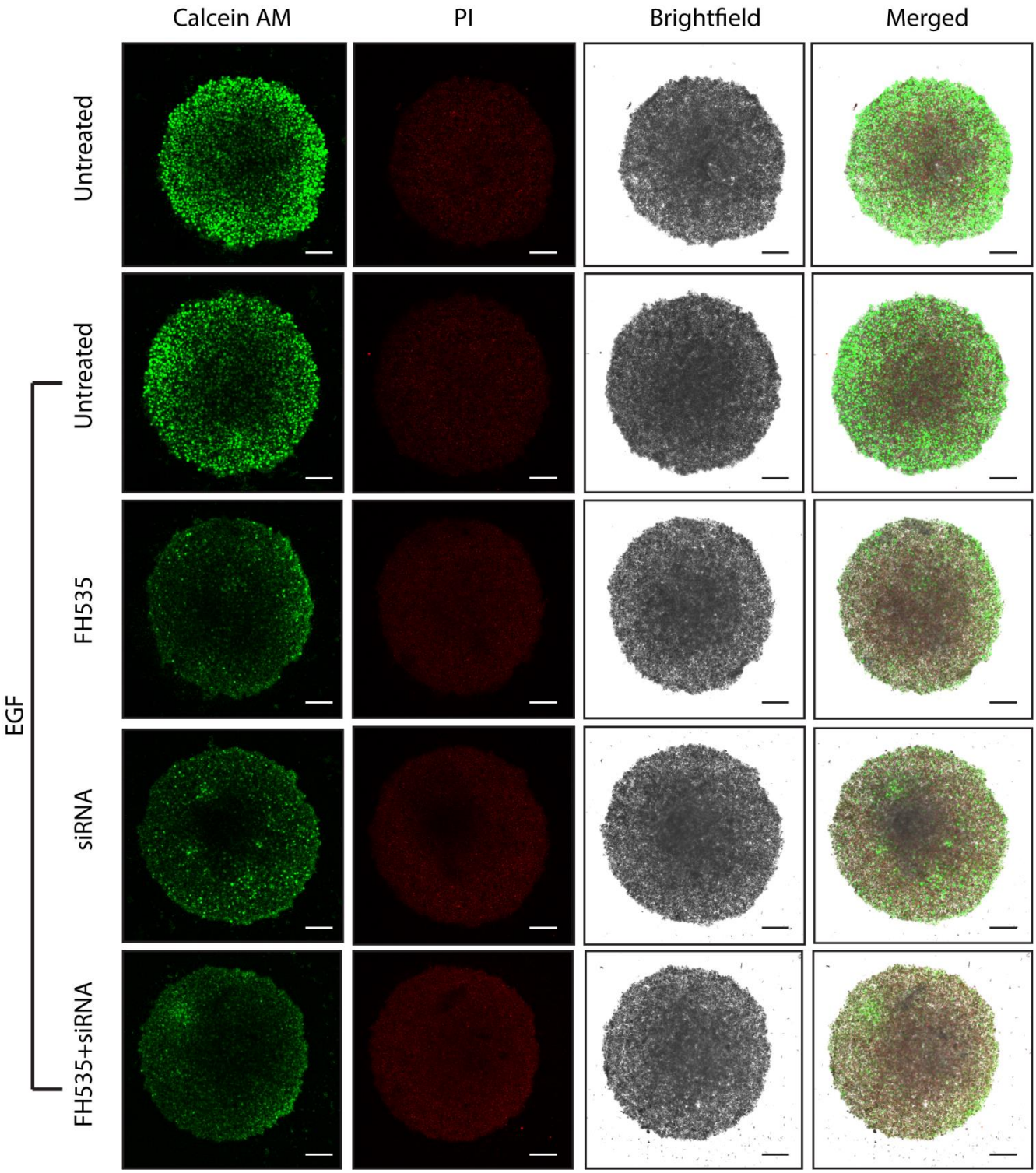

Figure. 3.2.61: Live-dead cell visualization of MDA-MB-231 spheroids using calcein-AM/propidium iodide (PI) dual staining. Green fluorescence by calcein-AM refers to live cells, whereas red fluorescence by PI refers to dead cells. Scale bar: 200 μM.

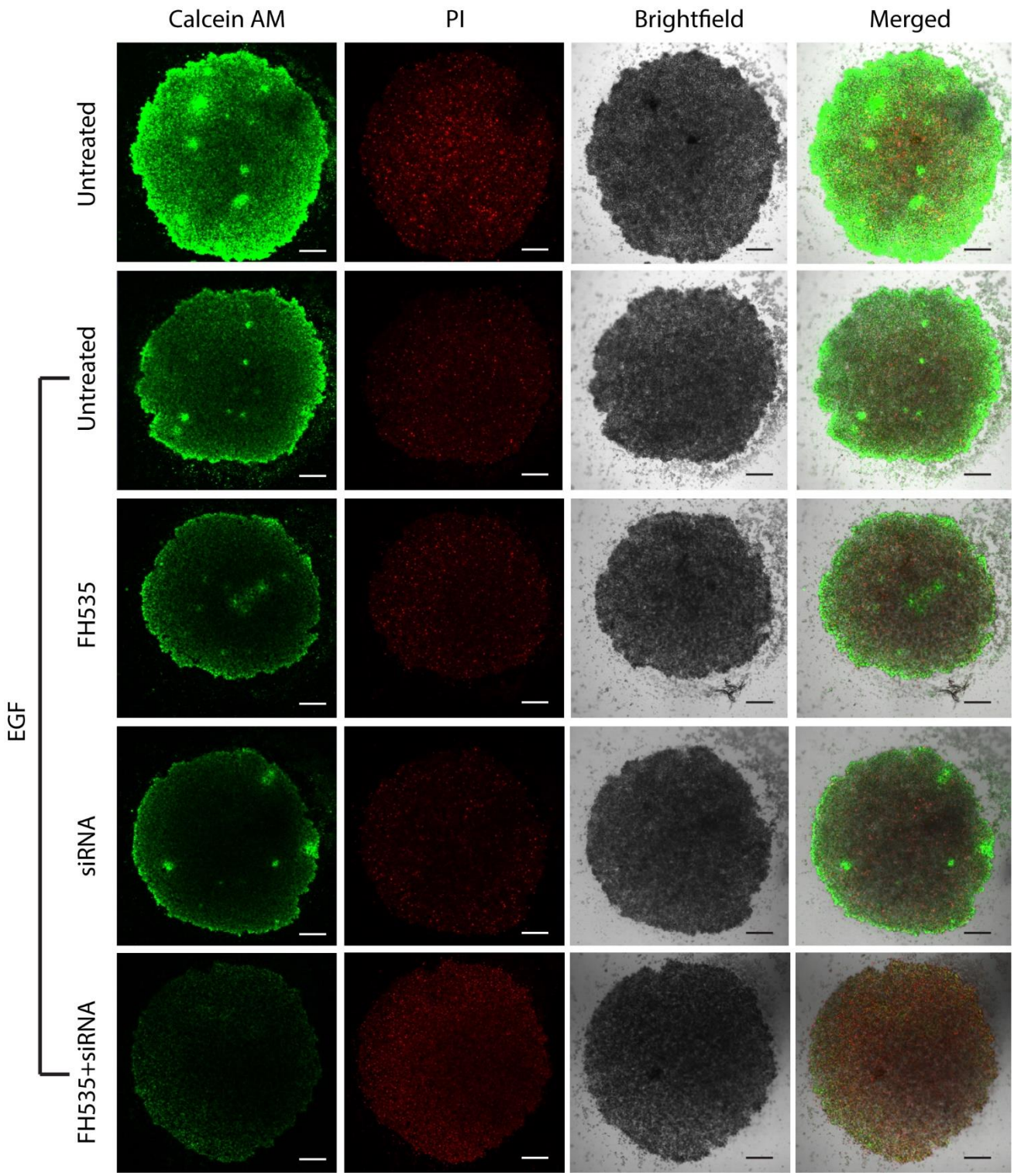

Figure. 3.2.62: Live-dead cell visualization of MDA-MB-468 spheroids using calcein-AM/propidium iodide (PI) dual staining. Green fluorescence by calcein-AM refers to live cells, whereas red fluorescence by PI refers to dead cells. Scale bar: 200 μM.

3.2.1.7 Modulation of SQSTM1/P62 and Wnt/β-Catenin Signaling Results in G0/G1 Phase Cell Cycle Arrest and Induces Apoptosis: To better document the effect of inhibition of SQSTM1/P62 and Wnt/β-Catenin signaling on cell growth/survival, cell cycle progression was monitored following 48 h treatment. A G0/G1 phase cell cycle arrest was observed in both MDA-MB-231 and MDA-MB-468 (**Figure. 3.2.63** and **Figure. 3.2.64**). The percentage of G0/G1 phase cells was increased to 27.27% in MDA-MB-231 and 22.6% in MDA-MB-468. Cyclin-D1 is a regulatory protein responsible for driving cell cycle progression from the G1 to S phase [152]. Thus, the expression levels of cyclin-D1 was analyzed using qRT-PCR to better understand the mechanism of action of the inhibitors (**Figure. 3.2.65** and **Figure. 3.2.66**). The expression levels of cyclin-D1 was found to be down-regulated by 2.67-fold in MDA-MB-231 (**Figure. 3.2.65**).

Following reduction of cell viability by co-treatment, it was investigated if the cell death was mechanized by apoptosis process. Thus, the increase in percentage of apoptotic cell population was analyzed following combination treatment using flow cytometry. It was found that co-therapy increased apoptotic cell populations by approximately 26.81% and 23.13% in MDA-MB-231 and MDA-MB-468, respectively (**Figure. 3.2.67** and **Figure. 3.2.68**).

Therefore, it is concluded that modulation of the SQSTM1/P62 and Wnt/β-Catenin signaling pathway ablates cyclin-D1, leading to G0/G1 cell cycle arrest. Furthermore, it mediates apoptotic cell death.

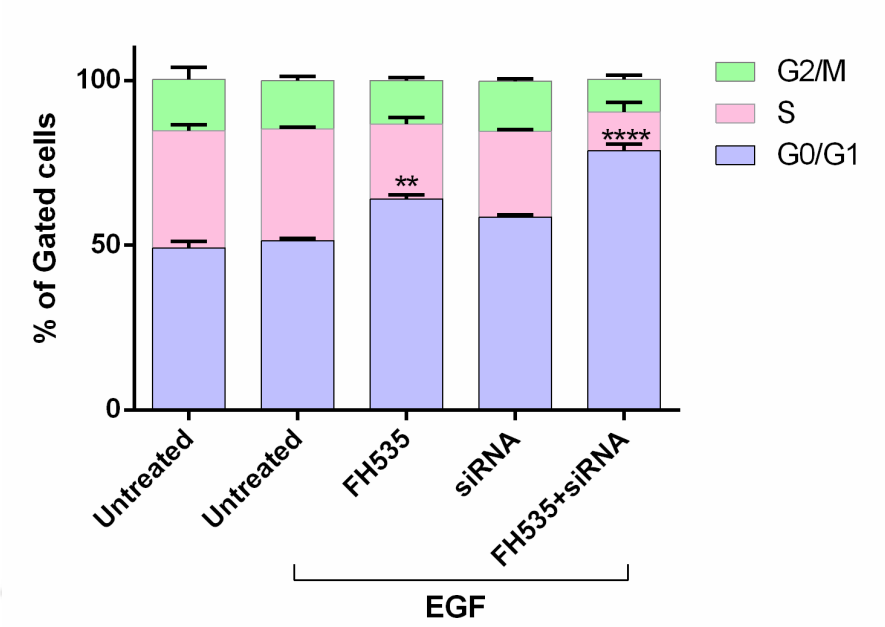

Figure. 3.2.63: Evaluation of cell cycle profile of MDA-MB-231 monolayer cultures. An increase in G0/G1 phase was observed following treatment with inhibitor/siRNA.

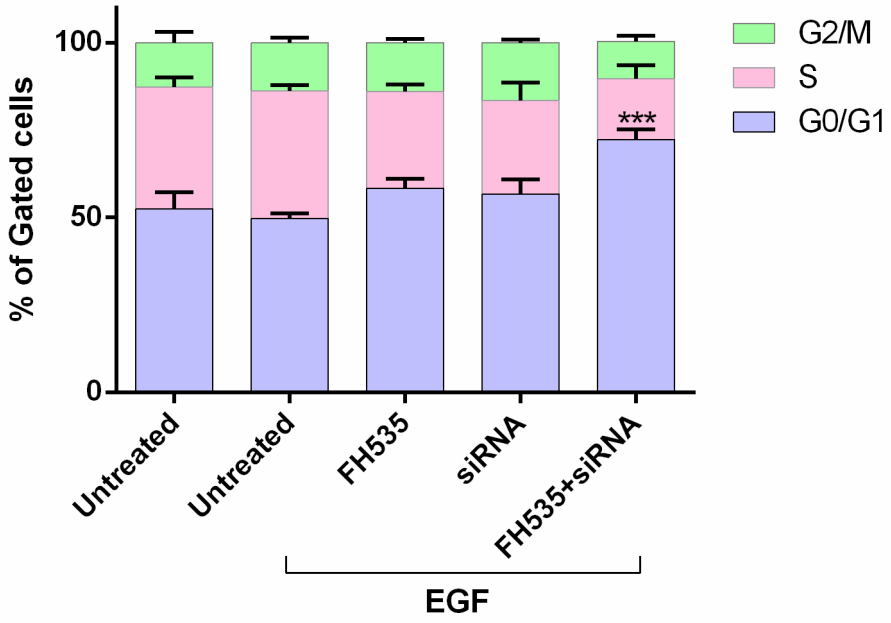

Figure. 3.2.64: Evaluation of cell cycle profile of MDA-MB-468 monolayer cultures. An increase in G0/G1 phase was observed following treatment with inhibitor/siRNA.

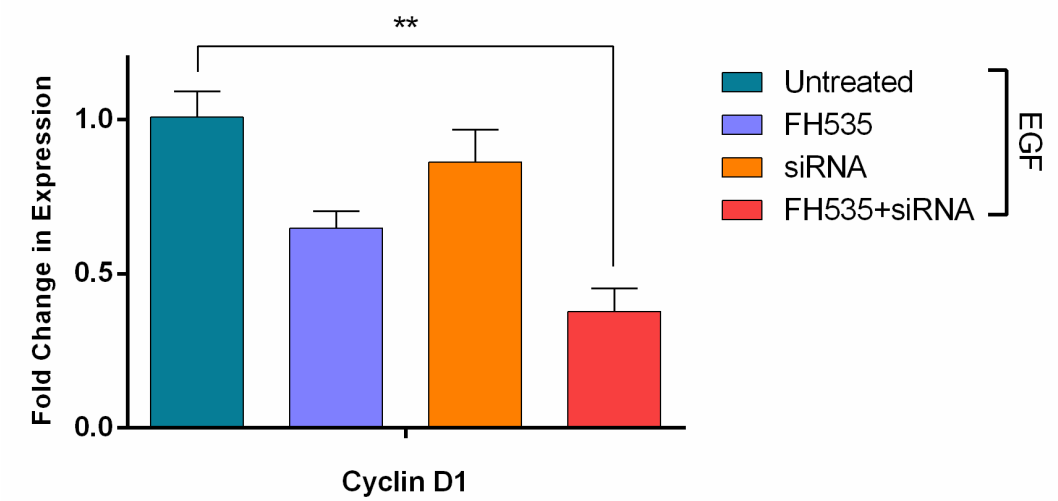

Figure. 3.2.65: Graphical representation of changes in gene expression levels in MDA-MB-231 following treatment with inhibitor/siRNA, quantified by qRT-PCR analysis. Results are expressed as mean relative gene expression level compared to β-actin ± SEM of three independent experiments, with $p < 0.05$ (*), $p < 0.01$ (**), $p < 0.001$ (***) or $p < 0.0001$ (****).

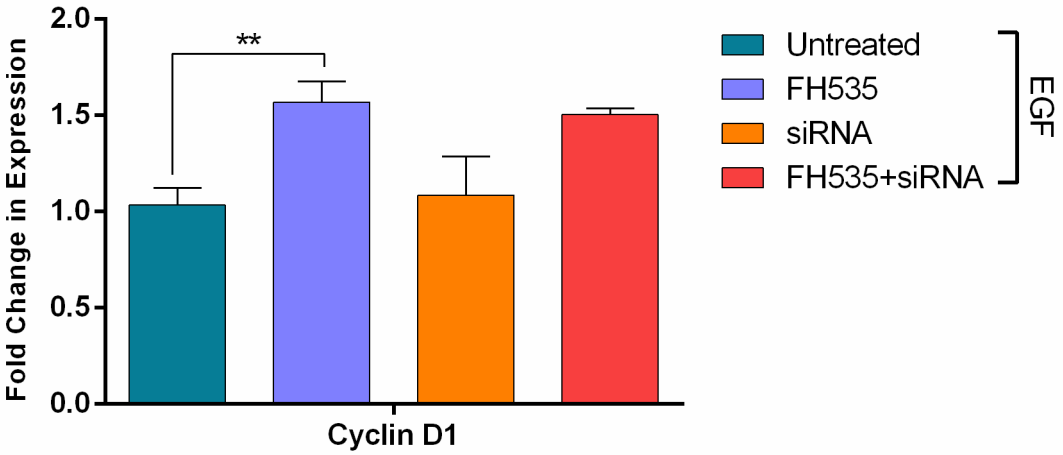

Figure. 3.2.66: Graphical representation of changes in gene expression levels in MDA-MB-468 following treatment with inhibitor/siRNA, quantified by qRT-PCR analysis. Results are expressed as mean relative gene expression level compared to β-actin ± SEM of three independent experiments, with $p < 0.05$ (*), $p < 0.01$ (**), $p < 0.001$ (***) or $p < 0.0001$ (****).

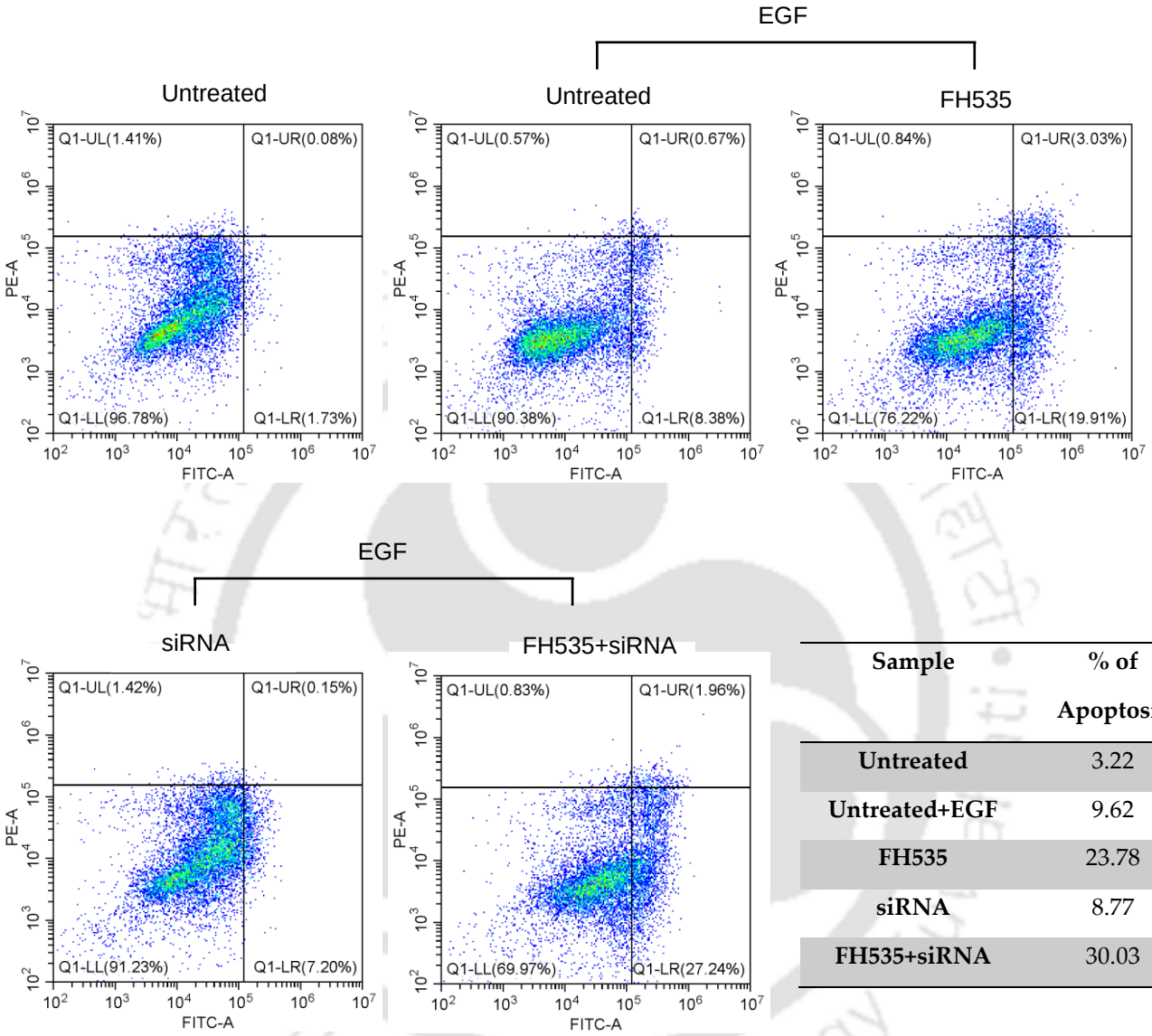

Sample	% of Apoptosis
Untreated	3.22
Untreated+EGF	9.62
FH535	23.78
siRNA	8.77
FH535+siRNA	30.03

Figure. 3.2.67: Flow cytometric analysis of apoptotic populations probed by annexin-V-FITC PI assay following treatment in MDA-MB-231 monolayer cultures.

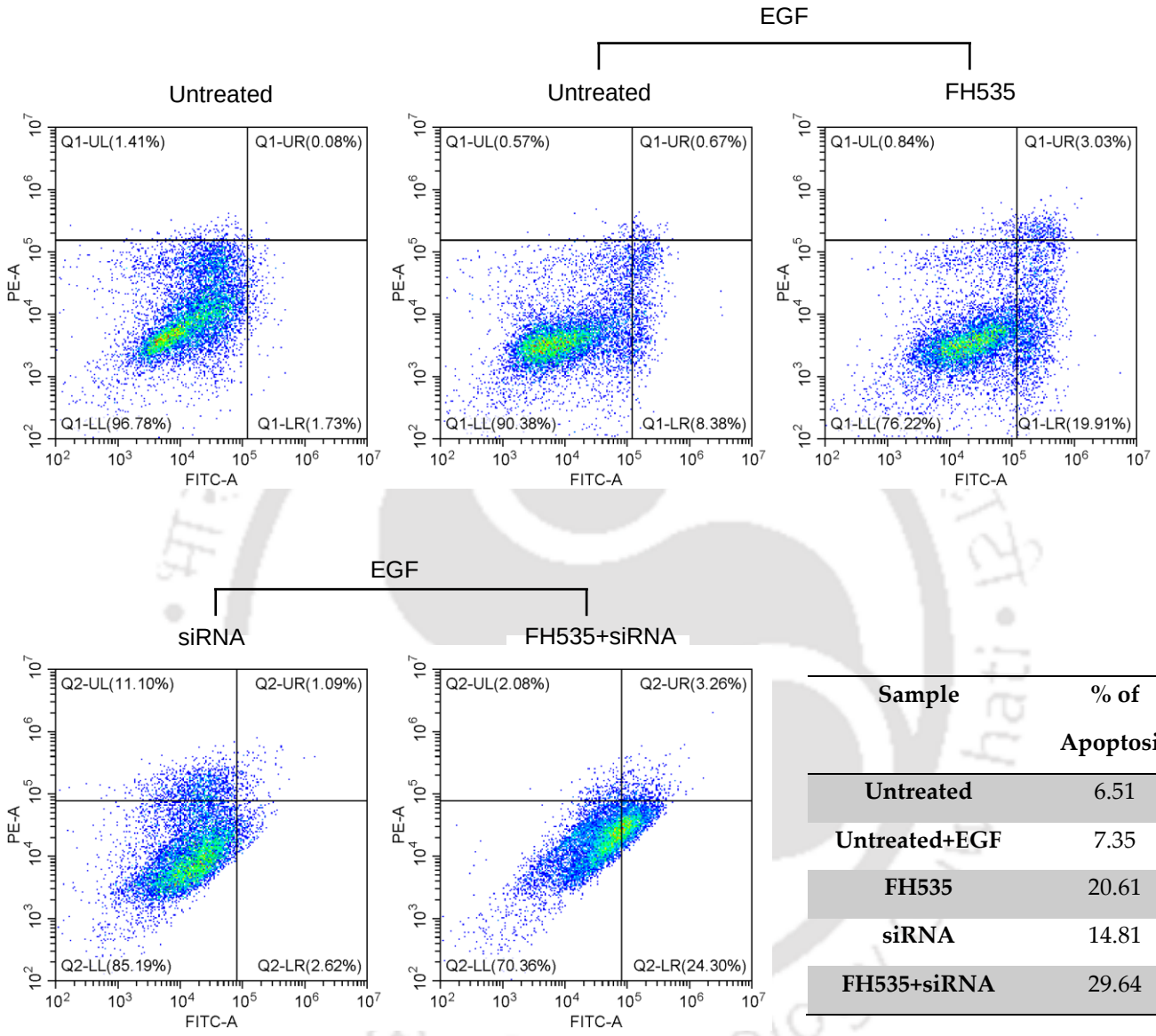

Sample	% of Apoptosis
Untreated	6.51
Untreated+EGF	7.35
FH535	20.61
siRNA	14.81
FH535+siRNA	29.64

Figure. 3.2.68: Flow cytometric analysis of apoptotic populations probed by annexin-V-FITC PI assay following treatment in MDA-MB-468 monolayer cultures.

3.2.1.8 Knockdown of SQSTM1/P62 Results in Inactivation of Non-Canonical Wnt VANGL2-JNK Signaling Axis: Besides canonical Wnt/β-Catenin signaling, the non-canonical Wnt signaling is also implicated in TNBC aggressiveness [153]. TNBC cells orchestrates its evasive property via the planar cell polarity pathway or Wnt VANGL2-JNK signaling axis [154]. It was examined whether co-treatment had any impact on this signaling pathway. Inhibition of SQSTM1/P62 or Wnt/β-Catenin signaling didn't alter the expression of VANGL2 (**Figure. 3.2.69** and **Figure. 3.2.70**). However, knockdown of SQSTM1/P62 decreased p-JNK in both MDA-MB-231 and MDA-MB-468 (**Figure. 3.2.71** and **Figure. 3.2.72**). In immunofluorescence cytochemistry VANGL2 and SQSTM1/P62 are detected to be colocalized in punctate cytoplasmic pattern in late endosomal compartments of both TNBC cell lines (**Figure. 3.2.73** and **Figure. 3.2.74**). As expected, the colocalization is not visible in SQSTM1/P62 knockout cells.

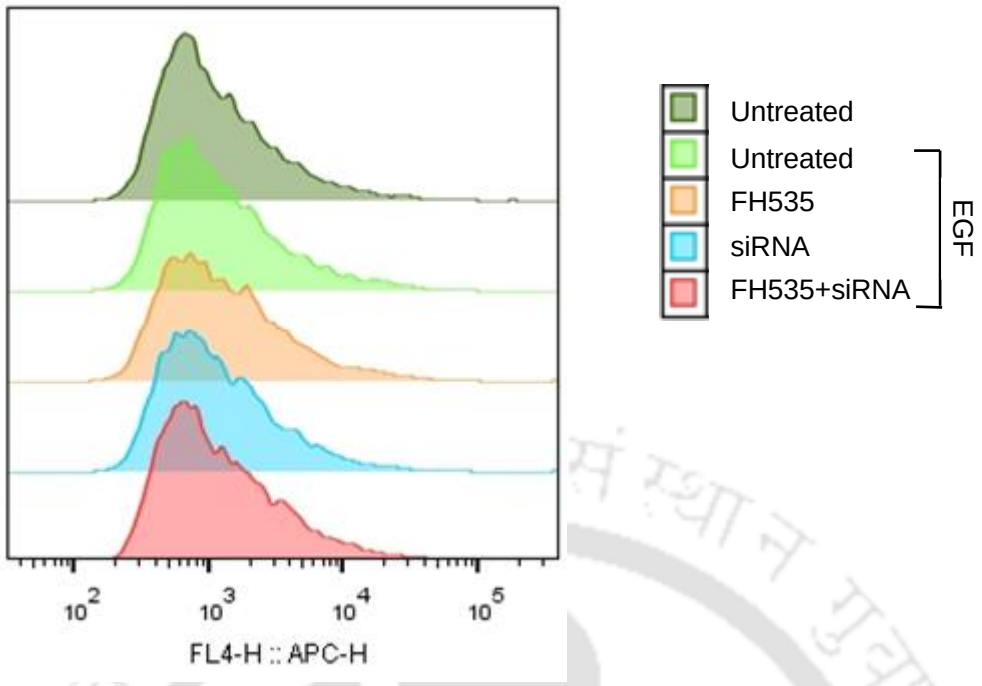

Figure. 3.2.69: The histogram of immunofluorescence flowcytometry detecting VANGL2 of MDA-MB-231 monolayer cultures.

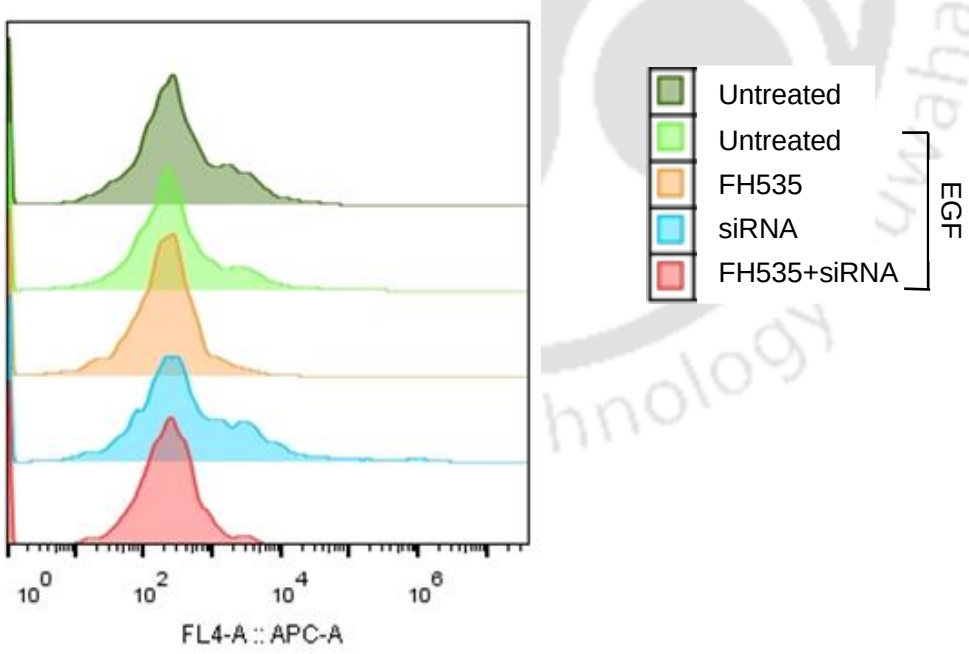

Figure. 3.2.70: The histogram of immunofluorescence flowcytometry detecting VANGL2 of MDA-MB-231 monolayer cultures.

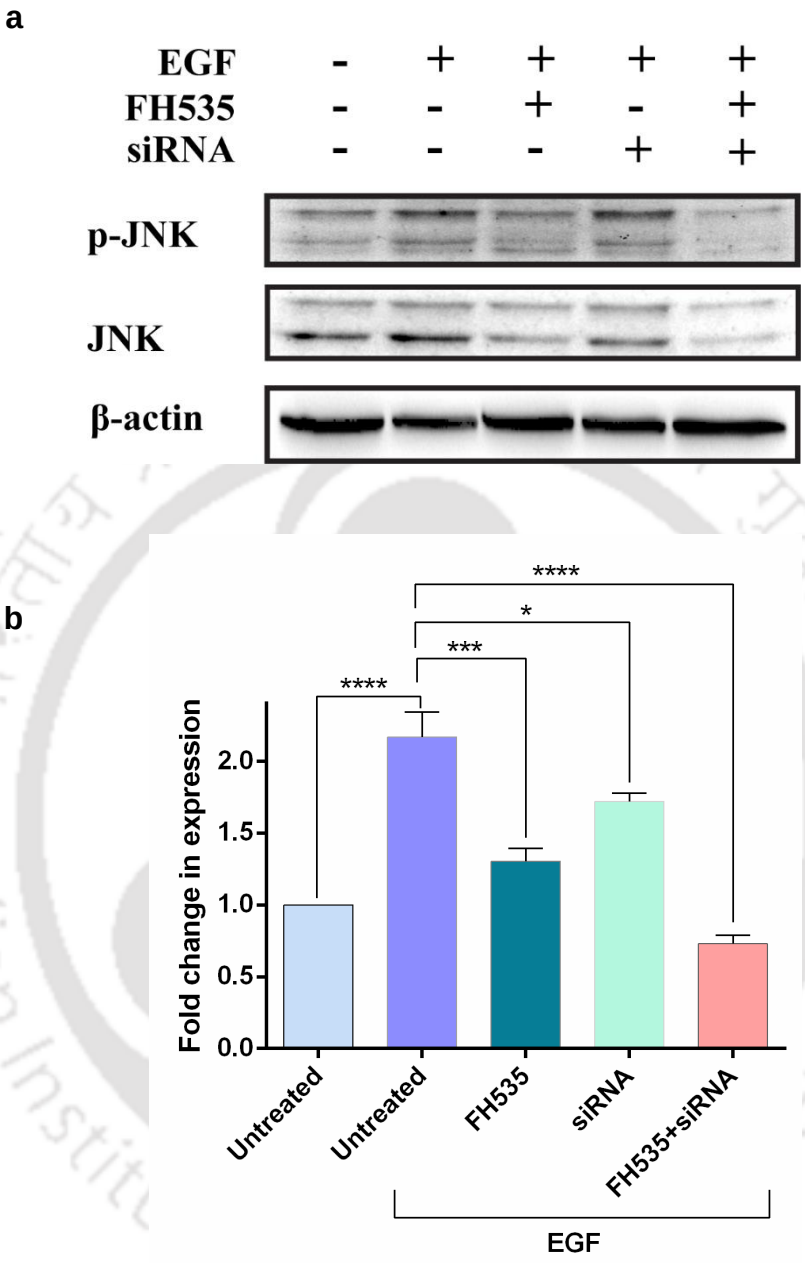

Figure. 3.2.71: (a) Representative Western blots showing phospho-JNK and JNK levels in MDA-MB-231 monolayer culture. β-actin serves as a loading control. (b) Graphs depicts the alteration in the expression levels of phospho JNK with respect to untreated samples following inhibitor/siRNA treatment. The expression levels were deduced from the blots using ImageJ software.

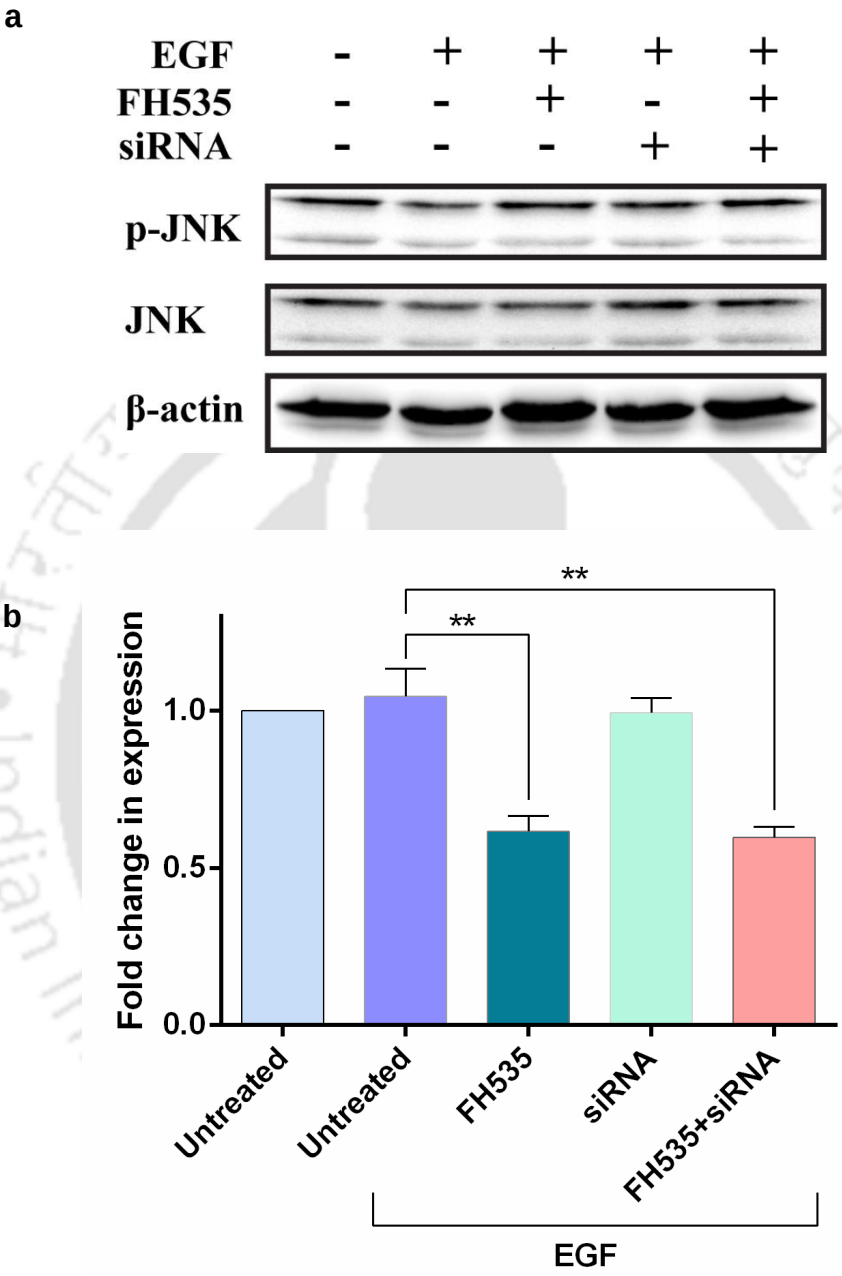

Figure. 3.2.72: (a) Representative Western blots showing phospho-JNK and JNK levels in MDA-MB-468 monolayer culture. β-actin serves as a loading control. (b) Graphs depicts the alteration in the expression levels of phospho JNK with respect to untreated samples following inhibitor/siRNA treatment. The expression levels were deduced from the blots using ImageJ software.

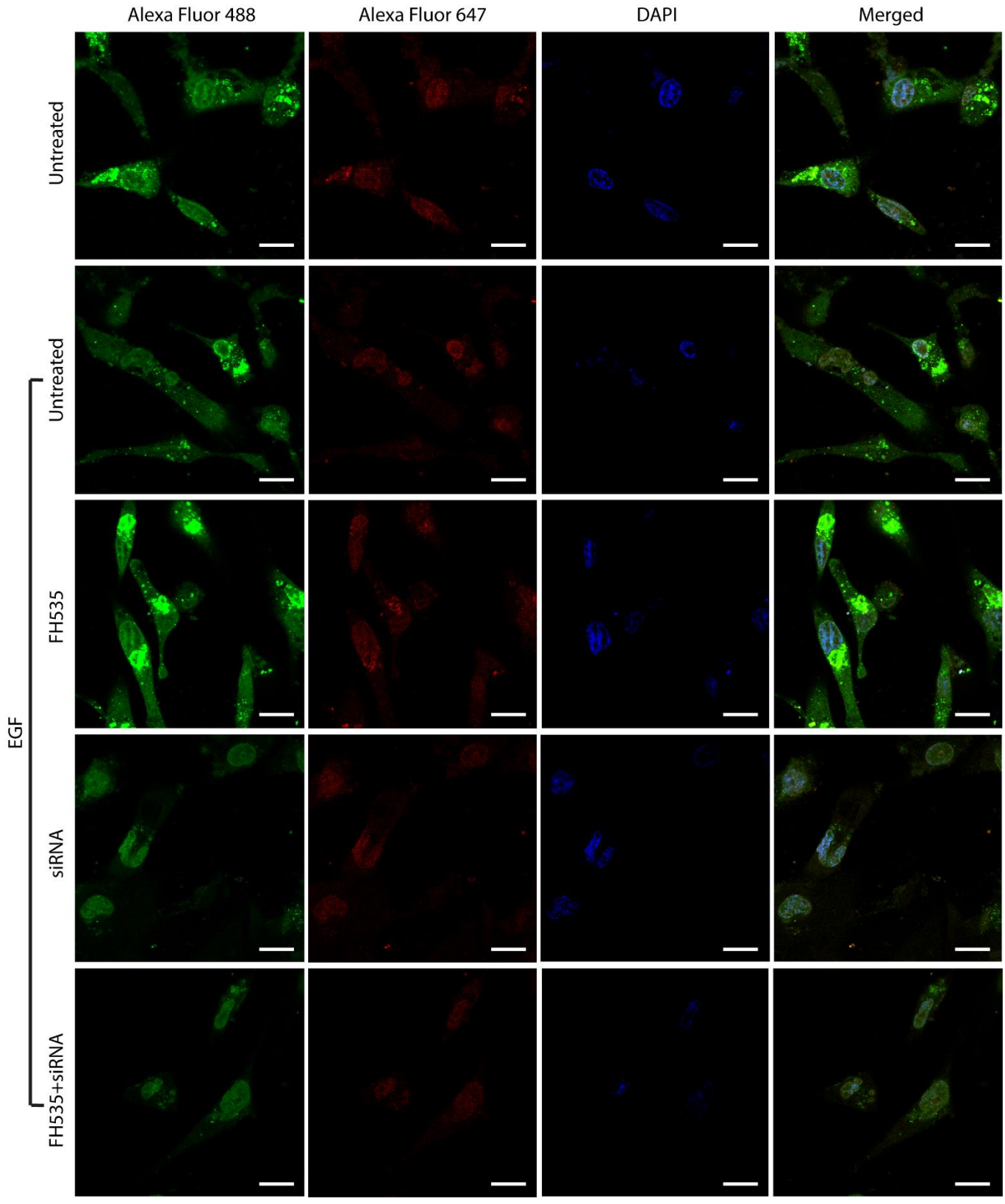

Figure. 3.2.73: Immunocytochemistry depicting SQSTM1/VANGL2 interaction in MDA-MB-231 monolayer culture. Green fluorescence refers to SQSTM1/P62 and red fluorescence refers to VANGL2. Scale bar represents 20 μM.

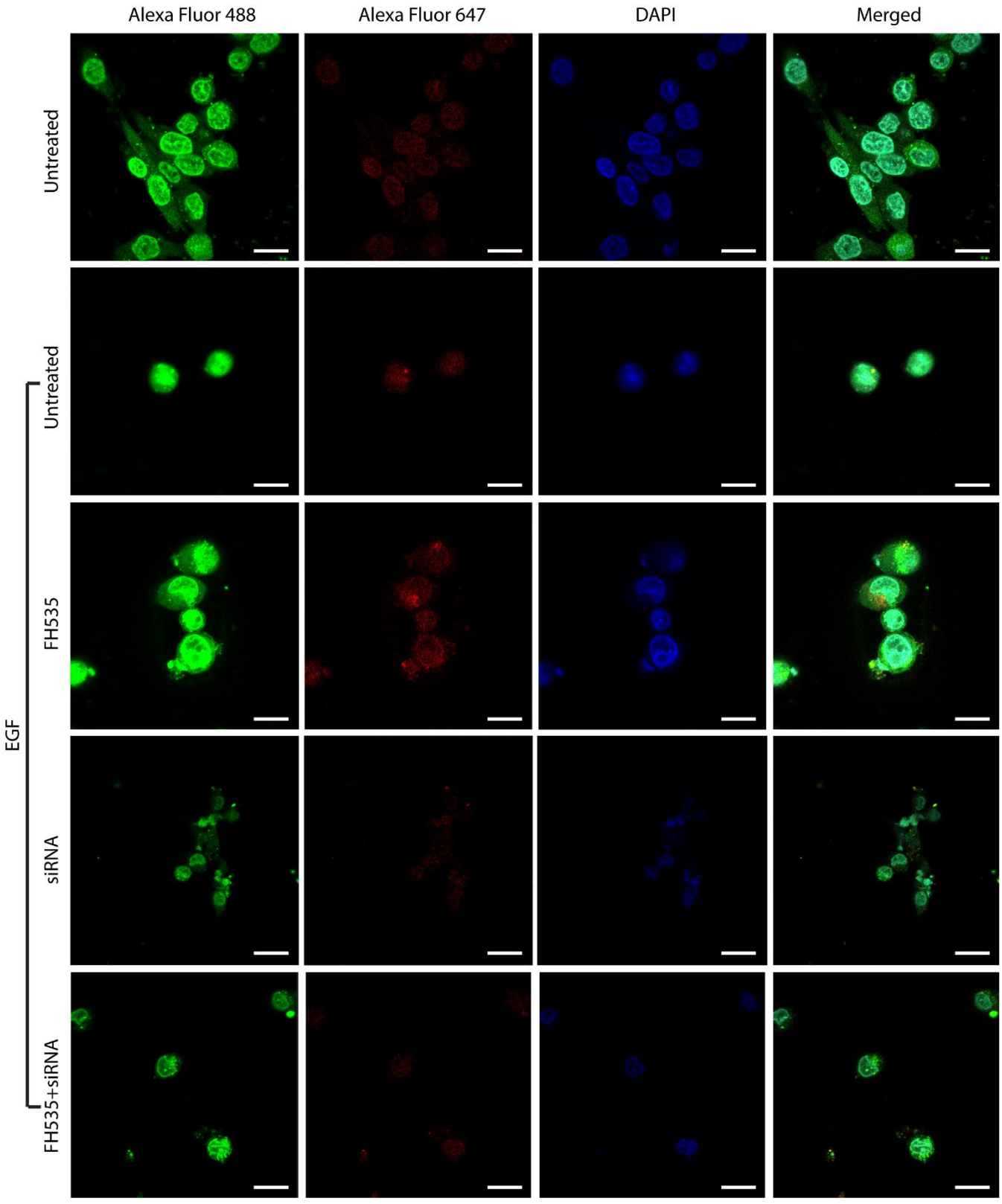

Figure. 3.2.74: Immunocytochemistry depicting SQSTM1/VANGL2 interaction in MDA-MB-468 monolayer culture. Green fluorescence refers to SQSTM1/P62 and red fluorescence refers to VANGL2. Scale bar represents 20 μM.

3.2.1.9 Suppression of SQSTM1/P62 Does Not Alter NF-κβ Expression but Depletes the Activated Form of AKT: It was important to examine whether SQSTM1/P62 had any role on the stability of NF-κβ. Thus, the protein expression of total NF-κβ was evaluated following knockdown of SQSTM1/P62 and inhibition of Wnt/β-Catenin signaling. Immuno-flowcytometry revealed unaltered NF-κβ expression (**Figure. 3.2.75 and Figure. 3.2.76**). Furthermore, the effect of co-treatment on PI3K/AKT/mTOR signaling pathway was also examined. Western blot revealed depletion of activated form of AKT i.e. phospho AKT following knockdown of SQSTM1/P62 by siRNA (**Figure. 3.2.77** and **Figure. 3.2.78**). However, inhibition of Wnt/β-Catenin signaling by FH535 didn't alter the expression of pAKT (**Figure. 3.2.77** and **Figure. 3.2.78**). Confocal images of immunofluorescence cytometry confirmed the SQSTM1/P62-siRNA mediated repression of pAKT in both MDA-MB-231 and MDA-MB-468 (**Figure. 3.2.79** and **Figure. 3.2.80**).

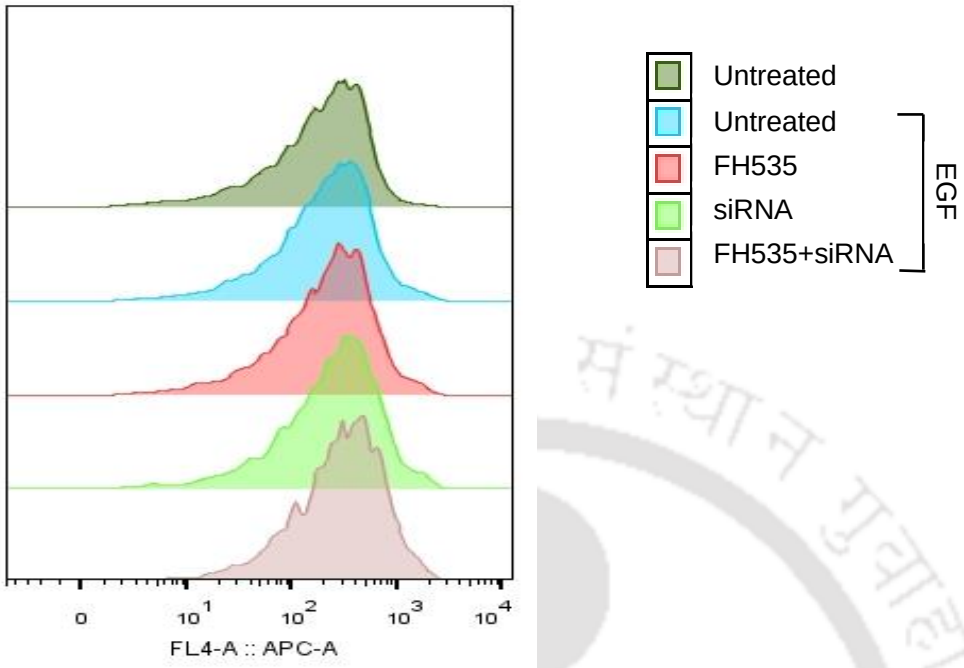

Figure. 3.2.75: The histogram of immunofluorescence flowcytometry detecting NF-κβ of MDA-MB-231 monolayer cultures.

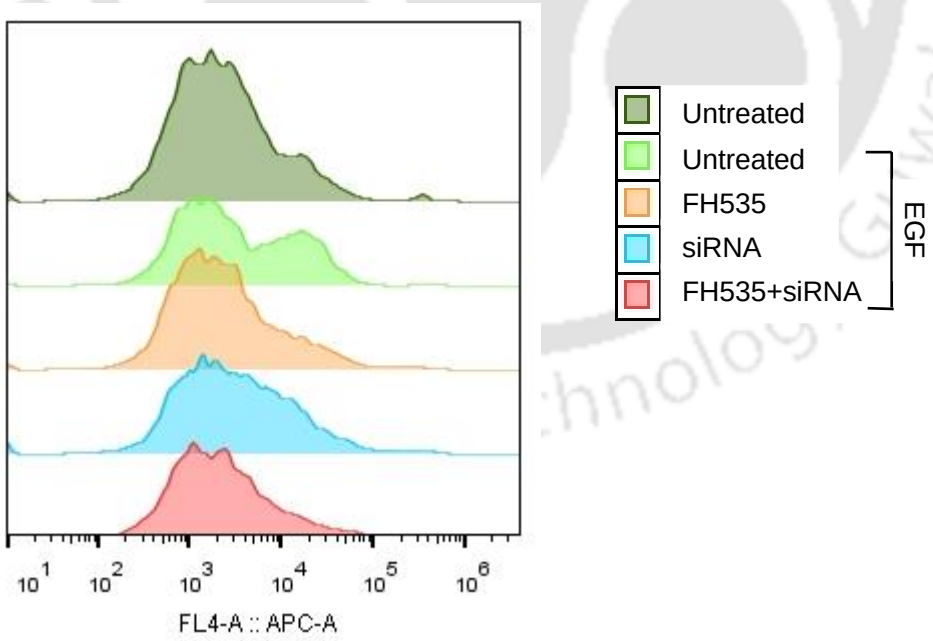

Figure. 3.2.76: The histogram of immunofluorescence flowcytometry detecting NF-κβ of MDA-MB-468 monolayer cultures.

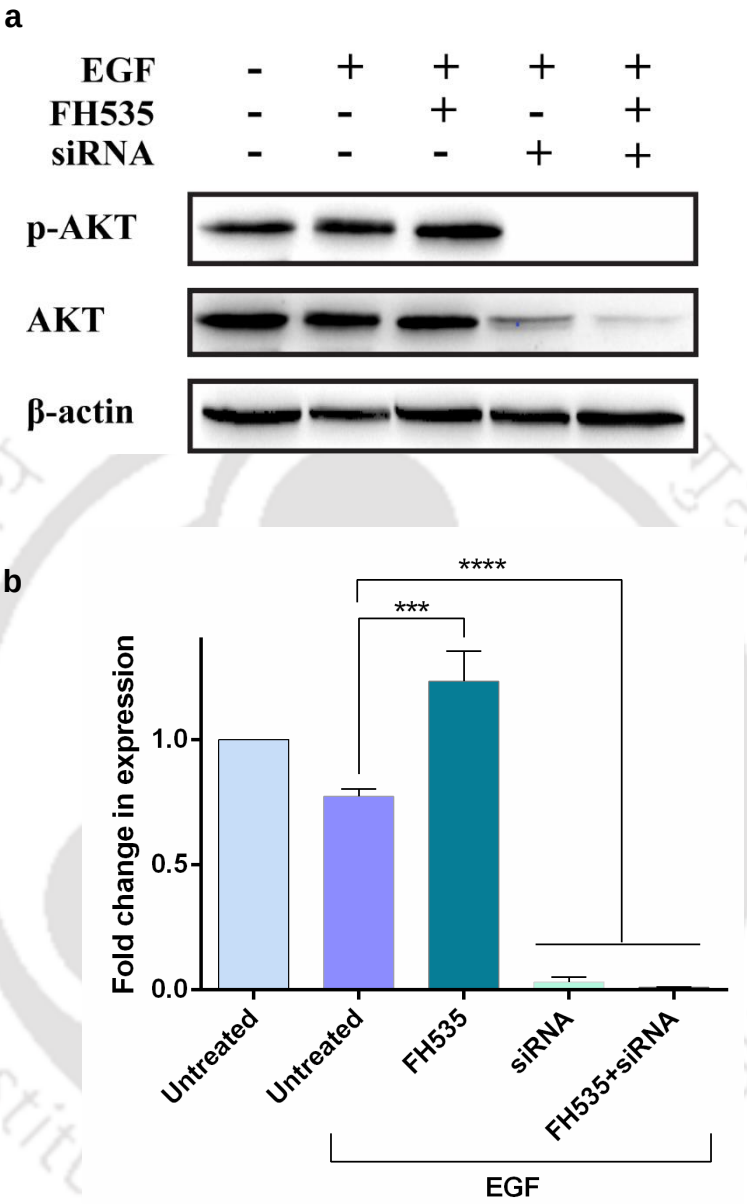

Figure. 3.2.77: (a) Representative Western blots showing phospho-AKT and AKT levels in MDA-MB-231 monolayer culture. β-actin serves as a loading control. (b) Graphs depicts the alteration in the expression levels of phospho AKT with respect to untreated samples following inhibitor/siRNA treatment. The expression levels were deduced from the blots using ImageJ software.

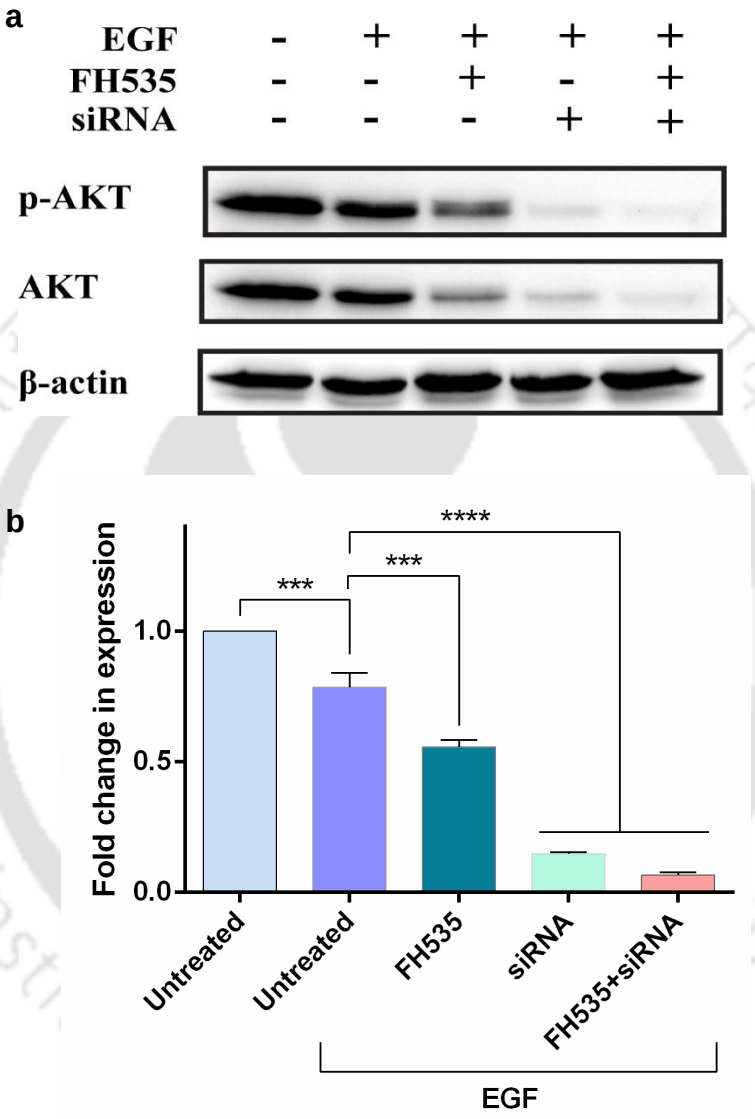

Figure. 3.2.78: (a) Representative Western blots showing phospho-AKT and AKT levels in MDA-MB-468 monolayer culture. β-actin serves as a loading control. (b) Graphs depicts the alteration in the expression levels of phospho AKT with respect to untreated samples following inhibitor/siRNA treatment. The expression levels were deduced from the blots using ImageJ software.

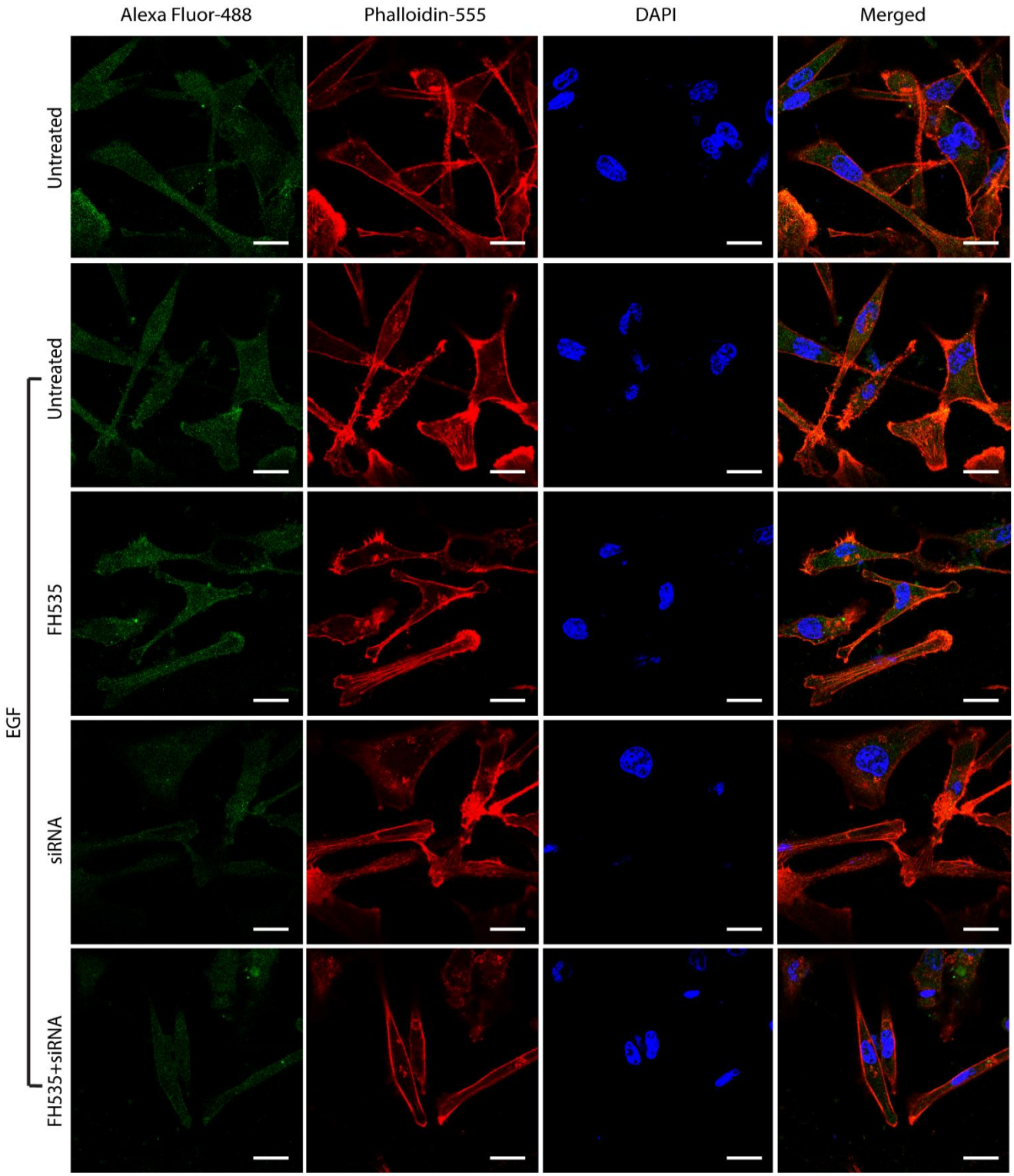

Figure. 3.2.79: Confocal images of MDA-MB-231 monolayer cultures immune-stained with anti-phospho AKT antibody visualized by Alexa Flour-488. Actin cytoskeleton were stained with Alexa Flour-555 conjugated phalloidin. Nuclei were stained with DAPI. Scale bar represents 20 μM.

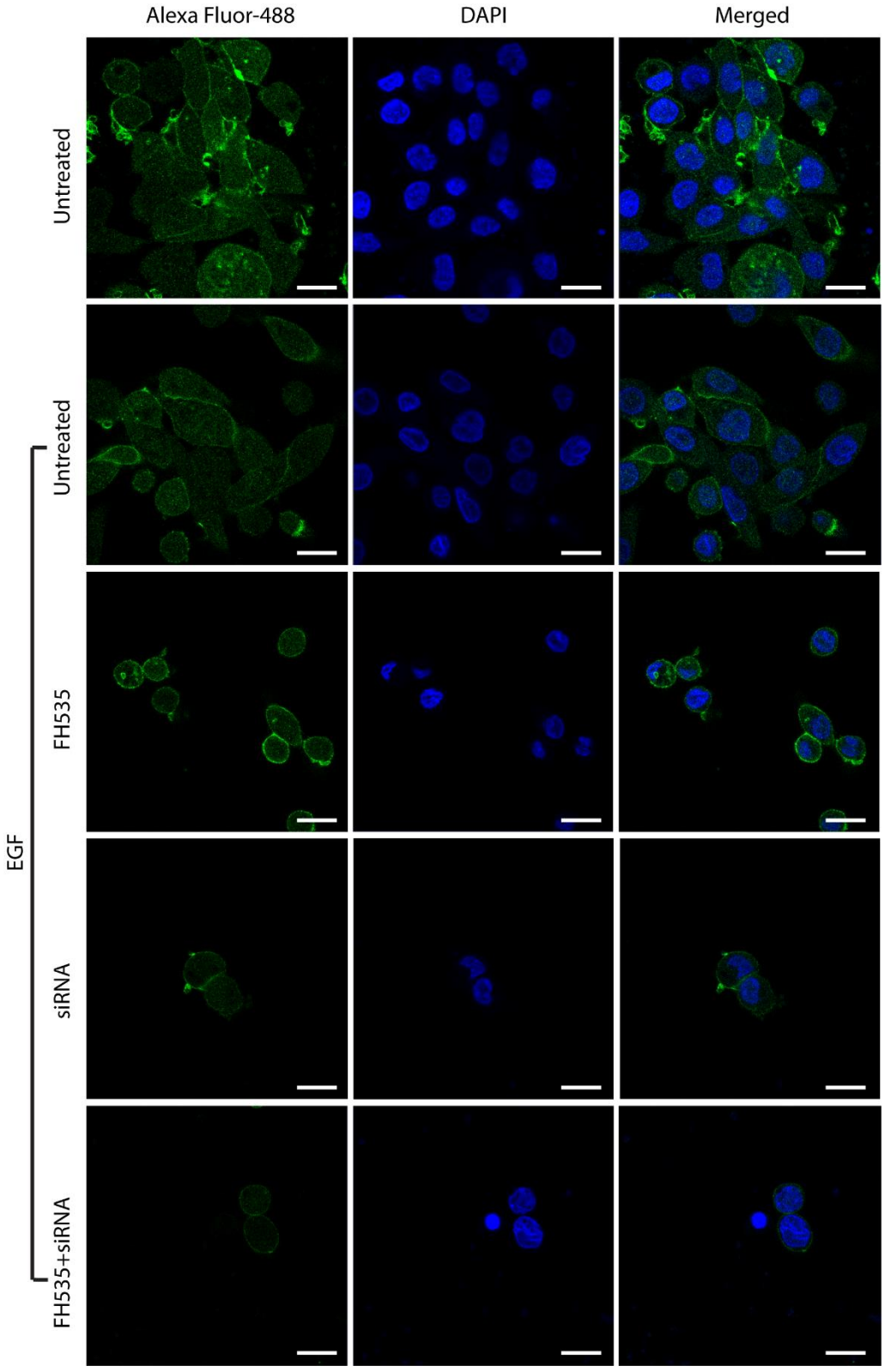

Figure. 3.2.80: Confocal images of MDA-MB-468 monolayer cultures immune-stained with anti-phospho AKT antibody visualized by Alexa Flour-488. Nuclei were stained with DAPI. Scale bar represents 20 μM.

3.2.1.10 Alteration of Wnt/β-Catenin Signaling Down-regulates Activated Form of STAT-3 But Co-treatment Does Not Alter MAPK Expression: Clinical and preclinical data indicates the involvement of overexpressed and constitutively activated STAT-3 and MAPK in the progression, proliferation, metastasis and chemoresistance of TNBC [155, 156]. Protein expression analysis revealed knockdown of SQSTM1/P62 has almost no effect on the expression of pSTAT-3 or pMAPK in both the cell lines (**Figure. 3.2.81 and Figure. 3.2.82**). However, inhibition of Wnt/β-Catenin signaling by FH535 effectively reduced the expression of pSTAT-3 by 3.22 and 3.9-fold in MDA-MB-231 and MDA-MB-468, respectively. Treatment with FH535 slightly increased the pMAPK. In fact, co-treatment increased the expression of pMAPK marginally (**Figure. 3.2.81 and Figure. 3.2.82**).

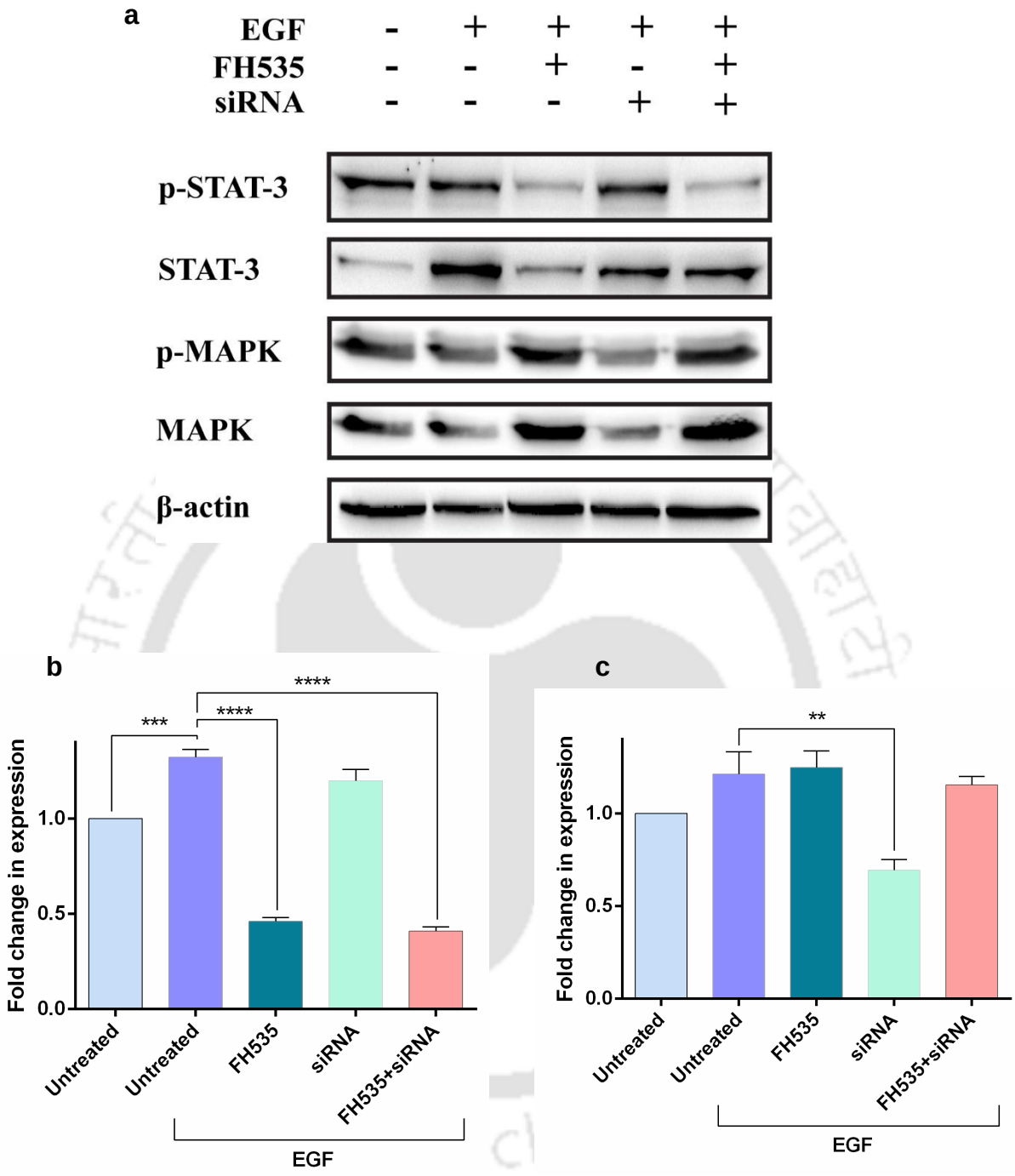

Figure. 3.2.81: (a) Representative Western blots showing phospho-STAT-3, STAT-3, phospho-MAPK and MAPK levels in MDA-MB-231 monolayer culture. β-actin serves as a loading control. Graphs depicts the alteration in the expression levels of (b) phospho-STAT-3 and (c) phosphor-MAPK with respect to untreated samples following inhibitor/siRNA treatment. The expression levels were deduced from the blots using ImageJ software.

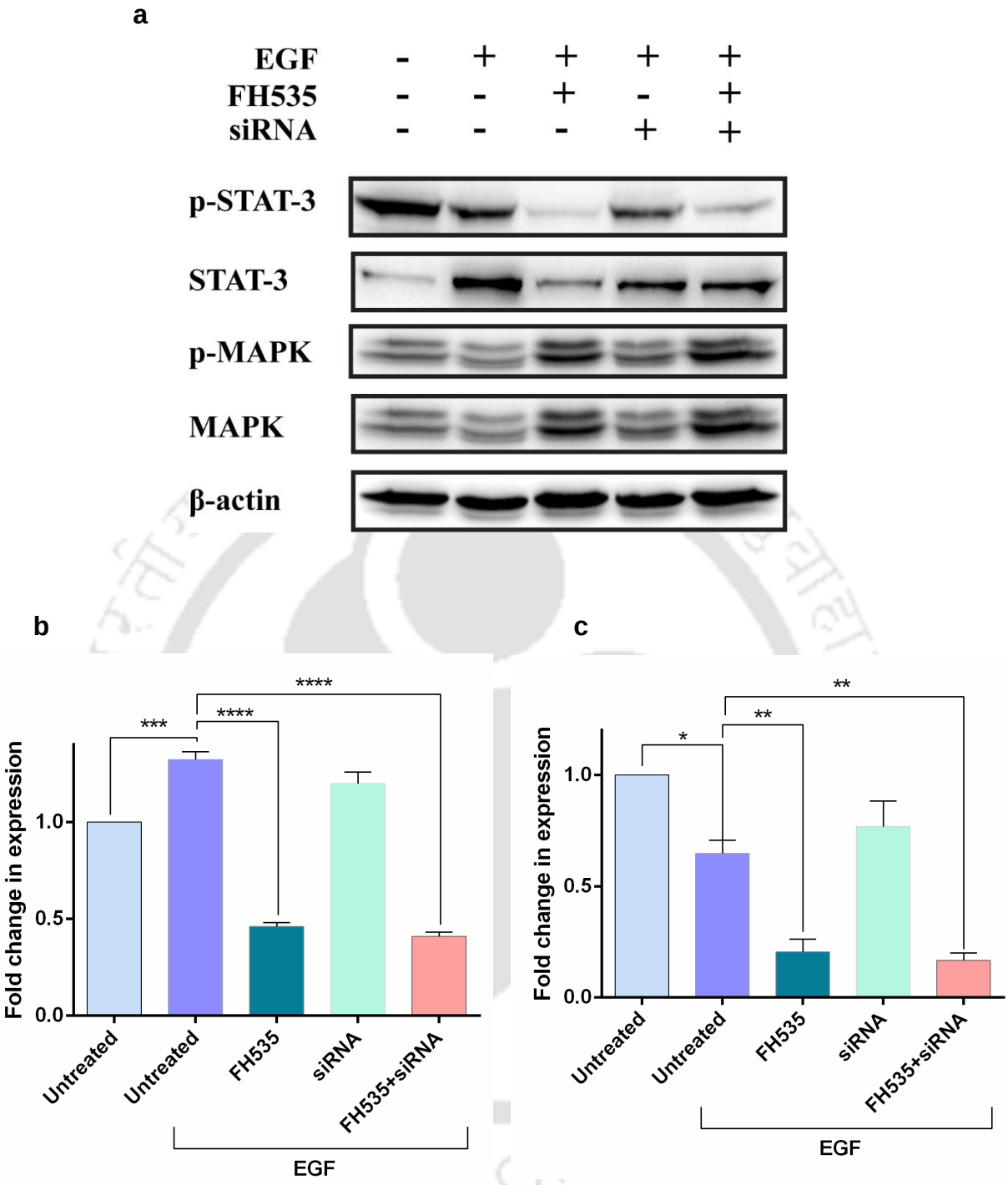

Figure. 3.2.82: (a) Representative Western blots showing phospho-STAT-3, STAT-3, phospho-MAPK and MAPK levels in MDA-MB-468 monolayer culture. β-actin serves as a loading control. Graphs depicts the alteration in the expression levels of (b) phospho-STAT-3 and (c) phosphor-MAPK with respect to untreated samples following inhibitor/siRNA treatment. The expression levels were deduced from the blots using ImageJ software.

3.2.1.11 EMT Induction by EGF Induces Autophagy and Inhibition of Wnt/β-Catenin Signaling by FH535 Repress Autophagic Activity: Next, the effect of suppression of SQSTM1/P62 and Wnt/β-Catenin signaling in autophagic activity of TNBC cells were documented. Following EMT induction the LC3 II/1 ratio increased indicating the induction of autophagic activity (**Figure. 3.2.83** and **Figure. 3.2.84**). No significant change in LC3 II/1 ratio was observed when cells were treated for a period of 48 h. However, a significant inhibition of autophagic activity by FH535 was observed in MDA-MB-468 when cells were treated for a period of 24 h (**Figure. 3.2.84**).

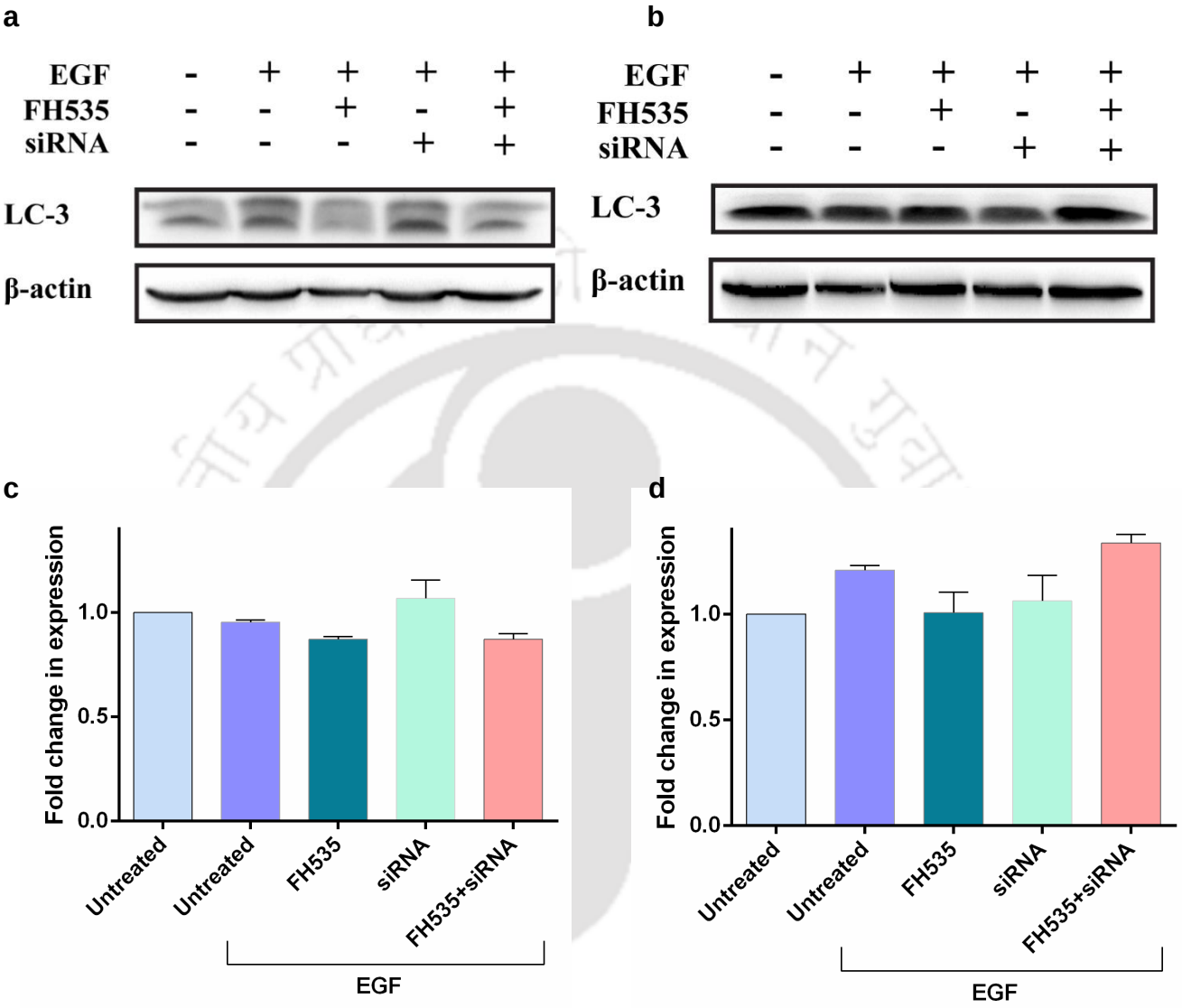

Figure. 3.2.83: Representative Western blots showing LC3-I and LC3-II levels in MDA-MB-231 monolayer culture following treatment of (a) 24 h and (b) 48 h. β-actin serves as a loading control. Graphs depicts the normalized ratio of LC3-II to LC3-I expression obtained following treatment period of (c) 24 h and (d) 48 h with respect to untreated samples. The expression levels were deduced from the blots using ImageJ software.

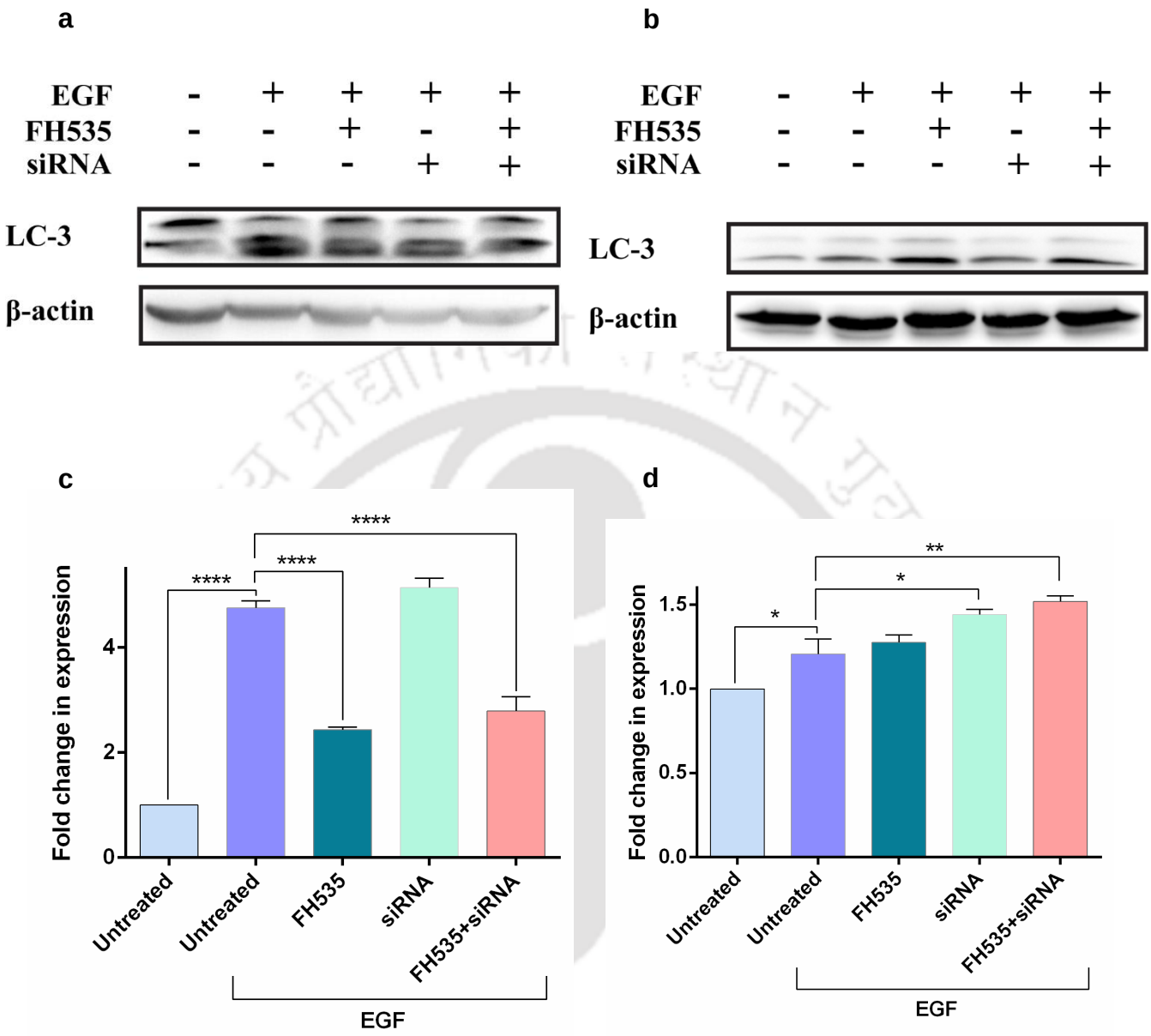

Figure. 3.2.84: Representative Western blots showing LC3-I and LC3-II levels in MDA-MB-468 monolayer culture following treatment of (a) 24 h and (b) 48 h. β-actin serves as a loading control. Graphs depicts the normalized ratio of LC3-II to LC3-I expression obtained following treatment period of (c) 24 h and (d) 48 h with respect to untreated samples. The expression levels were deduced from the blots using ImageJ software.

3.2.2 Discussion:

Several signaling pathways have been implicated in maintaining EMT and stemness of TNBC cells. An array of crosstalks, feedback mechanisms, as well as their critical involvement in normal cellular developmental process renders it challenging to successfully target them and prevent EMT. Therefore, to combat EMT and stemness of TNBC, the crosstalk between signaling pathways has to be obliterated. Mining large dataset on TNBC from public databases have shown that the mRNA and protein expression of both β-catenin and SQSTM1/P62 are elevated in TNBC tumors with respect to non-TNBC tumors. From the Kaplan-Meier survival analysis it can be observed that higher expression of SQSTM1/P62 and β-Catenin leads to reduced overall survival of the TNBC patients. Similarly, SQSTM1/P62 expression is found to be elevated with the progression of cancer stages.

Given the strong correlation of Wnt/β-catenin signaling and SQSTM1/P62 in TNBC pathogenesis, the critical roles played by these two pathways in TNBC progression was elucidated. Earlier reports suggest that Wnt/β-catenin signaling contributes to stemness of TNBC. TCF and LEF mediates Wnt signals and overactived Wnt signal drives TCF/LEF to transform cells and induce stem cell like property [157]. Similarly, reports by Xu et al. suggests that SQSTM1/P62 enhances breast cancer stem cell like properties [158]. Suppression of Wnt/β-catenin and SQSTM1/P62 reduced the expression of TCF and LEF. Furthermore, the inhibition of Wnt/β-catenin signaling and silencing of SQSTM1/P62 led to reduced sphere forming and colony forming ability suggesting Wnt/β-catenin and SQSTM1/P62 as a potential target to limit TNBC stemness. Additionally, the gene expression alteration of CSC markers were evaluated to validate the finding. Soysal et al. reported that EpCAM is highly expressed in TNBC and positively correlated with TNBC lymph node metastasis and distant metastasis [159]. Moreover, higher EpCAM expression corresponds to CSC population generation through OCT4,

NANOG, c-MYC, and SOX2 [160]. ALDH1A3, a CSC biomarker is abundantly expressed in cancer stem cells, which have significant treatment resistance as well as the ability to induce self-renewal, clonogenic development, and tumor-initiating potential [161]. It was found that after treatment, ALDH1A3 remained almost unaltered in MDA-MB-231 and reduced by 1.76-fold in MDA-MB-468. EpCAM was reduced by 5.35-fold by knockdown of SQSTM1/P62 and Wnt/β-catenin inhibition in MDA-MB-231 and remained almost unaltered in MDA-MB-468. In addition to stemness markers, the expression of genes responsible for promoting and maintaining cancer stem cells were also analyzed. Reports by Cidado et al. suggests that Ki-67 is required for maintenance of cancer stem cells but not cell proliferation [142]. Wienken et al. described the role of MDM2 in maintaining stemness and cancer cell survival via stabilizing histone modifications, such as H2AK119ub1 and H3K27me3 [162]. The results in this study showed that co-treatment reduced the expression of both Ki-67 and MDM2 and the knockdown of SQSTM1/P62 depleted MDM2 expression. Karin et al. reported that SQSTM1/P62-mediated activation of Nrf2 triggers MDM2 expression in premalignant pancreatic intraepithelial neoplasia 1, which supports the findings [163]. Transcription factor cMYC is known to cooperate with HIF2α, a stemness-associated transcription factor that increases self-renewal of embryonic stem cells through coordinated upregulation of Oct-4 and Nanog [164]. Protein expression analysis revealed that knockdown of SQSTM1/P62 decreased the expression of cMYC by 2.9-fold in MDA-MB-231. Similarly, Xu et al. has reported that SQSTM1/P62 enhances breast cancer stem like properties by stabilizing MYC mRNA at the post-transcriptional level, rather than influencing its promoter activity [158].

EMT is induced in tumor cells during metastasis and invasion, allowing cells to detach from the basement membrane and link with other cells, allowing them to spread beyond their initial location and infiltrate nearby organs [149]. Since Wnt/β-catenin and SQSTM1/P62 are known to contribute to EMT

progression, the effect of their modulation was evaluated. Following treatment with FH535 and siRNA, the upregulation of epithelial marker E-cadherin and downregulation of mesenchymal marker Vimentin, N-cadherin, Fibronectin and Caveolin-1 indicates the phase transition from EMT to MET. From the experimental data it can be observed that knockdown of SQSTM1/P62 upregulated the expression of E-cadherin in both TNBC cell lines. Damiano et al. has reported that SQSTM1/P62 interacts with E-cadherin and delivers it to autophagosome for degradation [165], which supports the experimental finding. Furthermore, reports by Li et al. states that SQSTM1/P62 interacts with Vimentin and positively upregulates its expression [165]. Similarly, Gilles et al. has shown that β-catenin/TCF could directly transactivate Vimentin [165]. The here observed decreased level of Vimentin after FH535 and siRNA treatment correlates with these studies. Transcription factor Twist1 was downregulated by knockdown of SQSTM1/P62 in both MDA-MB-231 and MDA-MB-468. In line with the finding, Quing et al. found that autophagy deficiency promotes cell proliferation and migration through SQSTM1/P62-dependent stabilization of the oncogenic transcription factor Twist1. SQSTM1/P62 binds to Twist1 and inhibits degradation of Twist1 [61]. Activation of the Wnt/β-catenin signaling pathway is known to contribute to cervical cancer pathogenesis via upregulation of Twist1 [166]. Similar to these findings, treatment with FH535 was found to effectively downregulate Twist1 expression. Silencing SQSTM1/P62 didn't alter the Snail expression in MDA-MB-231 and MDA-MB-468 monolayer. Strikingly, Snail was almost depleted in SQSTM1/P62 knockdown spheroids. Bertrand et al. shown that inhibition of SQSTM1/P62 expression by siRNA strongly decreased Snail level after EMT induction [63]. Therefore, the experimental findings indicate the pivotal role played by Wnt/β-catenin and SQSTM1/P62 pathway in regulating EMT in TNBC.

Overexpression of SQSTM1/P62 is known to promote cell migration in hepatocellular carcinoma via activation of the Wnt/β-Catenin pathway [167].

Similarly, in TNBC cells line MDA-MB-231 and MDA-MB-468, modulation of Wnt/β-Catenin pathway and SQSTM1/P62 reduced the migration and invasion potential.

Multidrug resistance (MDR), which is primarily caused by overexpression of ATP-binding cassette (ABC) transporters, is a major impediment in achieving an effective chemotherapy treatment [104]. Indeed, Wnt/β-catenin pathway has been reported to regulate ABCB1 transcription in chronic myeloid leukemia [168]. Alteration of Wnt/β-Catenin pathway and SQSTM1/P62 effectively reduced the expression of ABC transporters signifying the positive correlation between the pathways and ABC transporters.

Cyclin-D1 promotes cell cycle progression from G1 to S phase by phosphorylating and inactivating the retinoblastoma (Rb) protein, which leads to the release of E2F transcription factors [94]. Tetsu et al. found that β-catenin controls Cyclin-D1 expression in colon cancer cells, and that aberrant β-catenin expression levels can lead to Cyclin-D1 accumulation, which can lead to neoplastic transformation [112]. Qi et al. reported that SQSTM1/P62 regulate breast cancer progression and metastasis by inducing cell cycle arrest and regulating immune cell infiltration [169]. Evidently, modulation of Wnt/β-catenin signaling pathway and SQSTM1/P62 resulted in reduced expression of Cyclin-D1, leading to G0/G1 cell cycle arrest. The propensity of an anticancer medicine to induce apoptosis in the targeted cells determines its cytotoxicity. The increase in 26.81% and 23.13% apoptotic cell population in MDA-MB-231 and MDA-MB-468 implies the importance of these pathways in TNBC survival.

The Wnt/PCP protein VANGL2 is found to be overexpressed in TNBC. Furthermore, SQSTM1/P62 is required to recruit and activate JNK in breast cancer cells through VANGL2- SQSTM1/P62 signaling cascade. SQSTM1/P62 recruits JNK to VANGL2 and contributes to its activation [170]. Therefore, knockdown of

SQSTM1/P62 results in the inactivation of non-canonical Wnt VANGL2-JNK signaling axis, thereby resulting in reduced activated form of JNK in both cell lines.

Schwob et al. reported unaltered expression of NF-κβ following SQSTM1/P62 silencing [171]. Herein, no change in NF-κβ expression was detected by alteration of SQSTM1/P62. However, western blot revealed depletion of activated form of AKT i.e. phospho AKT following knockdown of SQSTM1/P62 by siRNA. A plausible explanation for this phenomenon may be linked to PKCzeta. PKCzeta is known as a negative regulator of AKT activation. Joung et al. found that SQSTM1/P62 dependent AKT phosphorylation occurred via the release of AKT from PKCzeta by association of SQSTM1/P62 and PKCzeta [172].

Through GSK3β, the Wnt/β-catenin pathway forms a bidirectional positive feedback loop involving MAPK and STAT3 [133]. MAPK and STAT-3 have been implicated in EMT in prior studies [137]. After incubation with the inhibitor/siRNA, the expression of pMAPK and pSTAT-3, both important downstream components of cell survival signaling pathways, decreased, indicating the intricacy and web-like interconnectedness between the receptors studied and the suppression of EMT and growth signals.

Induction of EMT by EGF was found to induce autophagy. Similarly, inhibition of Wnt/β-Catenin signaling by FH535 repressed autophagic activity. Earlier studies by Kuhn et al. also indicated Wnt/β-Catenin mediated decrease in autophagic activity [173]. Knockdown of SQSTM1/P62 by siRNA had no effect on autophagic activity of TNBC cells. Xu et al. found that LC-3 conversion was not significantly changed by either knockdown or overexpression of SQSTM1/P62, indicating that SQSTM1/P62 does not alter autophagic activity under normal condition [158].

These findings are clear indicators of the pivotal role played by Wnt/β-Catenin signaling pathway and SQSTM1/P62 in TNBC survival through downstream signaling.

3.2.3 Conclusion: The key drivers of therapeutic resistance in TNBC include anomalous EMT activation and associated cancer stem cell-like characteristics. In search of successful therapy, autophagy adaptor protein SQSTM1/P62 and Wnt/β-Catenin pathway, two important signaling pathways governing EMT were targeted. In conjunction with reversal of EMT phenotype by co-treatment, genes involved in cancer stemness and MDR was similarly reduced. Furthermore, impeding EMT inhibited TNBC cell migration and invasion. Nonetheless, by targeting numerous signaling nodes and limiting downstream crosstalk, the suggested combination treatment was able to avoid most of the issues concerning EMT regulation.

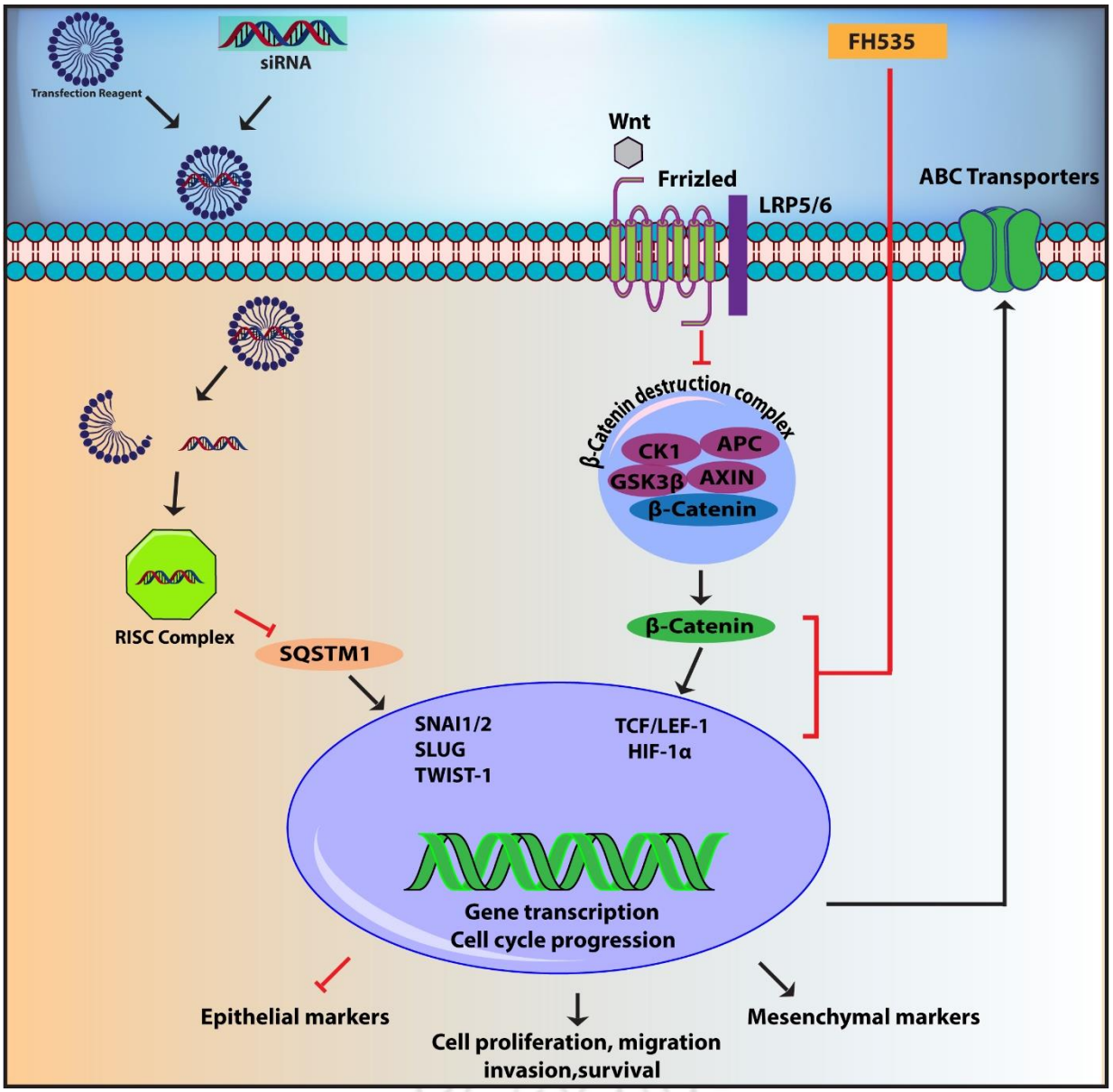

Scheme 3.2: Schematic illustration of details of intracellular signaling upon siRNA against SQSTM1/P62 and FH535 co-treatment regulating EMT and MDR dynamics

3.3. Targeting TNBC by Nanocarrier Mediated Targeted Delivery of Novel Drugs

ACS Applied Bio Materials 2021, 4, 6, 5033–5048.

Results and Discussion

Abstract: In continuation of Section-I and Section-II to target the signaling pathways for TNBC therapy, targeted drug delivery approach was pursuaded to combat the dreadful TNBC. A therapeutic module has been established in this regard by coating PLGA nanoparticle with d-penicillamine templated Au–Cu bimetallic nanoclusters. Further, the resultant nanomaterials were coated with recombinant transferrin protein to specifically target transferrin receptor overexpressing TNBC. The synthesized nanocomposites showed strong orange emission band at 630 nm with fluorescence quantum yield of 2%, rendering it suitable for theranostic applications. Experimental results demonstrated efficient cellular internalization and significant innate anti-cell proliferative potential of the nanocomposites. The fabricated nanocomposites were also able to induce cell death in spheroids, which was confirmed by live/dead dual staining results. Furthermore, when EMT-induced TNBC cells were treated with nanocomposites, they generated reactive oxygen species (ROS), depolarized the mitochondrial membrane potential, and induced apoptosis. Gene expression by real-time PCR indicated that treatment of EMT-induced TNBC cells with nanocomposites facilitated mesenchymal to epithelial transition (MET). In MDA-MB-468 cells, treatment with nanocomposites resulted in a 1.35-fold rise in E-cadherin an epithelial marker and a 1.36-fold decrease in vimentin a mesenchymal marker. Similarly, 2.87-fold and 1.76-fold decrease in stemness markers ALDH1A3 and EpCAM were observed in MDA-MB-231. Furthermore, 4.63-fold decrease in expression of ABCC1, a prominent contributor of MDR, was observed in MDA-

MB-231. Protein expression studies revealed that nanocomposites reduced p-STAT-3 by 1.61-fold in MDA-MB-231 and by 7.8-fold in MDA-MB-468. Importantly, nanocomposites downregulated the expression of β-catenin by 3-fold in MDA-MB-231 and by 3.11-fold in MDA-MB-468. Downregulation of EMT with concomitant alteration of STAT-3 and β-catenin signaling pathways led to reduced migration ability of the TNBC cells.

3.3.1 Results:

3.3.1.1. Characterization of the Nanocomposites: Herein, the water-dispersible (PLGA-d-penicillamine Au–Cu-transferrin) nanocomposites has been successfully formulated. Biodegradable PLGA nanoparticles were synthesized using the solvent evaporation technique, as described in the Materials and Methods section. The prepared PLGA nanoparticles were further characterized for morphology, surface charge, and hydrodynamic diameter. FESEM image revealed the particles having a diameter of 214.1 ± 12 nm (**Figure. 3.3.1 a**). Imaging of the nanoparticle using FETEM confirmed the diameter to be approximately 151.7 ± 10 nm (**Figure. 3.3.1 b**). For nanoparticles, the obtained hydrodynamic diameter was 251.5 nm (**Figure. 3.3.2**). The PLGA nanoparticles were found to be negatively charged (−17.4 mV) (**Figure. 3.3.3 a**).

The formation of the d-penicillamine Au–Cu nanocluster was validated from the FETEM images with distribution of particle sizes on average 2.08 nm ±0.84 (**Figure. 3.3.1 c**). Zeta potential analysis revealed that the synthesized d-penicillamine Au–Cu bimetallic nanocluster is having a positive surface charge of +3.67 mV (**Figure. 3.3.3 b**).

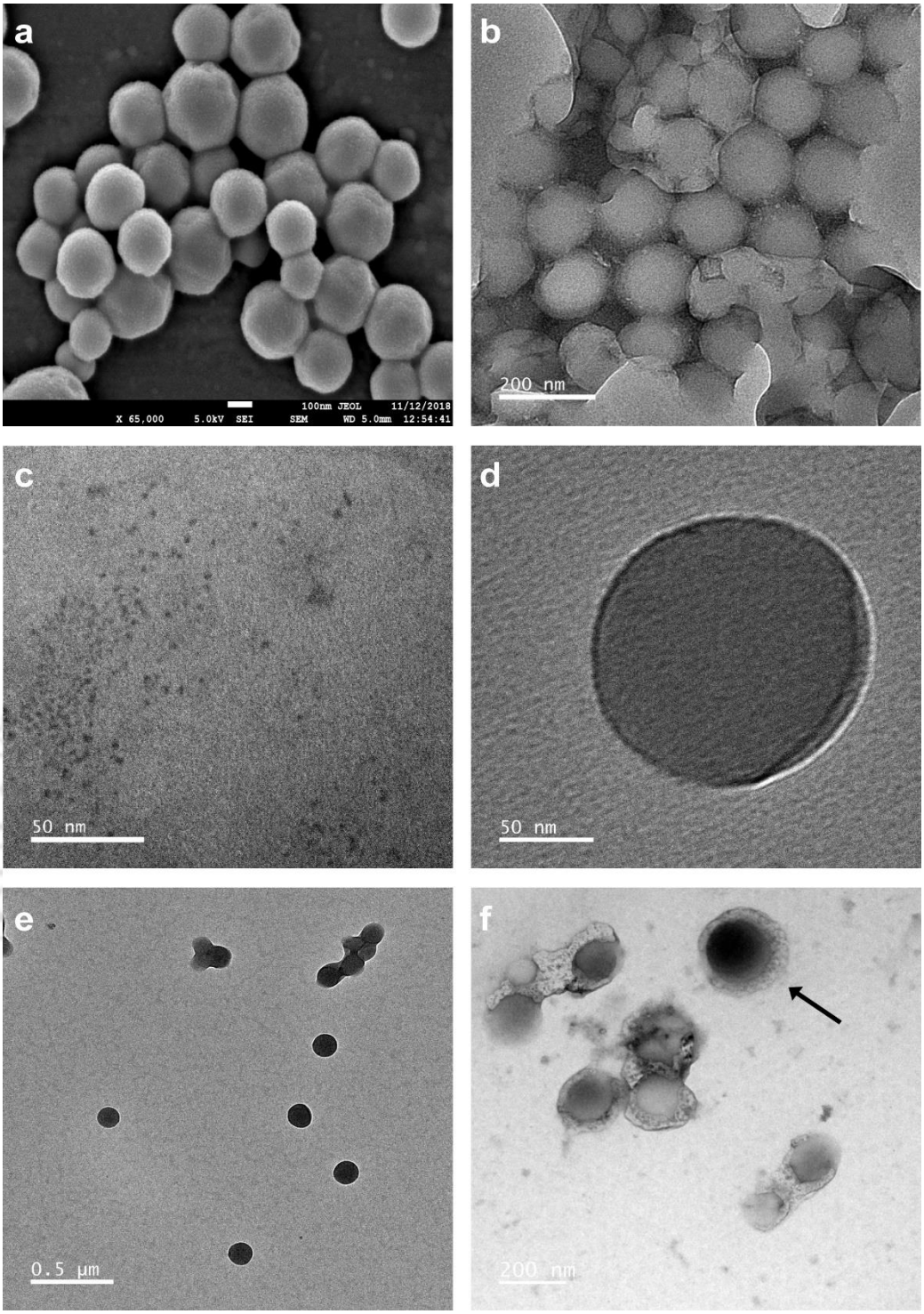

Figure. 3.3.1: (a) FESEM image of PLGA nanoparticles. (b) TEM image of PLGA nanoparticles. (c) TEM image of d-penicillamine Au–Cu nanoclusters. (d, e) TEM image of nanocomposites. (f) Distinct halos around the PLGA NPs denote coating of the d-penicillamine Au–Cu nanocluster and transferrin on the nanocomposites.

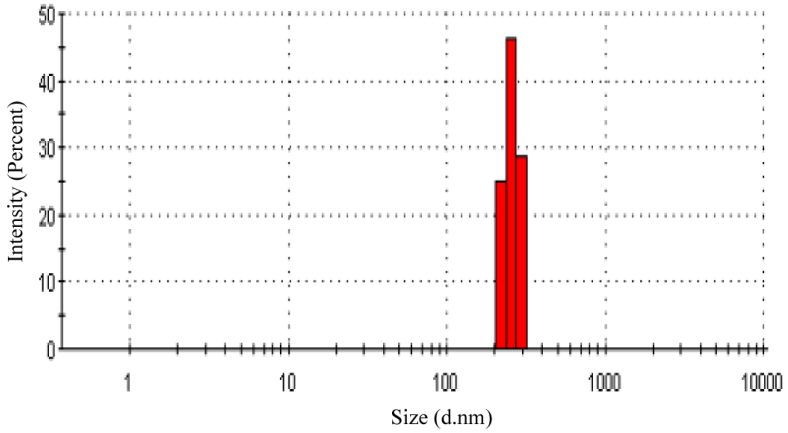

Figure. 3.3.2: Hydrodynamic diameter of PLGA nanoparticles.

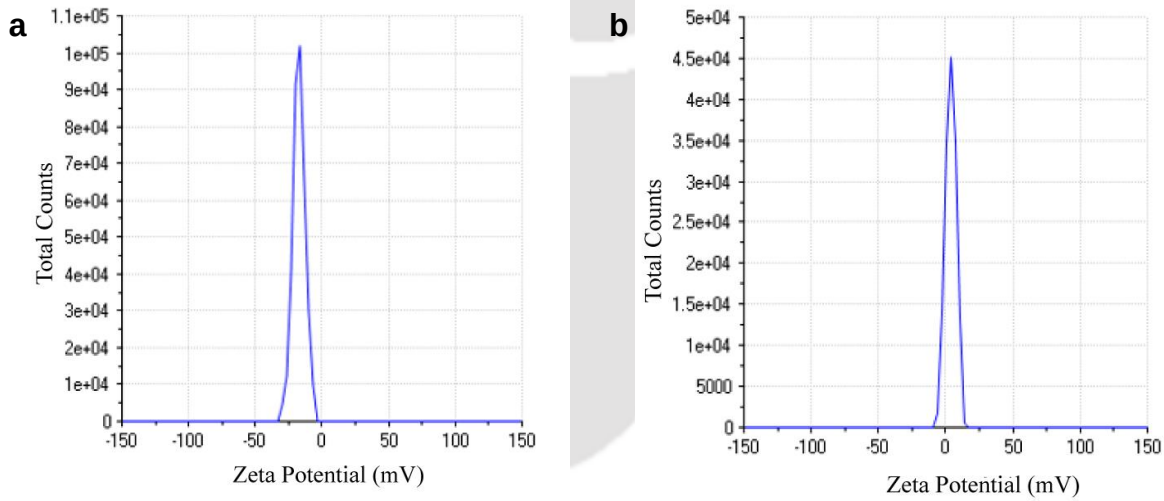

Figure. 3.3.3: Zeta potential of (a) PLGA nanoparticles and (b) d-penicillamine Au–Cu bimetallic nanocluster.

The d-penicillamine Au–Cu nanocluster was coated on the surface of the PLGA nanoparticle by electrostatic interaction between PLGA nanoparticles and d-penicillamine Au–Cu nanoclusters. It is well reported that receptor of transferrin protein is overexpressed in TNBC cells [174]. Thus, targeting of TNBC was achieved by decorating the PLGA nanoparticles d-penicillamine Au–Cu

nanoclusters with recombinant transferrin protein using electrostatic interaction. The average size of the nanocomposites determined by FETEM was estimated to be (162.15 ± 13 nm) (**Figure. 3.3.1 d,e**). From the TEM imaging, distinct halos around the inner PLGA nanoparticles were observed, signifying successful conjugation of the d-penicillamine Au–Cu nanocluster and transferrin on the nanocomposites (**Figure. 3.3.1 f**). DLS and zeta potential analysis reveals the nanocomposites having a hydrodynamic diameter of 260.2 nm (**Figure. 3.3.4**) and a positive charge of +1.37 mV (**Figure. 3.3.5**).

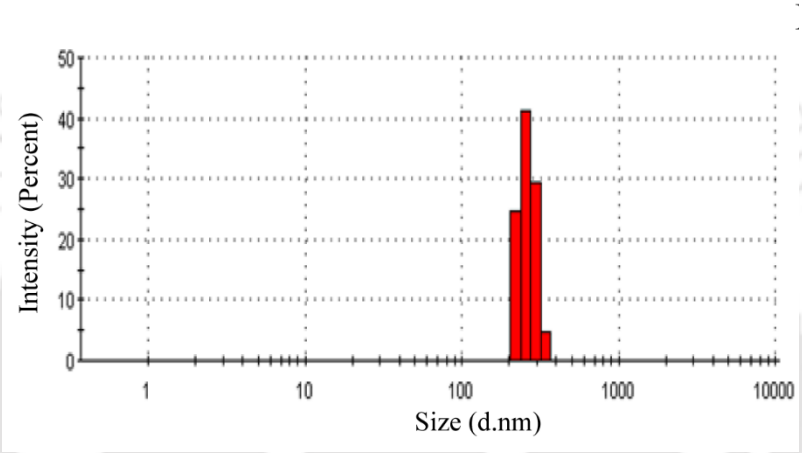

Figure. 3.3.4: Hydrodynamic diameter of the nanocomposites having an average hydrodynamic diameter of 260.2 nm.

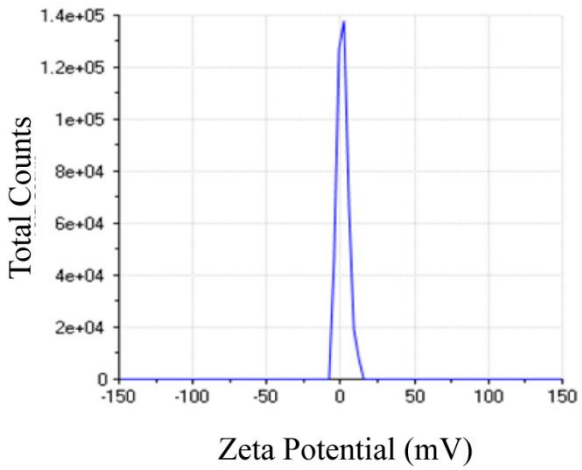

Figure. 3.3.5: Zeta potential of the nanocomposites indicating a positive charge of +1.37 mV.

The nanocomposites did not show any significant selected area electron diffraction (SAED) patterns (**Figure. 3.3.6**). The presence of Au and Cu atoms was confirmed by energy-dispersive X-ray (EDX) spectroscopy (**Figure. 3.3.7**). In addition, circular dichroism (CD) spectra analysis was done to test the transferrin functional integrity by assessing conformational modification after synthesis of nanocomposites. Following synthesis, slight conformation alteration of α -helix from 24.3 to 19.2% and β-sheet from 20.5 to 10.2%, respectively, was observed (**Figure. 3.3.8 a and b**). These suggested that the transferrin targeting performance could have remained unchanged after nanocomposites synthesis.

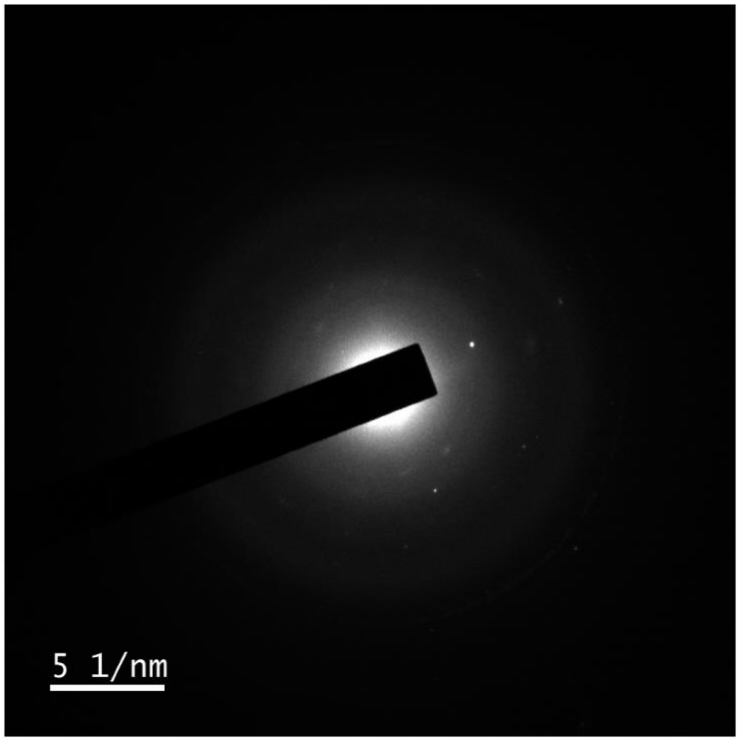

Figure. 3.3.6: Selected area (electron) diffraction (SAED) pattern of the nanocomposites.

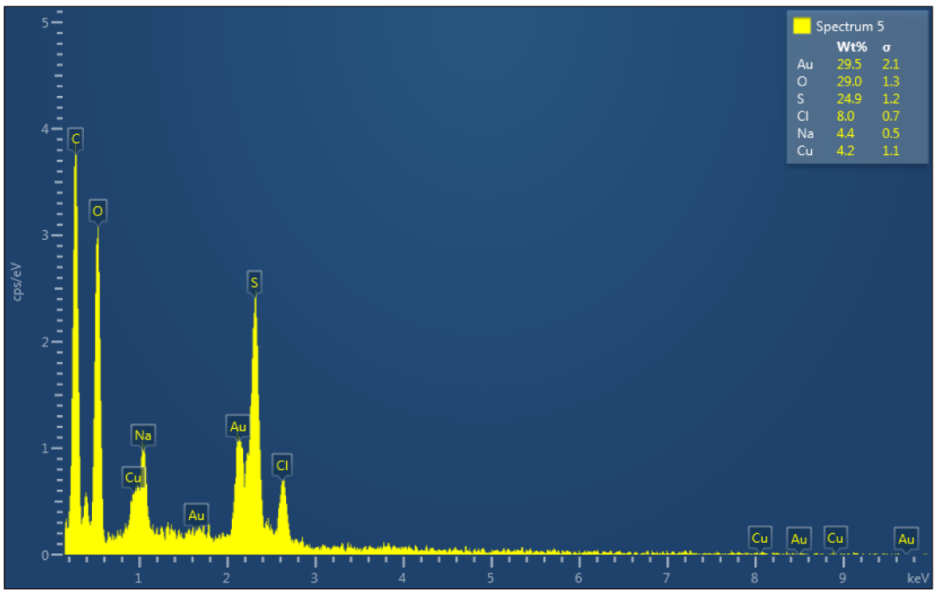

Figure. 3.3.7: Energy-dispersive X-ray (EDX) spectrum of the nanocomposites

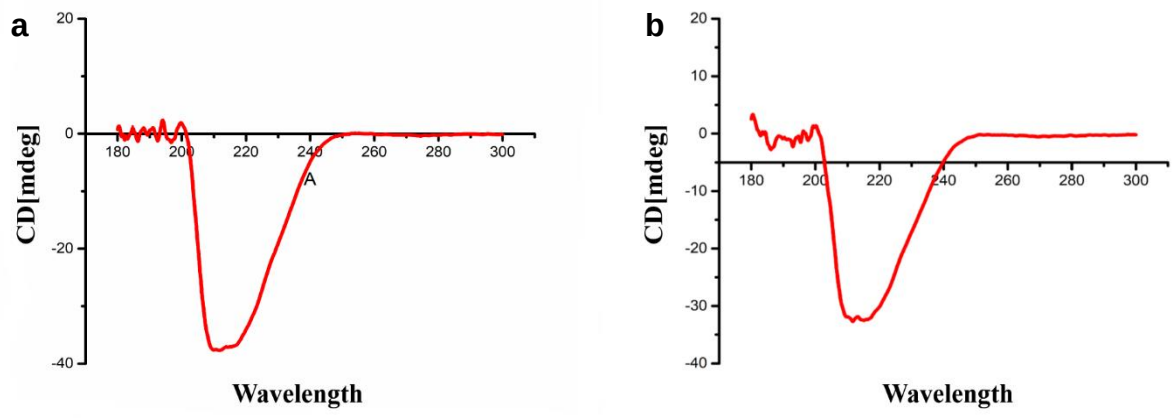

Figure. 3.3.8: Circular dichroism (CD) spectra of (a) free-transferrin and (b) transferrin loaded on nanocomposites.

The synthesized d-penicillamine Au–Cu bimetallic nanocluster exhibited a broad absorption profile (**Figure. 3.3.9**). The nanocluster and the nanocomposites exhibited a strong orange emission band at 630 nm (λex = 270 nm) (**Figure. 3.3.10**). Under UV trans-illumination, the nanocluster and nanocomposites exhibited strong orange emission (**Figure. 3.3.11 a and b**). The fluorescence quantum yield of the nanocluster and nanocomposites was quantified as 2.94% and 1.99% (using tyrosine QY 14% λex = 275 nm as a standard) (**Figure. 3.3.12 a and b**). From atomic absorption spectroscopy (AAS) the amount of Cu present in nanocomposites was determined to be 6.8 μg/mL (**Figure. 3.3.13**). Whereas the amount of d-penicillamine present in the nanocomposites was estimated to be 8.36 mM (**Figure. 3.3.14**). Coating of transferrin on nanocomposites was confirmed by SDS PAGE and FTIR spectroscopy. The presence of characteristic absorption peaks at ≈1600 cm–1 confirms the presence of protein on the nanocomposites (**Figure. 3.3.15**). Further, the distinct 80 kDa band in SDS PAGE indicates the presence of transferrin (**Figure. 3.3.16**). The amount of protein adsorbed on nanocomposites was found to be 22.21 μg/mL

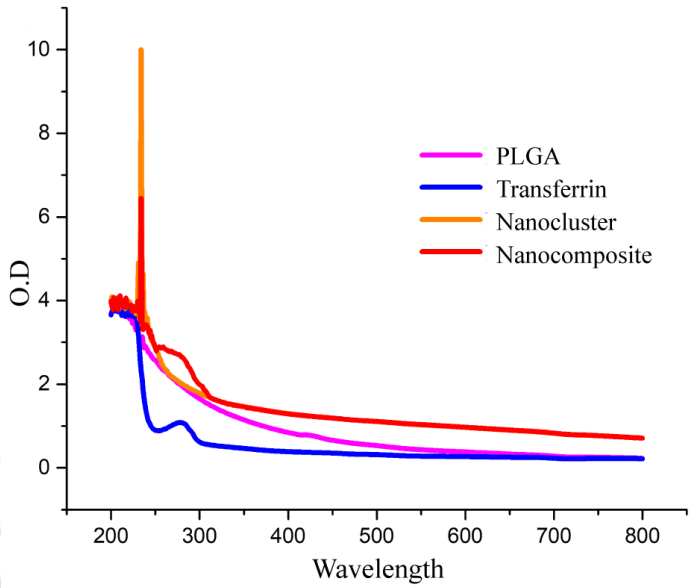

Figure. 3.3.9: UV–Vis spectra of PLGA nanoparticles, transferrin, nanoclusters, and nanocomposites.

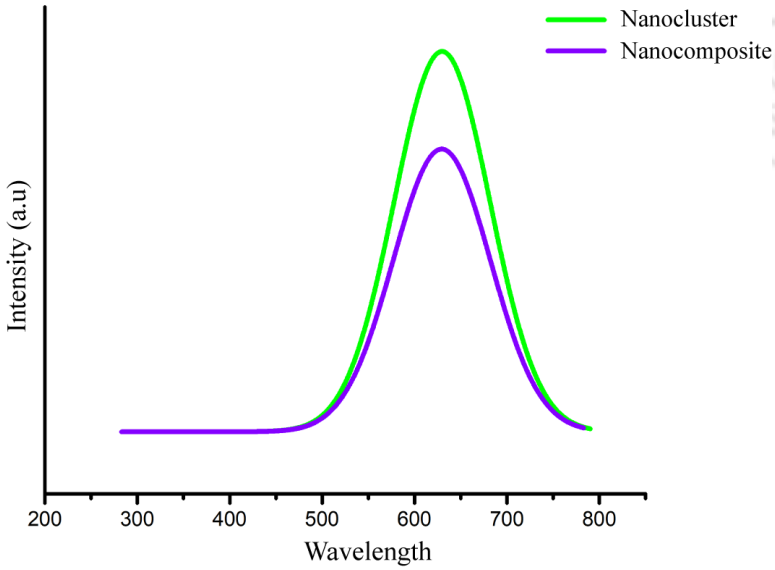

Figure. 3.3.10: Fluorescence emission spectra of the nanocluster and nanocomposites.

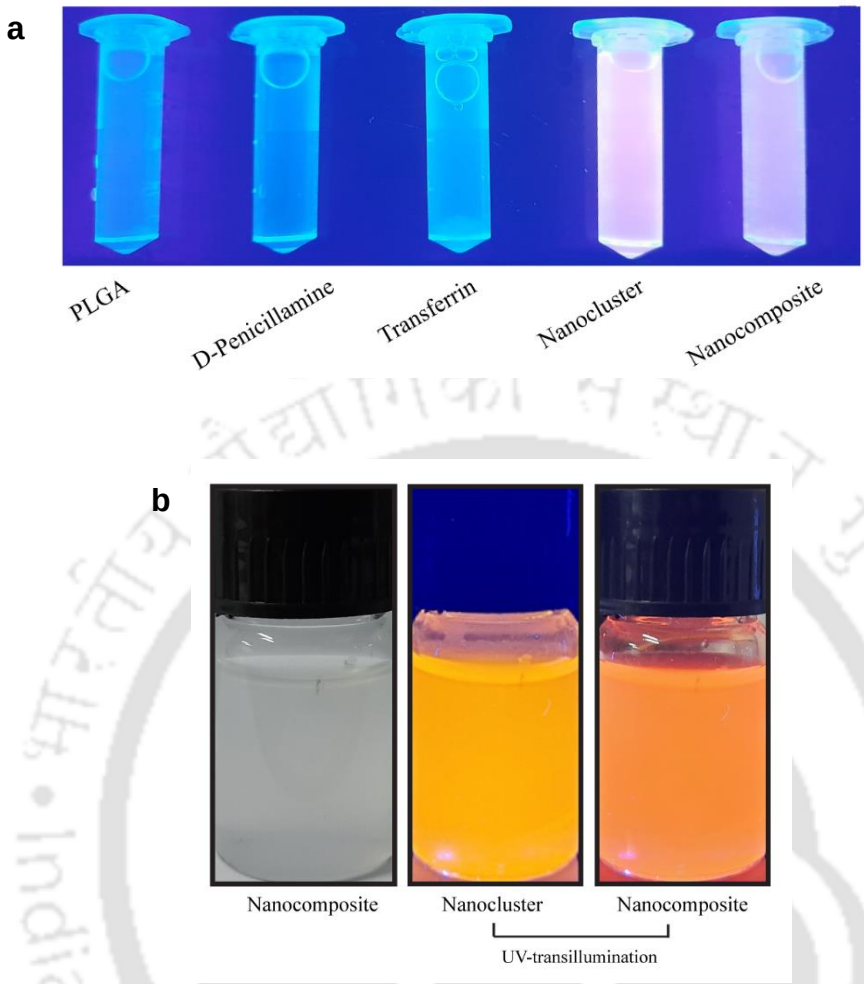

Figure. 3.3.11: Individual components of the nanoclusters and nanocomposites visualized under UV-transillumination.

Parameters	Values
QY_{ref}	14
I	1.28E+08
A	0.093029231
A_{ref}	0.093944
I_{ref}	6.16E+08
$QY_{calculated}$	2.944051

Parameters	Values
QY_{ref}	14
I	90319189.77
A	0.096944436
A_{ref}	0.093943536
I_{ref}	615786159.8
$QY_{calculated}$	1.9898583

Figure. 3.3.12: QY parameters of nanoclusters (a) and QY parameters of nanocomposites (b).

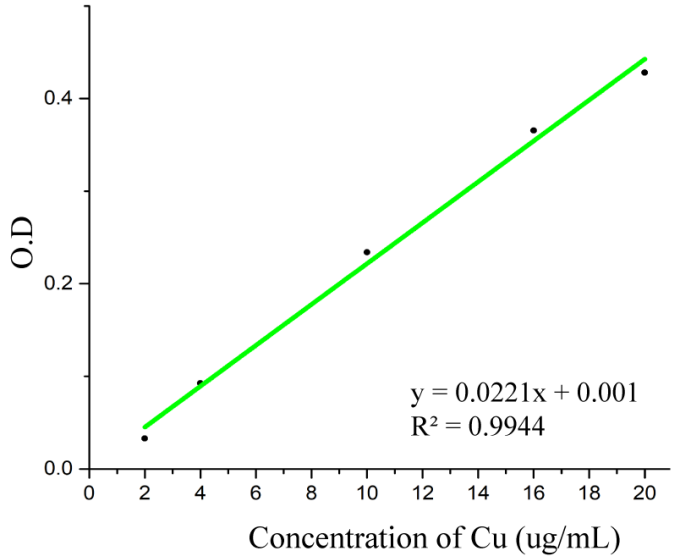

Figure. 3.3.13: Concentration of copper clusters based on the standard curve obtained from atomic absorption spectroscopy.

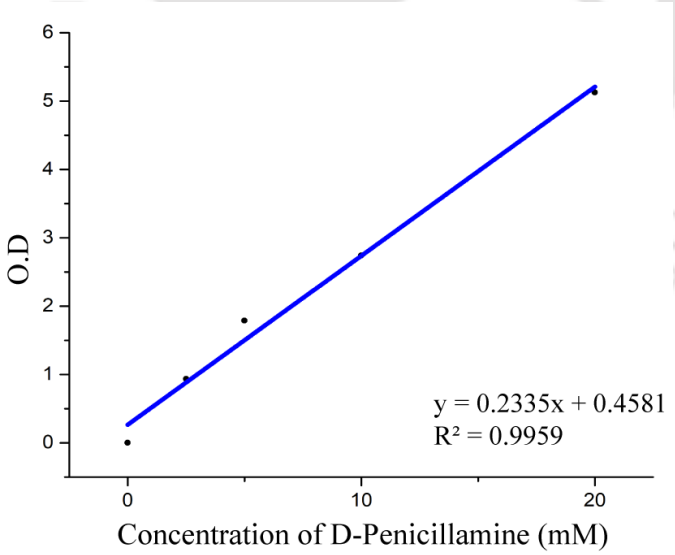

Figure. 3.3.14: Concentration of D-penicillamine based on the standard curve obtained from UV-Vis spectroscopy.

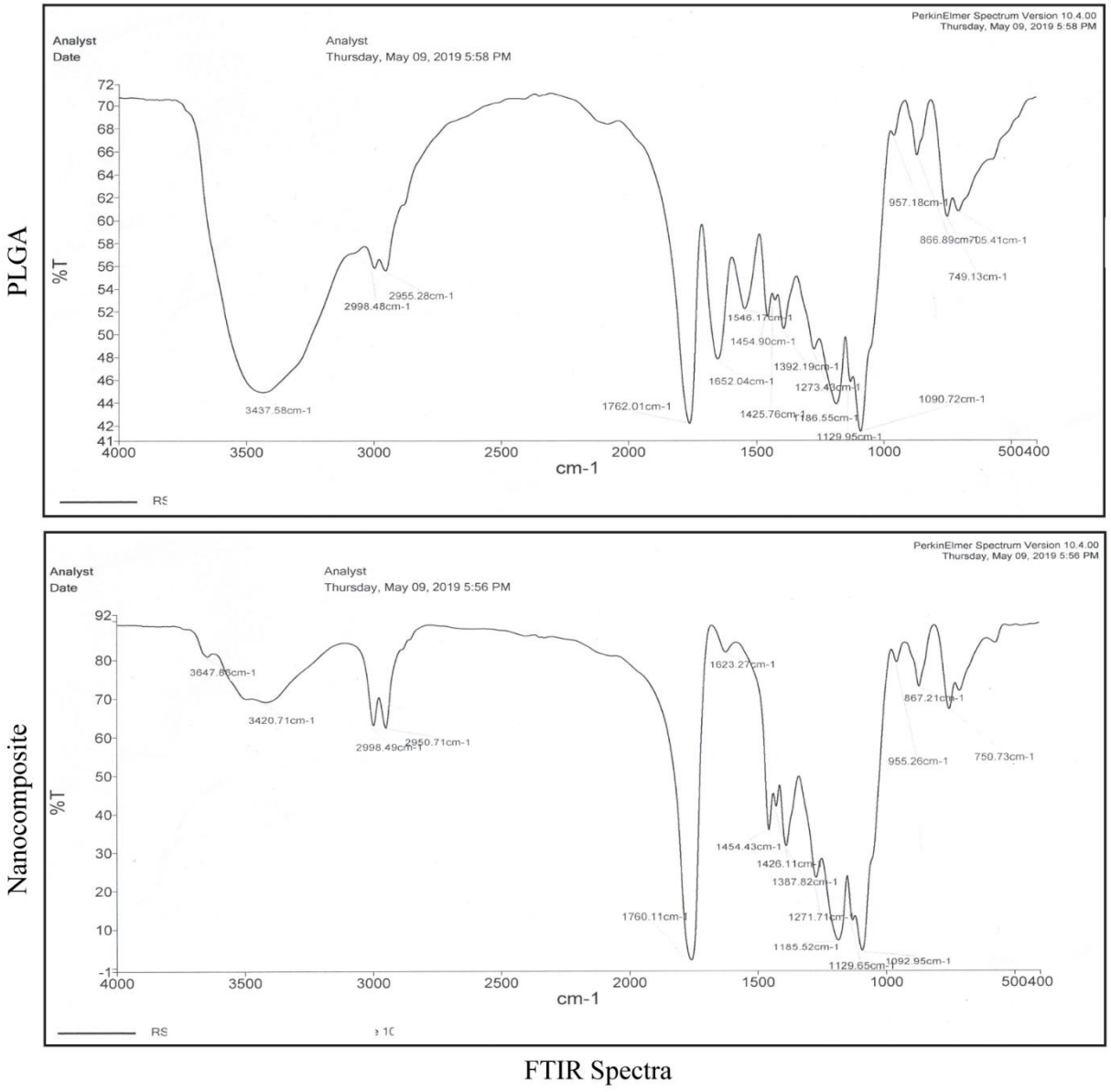

FTIR Spectra

Figure. 3.3.15: Fourier Transform Infrared **(**FTIR) spectra of PLGA nanoparticles and nanocomposites. Presence of characteristic absorption peaks at ≈1600 cm–1 confirms the presence of protein on the nanocomposites.

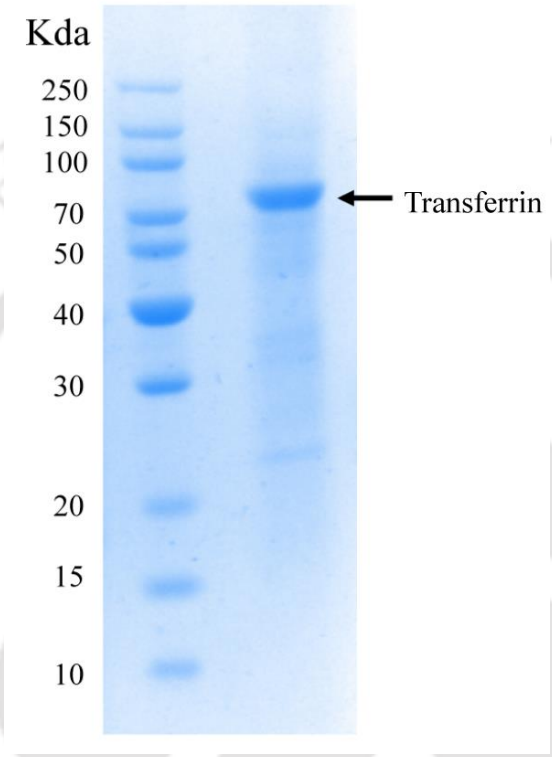

Figure. 3.3.16: SDS-PAGE gel image of nanocomposites. Distinct band at 80 kda corresponds to recombinant transferrin protein.

3.3.1.2. Photostability of the Nanocomposites: To achieve sufficient theranostic potential, photostability is critical for nanocarriers. Therefore, the photostability of the nanocarrier was assessed for 8 days period by recording the fluorescence intensity (**Figure. 3.3.17 a and b**). The nanocomposites exhibited a negligible difference in fluorescence intensity for a period of 8 days, confirming the benefits of the nanocomposites.

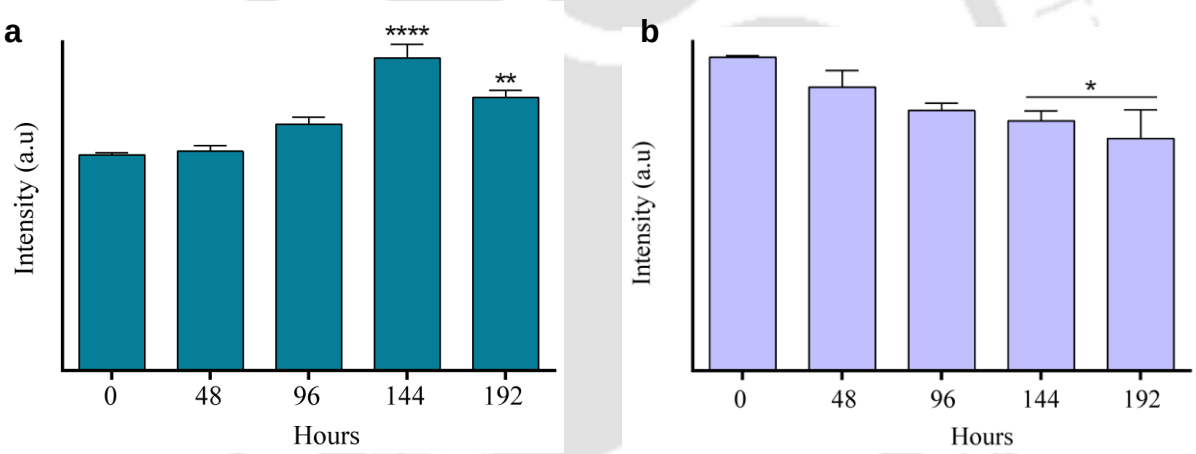

Figure. 3.3.17: Time dependent fluorescence intensity plot obtained from (a) nanoclusters and (b) nanocomposites.

3.3.1.3. Hemocompatibility of the Nanocomposites: The cause of RBC hemolysis is another indication of nanoparticle toxicity in the blood, which concerns the integrity of the RBC. The hemocompatibility of the nanocomposites was assessed by incubating the nanoparticles in isolated RBCs. RBCs incubated with 1% Triton-X 100 were considered positive control whereas, RBCs incubated with PBS were considered as the negative control. It is evident from (**Figure. 3.3.18 a and b**) that no hemolysis occurred after incubation of RBCs with nanocomposites, while significant lysis of RBCs occurred in positive control. These data impart the hemocompatibility of the nanocomposites.

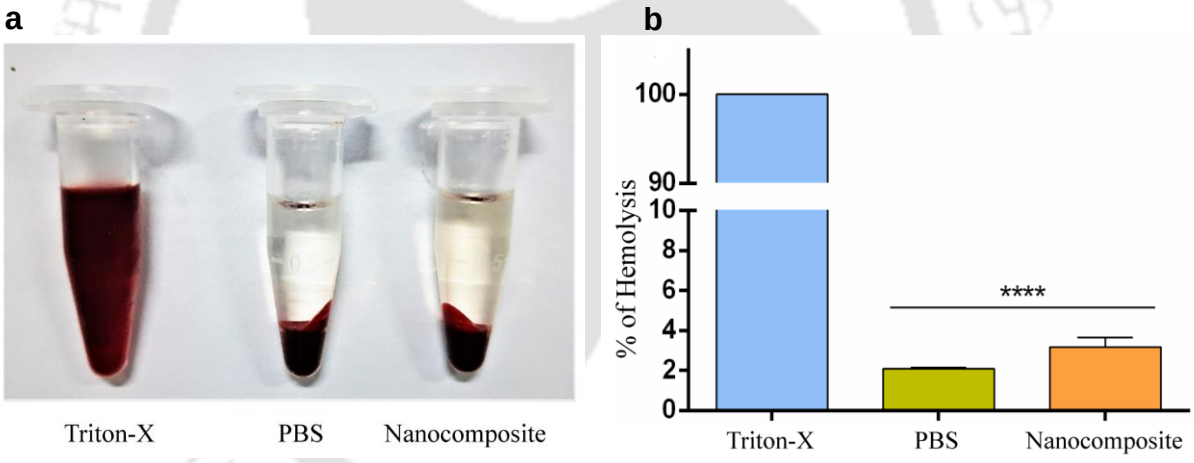

Figure. 3.3.18: (a) Hemolysis of the RBC in Triton-X, PBS, and nanocomposites. (b) Graphical representation of the percentage of hemolysis.

3.3.1.4. Cellular Uptake of the Nanocomposites: To ascertain the use of nanocomposites in bioimaging purpose, TNBC cells were visualized under the confocal microscope following treatment with nanocomposites for 2 h. The microscopic image showed the uptake of the nanocomposites into the TNBC cells as indicated by the orange luminescence arising due to Au–Cu nanoclusters (**Figure. 3.3.19 and Figure. 3.3.20**). Similar orange luminescence was also observed for MCF-7 cells confirming successful uptake (**Figure. 3.3.21**).

The uptake of the nanocomposites inside the TNBC cells was further confirmed by flow cytometry. Cells were incubated with nanocomposites for different time periods, and shift in fluorescence peak was examined using a flow cytometer. The sharp shift in fluorescence peak in FL-2 channel was observed in treated cells with respect to untreated cells, confirming the uptake of the nanocomposites (**Figure. 3.3.22**).

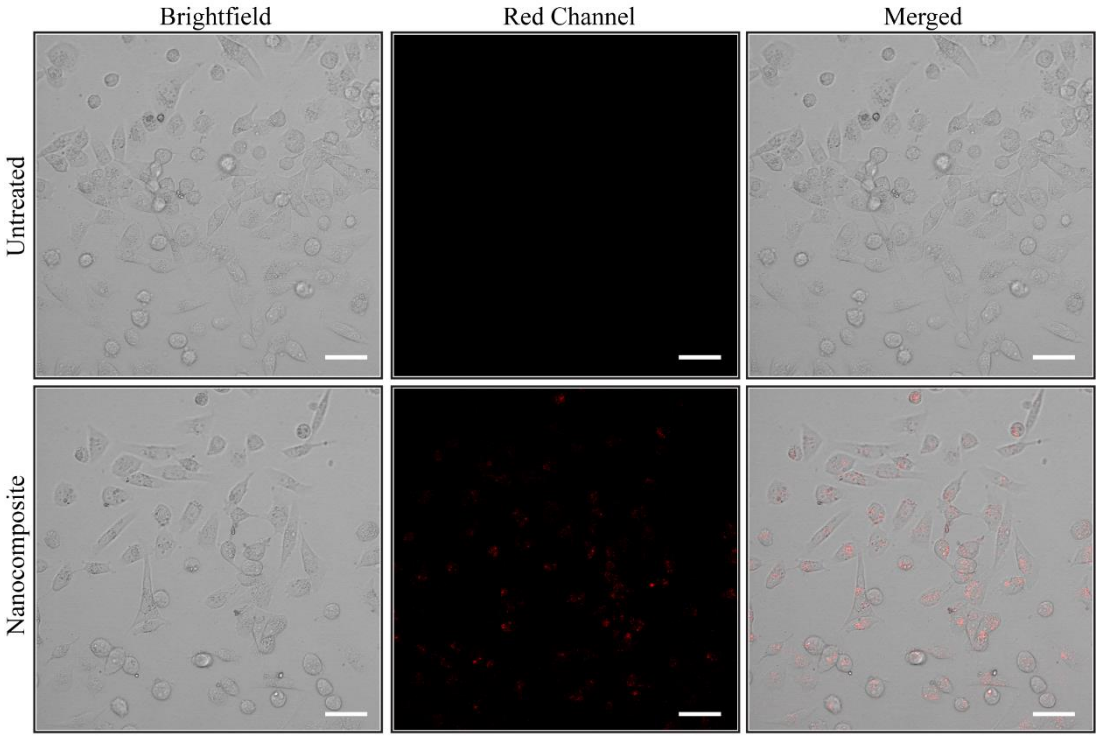

Figure. 3.3.19: Confocal microscope image of the uptake of nanocomposites in MDA-MB-231 cells. Scale bar represents 50 μm.

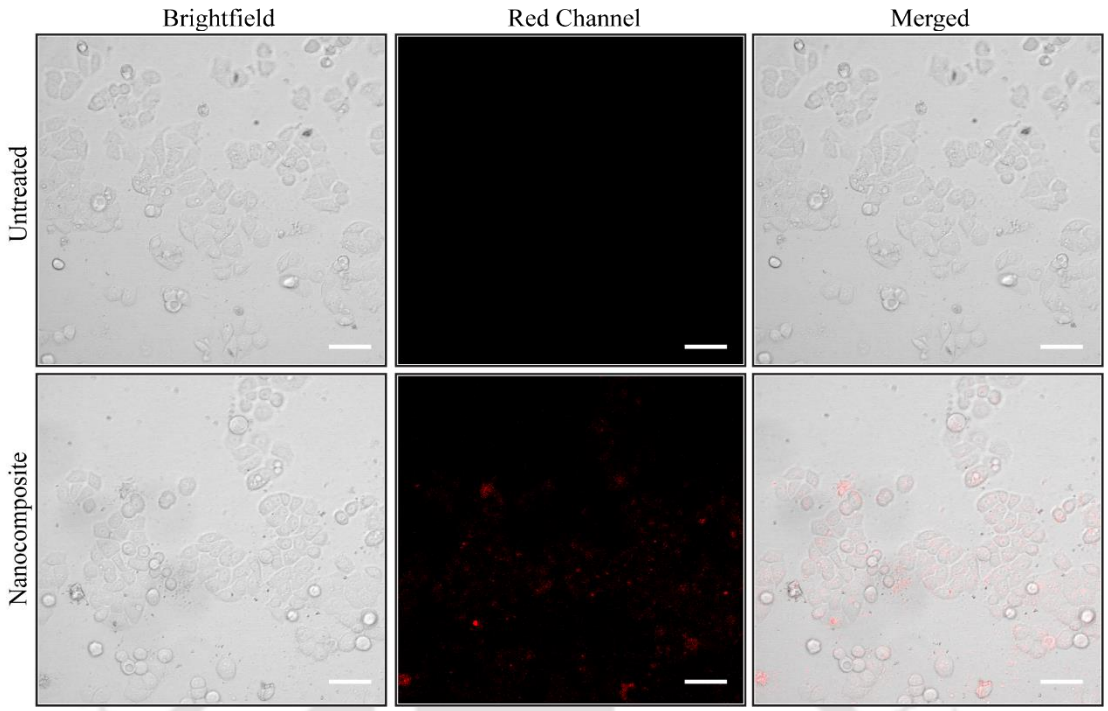

Figure. 3.3.20: Confocal microscope image of the uptake of nanocomposites in MDA-MB-468 cells. Scale bar represents 50 μm.

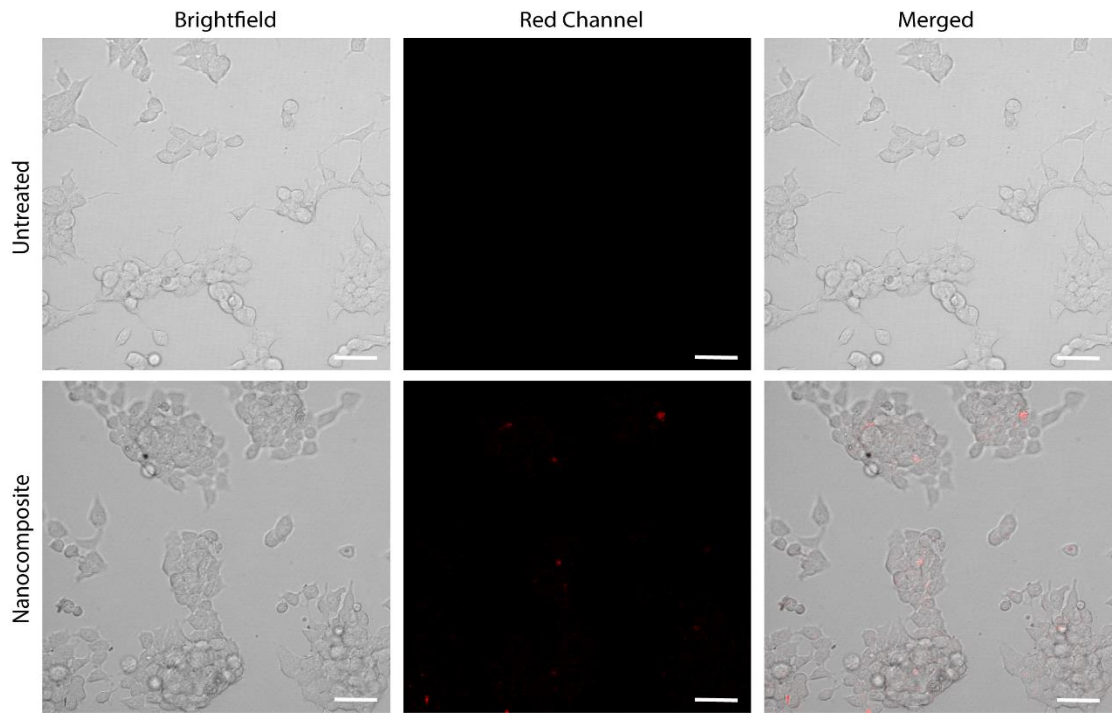

Figure. 3.3.21: Confocal microscope image of the uptake of nanocomposites in MCF-7 cells. Scale bar represents 50 μm

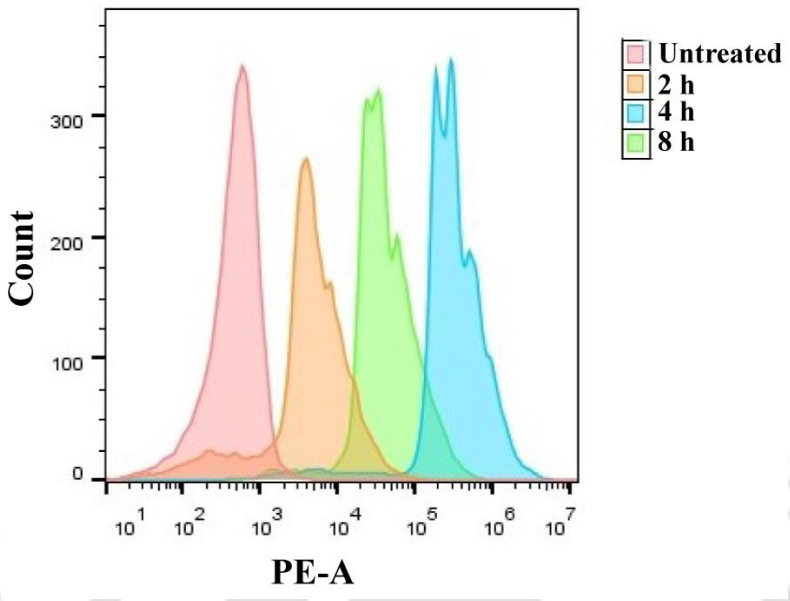

Figure. 3.3.22: Time-dependent uptake of nanocomposites in MDA-MB-231 cells as analyzed by flow cytometry

It has been reported that transferrin receptor is overexpressed in TNBC cells with respect to normal cells, and the same has been confirmed by semiquantitative RT-PCR (**Figure. 3.3.23**) [175]. Transferrin receptor inhibitor Chlorazole Black E was used to confirm receptor-mediated active endocytosis. The MDA-MB-468 cells showed less uptake of nanocomposites in the presence of Chlorazole Black E rather than only nanocomposites (**Figure. 3.3.24**). Apparently, without inhibitor the uptake of nanocomposites was more facile.

Collectively, these data indicate the potential of the nanocomposites to be used for imaging of the cancer cells for theranostic purposes.

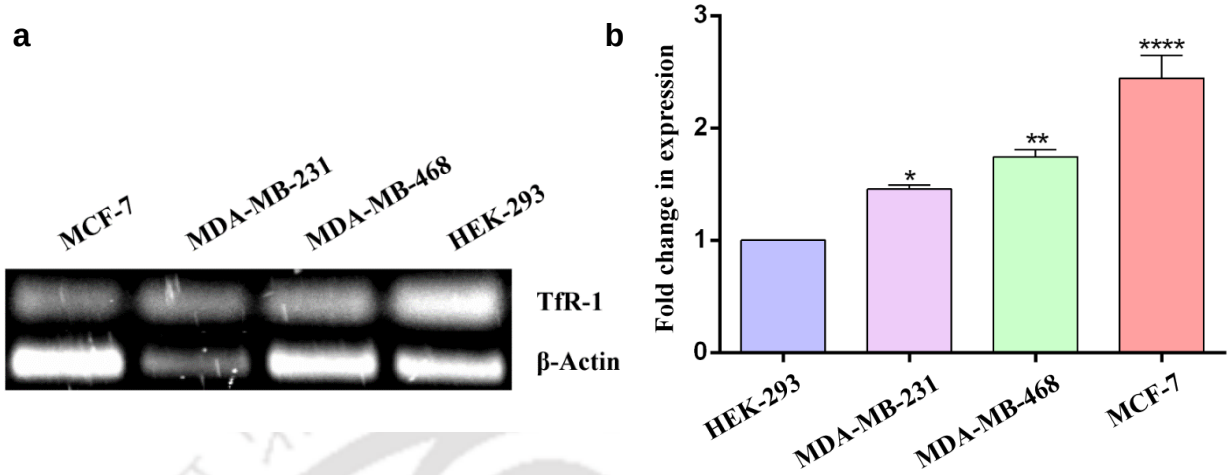

Figure. 3.3.23: (a) Semi-quantitative PCR of transferrin receptor-1 (TfR-1) (upper panel) in different cell lines and β-actin (lower panel). (b) Graphical representation of expression of TfR-1 in different cell lines.

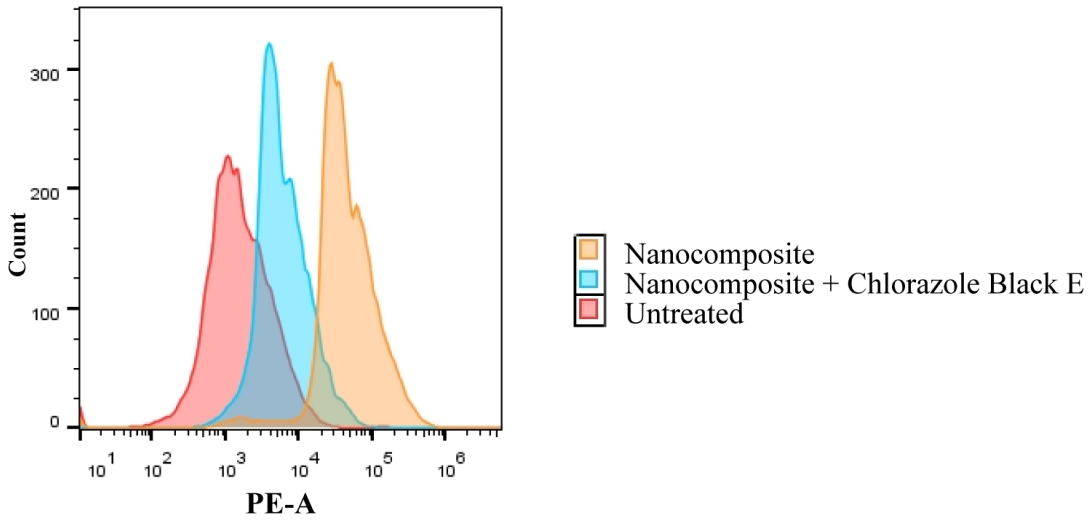

Figure. 3.3.24: Histogram representing the reduced uptake of nanocomposite in presence of transferrin receptor inhibitor Chlorazole Black E.

3.3.1.5. Nanocomposites Incite Cellular ROS Generation, Mitochondrial Membrane Potential Depolarization and Apoptosis in TNBC: Earlier, Gupte et al. has reported that in the presence of copper, d-penicillamine is oxidized, and subsequently, hydrogen peroxide is generated [176]. Following synthesis, the amount of hydrogen peroxide generated per mL of nanocomposites was investigated and found to be 16 μM (**Figure. 3.3.25**). Gupte et al. have also reported that d-penicillamine in the presence of cupric sulfate generates ROS in breast cancer cells [76]. To ascertain the cell death mechanism by nanocomposites, following treatment, the generation of cellular ROS was evaluated. It can be observed that with respect to untreated cells, treatment with nanocomposites generated 8.34-fold and 4-fold increase in ROS in MDA-MB-231 and MDA-MB-468 (**Figure. 3.3.26**). The increase in cellular ROS jeopardizes membrane integrity of mitochondria and eliminates redox potential [177]. JC-1 stain analysis was carried out in order to determine the effect of ROS accumulation on mitochondria. In polarized mitochondria, the cyanine dye JC-1 forms red aggregates, while it persists as a monomer in depolarized mitochondria. From the healthy mitochondria of the untreated cells, prominent red fluorescence was detected. Whereas nanocomposites treated MDA-MB-231 and MDA-MB-468 exhibited 15.7 and 21.4% increase in green fluorescence, signaling mitochondrial membrane depolarization (**Figure. 3.3.27 and Figure. 3.3.28**).

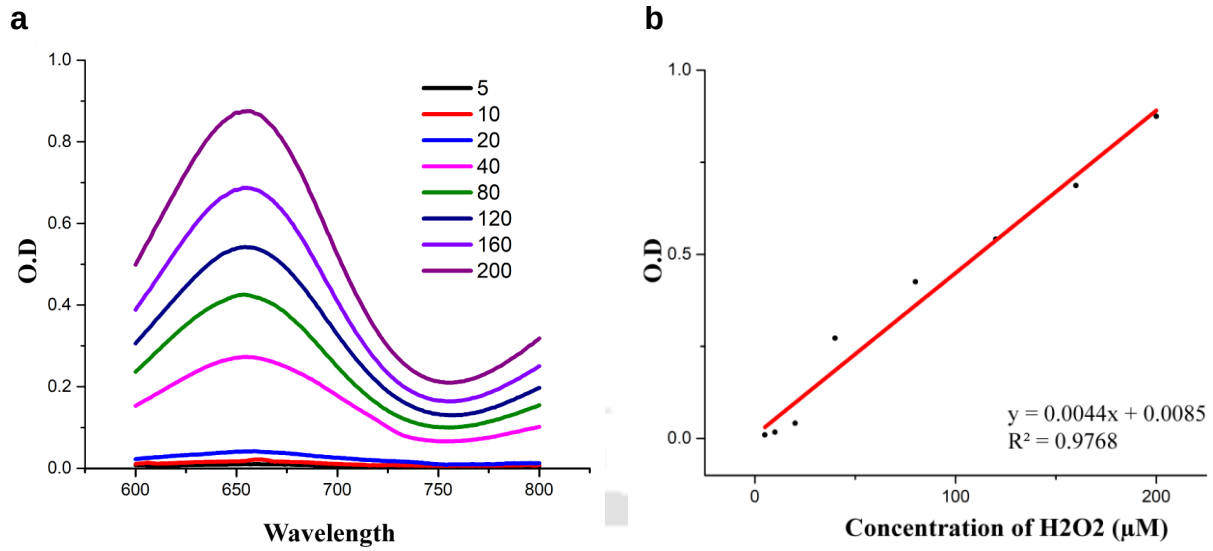

Figure. 3.3.25: (a), (b) Concentration of H_2O_2 based on the standard curve obtained from UV-Vis spectroscopy.

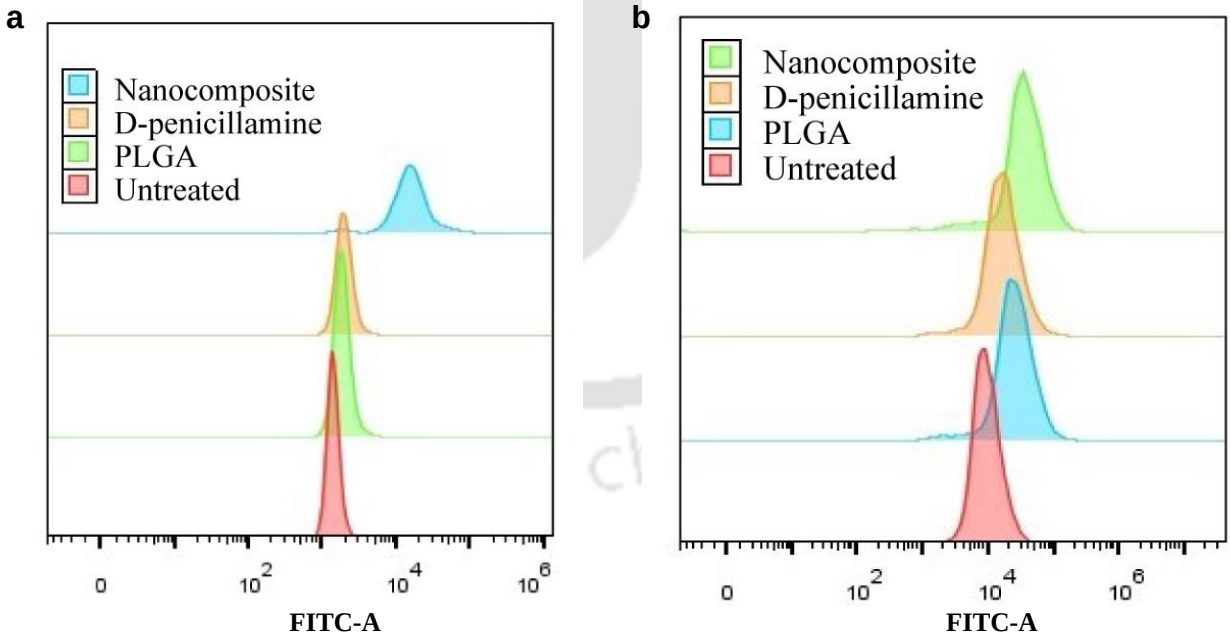

Figure. 3.3.26: Flow cytometric detection of cellular ROS in (a) MDA-MB-231 and (b) MDA-MB-468.

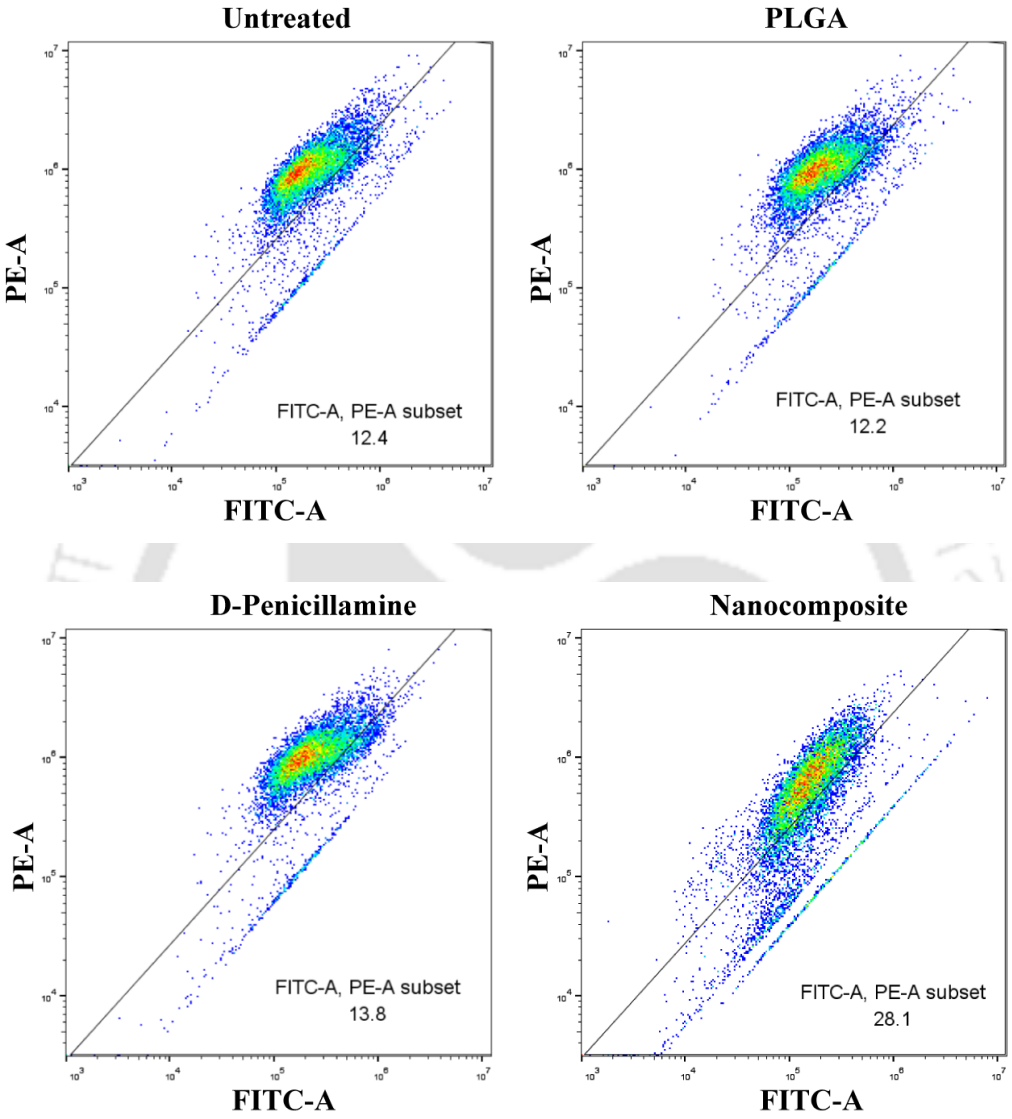

Figure. 3.3.27: Mitochondrial membrane potential detection of MDA-MB-231 by JC-1 staining.

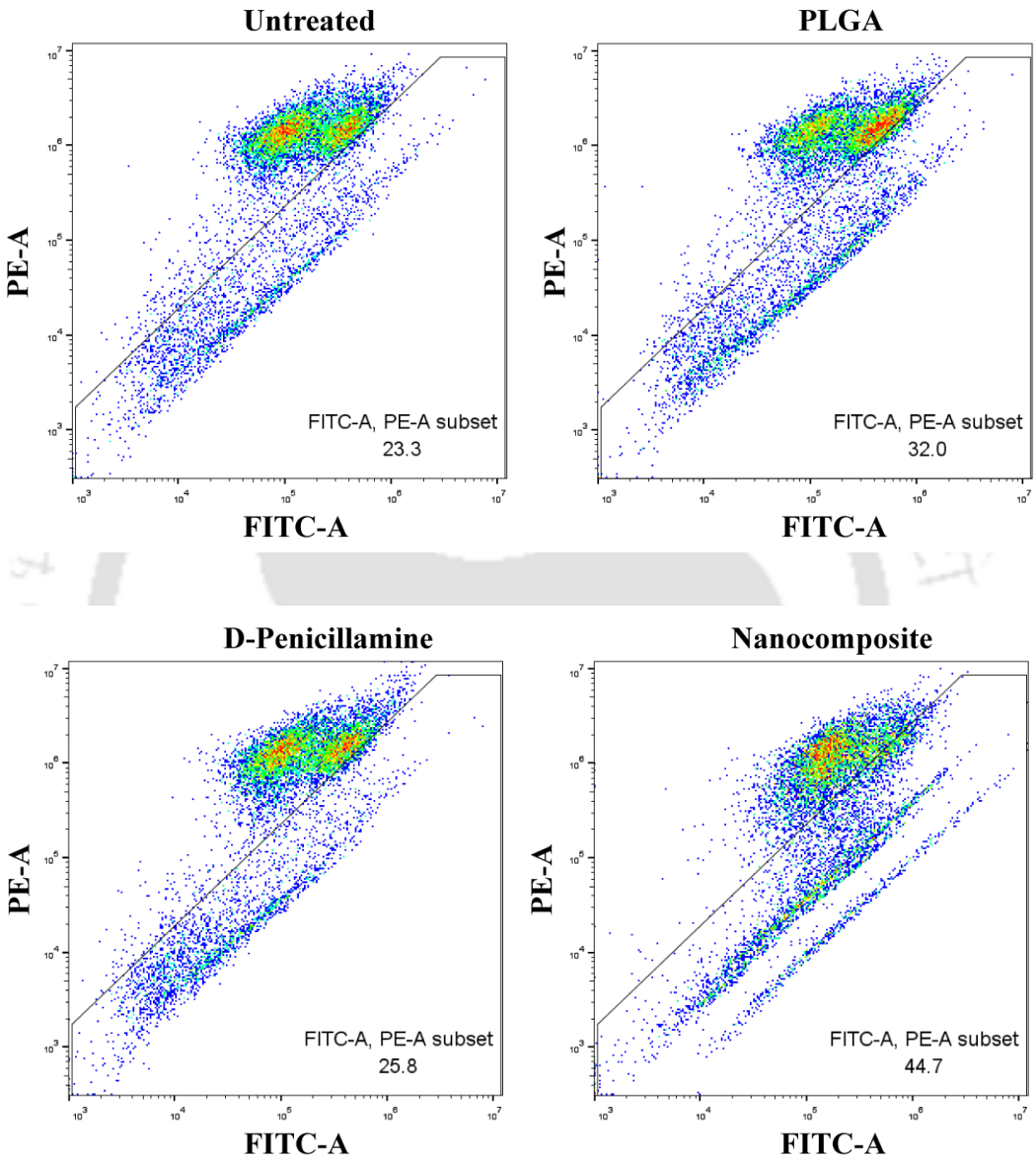

Figure. 3.3.28: Mitochondrial membrane potential detection of MDA-MB-468 by JC-1 staining.

Depolarization of mitochondrial membrane potential has been shown to be an early event in apoptosis [178]. Following the trail of ROS generation and redox imbalance, the percentage of the apoptotic cell population was examined after treatment with nanocomposites. From the flow cytometry, it was observed that treatment with nanocomposites incurred to 41.35 and 31.88% increase in apoptotic cell population in MDA-MB-231 (**Figure. 3.3.29**) and MDA-MB-468 (**Figure. 3.3.30**). Further, the effect of nanocomposites on MCF-7 cells was evaluated. Similar to TNBC, nanocomposites induced ROS generation, mitochondrial membrane depolarization, and apoptosis in MCF-7 cells (**Figure. 3.3.31, Figure. 3.3.32** and **Figure. 3.3.33**). Altogether, these data indicate the mechanism of cell death imparted by nanocomposites on TNBC cells.

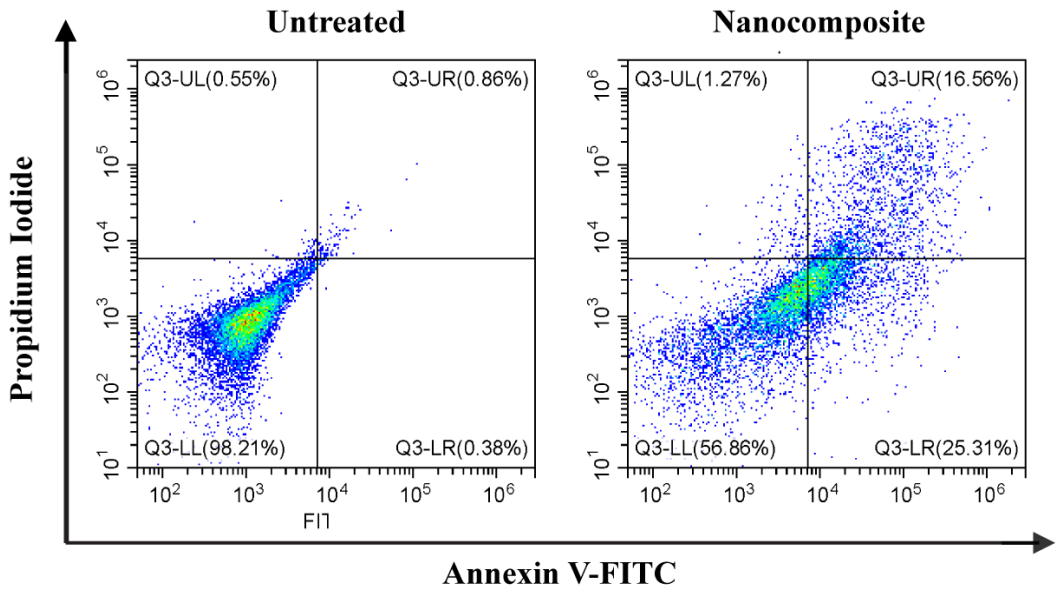

Figure. 3.3.29: Apoptotic cell populations detected by annexin-V-FITC PI flow cytometric assay following treatment with nanocomposites in MDA-MB-231.

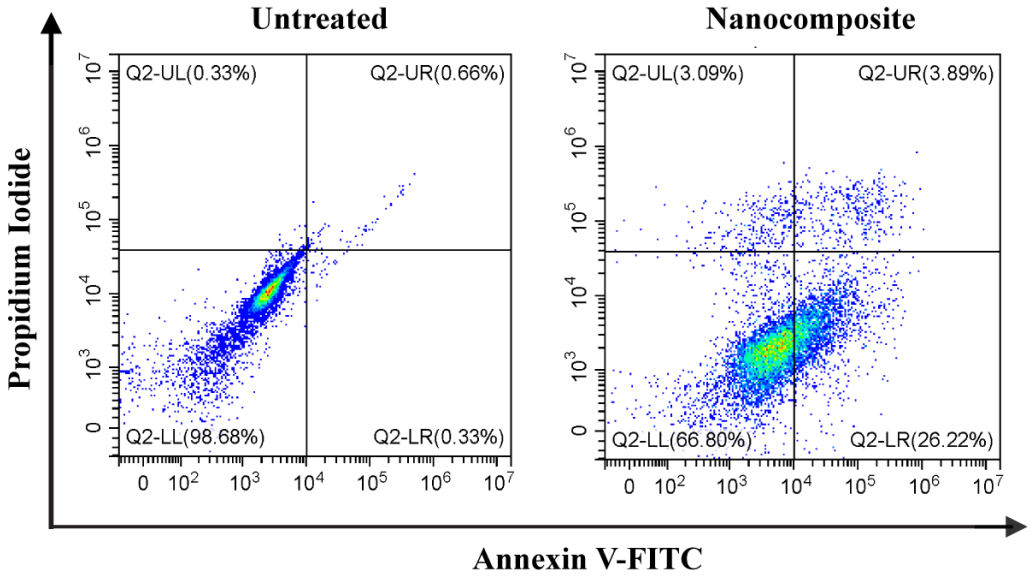

Figure. 3.3.30: Apoptotic cell populations detected by annexin-V-FITC PI flow cytometric assay following treatment with nanocomposites in MDA-MB-468.

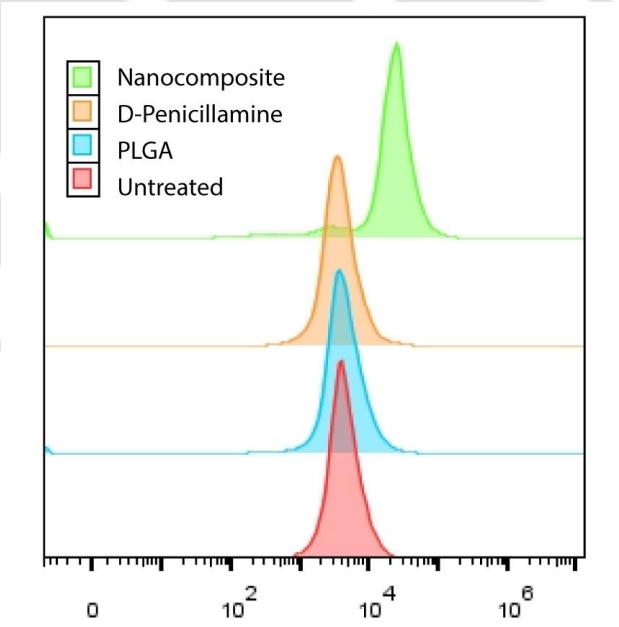

Figure. 3.3.31: Flow cytometric detection of cellular ROS in MCF-7 cells.

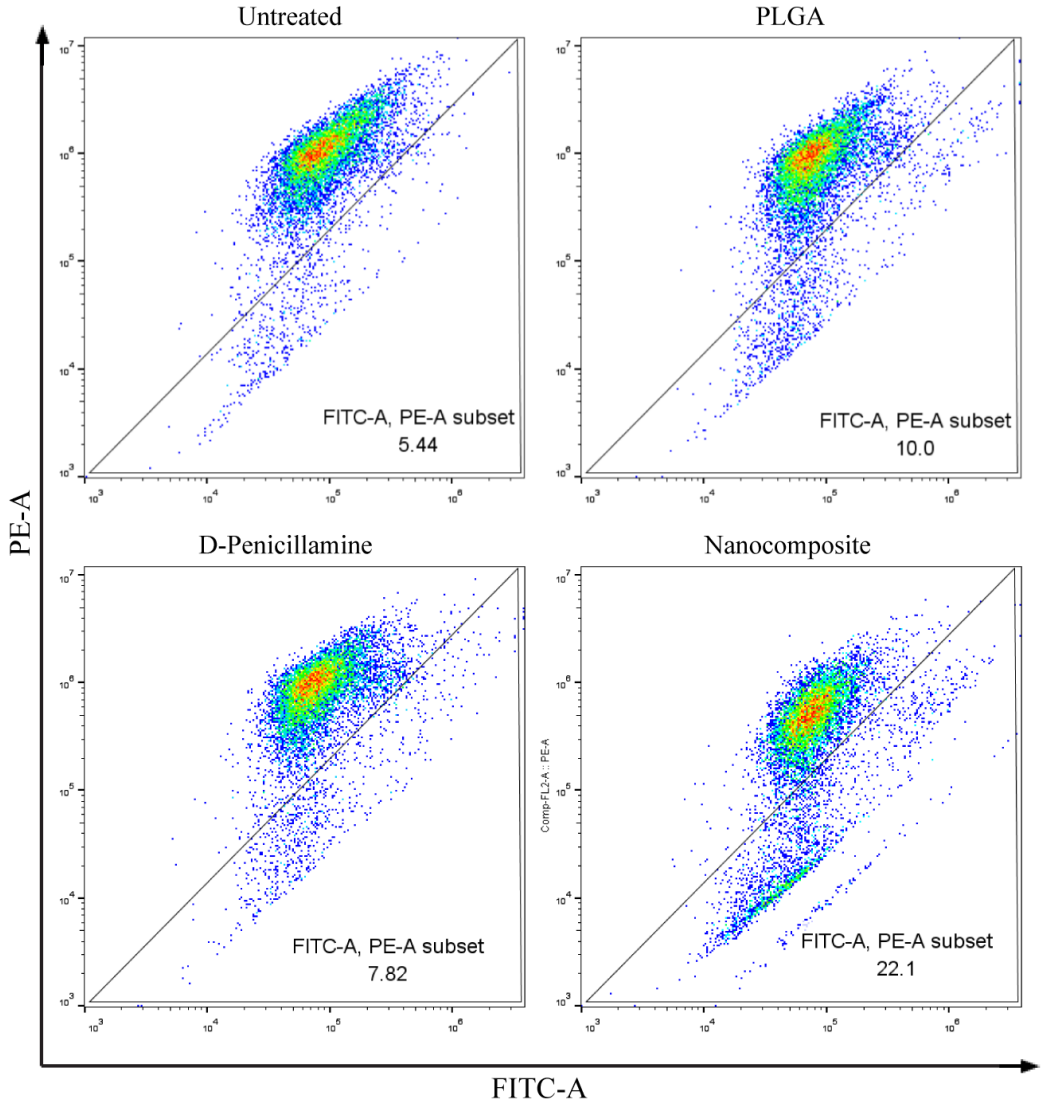

Figure. 3.3.32: Mitochondrial membrane potential detection of MCF-7 by JC-1 staining.

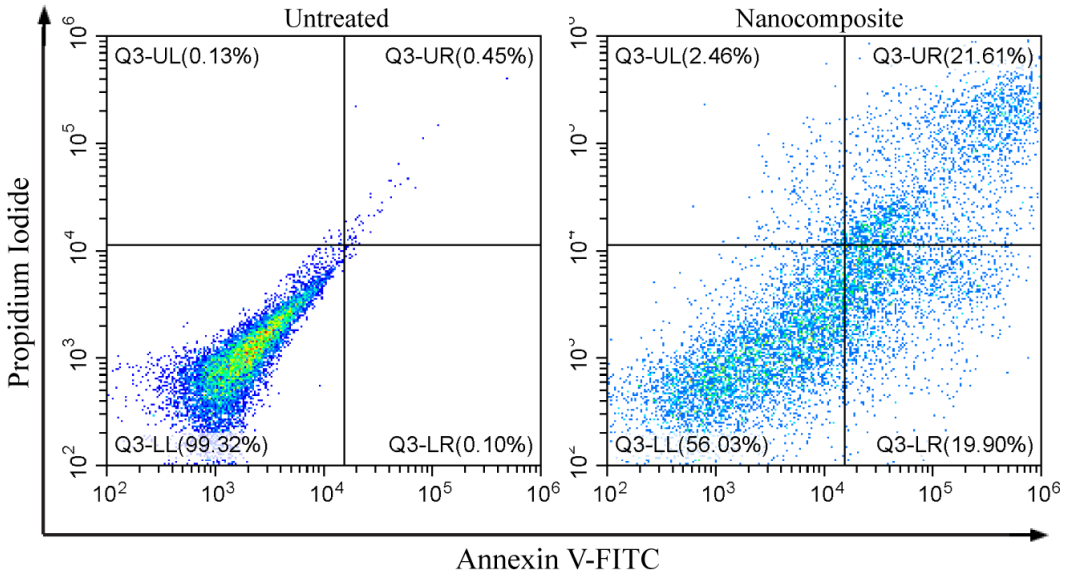

Figure. 3.3.33: Apoptotic cell populations detected by annexin-V-FITC PI flow cytometric assay following treatment with nanocomposites in MCF-7.

3.3.1.6. Nanocomposites Show Significant Anti-Cell Proliferative Activity in TNBC: After successfully evaluating the safety and stability of the nanocomposites, the anti-cell proliferative activity was determined using alamarBlue assay. TNBC cells were treated with nanocomposites with a concentration gradient. Monolayer culture and spheroids were incubated for 48 and 72 h, respectively. Results from alamarBlue assay exhibited dose-dependent reduction of cell viability in both MDA-MB-231 (**Figure. 3.3.34 a**) and MDA-MB-468 (**Figure. 3.3.34 b**) with an increase in the concentration of nanocomposites. It is quite observable that the amount of nanocomposites required to bring the IC_{50} in case of spheroids is much higher than monolayer culture (**Figure. 3.3.35 a and b**). At the same time, cells treated with PLGA and d-penicillamine did not show any signs of cytotoxicity (**Figure. 3.3.36 a and b**). However, d-penicillamine Au–Cu nanocluster was found to be more potent in reducing cell viability than nanocomposites (**Figure. 3.3.37 a and b**).

To discern the therapeutic potential of the nanocomposites on other cancer cells, luminal breast cancer cells MCF-7 and cervical cancer cells HeLa were also treated with nanocomposites, and cell viability was assessed. Dose-dependent reduction of viability of MCF-7 and HeLa re-establishes the nanocomposite's therapeutic potency (**Figure. 3.3.38** and **Figure. 3.3.39**). Cell viability of human embryonic kidney cell line HEK-293 was also assessed (**Figure. 3.3.40**). The obtained IC_{50} values of nanocomposites on different cell lines are listed in **Table. 3.3.1**. Live–dead cell imaging of the monolayer culture depicted the nanocomposite's anti-cell proliferative effect (**Figure. 3.3.40 to Figure. 3.3.43**). Likewise, the visualization of spheroids after treatment highlights the impact of these inhibitors (**Figure. 3.3.44 to Figure. 3.3.47**). Taken together, these data indicate the noteworthy potential of nanocomposites in cancer therapy.

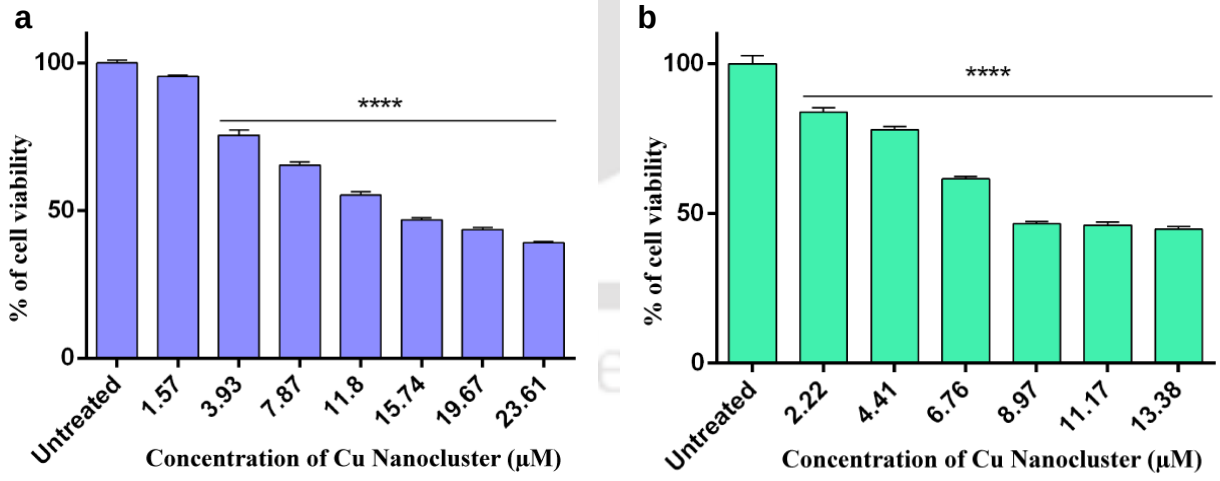

Figure. 3.3.34: Graphical representation of dose-dependent decrease in cell viability. (a) MDA-MB-231 and (b) MDA-MB-468 monolayer cultures treated for 48 h with nanocomposites. Results are presented as mean ± SEM.

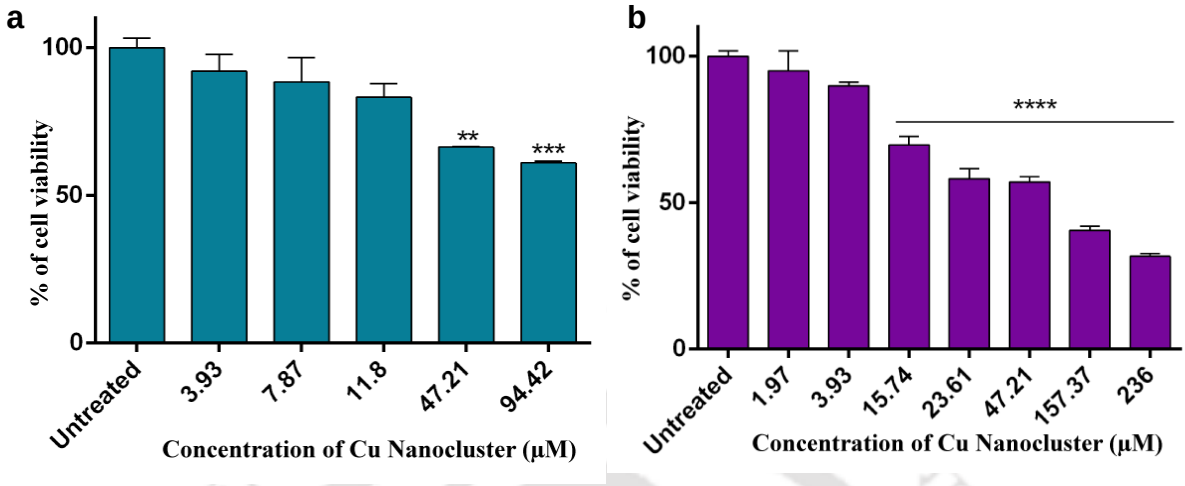

Figure. 3.3.35: Graphical representation of dose-dependent decrease in cell viability. (a) MDA-MB-231 and (b) MDA-MB-468 spheroids treated for 72 h with nanocomposites. Results are presented as mean ± SEM.

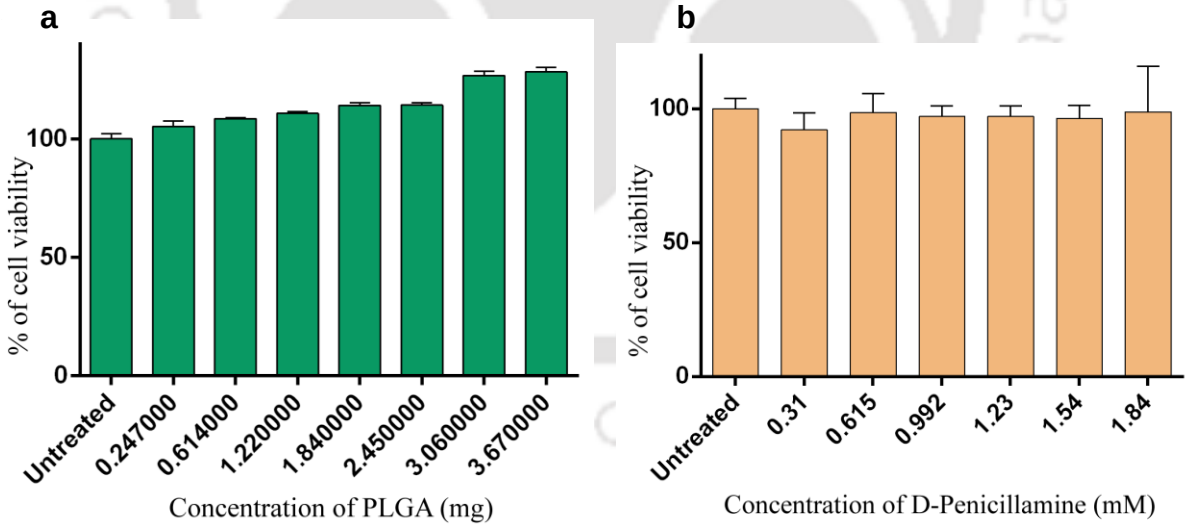

Figure. 3.3.36: Determination of viability of MDA-MB-468 monolayer culture by alamarBlue assay upon treatment with (a) PLGA nanoparticles, (b) d-penicillamine for 48 h. Results expressed as the mean ± SEM.

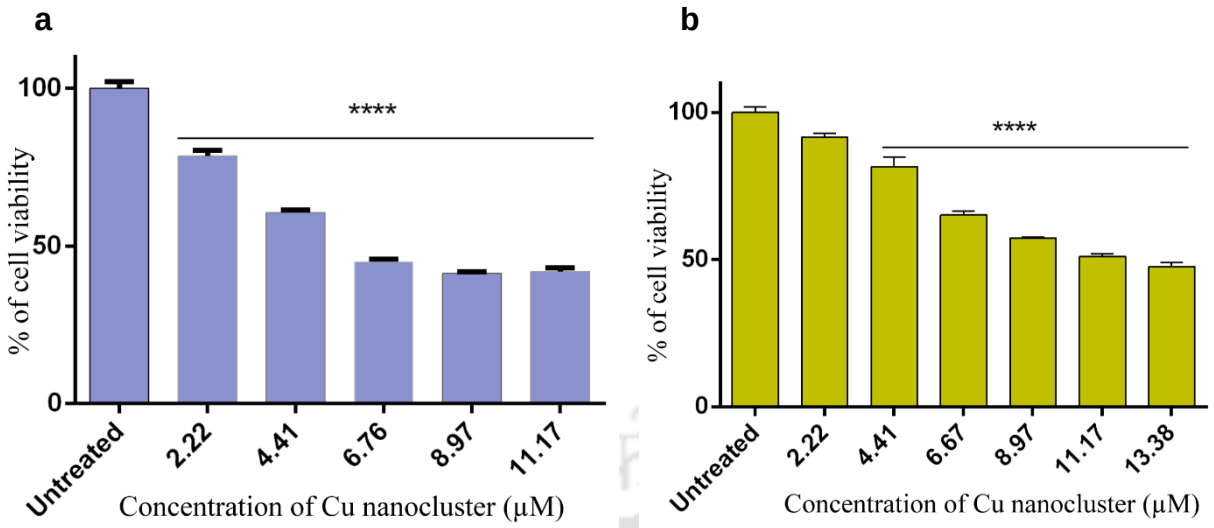

Figure. 3.3.37: Determination of viability of MDA-MB-468 monolayer culture by alamarBlue assay upon treatment with (a) nanoclusters and (b) nanocomposites for 48 h. Results expressed as the mean ± SEM.

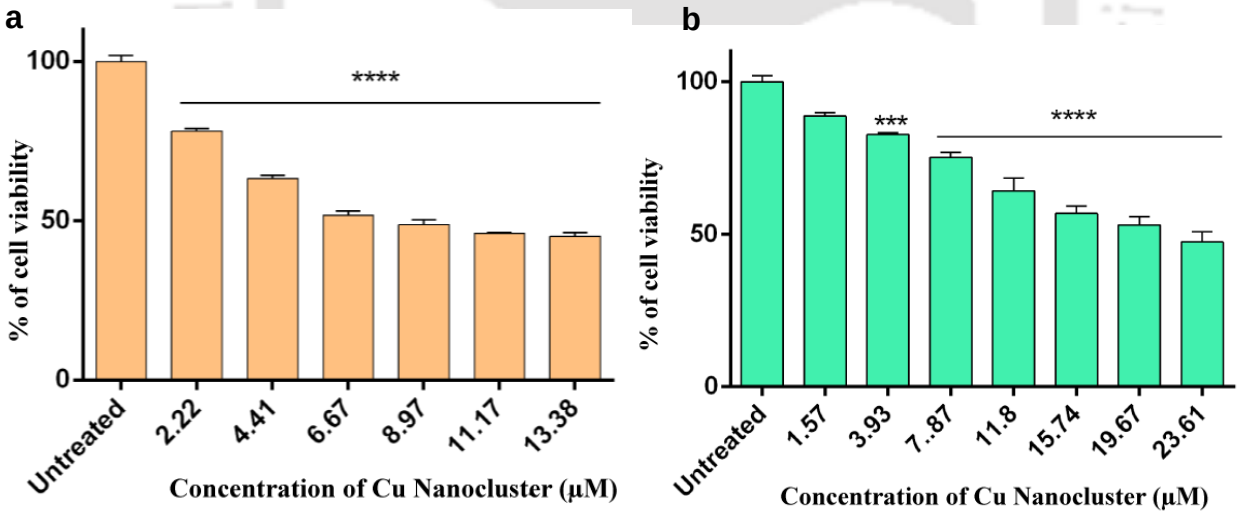

Figure. 3.3.38: Graphical representation of dose-dependent decrease in cell viability. (a) MCF-7 and (b) HeLa monolayer cultures treated for 48 h with nanocomposites. Results are presented as mean ± SEM.

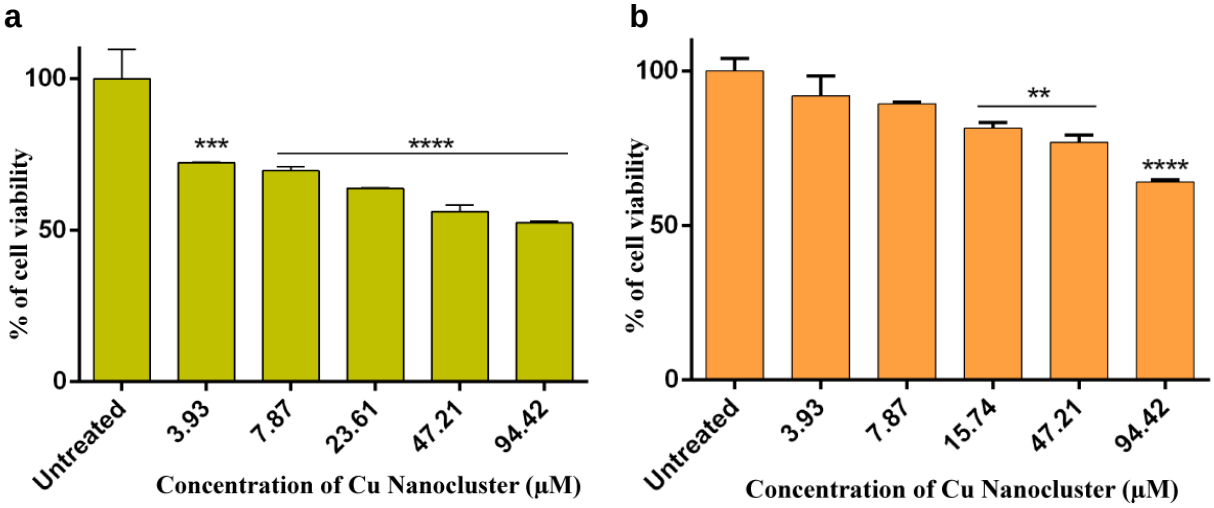

Figure. 3.3.39: Graphical representation of dose-dependent decrease in cell viability. (a) MCF-7 and (b) HeLa spheroids treated for 72 h with nanocomposites. Results are presented as mean ± SEM.

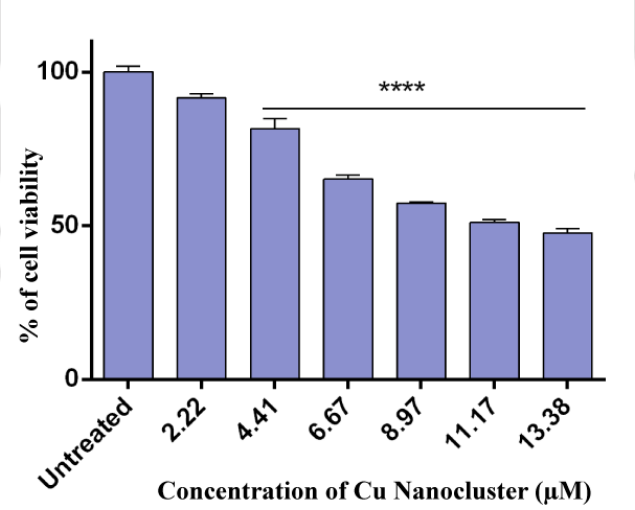

Figure. 3.3.40: Graphical representation of dose-dependent decrease in cell viability of HEK-239 monolayer culture treated for 48 h with nanocomposites. Results are presented as mean ± SEM.

	Monolayer Culture	Spheroids
MDA-MB-231	14.61	113.74
MDA-MB-468	10.38	60.13
MCF-7	9.22	52.28
HeLa	21.21	142.72

Table. 3.3.1: The obtained IC_{50} values of the nanocomposites in monolayer culture and spheroids of different cell lines. The values represent μM concentration of copper nanoclusters present in nanocomposites.

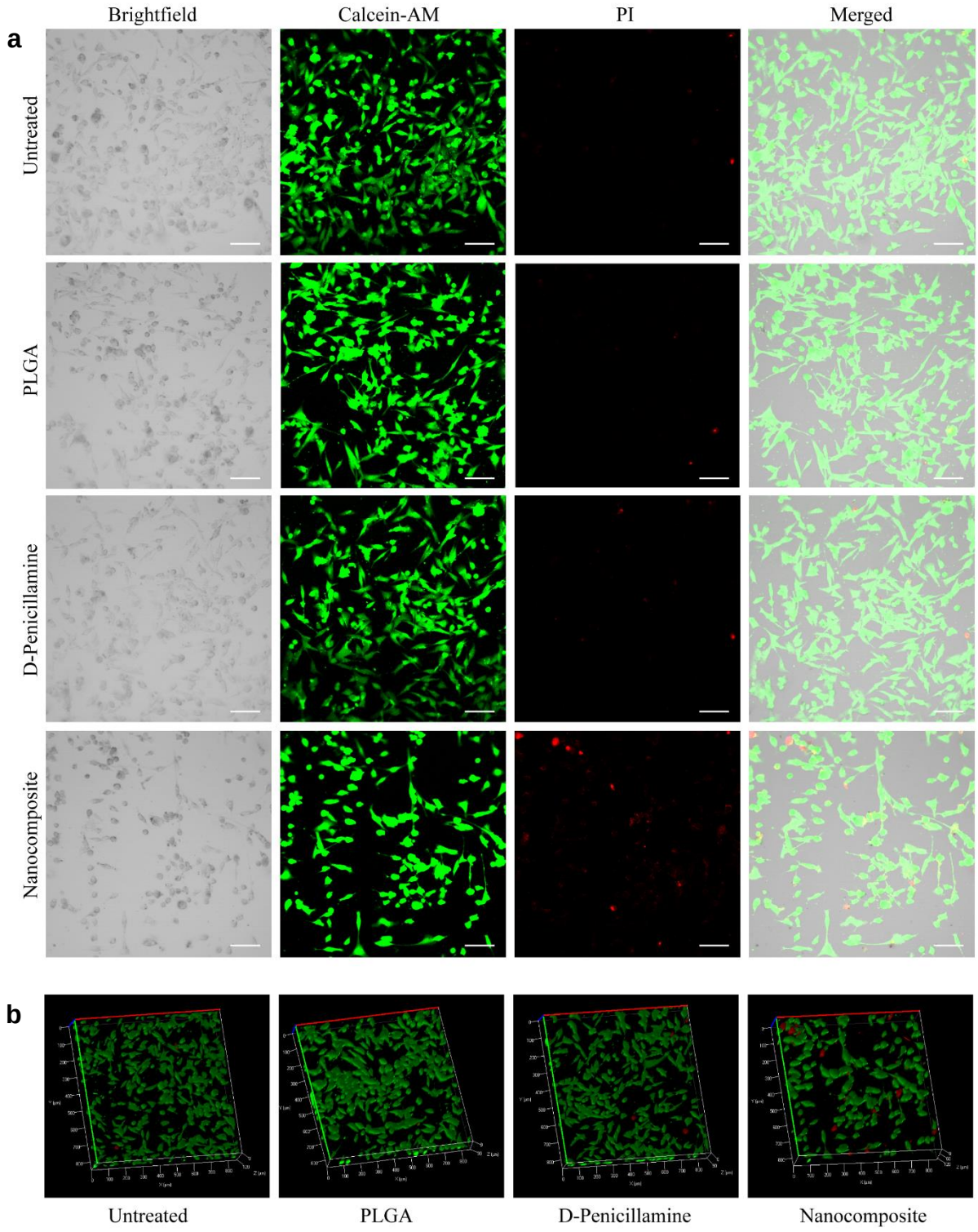

Figure. 3.3.41: (a) Live-dead cell visualization of MDA-MB-231 monolayer culture using calcein-AM/propidium iodide (PI) dual staining. Green fluorescence by calcein-AM refers to live cells, whereas red fluorescence by PI refers to dead cells. Scale bar: 50 μm. (b) Z-stack projections of live dead cell imaging of MDA-MB-231 monolayer culture.

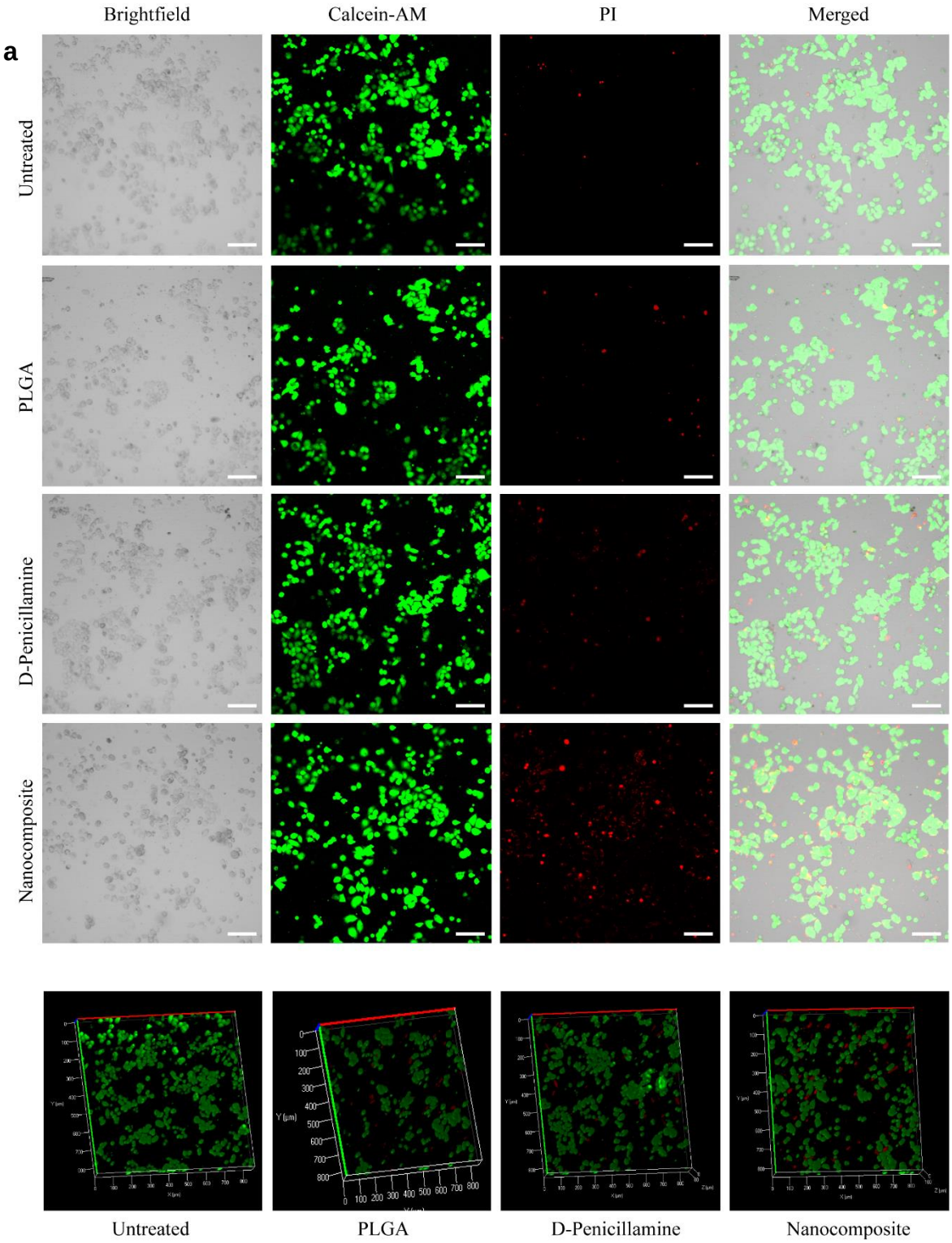

Figure. 3.3.42: (a) Live-dead cell visualization of MDA-MB-468 monolayer culture using calcein-AM/propidium iodide (PI) dual staining. Green fluorescence by calcein-AM refers to live cells, whereas red fluorescence by PI refers to dead cells. Scale bar: 50 μm. (b) Z-stack projections of live dead cell imaging of MDA-MB-468 monolayer culture.

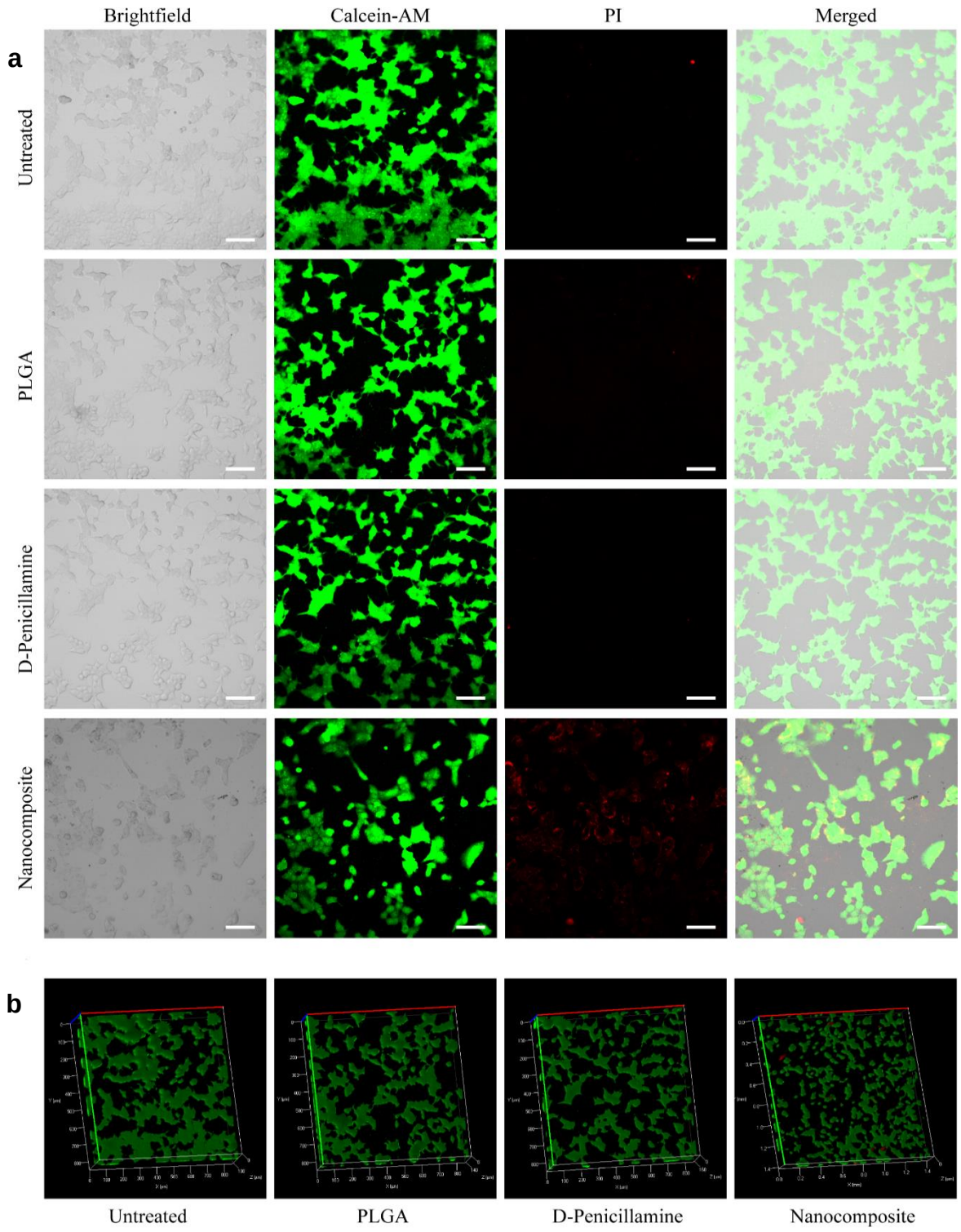

Figure. 3.3.43: (a) Live-dead cell visualization of MCF-7 monolayer culture using calcein-AM/propidium iodide (PI) dual staining. Green fluorescence by calcein-AM refers to live cells, whereas red fluorescence by PI refers to dead cells. Scale bar: 50 μm. (b) Z-stack projections of live dead cell imaging of MCF-7 monolayer culture.

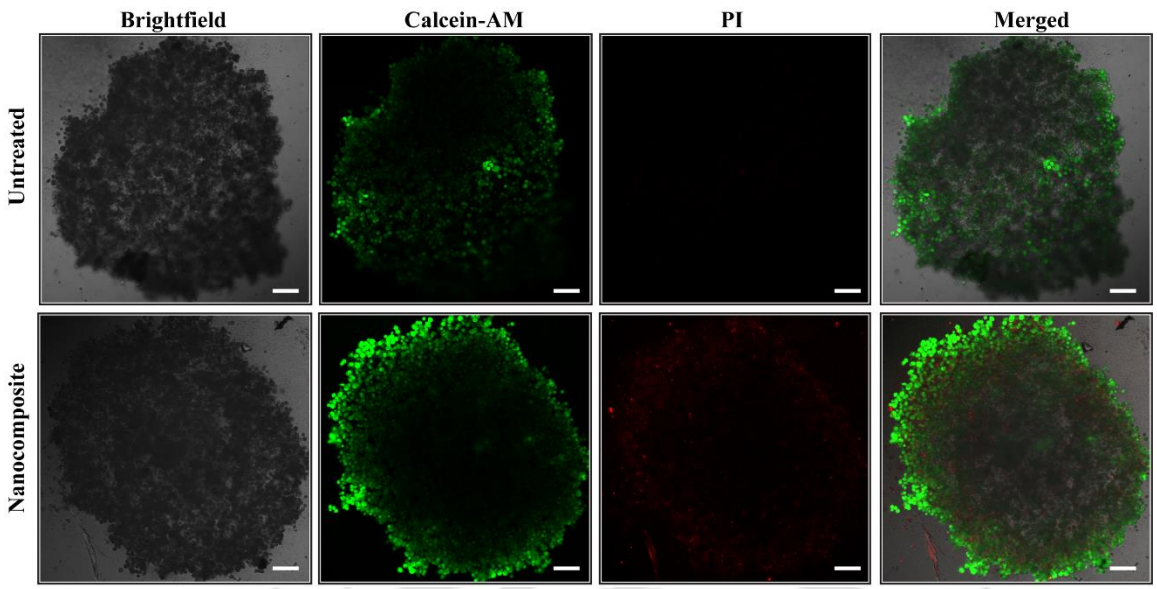

Figure. 3.3.44: Imaging of Live and dead cell population. Live cells are denoted by green fluorescence, whereas dead cells are denoted by red fluorescence. MDA-MB-231 spheroids were treated for 72 h with nanocomposites. Scale bar represents 250 μM.

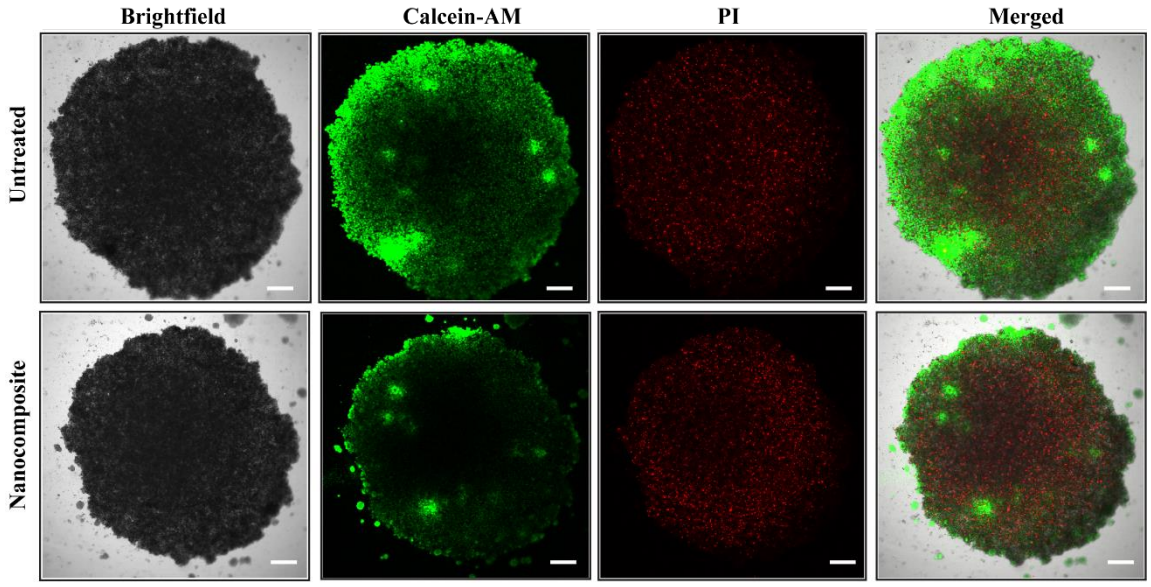

Figure. 3.3.45: Imaging of Live and dead cell population. Live cells are denoted by green fluorescence, whereas dead cells are denoted by red fluorescence. MDA-MB-468 spheroids were treated for 72 h with nanocomposites. Scale bar represents 250 μM.

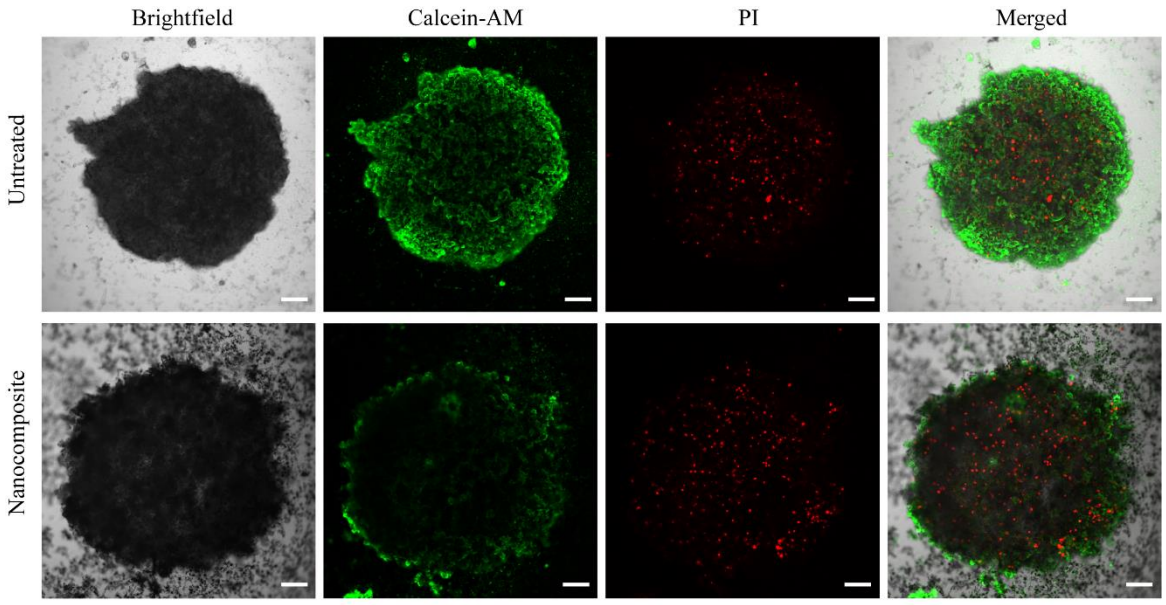

Figure. 3.3.46: Imaging of Live and dead cell population. Live cells are denoted by green fluorescence, whereas dead cells are denoted by red fluorescence. MCF-7 spheroids were treated for 72 h with nanocomposites. Scale bar represents 250 μM.

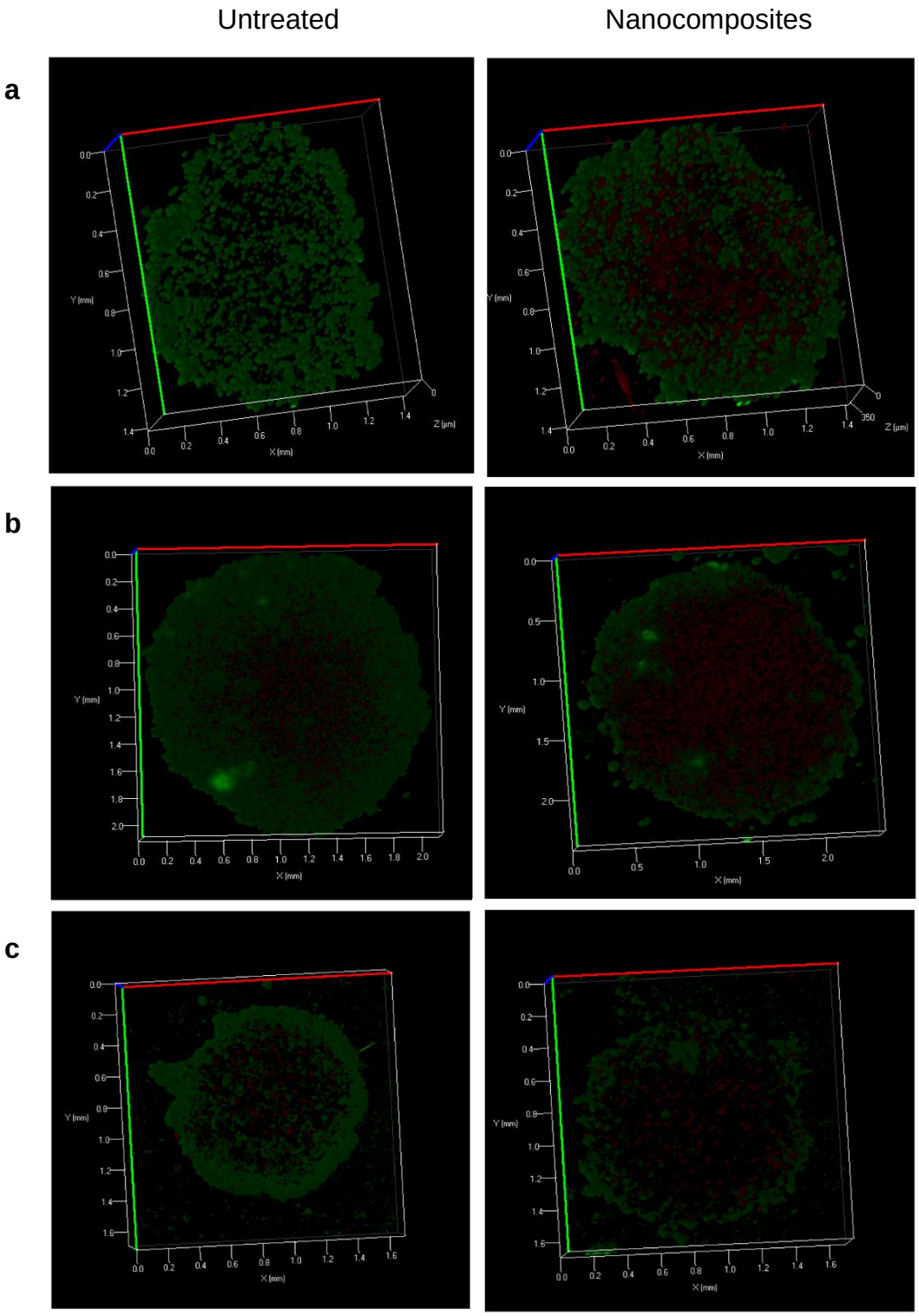

Figure. 3.3.47: Z-stacking images of (a) MDA-MB-231, (b) MDA-MB-468 and (c) MCF-7. Live cells are denoted by green fluorescence, whereas dead cells are denoted by red fluorescence. Spheroids were treated for 72 h with nanocomposites.

3.3.1.7. Treatment with Nanocomposites Results in Reversal of EMT in TNBC: TNBCs exploit the development program EMT to transform from a sessile epithelial state to an invasive mesenchymal state to facilitate escape from the primary tumor. Earlier reports suggest the inhibition of EMT and thus metastasis by copper chelation [179]. Therefore, to evaluate the alteration of gene expression, qRT-PCR was performed.

During the process of EMT, Epithelial markers (E-cadherin, occludin) are found to be downregulated, whereas mesenchymal markers (vimentin, N-cadherin, fibronectin) are found to be upregulated [58]. Following treatment, E-cadherin was upregulated in MDA-MB-468 whereas downregulated in MDA-MB-231 (**Figure. 3.3.48 and Figure. 3.3.49**). Simultaneously, vimentin was downregulated by 2.21-fold and 1.36-fold in MDA-MB-231 and MDA-MB-468 (**Figure. 3.3.48 and Figure. 3.3.49**). N-cadherin was downregulated by 1.92-fold and upregulated by 3.17- fold (**Figure. 3.3.48 and Figure. 3.3.49**), and fibronectin was downregulated by 2.17-fold and 3.31-fold (**Figure. 3.3.50 and Figure. 3.3.51**) in MDA-MB-231 and MDA-MB-468, respectively. Another prominent EMT marker, caveolin-1, was downregulated by 2.74-fold in MDA-MB-231 (**Figure. 3.3.50**). However, it was found to be upregulated by 6.6-fold in MDA-MB-468 (**Figure. 3.3.51**).

Additionally, the alteration of expression of EMT transcription factors was also evaluated. Transcription factor Twist1 was found to be downregulated by 1.78-fold in MDA-MB-231(**Figure. 3.3.52**) and almost unaltered in MDA-MB-468 (**Figure. 3.3.53**). Contrastingly, SNAI2 was found to be almost unaltered in MDA-MB-231(**Figure. 3.3.52**) and downregulated by 2.1-fold in MDA-MB-468 (**Figure. 3.3.53**). Altogether, these findings indicate that treatment with nanocomposites induces $CoCl_2$ induced EMT cells to reverse their phase transition to MET.

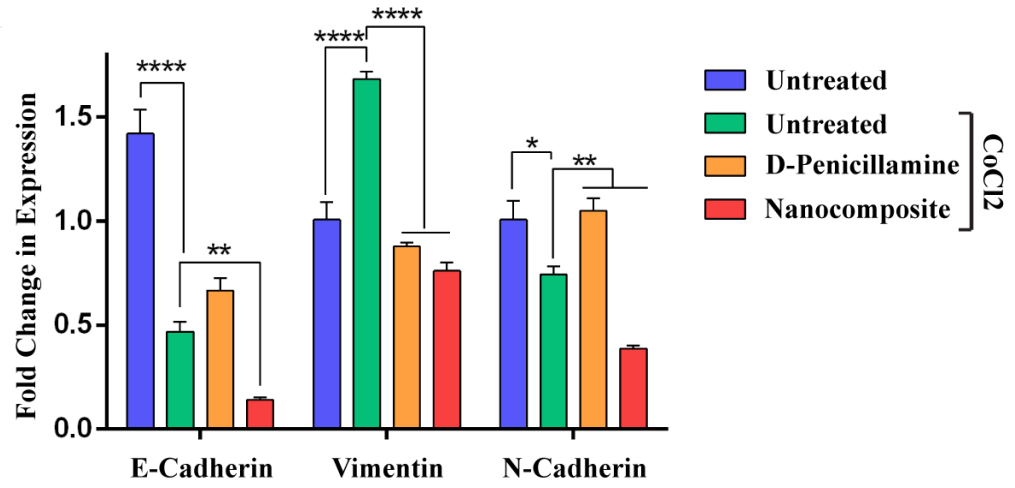

Figure. 3.3.48: Alteration of gene expression in MDA-MB-231 following treatment with nanocomposites quantified by qRT-PCR. The results of three separate studies are represented as the mean relative gene expression standard compared to GAPDH ± SEM.

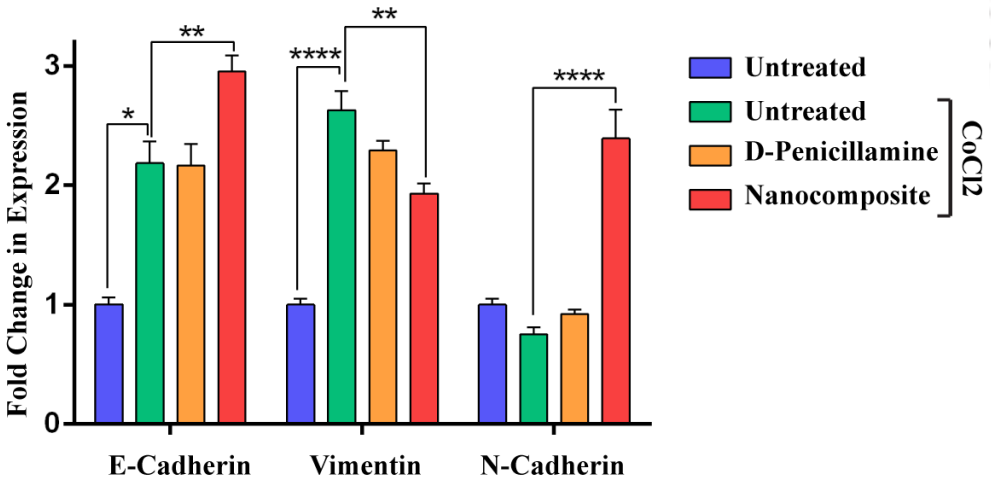

Figure. 3.3.49: Alteration of gene expression in MDA-MB-468 following treatment with nanocomposites quantified by qRT-PCR. The results of three separate studies are represented as the mean relative gene expression standard compared to GAPDH ± SEM.

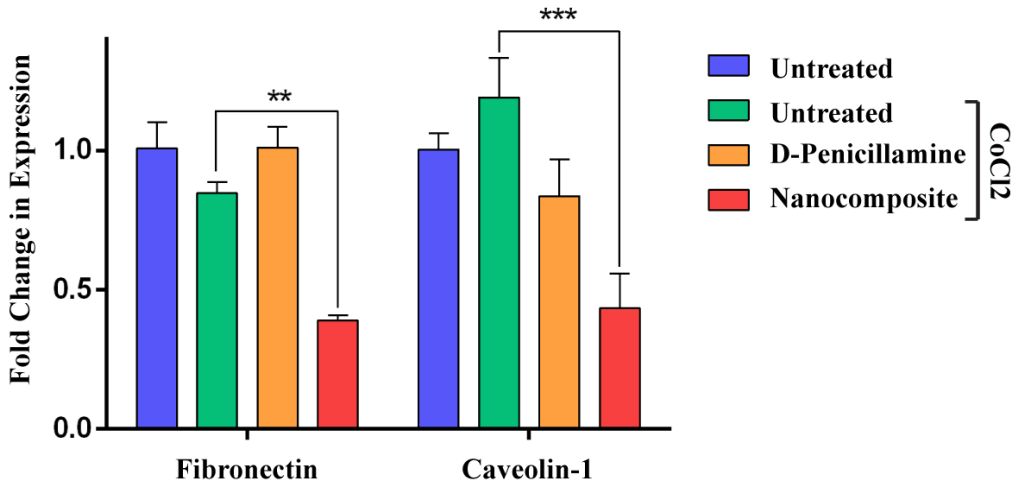

Figure. 3.3.50: Alteration of gene expression in MDA-MB-231 following treatment with nanocomposites quantified by qRT-PCR. The results of three separate studies are represented as the mean relative gene expression standard compared to GAPDH ± SEM.

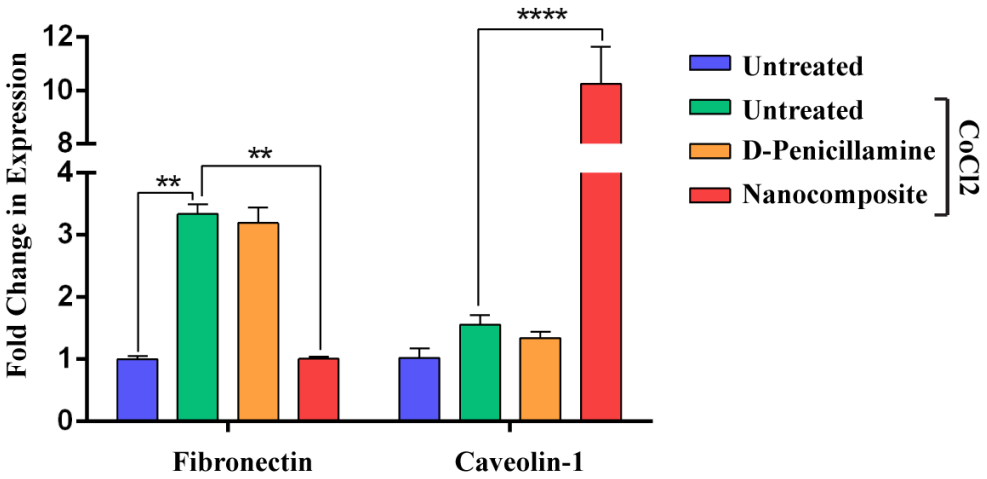

Figure. 3.3.51: Alteration of gene expression in MDA-MB-468 following treatment with nanocomposites quantified by qRT-PCR. The results of three separate studies are represented as the mean relative gene expression standard compared to GAPDH ± SEM.

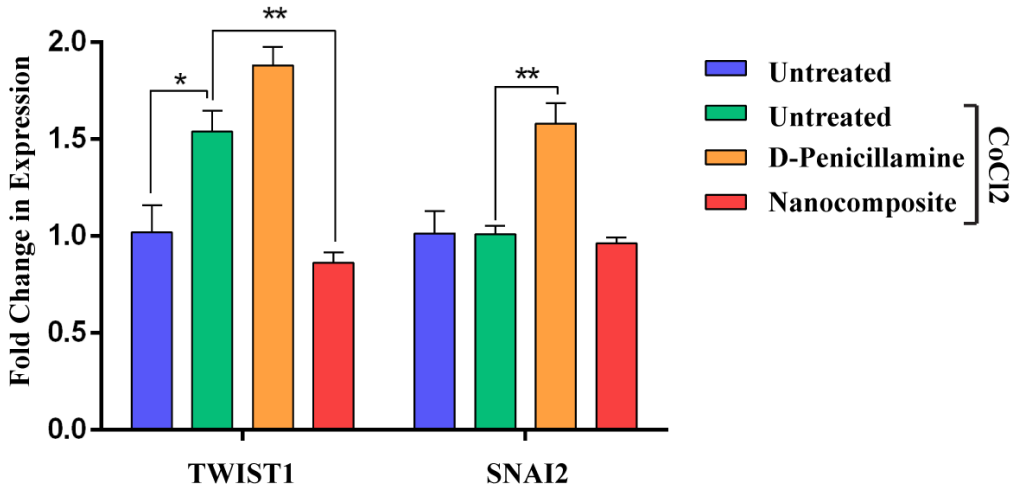

Figure. 3.3.52: Alteration of gene expression in MDA-MB-231 following treatment with nanocomposites quantified by qRT-PCR. The results of three separate studies are represented as the mean relative gene expression standard compared to GAPDH ± SEM.

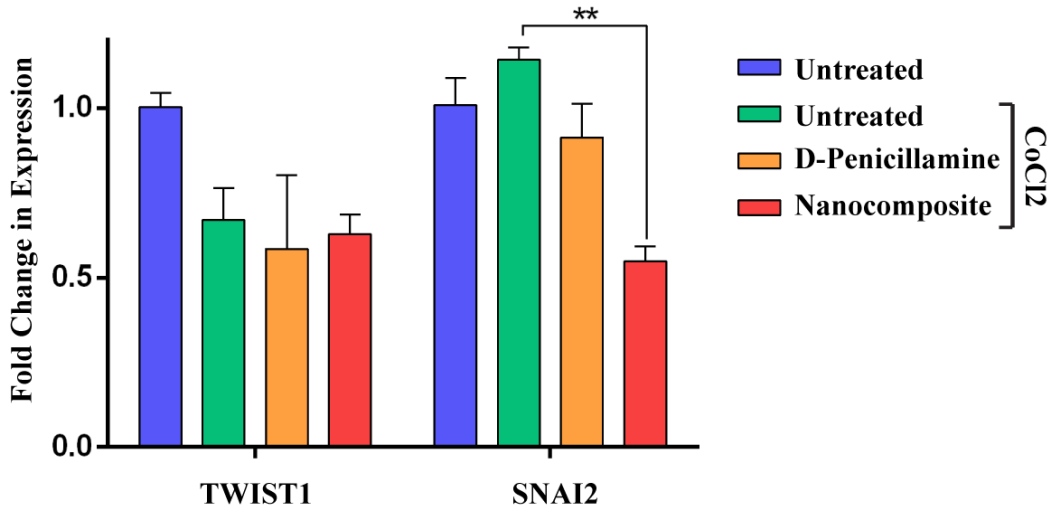

Figure. 3.3.53: Alteration of gene expression in MDA-MB-468 following treatment with nanocomposites quantified by qRT-PCR. The results of three separate studies are represented as the mean relative gene expression standard compared to GAPDH ± SEM.

3.3.1.8. Nanocomposites Represses Mesenchymal Differentiation and Stemness of TNBC: In addition to hypoxia and EMT, $CoCl_2$ supplementation is known to induce mesenchymal differentiation and stem-cell marker expression in TNBC [180]. Therefore, the change of gene expression of ALDH1A3 and EpCAM, two stemness markers, were evaluated using qRT-PCR. Following treatment with nanocomposites, EpCAM was downregulated by 1.76-fold in MDA-MB-231 (Figure 7G) and upregulated by 1.75-fold in MDA-MB-468 (Figure 7H). Concurrently, for ALDH1A3, 2.89-fold downregulation in MDA-MB-231 (Figure 7G) and 1.57-fold downregulation in MDA-MB-468 (Figure 7H) was observed. Taken together, these results suggest the inhibition of stemness and ultimately tumorigenesis upon treatment with nanocomposites.

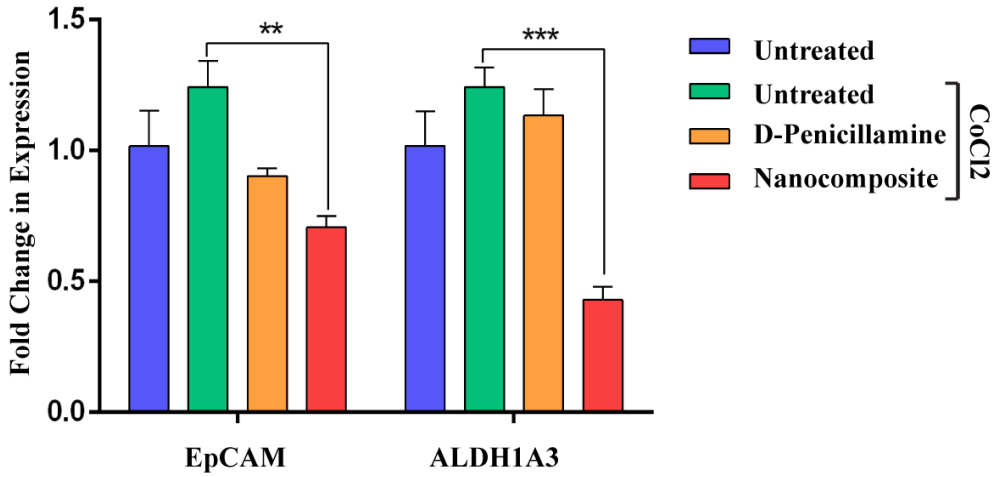

Figure. 3.3.54: Alteration of gene expression in MDA-MB-231 following treatment with nanocomposites quantified by qRT-PCR. The results of three separate studies are represented as the mean relative gene expression standard compared to GAPDH ± SEM.

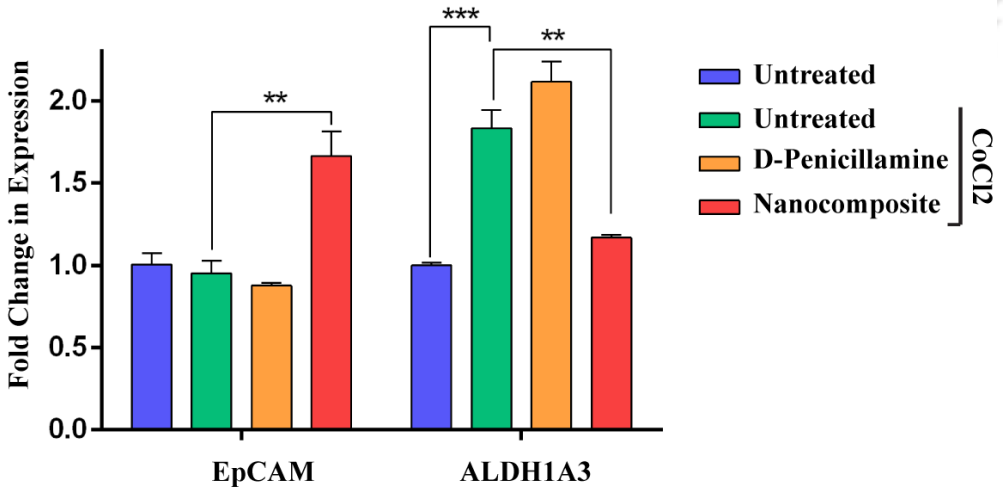

Figure. 3.3.55: Alteration of gene expression in MDA-MB-468 following treatment with nanocomposites quantified by qRT-PCR. The results of three separate studies are represented as the mean relative gene expression standard compared to GAPDH ± SEM.

3.3.1.9. Application of Nanocomposites to TNBC Alters the Expression of ABC Transporters: Apart from EMT, another critical factor influencing metastasis is MDR [181]. Due to MDR, multiple cytotoxic anticancer medications become cross-resistant in cancer cells. In MDR, drug expulsion is mainly carried out by ABC transporters [182]. To investigate the effect of nanocomposites on MDR, the alteration of expression of ABCB1 and ABCC1, the significant members responsible for MDR were studied [183]. Following treatment with nanocomposites, the expression of ABCB1 and ABCC1 was reduced by 1.57-fold and 4.63-fold in MDA-MB-231 (**Figure. 3.3.56**). However, nanocomposites elevated the expression of ABCG2 by 1.47-fold (**Figure. 3.3.56**). Similarly, in MDA-MB-468, both ABCB1 and ABCC1 were downregulated by 3.5-fold and 1.21-fold, respectively (**Figure. 3.3.57**). Akin to MDA-MB-231, here also the expression of ABCG2 was upregulated by 3.8-fold (**Figure. 3.3.57**). From the obtained data, it can be inferred that for MDR-related genes, nanocomposites act as an antagonist for ABCB1 and ABCC1 whereas, it acts as an agonist for ABCG2.

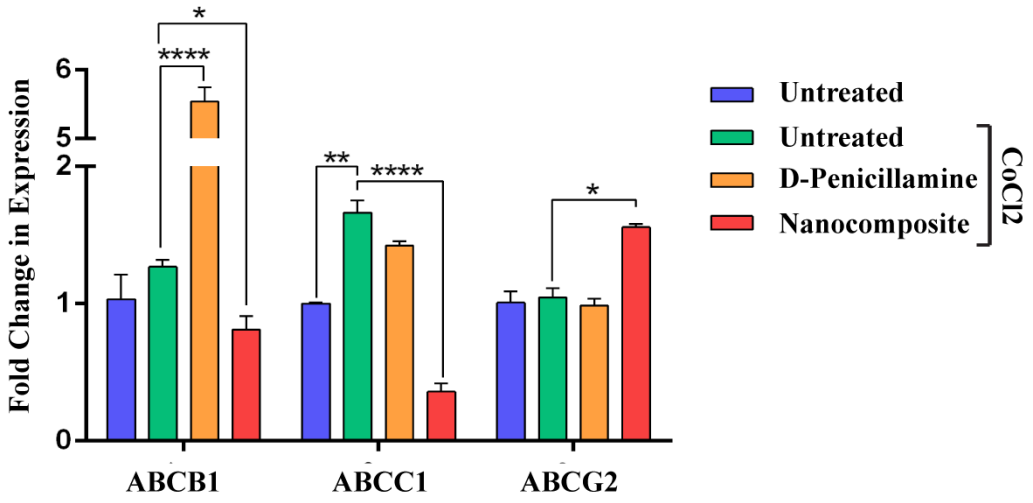

Figure. 3.3.56: Alteration of gene expression in MDA-MB-231 following treatment with nanocomposites quantified by qRT-PCR. The results of three separate studies are represented as the mean relative gene expression standard compared to GAPDH ± SEM.

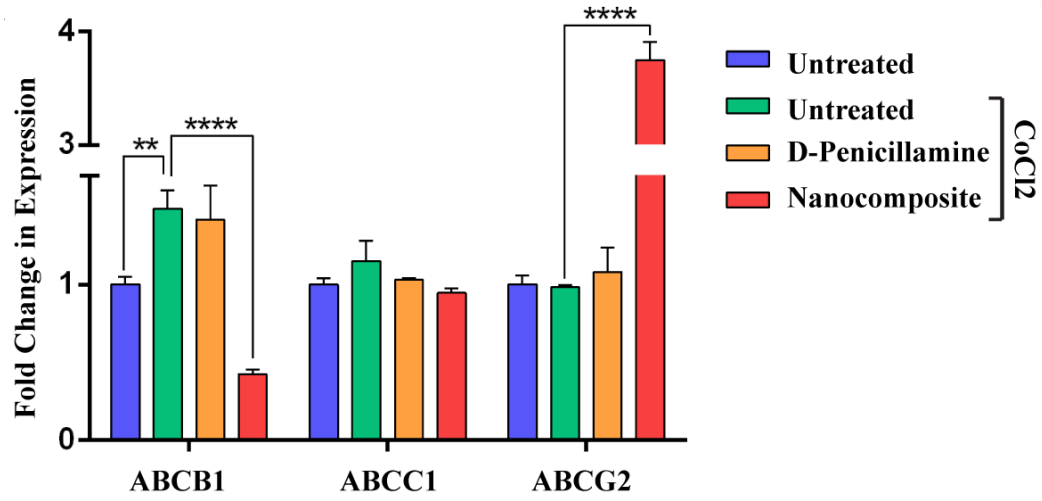

Figure. 3.3.57: Alteration of gene expression in MDA-MB-468 following treatment with nanocomposites quantified by qRT-PCR. The results of three separate studies are represented as the mean relative gene expression standard compared to GAPDH ± SEM.

3.3.1.10. Administration of Nanocomposites Decreases the Migration Potential of TNBC: EMT is a cellular mechanism that promotes metastasis by migrating primary cancer cells to secondary sites [184]. To validate the finding of downregulation of EMT markers, the effect of nanocomposites was investigated on the migration capacity of TNBC cells. The ability to migrate was tested using a wound-healing scratch assay, in which the migration rate toward the wound region (created by scratch) was measured. As anticipated, 2.12-fold reduction in wound healing in the case of MDA-MB-231 and 5.32-fold reduction in case of MDA-MB-468 were observed with respect to untreated cells (**Figure. 3.3.58** and **Figure. 3.3.59**). However, the application of PLGA or d-penicillamine did not alter the cell's migratory property. These data indicate the reduction in migration property and validates the induction of MET.

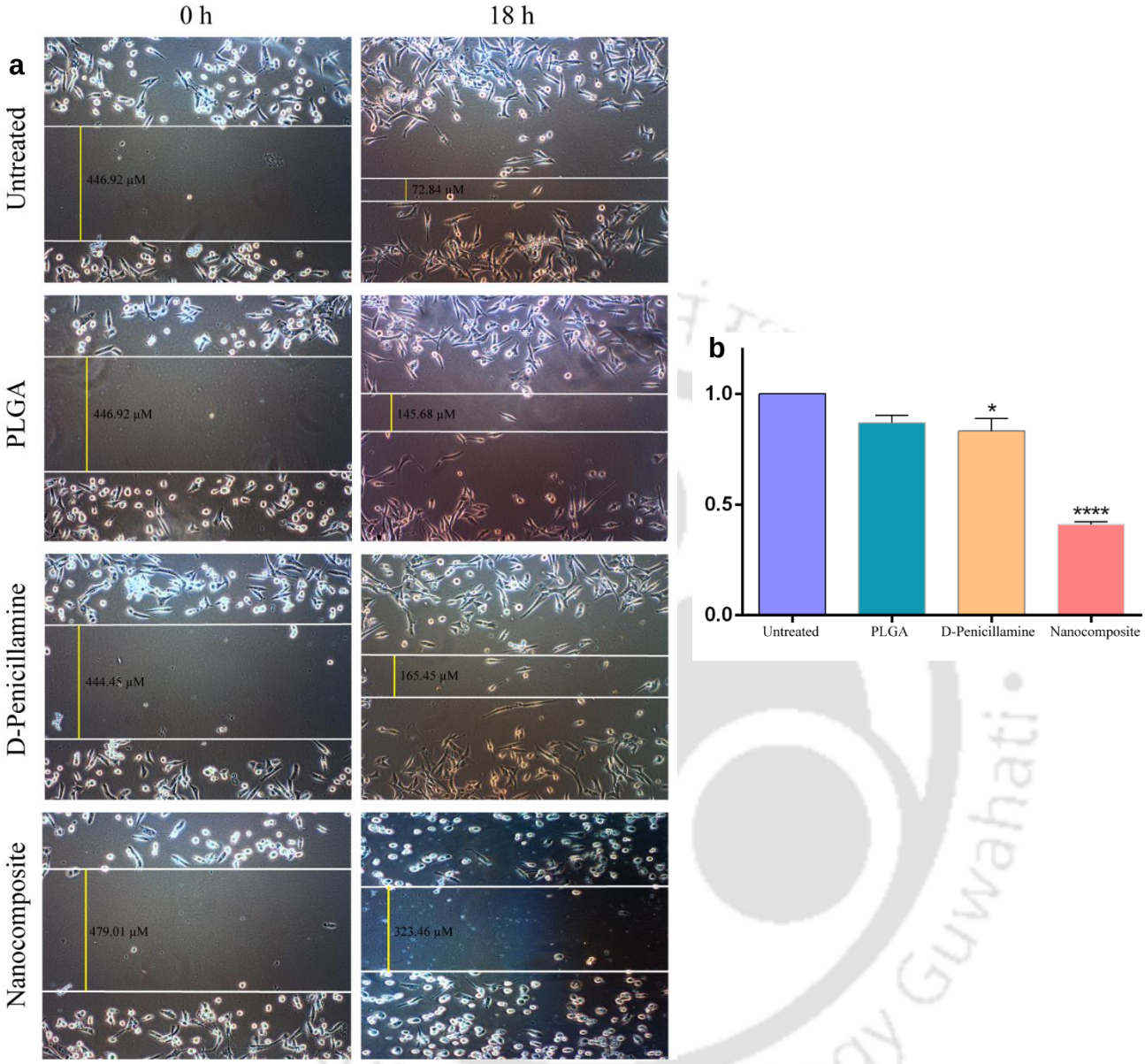

Figure. 3.3.58: (a) Scratch wound-healing assays of MDA-MB-231 monolayer culture following treatment with PLGA nanoparticles, d-penicillamine, and nanocomposites for 18 h. (b) Graphical representation of fold change in migration potential. The area of gap closure was analyzed using ImageJ software.

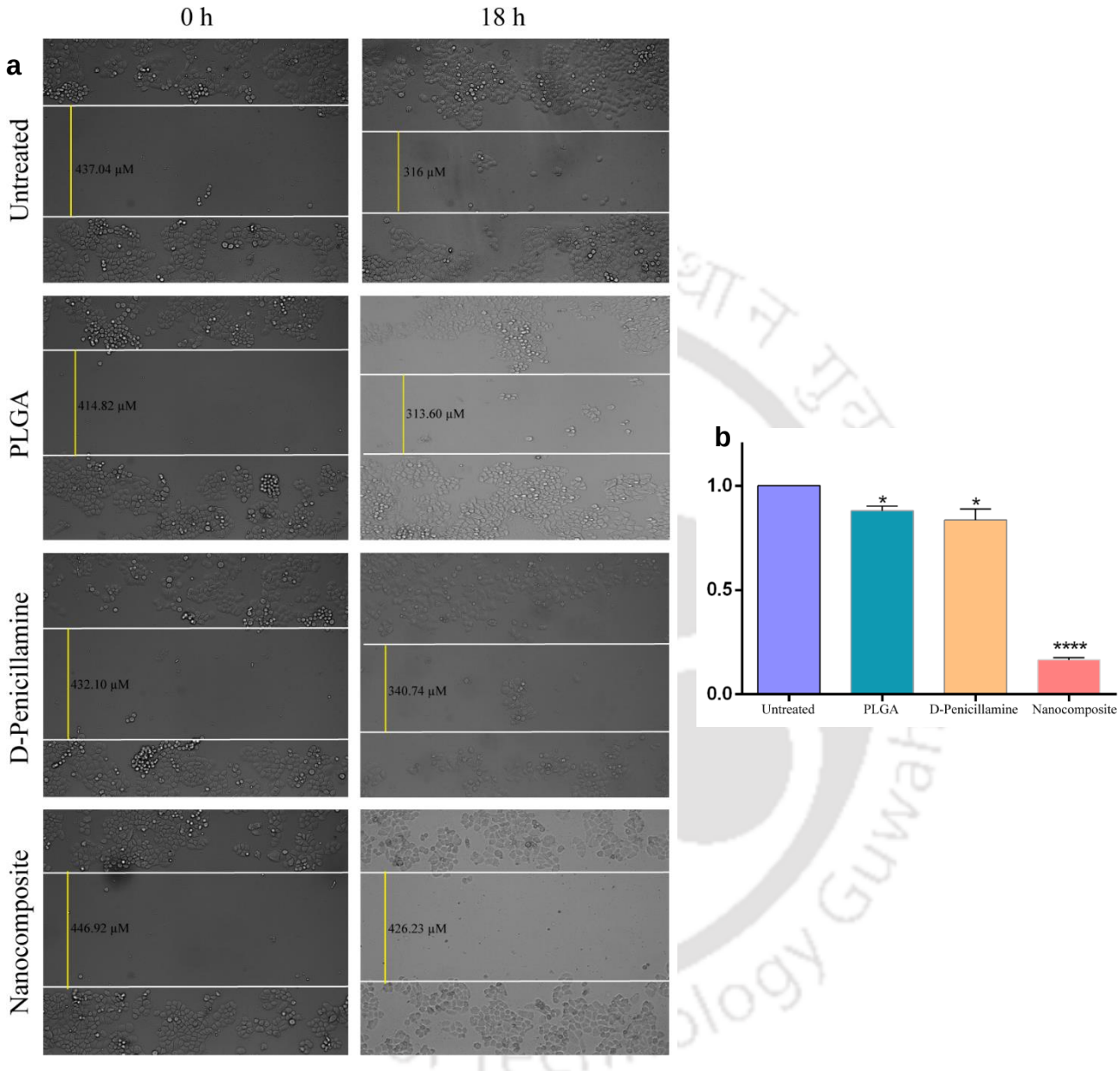

Figure. 3.3.59: (a) Scratch wound-healing assays of MDA-MB-468 monolayer culture following treatment with PLGA nanoparticles, d-penicillamine, and nanocomposites for 18 h. (b) Graphical representation of fold change in migration potential. The area of gap closure was analyzed using ImageJ software.

3.3.1.11. Nanocomposites Differentially Modulates Downstream Pro-Survival Signals in TNBC: In the process of EMT, several downstream signaling pathways are found to be hyperactivated, which helps in survival and tumorigenicity [146]. To elucidate the molecular mechanism of reversal of EMT following treatment with nanocomposites, Western blot assay was used to assess the protein expression of essential cell survival proteins. Protein expression analysis revealed that nanocomposites reduced the level of β-catenin by 3-fold in case of MDA-MB-231 (**Figure. 3.3.60**) and by 3.11-fold in case of MDA-MB-468 (**Figure. 3.3.61**). Noticeably, d-penicillamine alone was able to reduce the level β-catenin much effectively in MDA-MB-231 than nanocomposites (**Figure. 3.3.60**). Similar to β-catenin, the activated form of STAT-3 (p-STAT-3) was downregulated by 1.61-fold in MDA-MB-231 (**Figure. 3.3.60**) and by 7.8-fold in MDA-MB-468 (**Figure. 3.3.6).**

Application of nanocomposites reduced the level of p-ERK1/2 by 1.3-fold in MDA-MB-231(**Figure. 3.3.60**) and increased by 3.04-fold in MDA-MB-468 (**Figure. 3.3.61**). Interestingly, following treatment with nanocomposites, p-AKT was upregulated by 5.41-fold in MDA-MB-231(**Figure. 3.3.60**), whereas it was found to be downregulated by 2.3-fold in MDA-MB-468 (**Figure. 3.3.61**). The fold change in protein expression following treatment with nanocomposites is listed in **Table. 3.3.2.** In addition, the alteration in expression of HIF-1α by $COCl_2$ treatment is also quantified (**Figure. 3.3.62).**

The current results indicate that nanocomposites exert its antiproliferative activity and induction of MET chiefly through inhibiting STAT-3 and β-catenin signaling pathways. On the other hand, cells try to evade apoptosis using the AKT pathway in case of MDA-MB-231 and MAPK pathway in MDA-MB-468.

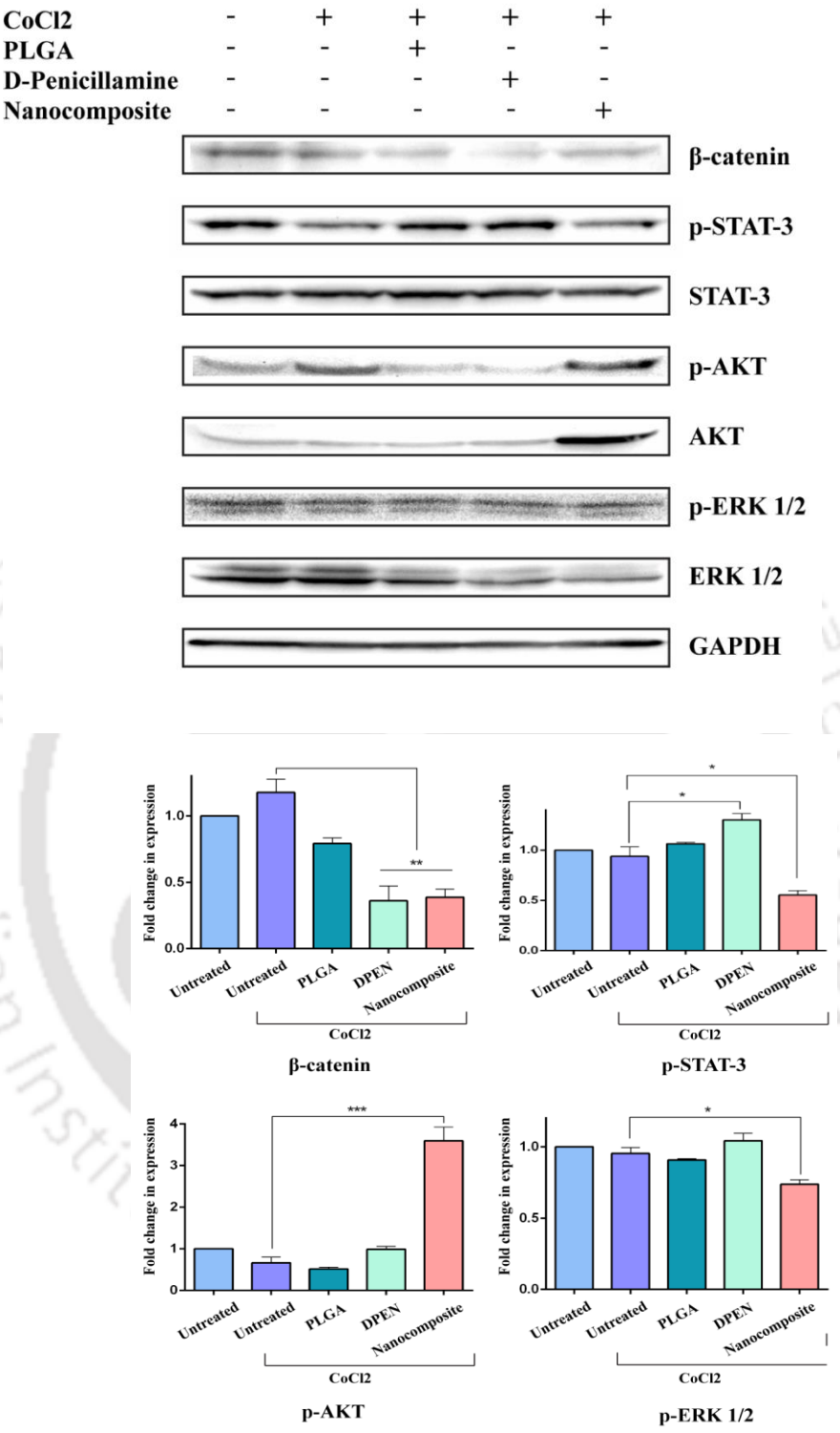

Figure. 3.3.60: Representative Western blots showing β-catenin, p-STAT-3/STAT-3, p-AKT/AKT, p-ERK1/2/ERK1/2, and GAPDH levels in MDA-MB-231 cell extracts. Cells were treated with nanocomposites for 48 h. GAPDH is used as a loading control.

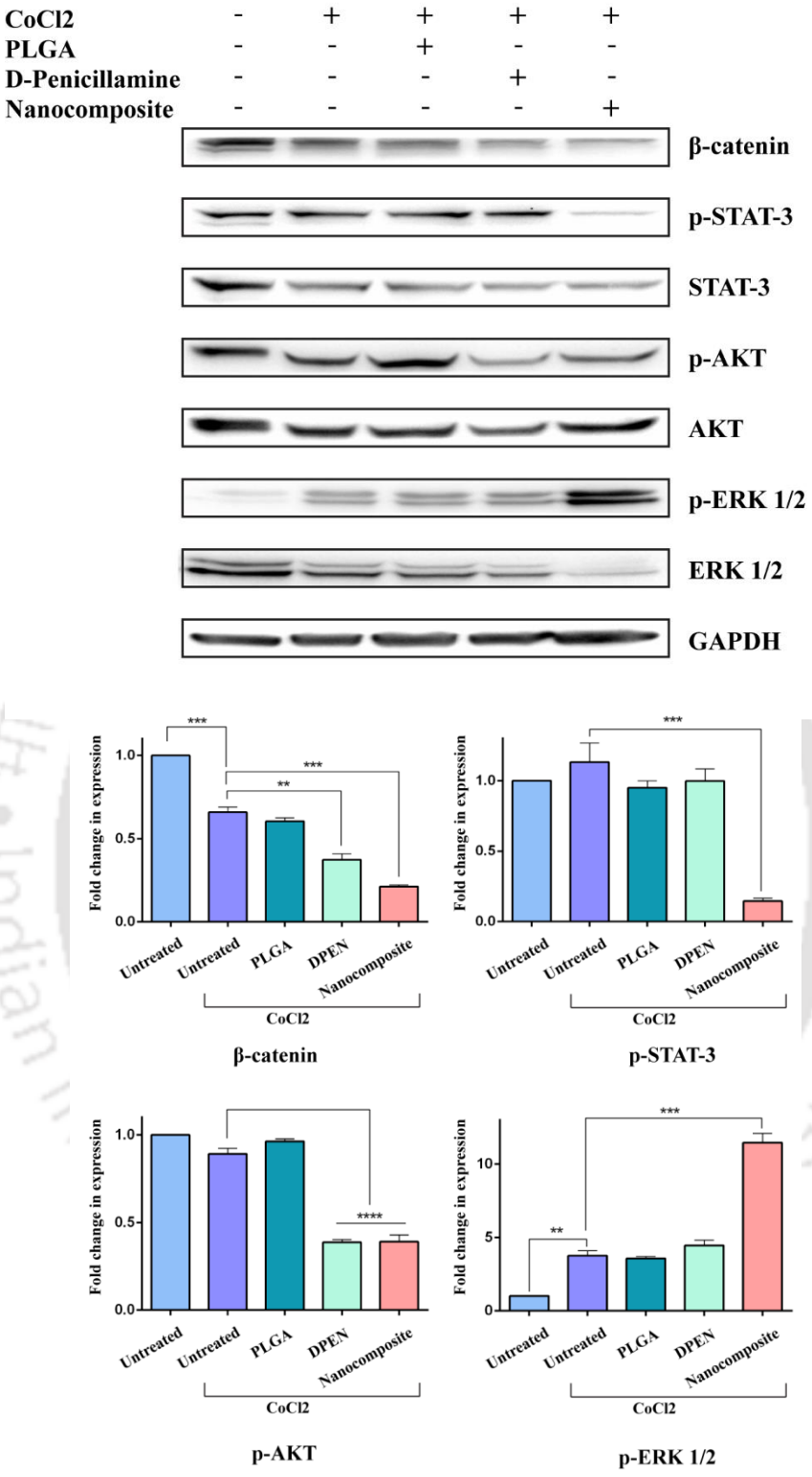

Figure. 3.3.61: Representative Western blots showing β-catenin, p-STAT-3/STAT-3, p-AKT/AKT, p-ERK1/2/ERK1/2, and GAPDH levels in MDA-MB-468 cell extracts. Cells were treated with nanocomposites for 48 h. GAPDH is used as a loading control.

Protein	MDA-MB-231	MDA-MB-468
B-Catenin	3.04 ↓	3.11 ↓
p-STAT-3	1.61 ↓	7.80 ↓
p-AKT	5.41 ↑	2.30 ↓
p-ERK1/2	1.30 ↓	3.04 ↑

Table 3.3.2: Tabular representation of the fold change in protein expression in MDA-MB-231 and MDA-MB-468 following treatment with nanocomposite.

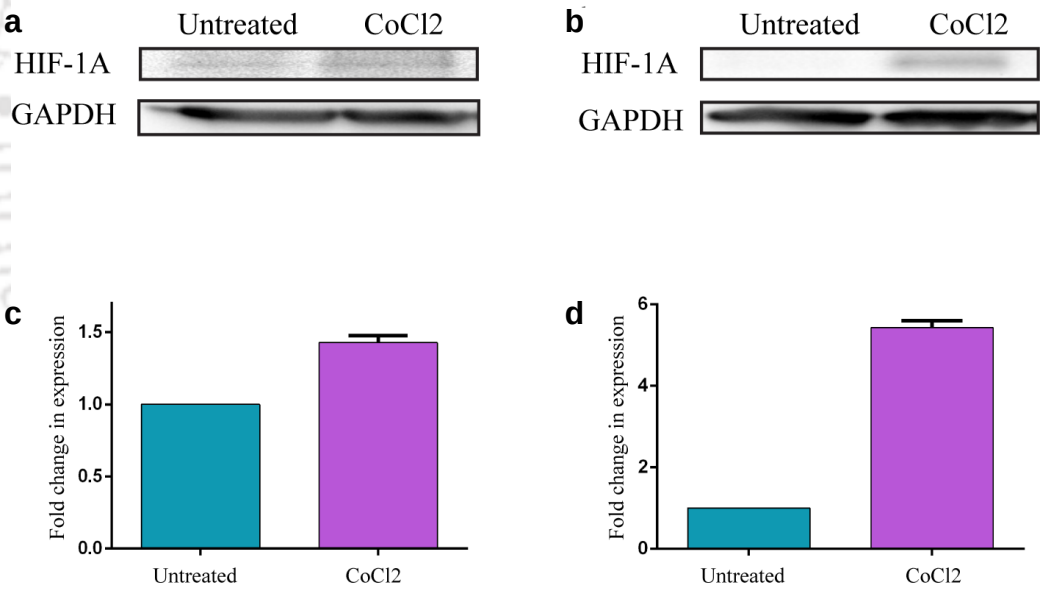

Figure. 3.3.62: Representative western blots showing HIF-1α and GAPDH levels in (a) MDA-MB-231 and (b) MDA-MB-468 cell extracts. MDA-MB-231 cells were treated with 25 μM $CoCl_2$ whereas MDA-MB-468 cells were treated with 100 μM $CoCl_2$ for 48 h. GAPDH serves as a loading control. Graphs represent the changes in the expression levels in (c) MDA-MB-231 and (d) MDA-MB-468.

3.3.2 Discussion: It is of paramount importance to find new treatment approaches, as highly invasive and drug resistive nature of TNBC renders chemotherapeutics ineffective. The development of new therapeutic agents targeting different molecular and genetic drivers is at an early stage with unpredictable output. Hence, parallel attempts are being persuaded to improve the potency and delivery of well-established drugs as anticancer medicine. In this study, it is shown that d-penicillamine, an FDA-approved drug, in conjunction with Au–Cu bimetallic nanoclusters, offers a promising strategy to enhance TNBC inhibition. In addition, PLGA, an FDA-approved biodegradable polymer and recombinant transferrin protein, was also used for systemic biodistribution and targeted delivery. The conglomeration of these components resulted in production of nanocomposites. Nanomedicine exploits the enhanced permeability and retention effect (EPR) of the tumor cells for passive targeting. The size of the nanomedicine needs to be <200 nm for active extravasation through leaky tumor cells via EPR effect [185]. The average size detected of the synthesized PLGA nanoparticle is 151.7 ± 10 nm is well suited for EPR effect mediated targeting of TNBC. Although EPR mediated passive targeting is efficient, intracellular drug targeting poses its own range of difficulties such as cellular uptake, systemic toxicity, and efflux pumping [186]. Additionally, the need to track the nanomedicines for theranostics purpose presents its own set of challenges.

An important class of nanomaterials used for theranostics is metal nanoclusters. Capitalizing on the excellent luminescence property and photostability, d-penicillamine templated Au–Cu bimetallic nanoclusters were incorporated into the nanocomposites system. d-penicillamine, an FDA-approved drug for Wilson's disease, was selected as a template due to its unique property of copper chelation. Since copper is vital for metastatic cancer, copper chelation has

been identified as promising therapeutic technique for cancer therapy [187]. Matsubara et al. also found that d-penicillamine inhibited tritiated thymidine incorporation in human endothelial cells in a dose-dependent manner when used in the presence of copper sulfate [188]. However, this nonconventional therapy does not fulfill the objective of targeted therapy. Selective targeting of transferrin receptors has been of interest as most cancer cells overexpressed transferrin receptors to compensate for the increased demand for Fe3+ [189]. Therefore, this increased iron metabolism was exploited for selective targeting by coating transferrin protein on the surface of nanocomposites. Thus, to integrate the property of selective targeting, luminescence for theranostics, and copper chelation, novel nanocomposites was synthesized by multiplexing d-penicillamine Au–Cu nanocluster, PLGA nanoparticle, and transferrin protein.

The obtained data from the stability assay insinuates high photostability and hemocompatibility of the nanocomposites. The administration of nanocomposites exhibited high anti-cell proliferative activity in TNBC cells as well as some non-TNBC cells. These data indicate the functional integrity of the individual components of the nanocomposites. Further, the mechanism of action of the nanocomposites was investigated. Gupte et al. previously reported that in the presence of copper, d-penicillamine produces cytotoxic hydrogen peroxide (H_2O_2) at low concentrations [76]. Lipsky et al. have also demonstrated that the cytotoxic effect of d-penicillamine plus copper could be abolished by the presence of catalase, proving the role of H_2O_2 mediated cytotoxicity [190]. To investigate whether the mode of cell death incurred by nanocomposites is due to cellular ROS generation as per earlier reports, cellular ROS production was examined. A sharp increase in cellular ROS level was observed following treatment in both MDA-MB-231 and MDA-MB-468, which confirms the earlier reports. Cancer cells, interestingly, are thought to be in an altered redox environment with increased oxidative stress. It is often assumed that a small rise in ROS improves cell viability

and proliferation. Rise in ROS can therefore facilitate tumorigenesis. Nevertheless, increased basal ROS in cancerous cells brings them closer to the toxicity limit, where their antioxidant ability to contain toxic ROS levels becomes insufficient [191]. Thus, elevated oxidative stress is instrumental for the elimination of cancer cells.

In summary, the transition metal–chelator complex in nanocomposites engages in redox cycling and hydroxyl radicals, which can effectively abolish TNBC cells. This is potential enticing treatment strategy as its mode of action relies on the physiology of cancer cells, including the substantial copper deposition and endogenic increased oxidative stress. Elevated ROS causes hyperpolarization of the mitochondrial membrane, which prompts the mitochondrial membrane potential to collapse, triggering apoptosis [192]. Also, the effectiveness of an anticancer drug is highly dependent on the ability of the compound to induce apoptosis [193]. Following treatment, an increase in 41.35% apoptotic cells in MDA-MB-231 and 31.88% increase in MDA-MB-468 substantiates the efficacy of the proposed treatment. Apart from the effect on cell viability, the impact of nanocomposites on TNBC metastasis was examined. Wang et al. have reported the inhibition of EMT in hepatocellular carcinoma by copper chelator disulfiram in the presence of copper [194]. Considering the presence of copper chelator and copper in synthesized nanocomposites, its effect on EMT was evaluated. The reversal of EMT, that is, induction of MET, is indicated by suppression of vimentin, fibronectin, N-cadherin, and increased expression of E-Cadherin following treatment. Several transcription factors such as SNAI, Twist, and Zeb family members have been identified as the master regulator of EMT [195]. In addition to EMT markers, downregulation of the EMT transcription factors proves the efficacy of the proposed treatment.

A significant oncogenic driver of TNBC is MDR which is facilitated by overexpression of ABC transporters [182]. Earlier studies have reported the

upregulation of ABC transporters by upregulated EMT transcription factors [196]. In addition, patients with drug-resistant tumors show a higher relapse and mortality rate. Following successful downregulation of EMT markers, the change in the expression level of ABC transporters were analyzed. As anticipated, the ABC transporters were found to be downregulated in both the cell lines following treatment with nanocomposites. Obtained data from the study indicate that, in parallel to all other processes that might be operating, inhibition of EMT by nanocomposites leads to the detrimental effect on the migratory properties of TNBC cells. In line with the finding, Baldari et al. have demonstrated that copper chelation resulted in reduced migration of BRAF mutant colon cancer cells acting via differential phosphorylation levels of ERK1/2 [197]. It should be noted that activation of the RAS-RAF-MEK-ERK pathway is essential for the induction of EMT in TNBC [198]. Intriguingly, Copper (Cu) availability appears to be critical for MEK1/2 kinase function. In addition, the ERK1/2 phosphorylation by MEK1 is facilitated by copper influx [199]. Considering these factors, the potential of nanocomposites to impact signal transduction via the RAF/MEK/ERK pathway in TNBC cells was investigated. The obtained result from the immunoblot of MDA-MB-231 indicates a significant reduction in the phosphorylation status of ERK1/2. However, phosphorylated ERK1/2 is found to be significantly upregulated in MDA-MB-468. This is possibly observed due to cells try to evade the detrimental effect of the nanocomposites by upregulating ERK1/2 in MDA-MB-468. Increased tumor cell invasion has been related to AKT activation. By upregulating IGF-I, AKT, increases the invasive property of pancreatic carcinoma, enhances matrix metalloproteinases 2 and 9 secretions from ovarian carcinomas, and immortalized mammary epithelial cells [200]. Upon treatment with nanocomposites, phosphorylated AKT was found to be downregulated by 2.3-fold in MDA-MB-468. However, pAKT was found to be upregulated in MDA-MB-231 by several folds. Indeed, the different upregulation/downregulation of pERK1/2 and pAKT in

MDA-MB-231 versus MDA-MB-468 are very striking, considering both of them are TNBC cell lines. However, it should be noted that TNBC is highly heterogeneous, with complex biological behavior and a great clinical variability [201]. The MDA-MB-231 cell line is classified as a mesenchymal stem-like (MSL) subtype of TNBC with major mutations in BRAF, CDKN2A, RAS, and TP53 genes. Whereas, MDA-MB-468 cell line is classified as basal like-2 (BL-2) subtype of TNBC with major mutations in PTEN, RB1, SMAD4, and TP53 genes [202]. Therefore, the observed difference in the study is due to the heterogenicity and different mutations in critical genes governing the malignant behavior of the cell lines.

The Wnt–β-catenin signaling pathway is crucial for EMT, invasion, metastasis, drug resistance, and tumorigenesis by acting as a transcriptional coactivator in this process [203]. From the Western blot data, it can be visualized that β-catenin is downregulated by several folds in both MDA-MB-231 and MDA-MB-468. The downregulation of β-catenin following treatment with nanocomposites marks the inhibition of EMT and growth signals. STAT-3 controls the expression of "master" EMT transcription factors, which are involved in integrating signals from a number of extracellular inputs to affect EMT phenotypes. Additionally, during EMT induction, STAT-3 facilitates nongenomic implications on the cytoskeleton [204]. Similar to β-catenin, several-fold reductions in p-STAT-3 in both MDA-MB-231 and MDA-MB-468 were observed following treatment with nanocomposites. This is in line with the reports by Voli et al., where copper chelators strongly inhibited phosphorylation of STAT-3 [205]. Hypoxia-induced EMT activates pro-oncogenic STAT-3, AKT, and MAPK in metastatic TNBC. STAT-3, AKT, and MAPK are known to share a bidirectional positive feedback loop with Wnt/β-catenin pathway [134]. After incubation with the nanocomposites, the observed decrease in expression of pSTAT-3, pMAPK, pAKT, and β-catenin, crucial downstream components of the cell survival pathways, represents the sophistication and web-like interaction between the examined

pathways and marks the repression of EMT and growth signals. From the obtained data it can be interpreted that besides other functioning mechanisms, nanocomposites primarily operate through inhibition of β-catenin and STAT-3 pathway regulation. These results demonstrate that nanocomposite exhibits anticancer cell survival actions through modulation of downstream signaling. The crux of the studies has been depicted in **Scheme. 3.3.**

3.3.3 Conclusion: EMT, stemness, and associated MDR are the major hurdles of resistance in TNBC treatment. In the quest for successful targeted therapy, an alternative nanotherapeutics was adopted using FDA-approved drugs and biocompatible nanocarrier. The transferrin D-penicillamine Au-Cu bimetallic nanocluster coated PLGA nanoparticles termed as nanocomposites were successfully prepared and characterized. Nanocomposites didn't elicit hemolytic action confirming the biocompatible nature. Furthermore, the nanocomposites accumulated in TNBC cells specifically through transferrin receptor binding, confirming selective targeting of transferrin overexpressed cancer cells. Moreover, the excellent photoluminescent property of the nanocomposite facilitated cellular imaging for theranostic purposes. The nanocomposites demonstrated excellent antiproliferative response in TNBC monolayer culture and spheroids. Notably, the nanocomposites successfully reversed the EMT phase transition and induced MET by downregulating the master regulator, i.e., EMT transcription factors. EMT reversal was followed by decline in expression of genes involved in stemness and MDR. Furthermore, EMT inhibition decreased TNBC cell migration. Nonetheless, treatment with the nanocomposites reduced prominent cell survival signals and prevented downstream crosstalk by targeting multiple signal-nodes. The translation of cell retardation activity, phase transition of EMT to MET, and reversal of MDR phenomena demonstrates the enormous possibility of new therapeutic nanocomposites as a 'nanodrug' against the dreadful TNBC. Overall, the findings indicate that with further standardization, the nanocomposites have therapeutic potential to combat the dreadful TNBC.

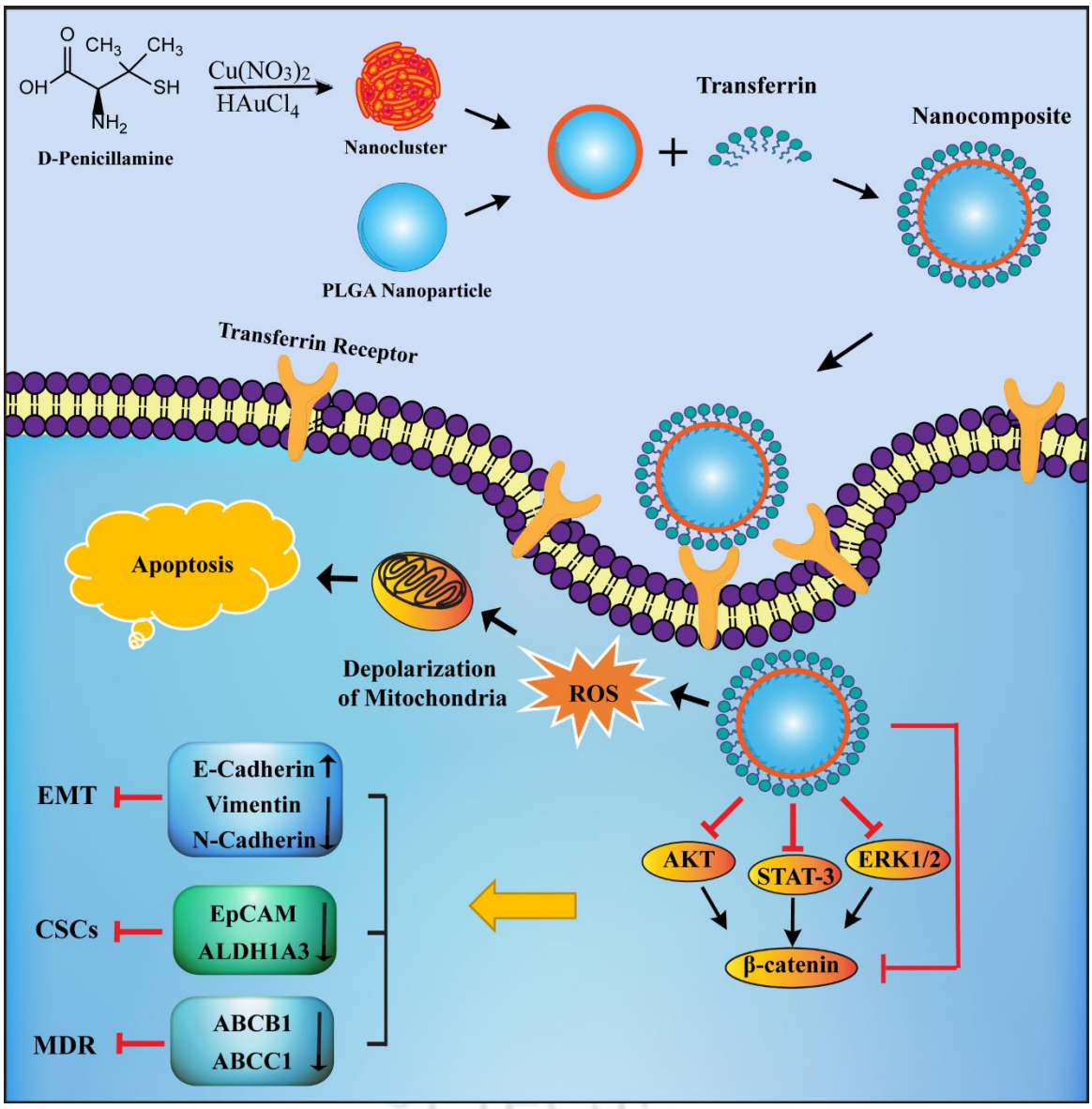

Scheme 3.3: Synthesis of nanocomposites and overall observable cellular events following uptake.

Section 4

Conclusion and Future Prospects

Conclusion and Future Prospects

Multiple signaling pathways have been discovered in TNBC to be involved in triggering EMT and sustaining CSC characteristics. Numerous cross-talks and feedback loops, as well as their critical involvement in normal cellular developmental processes, make it nearly impossible to precisely target them and stop EMT progression. The current study has focused on finding and targeting the pathways, which represents significant vulnerability of TNBC and assist in EMT advancement. Furthermore, FDA approved drug was repurposed for TNBC therapy using nanocarrier mediated targeted drug delivery.

The salient conclusions of the work have been categorized under three major subheadings and delineated below:

Targeting Signaling Pathways to Alter EMT and MDR Dynamics of TNBC.

- EGFR and Wnt/β-catenin signaling pathway were co-targeted to modulate the EMT and MDR dynamics of TNBC.
- Co-targeting these pathways incurred the phase transition from epithelial to mesenchymal transition (EMT) to mesenchymal to epithelial transition (MET).
- The inhibitor combination successfully downregulated the expression of ABC transporters ABCB1, ABCG2 and ABCC1 responsible for MDR.
- Regulation of EMT and MDR adroitly inhibited the migration and invasion capacity of TNBC cell line MDA-MB-231.
- The reduced expression level of pro-survival signals such as pEGFR, pAKT, pMAPK, pSTAT-3, pGSK-3β and β-catenin reveals the complex crosstalk of downstream signaling associated with EGFR and Wnt/β-catenin.

- Cytotoxicity studies on several cancer cell lines demonstrated a remarkable dose-dependent decrease in cell viability following combination treatment and synergistic interaction between inhibitors.
- Deploying multicellular tumor spheroids, which mimicked *in vivo* condition, helped to understand the complex signaling behavior of the solid tumor and assess the efficacy of the inhibitor combination.
- The findings highlight the potential of incapacitating EMT and MDR by co-targeting EGFR and WNT/β-catenin signaling pathway components for better efficacy in TNBC.
- In conclusion, the insight gained in the present study reveals the complex EMT and MDR associated crosstalk, which was explored systematically to target its components effectively and circumscribe invasiveness and metastasis.

Exploiting the Interplay Between EMT and Autophagy to Restrain Metastatic TNBC.

- A multifunctional stress-inducible scaffold protein SQSTM1/P62 was targeted using siRNA which is critically involved at the interface of autophagy and EMT.
- Co-targeting SQSTM1/P62 and Wnt/β-catenin pathway induced the phase transition from epithelial to mesenchymal transition (EMT) to mesenchymal to epithelial transition (MET).
- Regulation of SQSTM1/P62 and Wnt/β-catenin pathway repressed mesenchymal differentiation and stemness of TNBC.
- Gene expression analysis revealed downregulated the expression of ABC transporters ABCB1, ABCG2 and ABCC1 responsible for MDR following co-treatment.

- Suppression of SQSTM1/P62 and Wnt/β-Catenin signaling decreases the migration and invasion potential of TNBC.
- Knockdown of SQSTM1/P62 resulted in inactivation of non-canonical Wnt VANGL2-JNK signaling axis
- Suppression of SQSTM1/P62 depleted activated form of AKT and alteration of Wnt/β-Catenin signaling down-regulated activated form of STAT-3
- EMT induction by EGF induced autophagy and inhibition of Wnt/β-Catenin signaling by FH535 repressed autophagic activity.
- The molecular alterations in downstream signaling have been mapped out in great detail. Nonetheless, the results of the experiments show that modulation of SQSTM1/P62 and Wnt/β-Catenin signaling have the ability to disable EMT and stemness of TNBC for enhanced effectiveness.
- To summarize, the findings of this study highlight the complicated EMT and Autophagy linked crosstalk, which was investigated in depth in order to effectively target its components and limit invasiveness and metastasis.

Targeting TNBC by Nanocarrier Mediated Targeted Delivery of Novel Drugs.

- A novel therapeutic module has been fabricated by coating a non-toxic, biodegradable PLGA nanoparticle core with D-penicillamine templated Au-Cu bimetallic nanoclusters. Further, the resultant nanomaterials were coated with recombinant transferrin protein to specifically target transferrin receptor overexpressing cancer cells.
- The synthesized nanocomposites showed strong orange emission band at 630 nm with fluorescence quantum yield of 2%, rendering it suitable for theranostic applications.

- Application of the nanocomposites incurred the phase transition from epithelial to mesenchymal transition (EMT) to mesenchymal to epithelial transition (MET).
- The nanocomposites successfully downregulated the expression of ABC transporters ABCB1 and ABCC1 responsible for multidrug resistance (MDR).
- Regulation of EMT and MDR adroitly inhibited the migration capacity of TNBC cell line MDA-MB-231 and MDA-MB-468.
- The application of the nanocomposites reduced the expression level of pro-survival signals such as pAKT, pMAPK, pSTAT-3, and β-catenin and prevented downstream crosstalk by targeting multiple signal-nodes
- Cytotoxicity studies on several cancer cell lines demonstrated a remarkable dose-dependent decrease in cell viability following treatment with nanocomposites.
- Calcein AM/PI dual staining and apoptosis assay reveal efficient apoptosis mediated cell death upon treatment with the nanocomposites.
- Deploying multicellular tumor spheroids, which mimicked *in vivo* conditions, helped to assess the efficacy of the nanocomposites.
- The detailed molecular changes in downstream signaling have been delineated. Nonetheless, experimental findings highlight the potential of incapacitating EMT and MDR by nanocomposites for better efficacy in TNBC.
- In conclusion, the insight gained in the study reveals that with further standardization, the nanocomposites have therapeutic potential to combat the dreadful TNBC.

Future Prospects:

The future scope of the work based on current investigations include

- Insights gained into the signaling pathways contributing to EMT, stemness and MDR may open a new vista for TNBC therapy.

- Alternative signaling pathways contributing to EMT may be studied in detail.
- The difference in molecular response following treatment in monolayer culture and spheroids may be explored in detail.
- To test the efficacy of the co-treatments, the reduction in migration and invasion potential may be examined *in vivo* for its translational potential.
- *In vivo* investigations might help to improve the nanocomposite and standardize it for use as a therapeutic module.

References

1 J.E. TalmadgeI.J.J.C.r. Fidler, AACR centennial series: the biology of cancer metastasis: historical perspective. **70**, 5649-5669 (2010)

2 C.-J. Li, P.-Y. Chu, G.-T. YiangM.-Y.J.B. Wu, The Molecular Mechanism of Epithelial–Mesenchymal Transition for Breast Carcinogenesis. **9**, 476 (2019)

3 J.M. Lee, S. Dedhar, R. KalluriE.W.J.J.o.C.B. Thompson, The epithelial–mesenchymal transition: new insights in signaling, development, and disease. **172**, 973-981 (2006)

4 V.L. Battula, K.W. Evans, B.G. Hollier, Y. Shi, F.C. Marini, A. Ayyanan, R.y. Wang, C. Brisken, R. GuerraM.J.S.c. Andreeff, Epithelial-mesenchymal transition-derived cells exhibit multilineage differentiation potential similar to mesenchymal stem cells. **28**, 1435-1445 (2010)

5 S. Lamouille, J. XuR.J.N.r.M.c.b. Derynck, Molecular mechanisms of epithelial–mesenchymal transition. **15**, 178-196 (2014)

6 J.P. Thiery, H. Acloque, R.Y. HuangM.A.J.c. Nieto, Epithelial-mesenchymal transitions in development and disease. **139**, 871-890 (2009)

7 J.J.C. Roche, (Multidisciplinary Digital Publishing Institute, 2018), p. 52

8 B. De CraeneG.J.N.R.C. Berx, Regulatory networks defining EMT during cancer initiation and progression. **13**, 97-110 (2013)

9 V. Petrova, M. Annicchiarico-Petruzzelli, G. MelinoI.J.O. Amelio, The hypoxic tumour microenvironment. **7**, 1-13 (2018)

10 R. Xu, J.-Y. Won, C.-H. Kim, D.-E. KimH.J.J.o.o. Yim, Roles of the phosphorylation of transcriptional factors in epithelial-mesenchymal transition. **2019**, (2019)

11 W. LuY.J.D.c. Kang, Epithelial-mesenchymal plasticity in cancer progression and metastasis. **49**, 361-374 (2019)

12 L. Bai, S. Shin, R.T. Burnett, J.C. Kwong, P. Hystad, A. van Donkelaar, M.S. Goldberg, E. Lavigne, S. WeichenthalR.V.J.I.j.o.c. Martin, Exposure to ambient air pollution and the incidence of lung cancer and breast cancer in the Ontario Population Health and Environment Cohort. **146**, 2450-2459 (2020)

13 C. AndersL.A.J.O. Carey, Understanding and treating triple-negative breast cancer. **22**, 1233 (2008)

14 S. Al-Mahmood, J. Sapiezynski, O.B. Garbuzenko, T.J.D.d. Minkot. research, Metastatic and triple-negative breast cancer: challenges and treatment options. **8**, 1483-1507 (2018)

15 L. Yin, J.-J. Duan, X.-W. BianS.-c.J.B.C.R. Yu, Triple-negative breast cancer molecular subtyping and treatment progress. **22**, 1-13 (2020)

16 E. Lee, R. McKean-Cowdin, H. Ma, D.V. Spicer, D. Van Den Berg, L. BernsteinG.J.J.o.C.O. Ursin, Characteristics of triple-negative breast cancer in patients with a BRCA1 mutation: results from a population-based study of young women. **29**, 4373 (2011)

17 A.C. Garrido-Castro, N.U. LinK.J.C.d. Polyak, Insights into molecular classifications of triple-negative breast cancer: improving patient selection for treatment. **9**, 176-198 (2019)

18 M. Fedele, L. CerchiaG.J.C. Chiappetta, The epithelial-to-mesenchymal transition in breast cancer: focus on basal-like carcinomas. **9**, 134 (2017)

19 S.A. Mani, W. Guo, M.-J. Liao, E.N. Eaton, A. Ayyanan, A.Y. Zhou, M. Brooks, F. Reinhard, C.C. ZhangM.J.C. Shipitsin, The epithelial-mesenchymal transition generates cells with properties of stem cells. **133**, 704-715 (2008)

20 E.M. De Francesco, F. SotgiaM.P.J.B.J. Lisanti, Cancer stem cells (CSCs): metabolic strategies for their identification and eradication. **475**, 1611-1634 (2018)

21 A. Agliano, A. CalvoC. Box, in Seminars in Cancer Biology, (Elsevier, 2017), p. 25-42

22 L. Yang, P. Shi, G. Zhao, J. Xu, W. Peng, J. Zhang, G. Zhang, X. Wang, Z. Dong, F.J.S.t. Chent. therapy, Targeting cancer stem cell pathways for cancer therapy. **5**, 1-35 (2020)

23 G.V. Vijay, N. Zhao, P. Den Hollander, M.J. Toneff, R. Joseph, M. Pietila, J.H. Taube, T.R. Sarkar, E. Ramirez-PenaS.J.J.B.C.R. Werden, GSK3β regulates epithelial-mesenchymal transition and cancer stem cell properties in triple-negative breast cancer. **21**, 1-14 (2019)

24 D. HanahanR.A.J.c. Weinberg, Hallmarks of cancer: the next generation. **144**, 646-674 (2011)
25 C.A. O'Brien, A. Pollett, S. GallingerJ.E.J.N. Dick, A human colon cancer cell capable of initiating tumour growth in immunodeficient mice. **445**, 106-110 (2007)
26 A. Kreso, C.A. O'Brien, P. Van Galen, O.I. Gan, F. Notta, A.M. Brown, K. Ng, J. Ma, E. WienholdsC.J.S. Dunant, Variable clonal repopulation dynamics influence chemotherapy response in colorectal cancer. **339**, 543-548 (2013)
27 W. Matsui, C.A. Huff, Q. Wang, M.T. Malehorn, J. Barber, Y. Tanhehco, B.D. Smith, C.I. CivinR.J.J.B. Jones, Characterization of clonogenic multiple myeloma cells. **103**, 2332-2336 (2004)
28 D. BonnetJ.E.J.N.m. Dick, Human acute myeloid leukemia is organized as a hierarchy that originates from a primitive hematopoietic cell. **3**, 730-737 (1997)
29 M.J. Bissell, H.G. HallG.J.J.o.t.b. Parry, How does the extracellular matrix direct gene expression? **99**, 31-68 (1982)
30 X. Zheng, J.L. Carstens, J. Kim, M. Scheible, J. Kaye, H. Sugimoto, C.-C. Wu, V.S. LeBleuR.J.N. Kalluri, Epithelial-to-mesenchymal transition is dispensable for metastasis but induces chemoresistance in pancreatic cancer. **527**, 525-530 (2015)
31 S. Senapati, A.K. Mahanta, S. Kumar, P.J.S.t. Maitit. therapy, Controlled drug delivery vehicles for cancer treatment and their performance. **3**, 1-19 (2018)
32 Y. ChoY.K.J.F.i.O. Kim, Cancer stem cells as a potential target to overcome multidrug resistance. **10**, 764 (2020)
33 S.K. Singh, C. Hawkins, I.D. Clarke, J.A. Squire, J. Bayani, T. Hide, R.M. Henkelman, M.D. CusimanoP.B.J.n. Dirks, Identification of human brain tumour initiating cells. **432**, 396-401 (2004)
34 L. Zinzi, M. Contino, M. Cantore, E. Capparelli, M. LeopoldoN.A.J.F.i.p. Colabufo, ABC transporters in CSCs membranes as a novel target for treating tumor relapse. **5**, 163 (2014)
35 D.C. Rees, E. JohnsonO.J.N.r.M.c.b. Lewinson, ABC transporters: the power to change. **10**, 218-227 (2009)
36 R.-R. BegicevicM.J.I.j.o.m.s. Falasca, ABC transporters in cancer stem cells: beyond chemoresistance. **18**, 2362 (2017)
37 E.A.J.M.c.t. Perez, Microtubule inhibitors: Differentiating tubulin-inhibiting agents based on mechanisms of action, clinical activity, and resistance. **8**, 2086-2095 (2009)
38 T. Zhan, N. RindtorffM.J.O. Boutros, Wnt signaling in cancer. **36**, 1461-1473 (2017)
39 S.-L. Lai, A.J. ChienR.T.J.C.r. Moon, Wnt/Fz signaling and the cytoskeleton: potential roles in tumorigenesis. **19**, 532-545 (2009)
40 M.J. Parsons, T. TammelaL.E.J.C.D. Dow, WNT as a Driver and Dependency in Cancer. **11**, 2413-2429 (2021)
41 B.T. MacDonald, K. TamaiX.J.D.c. He, Wnt/β-catenin signaling: components, mechanisms, and diseases. **17**, 9-26 (2009)
42 Y. Lecarpentier, O. Schussler, J.-L. HébertA.J.F.i.o. Vallée, Multiple targets of the canonical WNT/β-catenin signaling in cancers. **9**, 1248 (2019)
43 G.S. Yochum, C.M. Sherrick, M. MacPartlinR.H.J.P.o.t.N.A.o.S. Goodman, A β-catenin/TCF-coordinated chromatin loop at MYC integrates 5' and 3' Wnt responsive enhancers. **107**, 145-150 (2010)
44 V.d. Stemmer, B. De Craene, G. BerxJ.J.O. Behrens, Snail promotes Wnt target gene expression and interacts with β-catenin. **27**, 5075-5080 (2008)
45 P. Mishra, S. Senthivinayagam, A. RanaB.J.J.o.m.s. Rana, Glycogen Synthase Kinase-3beta regulates Snail and beta-catenin during gastrin-induced migration of gastric cancer cells. **5**, 1-10 (2010)
46 H.S. Park, M.H. Jang, E.J. Kim, H.J. Kim, H.J. Lee, Y.J. Kim, J.H. Kim, E. Kang, S.-W. KimI.A.J.M.p. Kim, High EGFR gene copy number predicts poor outcome in triple-negative breast cancer. **27**, 1212-1222 (2014)
47 A. Simiczyjew, E. Dratkiewicz, M. Van Troys, C. Ampe, I. StyczeńD.J.C. Nowak, Combination of EGFR inhibitor lapatinib and MET inhibitor foretinib inhibits migration of triple negative breast cancer cell lines. **10**, 335 (2018)
48 E.-L. EskelinenP.J.B.e.B.A.-M.C.R. Saftig, Autophagy: a lysosomal degradation pathway with a central role in health and disease. **1793**, 664-673 (2009)
49 A.L. AndingE.H.J.D.c. Baehrecke, Cleaning house: selective autophagy of organelles. **41**, 10-22 (2017)
50 E.E. Mowers, M.N. SharifiK.F.J.O. Macleod, Autophagy in cancer metastasis. **36**, 1619-1630 (2017)
51 H.R. Yun, Y.H. Jo, J. Kim, Y. Shin, S.S. KimT.G.J.I.j.o.m.s. Choi, Roles of autophagy in oxidative stress. **21**, 3289 (2020)

52 D. Glick, S. BarthK.F.J.T.J.o.p. Macleod, Autophagy: cellular and molecular mechanisms. **221**, 3-12 (2010)
53 E. WhiteR.S.J.C.c.r. DiPaola, The double-edged sword of autophagy modulation in cancer. **15**, 5308-5316 (2009)
54 M. Gugnoni, V. Sancisi, G. Manzotti, G. Gandolfi, A.J.C.d. Ciarrocchidisease, Autophagy and epithelial–mesenchymal transition: an intricate interplay in cancer. **7**, e2520-e2520 (2016)
55 L. Bao, P.K. Chandra, K. Moroz, X. Zhang, S.N. Thung, T. Wu, S.J.E. Dashm. pathology, Impaired autophagy response in human hepatocellular carcinoma. **96**, 149-154 (2014)
56 L. Li, C. Shen, E. Nakamura, K. Ando, S. Signoretti, R. Beroukhim, G.S. Cowley, P. Lizotte, E. LiberzonS.J.C.c. Bair, SQSTM1 is a pathogenic target of 5q copy number gains in kidney cancer. **24**, 738-750 (2013)
57 Q. Yang, M.-X. Zhang, X. Zou, Y.-P. Liu, R. You, T. Yu, R. Jiang, Y.-N. Zhang, J.-Y. CaoM.-H.J.C.C.R. Hong, A prognostic bio-model based on SQSTM1 and N-stage identifies nasopharyngeal carcinoma patients at high risk of metastasis for additional induction chemotherapy. **24**, 648-658 (2018)
58 S.J. Serrano-Gomez, M. MaziveyiS.K.J.M.c. Alahari, Regulation of epithelial-mesenchymal transition through epigenetic and post-translational modifications. **15**, 1-14 (2016)
59 R. KalluriR.A.J.T.J.o.c.i. Weinberg, The basics of epithelial-mesenchymal transition. **119**, 1420-1428 (2009)
60 A.W. Lambert, D.R. PattabiramanR.A.J.C. Weinberg, Emerging biological principles of metastasis. **168**, 670-691 (2017)
61 L. Qiang, B. Zhao, M. Ming, N. Wang, T.-C. He, S. Hwang, A. ThorburnY.-Y.J.P.o.t.N.A.o.S. He, Regulation of cell proliferation and migration by p62 through stabilization of Twist1. **111**, 9241-9246 (2014)
62 A. Barrallo-GimenoM.A. Nieto, The Snail genes as inducers of cell movement and survival: implications in development and cancer. (2005)
63 M. Bertrand, V. Petit, A. Jain, R. Amsellem, T. Johansen, L. Larue, P. CodognoI.J.C.C. Beau, SQSTM1/p62 regulates the expression of junctional proteins through epithelial-mesenchymal transition factors. **14**, 364-374 (2015)
64 S.-S. Li, L.-Z. Xu, W. Zhou, S. Yao, C.-L. Wang, J.-L. Xia, H.-F. Wang, M. Kamran, X.-Y. XueL.J.C. Dong, p62/SQSTM1 interacts with vimentin to enhance breast cancer metastasis. **38**, 1092-1103 (2017)
65 C. HillY.J.C.d.r. Wang, The importance of epithelial-mesenchymal transition and autophagy in cancer drug resistance. **3**, 38 (2020)
66 R. Mathew, S. Kongara, B. Beaudoin, C.M. Karp, K. Bray, K. Degenhardt, G. Chen, S. Jin, E.J.G. Whitedevelopment, Autophagy suppresses tumor progression by limiting chromosomal instability. **21**, 1367-1381 (2007)
67 X. Jiang, Y. Huang, X. Liang, F. Jiang, Y. He, T. Li, G. Xu, H. Zhao, W. YangG.J.T.P. Jiang, Metastatic prostate cancer-associated P62 inhibits autophagy flux and promotes epithelial to mesenchymal transition by sustaining the level of HDAC6. **78**, 426-434 (2018)
68 R. Mathew, C.M. Karp, B. Beaudoin, N. Vuong, G. Chen, H.-Y. Chen, K. Bray, A. Reddy, G. BhanotC.J.C. Gelinas, Autophagy suppresses tumorigenesis through elimination of p62. **137**, 1062-1075 (2009)
69 C. Liang, J. Xu, Q. Meng, B. Zhang, J. Liu, J. Hua, Y. Zhang, S. ShiX.J.A. Yu, TGFB1-induced autophagy affects the pattern of pancreatic cancer progression in distinct ways depending on SMAD4 status. **16**, 486-500 (2020)
70 H.-T. Chen, H. Liu, M.-J. Mao, Y. Tan, X.-Q. Mo, X.-J. Meng, M.-T. Cao, C.-Y. Zhong, Y. LiuH.J.M.c. Shan, Crosstalk between autophagy and epithelial-mesenchymal transition and its application in cancer therapy. **18**, 1-19 (2019)
71 Y. Han, Y. An, G. Jia, X. Wang, C. He, Y. DingQ.J.J.o.n. Tang, Facile assembly of upconversion nanoparticle-based micelles for active targeted dual-mode imaging in pancreatic cancer. **16**, 1-13 (2018)
72 P. Wu, Q. Zhou, H. Zhu, Y. ZhuangJ.J.B.c. Bao, Enhanced antitumor efficacy in colon cancer using EGF functionalized PLGA nanoparticles loaded with 5-Fluorouracil and perfluorocarbon. **20**, 1-10 (2020)
73 Y. Su, T. Xue, Y. Liu, J. Qi, R. JinZ.J.N.R. Lin, Luminescent metal nanoclusters for biomedical applications. **12**, 1251-1265 (2019)
74 Y. Wang, X.H. Liu, S.A. Kovalenko, Q.Y. ChenN.J.C.A.E.J. Pinna, Atomically Precise Bimetallic Nanoclusters as Photosensitizers in Photoelectrochemical Cells. **25**, 4814-4820 (2019)
75 N. KerkarE.A. Roberts, Clinical and translational perspectives on WILSON DISEASE, (Academic Press, 2018).

76 A. Gupte, R.J.J.F.R.B. MumperMedicine, Copper chelation by D-penicillamine generates reactive oxygen species that are cytotoxic to human leukemia and breast cancer cells. **43**, 1271-1278 (2007)
77 E.L. Mackenzie, K. Iwasaki, Y.J.A. Tsujir. signaling, Intracellular iron transport and storage: from molecular mechanisms to health implications. **10**, 997-1030 (2008)
78 K.M. Mayle, A.M. LeD.T.J.B.e.B.A.-G.S. Kamei, The intracellular trafficking pathway of transferrin. **1820**, 264-281 (2012)
79 A. IvascuM.J.J.o.b.s. Kubbies, Rapid generation of single-tumor spheroids for high-throughput cell function and toxicity analysis. **11**, 922-932 (2006)
80 J. Friedrich, C. Seidel, R. EbnerL.A.J.N.p. Kunz-Schughart, Spheroid-based drug screen: considerations and practical approach. **4**, 309-324 (2009)
81 A. Walzl, C. Unger, N. Kramer, D. Unterleuthner, M. Scherzer, M. Hengstschläger, D. Schwanzer-PfeifferH.J.J.o.b.s. Dolznig, The resazurin reduction assay can distinguish cytotoxic from cytostatic compounds in spheroid screening assays. **19**, 1047-1059 (2014)
82 T.-C. ChouP.J.A.i.e.r. Talalay, Quantitative analysis of dose-effect relationships: the combined effects of multiple drugs or enzyme inhibitors. **22**, 27-55 (1984)
83 C. RiccardiI.J.N.p. Nicoletti, Analysis of apoptosis by propidium iodide staining and flow cytometry. **1**, 1458-1461 (2006)
84 A. Perelman, C. Wachtel, M. Cohen, S. Haupt, H. Shapiro, A.J.C.d. Tzurdisease, JC-1: alternative excitation wavelengths facilitate mitochondrial membrane potential cytometry. **3**, e430-e430 (2012)
85 D.J.C. Bratosin, Part A. A, Mitrofan L. Palii C. Estaquier J. Montreuil J. **66**, 78-84 (2005)
86 L.C. Crowley, A.P. Scott, B.J. Marfell, J.A. Boughaba, G. ChojnowskiN.J.J.C.S.H.P. Waterhouse, Measuring cell death by propidium iodide uptake and flow cytometry. **2016**, pdb. prot087163 (2016)
87 X. Rao, X. Huang, Z. Zhou, X.J.B. Lin, bioinformaticsbiomathematics, An improvement of the 2ˆ (–delta delta CT) method for quantitative real-time polymerase chain reaction data analysis. **3**, 71 (2013)
88 H. Wu, S. Wang, D. Weng, H. Xing, X. Song, T. Zhu, X. Xia, Y. Weng, G. XuL.J.C.l. Meng, Reversal of the malignant phenotype of ovarian cancer A2780 cells through transfection with wild-type PTEN gene. **271**, 205-214 (2008)
89 W.-L. Chen, K.-T. Kuo, T.-Y. Chou, C.-L. Chen, C.-H. Wang, Y.-H. WeiL.-S.J.B.c. Wang, The role of cytochrome c oxidase subunit Va in non-small cell lung carcinoma cells: association with migration, invasion and prediction of distant metastasis. **12**, 1-13 (2012)
90 L.C. Crowley, M.E. ChristensenN.J.J.C.S.H.P. Waterhouse, Measuring survival of adherent cells with the colony-forming assay. **2016**, pdb. prot087171 (2016)
91 W. HuangC.J.B.j. Zhang, Tuning the size of poly (lactic-co-glycolic acid)(PLGA) nanoparticles fabricated by nanoprecipitation. **13**, 1700203 (2018)
92 F.J.I.J.o.P. Nachtmann, Determination of the L-isomer in D-penicillamine by derivatization liquid chromatography. **4**, 337-345 (1980)
93 B. Bao, C. Mitrea, P. Wijesinghe, L. Marchetti, E. Girsch, R.L. Farr, J.L. Boerner, R. Mohammad, G. DysonS.R.J.S.r. Terlecky, Treating triple negative breast cancer cells with erlotinib plus a select antioxidant overcomes drug resistance by targeting cancer cell heterogeneity. **7**, 1-11 (2017)
94 B.R. Topacio, E. Zatulovskiy, S. Cristea, S. Xie, C.S. Tambo, S.M. Rubin, J. Sage, M. KõivomägiJ.M.J.M.c. Skotheim, Cyclin D-Cdk4, 6 drives cell-cycle progression via the retinoblastoma protein's C-terminal helix. **74**, 758-770. e754 (2019)
95 M. Redza-DutordoirD.A.J.B.e.B.A.-M.C.R. Averill-Bates, Activation of apoptosis signalling pathways by reactive oxygen species. **1863**, 2977-2992 (2016)
96 J.M. Matés, F.M.J.T.i.j.o.b. Sánchez-Jiménezc. biology, Role of reactive oxygen species in apoptosis: implications for cancer therapy. **32**, 157-170 (2000)
97 N.J.C.c.i. Pećina-Šlaus, Tumor suppressor gene E-cadherin and its role in normal and malignant cells. **3**, 1-7 (2003)
98 A. Satelli, S.J.C. Lim.l. sciences, Vimentin in cancer and its potential as a molecular target for cancer therapy. **68**, 3033-3046 (2011)
99 K.M. Mrozik, O.W. Blaschuk, C.M. Cheong, A.C.W. ZannettinoK.J.B.c. Vandyke, N-cadherin in cancer metastasis, its emerging role in haematological malignancies and potential as a therapeutic target in cancer. **18**, 1-16 (2018)
100 M.-H. Wang, R. Sun, X.-M. Zhou, M.-Y. Zhang, J.-B. Lu, Y. Yang, L.-S. Zeng, X.-Z. Yang, L. Shi, R.-W.J.C.d. Xiaodisease, Epithelial cell adhesion molecule overexpression regulates epithelial-mesenchymal

transition, stemness and metastasis of nasopharyngeal carcinoma cells via the PTEN/AKT/mTOR pathway. **9**, 1-16 (2018)
101 U.M. MollO.J.M.c.r. Petrenko, The MDM2-p53 interaction. **1**, 1001-1008 (2003)
102 W. SunL.J.C.m.c. Tang, MDM2 increases drug resistance in cancer cells by inducing EMT independent of p53. **23**, 4529-4539 (2016)
103 Z.C. Nwosu, M.P. Ebert, S. DooleyC.J.M.c. Meyer, Caveolin-1 in the regulation of cell metabolism: a cancer perspective. **15**, 1-12 (2016)
104 C.-l. Dai, A.K. Tiwari, C.-P. Wu, X.-d. Su, S.-R. Wang, D.-g. Liu, C.R. Ashby, Y. Huang, R.W. RobeyY.-j.J.C.r. Liang, Lapatinib (Tykerb, GW572016) reverses multidrug resistance in cancer cells by inhibiting the activity of ATP-binding cassette subfamily B member 1 and G member 2. **68**, 7905-7914 (2008)
105 C. Garay, G. Judge, S. Lucarelli, S. Bautista, R. Pandey, T. SinghC.N.J.M.b.o.t.c. Antonescu, Epidermal growth factor–stimulated Akt phosphorylation requires clathrin or ErbB2 but not receptor endocytosis. **26**, 3504-3519 (2015)
106 Y. Wang, S. Pennock, X. Chen, Z.J.M. Wangc. biology, Endosomal signaling of epidermal growth factor receptor stimulates signal transduction pathways leading to cell survival. **22**, 7279-7290 (2002)
107 Q. Ryan, A. Ibrahim, M.H. Cohen, J. Johnson, C.w. Ko, R. Sridhara, R. JusticeR.J.T.o. Pazdur, FDA drug approval summary: lapatinib in combination with capecitabine for previously treated metastatic breast cancer that overexpresses HER-2. **13**, 1114-1119 (2008)
108 N. KrishnamurthyR.J.C.t.r. Kurzrock, Targeting the Wnt/beta-catenin pathway in cancer: Update on effectors and inhibitors. **62**, 50-60 (2018)
109 M.J.N.r.D.d. Kahn, Can we safely target the WNT pathway? **13**, 513-532 (2014)
110 A.I. MinchintonI.F.J.N.R.C. Tannock, Drug penetration in solid tumours. **6**, 583-592 (2006)
111 E.C. Costa, A.F. Moreira, D. de Melo-Diogo, V.M. Gaspar, M.P. CarvalhoI.J.J.B.a. Correia, 3D tumor spheroids: an overview on the tools and techniques used for their analysis. **34**, 1427-1441 (2016)
112 O. TetsuF.J.N. McCormick, β-Catenin regulates expression of cyclin D1 in colon carcinoma cells. **398**, 422-426 (1999)
113 I. Hadžisejdić, E. Mustać, N. Jonjić, M. PetkovićB.J.M.p. Grahovac, Nuclear EGFR in ductal invasive breast cancer: correlation with cyclin-D1 and prognosis. **23**, 392-403 (2010)
114 C.P. MasamhaD.M.J.C.r. Benbrook, Cyclin D1 degradation is sufficient to induce G1 cell cycle arrest despite constitutive expression of cyclin E2 in ovarian cancer cells. **69**, 6565-6572 (2009)
115 Y. Jiang, X. Wang, D.J.C.D. HuDisease, Furanodienone induces G0/G1 arrest and causes apoptosis via the ROS/MAPKs-mediated caspase-dependent pathway in human colorectal cancer cells: a study in vitro and in vivo. **8**, e2815-e2815 (2017)
116 H.-R. Teppo, Y. Soini, P.J.O.m. Karihtalac. longevity, Reactive oxygen species-mediated mechanisms of action of targeted cancer therapy. **2017**, (2017)
117 K.M. Aird, J.L. Allensworth, I. Batinic-Haberle, H.K. Lyerly, M.W. Dewhirst, G.R.J.B.c.r. Devitreatment, ErbB1/2 tyrosine kinase inhibitor mediates oxidative stress-induced apoptosis in inflammatory breast cancer cells. **132**, 109-119 (2012)
118 J. Chandra, A. Samali, S.J.F.r.b. Orreniusmedicine, Triggering and modulation of apoptosis by oxidative stress. **29**, 323-333 (2000)
119 R. Nahta, L.X. Yuan, Y. DuF.J.J.M.c.t. Esteva, Lapatinib induces apoptosis in trastuzumab-resistant breast cancer cells: effects on insulin-like growth factor I signaling. **6**, 667-674 (2007)
120 X.-H. Tian, W.-J. Hou, Y. Fang, J. Fan, H. Tong, S.-L. Bai, Q. Chen, H. Xu, Y.J.J.o.E. LiC.C. Research, XAV939, a tankyrase 1 inhibitior, promotes cell apoptosis in neuroblastoma cell lines by inhibiting Wnt/β-catenin signaling pathway. **32**, 1-9 (2013)
121 C.-Y. Liu, M.-H. Hu, C.-J. Hsu, C.-T. Huang, D.-S. Wang, W.-C. Tsai, Y.-T. Chen, C.-H. Lee, P.-Y. ChuC.-C.J.O. Hsu, Lapatinib inhibits CIP2A/PP2A/p-Akt signaling and induces apoptosis in triple negative breast cancer cells. **7**, 9135 (2016)
122 K.B.J.B.C.-F.T.M. Yin, Stem cellsMetastasis, The mesenchymal-like phenotype of the MDA-MB-231 cell line. 385-402 (2011)
123 Y.-C. Hsiao, M.-H. Yeh, Y.-J. Chen, J.-F. Liu, C.-H. TangW.-C.J.O. Huang, Lapatinib increases motility of triple-negative breast cancer cells by decreasing miRNA-7 and inducing Raf-1/MAPK-dependent interleukin-6. **6**, 37965 (2015)
124 Z.C. Hartman, G.M. Poage, P. Den Hollander, A. Tsimelzon, J. Hill, N. Panupinthu, Y. Zhang, A. Mazumdar, S.G. HilsenbeckG.B.J.C.r. Mills, Growth of triple-negative breast cancer cells relies upon coordinate autocrine expression of the proinflammatory cytokines IL-6 and IL-8. **73**, 3470-3480 (2013)

125 J.W. Polli, J.E. Humphreys, K.A. Harmon, S. Castellino, M.J. O'mara, K.L. Olson, L.S. John-Williams, K.M. Koch, C.J.J.D.m. Serabjit-Singhdisposition, The role of efflux and uptake transporters in N-{3-chloro-4-[(3-fluorobenzyl) oxy] phenyl}-6-[5-({[2-(methylsulfonyl) ethyl] amino} methyl)-2-furyl]-4-quinazolinamine (GW572016, lapatinib) disposition and drug interactions. **36**, 695-701 (2008)
126 X. He, J. Wang, W. Wei, M. Shi, B. Xin, T. Zhang, X.J.C.b. Shentherapy, Hypoxia regulates ABCG2 activity through the activivation of ERK1/2/HIF-1α and contributes to chemoresistance in pancreatic cancer cells. **17**, 188-198 (2016)
127 Q.-Q. Li, J.-D. Xu, W.-J. Wang, X.-X. Cao, Q. Chen, F. Tang, Z.-Q. Chen, X.-P. LiuZ.-D.J.C.c.r. Xu, Twist1-mediated adriamycin-induced epithelial-mesenchymal transition relates to multidrug resistance and invasive potential in breast cancer cells. **15**, 2657-2665 (2009)
128 G. Civenni, T. HolbroN.E.J.E.r. Hynes, Wnt1 and Wnt5a induce cyclin D1 expression through ErbB1 transactivation in HC11 mammary epithelial cells. **4**, 166-171 (2003)
129 P. WeeZ.J.C. Wang, Epidermal growth factor receptor cell proliferation signaling pathways. **9**, 52 (2017)
130 M.K. Ghosh, P. Sharma, P.C. Harbor, S.O. RahamanS.J.J.O. Haque, PI3K-AKT pathway negatively controls EGFR-dependent DNA-binding activity of Stat3 in glioblastoma multiforme cells. **24**, 7290-7300 (2005)
131 J. Gyamfi, Y.-H. Lee, M. EomJ.J.S.r. Choi, Interleukin-6/STAT3 signalling regulates adipocyte induced epithelial-mesenchymal transition in breast cancer cells. **8**, 1-13 (2018)
132 W.-J. Jeong, E.J. RoK.-Y.J.N.P.o. Choi, Interaction between Wnt/β-catenin and RAS-ERK pathways and an anti-cancer strategy via degradations of β-catenin and RAS by targeting the Wnt/β-catenin pathway. **2**, 1-10 (2018)
133 M.A. Fragoso, A.K. Patel, R.E. Nakamura, H. Yi, K. SurapaneniA.S. Hackam, The Wnt/β-catenin pathway cross-talks with STAT3 signaling to regulate survival of retinal pigment epithelium cells. (2012)
134 N.T. Georgopoulos, L.A. KirkwoodJ.J.J.o.c.s. Southgate, A novel bidirectional positive-feedback loop between Wnt–β-catenin and EGFR–ERK plays a role in context-specific modulation of epithelial tissue regeneration. **127**, 2967-2982 (2014)
135 C. Metcalfe, C. Mendoza-Topaz, J. MieszczanekM.J.J.o.c.s. Bienz, Stability elements in the LRP6 cytoplasmic tail confer efficient signalling upon DIX-dependent polymerization. **123**, 1588-1599 (2010)
136 J.M. Dolle, J.R. Daling, E. White, L.A. Brinton, D.R. Doody, P.L. Porter, K.E.J.C.E. MaloneP. Biomarkers, Risk factors for triple-negative breast cancer in women under the age of 45 years. **18**, 1157-1166 (2009)
137 S.J. Grille, A. Bellacosa, J. Upson, A.J. Klein-Szanto, F. Van Roy, W. Lee-Kwon, M. Donowitz, P.N. TsichlisL.J.C.r. Larue, The protein kinase Akt induces epithelial mesenchymal transition and promotes enhanced motility and invasiveness of squamous cell carcinoma lines. **63**, 2172-2178 (2003)
138 H. Zheng, W. Li, Y. Wang, Z. Liu, Y. Cai, T. Xie, M. Shi, Z. WangB.J.E.j.o.c. Jiang, Glycogen synthase kinase-3 beta regulates Snail and β-catenin expression during Fas-induced epithelial–mesenchymal transition in gastrointestinal cancer. **49**, 2734-2746 (2013)
139 P. Jézéquel, W. Gouraud, F. Ben Azzouz, C. Guérin-Charbonnel, P.P. Juin, H. LaslaM.J.D. Campone, bc-GenExMiner 4.5: new mining module computes breast cancer differential gene expression analyses. **2021**, (2021)
140 D.S. Chandrashekar, B. Bashel, S.A.H. Balasubramanya, C.J. Creighton, I. Ponce-Rodriguez, B.V. ChakravarthiS.J.N. Varambally, UALCAN: a portal for facilitating tumor subgroup gene expression and survival analyses. **19**, 649-658 (2017)
141 Z. Tang, B. Kang, C. Li, T. ChenZ.J.N.a.r. Zhang, GEPIA2: an enhanced web server for large-scale expression profiling and interactive analysis. **47**, W556-W560 (2019)
142 J. Cidado, H.Y. Wong, D.M. Rosen, A. Cimino-Mathews, J.P. Garay, A.G. Fessler, Z.A. Rasheed, J. Hicks, R.L. CochranS.J.O. Croessmann, Ki-67 is required for maintenance of cancer stem cells but not cell proliferation. **7**, 6281 (2016)
143 H.A. Abbas, D.R. Maccio, S. Coskun, J.G. Jackson, A.L. Hazen, T.M. Sills, M.J. You, K.K. HirschiG.J.C.s.c. Lozano, Mdm2 is required for survival of hematopoietic stem cells/progenitors via dampening of ROS-induced p53 activity. **7**, 606-617 (2010)
144 S. Yin, V.T. Cheryan, L. Xu, A.K. RishiK.B.J.P.o. Reddy, Myc mediates cancer stem-like cells and EMT changes in triple negative breast cancers cells. **12**, e0183578 (2017)
145 W. Li, H. Ma, J. Zhang, L. Zhu, C. WangY.J.S.r. Yang, Unraveling the roles of CD44/CD24 and ALDH1 as cancer stem cell markers in tumorigenesis and metastasis. **7**, 1-15 (2017)

146 R. ShomeS.S.J.C.O. Ghosh, Tweaking EMT and MDR dynamics to constrain triple-negative breast cancer invasiveness by EGFR and Wnt/β-catenin signaling regulation. **44**, 405-422 (2021)
147 X.-L. Qian, Y.-H. Pan, Q.-Y. Huang, Y.-B. Shi, Q.-Y. Huang, Z.-Z. Hu, L.-X.J.O. Xiongtherapy, Caveolin-1: a multifaceted driver of breast cancer progression and its application in clinical treatment. **12**, 1539 (2019)
148 S. Ansieau, G. CollinL.J.F.i.o. Hill, EMT or EMT-promoting transcription factors, where to focus the light? **4**, 353 (2014)
149 J. Yang, P. Antin, G. Berx, C. Blanpain, T. Brabletz, M. Bronner, K. Campbell, A. Cano, J. CasanovaG.J.N.r.M.c.b. Christofori, Guidelines and definitions for research on epithelial–mesenchymal transition. **21**, 341-352 (2020)
150 B. Mansoori, A. Mohammadi, S. Davudian, S. ShirjangB.J.A.p.b. Baradaran, The different mechanisms of cancer drug resistance: a brief review. **7**, 339 (2017)
151 D. TheileP.J.N.-s.s.A.o.P. Wizgall, Acquired ABC-transporter overexpression in cancer cells: transcriptional induction or Darwinian selection? **394**, 1621 (2021)
152 L. Ding, J. Cao, W. Lin, H. Chen, X. Xiong, H. Ao, M. Yu, J. LinQ.J.I.j.o.m.s. Cui, The roles of cyclin-dependent kinases in cell-cycle progression and therapeutic strategies in human breast cancer. **21**, 1960 (2020)
153 X. Xu, M. Zhang, F. XuS.J.M.C. Jiang, Wnt signaling in breast cancer: biological mechanisms, challenges and opportunities. **19**, 1-35 (2020)
154 E. Martin-Orozco, A. Sanchez-Fernandez, I. Ortiz-ParraA.-S.J.F.i.i. Nicolas, WNT signaling in tumors: the way to evade drugs and immunity. **10**, 2854 (2019)
155 J.G. JacksonG.J.O. Lozano, TNBC invasion: downstream of STAT3. **8**, 20517 (2017)
156 J.M. GiltnaneJ.M.J.D.m. Balko, Rationale for targeting the Ras/MAPK pathway in triple-negative breast cancer. **17**, 275-283 (2014)
157 R. FoddeT.J.C.o.i.c.b. Brabletz, Wnt/β-catenin signaling in cancer stemness and malignant behavior. **19**, 150-158 (2007)
158 L. Xu, S. Li, W. Zhou, Z. Kang, Q. Zhang, M. Kamran, J. Xu, D. Liang, C. WangZ.J.O. Hou, p62/SQSTM1 enhances breast cancer stem-like properties by stabilizing MYC mRNA. **36**, 304-317 (2017)
159 S.D. Soysal, S. Muenst, T. Barbie, T. Fleming, F. Gao, G. Spizzo, D. Oertli, C.T. Viehl, E.C. ObermannW.E.J.B.j.o.c. Gillanders, EpCAM expression varies significantly and is differentially associated with prognosis in the luminal B HER2+, basal-like, and HER2 intrinsic subtypes of breast cancer. **108**, 1480-1487 (2013)
160 C.-W. Lin, M.-Y. Liao, W.-W. Lin, Y.-P. Wang, T.-Y. LuH.-C.J.J.o.B.C. Wu, Epithelial cell adhesion molecule regulates tumor initiation and tumorigenesis via activating reprogramming factors and epithelial-mesenchymal transition gene expression in colon cancer. **287**, 39449-39459 (2012)
161 E.L. Gelardi, G. Colombo, F. Picarazzi, D.M. Ferraris, A. Mangione, G. Petrarolo, E. Aronica, M. Rizzi, M. MoriC.J.C. La Motta, A selective competitive inhibitor of aldehyde dehydrogenase 1A3 hinders cancer cell growth, invasiveness and stemness in vitro. **13**, 356 (2021)
162 M. Wienken, A. Dickmanns, A. Nemajerova, D. Kramer, Z. Najafova, M. Weiss, O. Karpiuk, M. Kassem, Y. ZhangG.J.M.c. Lozano, MDM2 associates with polycomb repressor complex 2 and enhances stemness-promoting chromatin modifications independent of p53. **61**, 68-83 (2016)
163 J. Todoric, L. Antonucci, G. Di Caro, N. Li, X. Wu, N.K. Lytle, D. Dhar, S. Banerjee, J.B. FagmanC.D.J.C.c. Browne, Stress-activated NRF2-MDM2 cascade controls neoplastic progression in pancreas. **32**, 824-839. e828 (2017)
164 R. Petruzzelli, D.R. Christensen, K.L. Parry, T. Sanchez-ElsnerF.D.J.P.o. Houghton, HIF-2α regulates NANOG expression in human embryonic stem cells following hypoxia and reoxygenation through the interaction with an Oct-Sox cis regulatory element. **9**, e108309 (2014)
165 V. Damiano, P. Spessotto, G. Vanin, T. Perin, R. Maestro, M.J.F.i.c. Santarosad. biology, The autophagy machinery contributes to E-cadherin turnover in breast cancer. **8**, 545 (2020)
166 X. SunY.J.O.l. Liu, Activation of the Wnt/β-catenin signaling pathway may contribute to cervical cancer pathogenesis via upregulation of Twist. **14**, 4841-4844 (2017)
167 M. Xing, P. Li, X. Wang, J. Li, J. Shi, J. Qin, X. Zhang, Y. Ma, G. FranciaJ.-Y.J.C. Zhang, Overexpression of p62/IMP2 can promote cell migration in hepatocellular carcinoma via activation of the Wnt/β-catenin pathway. **12**, 7 (2020)
168 S. Corrêa, R. Binato, B. Du Rocher, M.T. Castelo-Branco, L. PizzattiE.J.B.c. Abdelhay, Wnt/β-catenin pathway regulates ABCB1 transcription in chronic myeloid leukemia. **12**, 1-11 (2012)

169 J.-l. Qi, J.-r. He, C.-b. Liu, S.-m. Jin, X. Yang, H.-m. Bai, Y.-b.J.G. MaDiseases, SQSTM1/p62 regulate breast cancer progression and metastasis by inducing cell cycle arrest and regulating immune cell infiltration. (2021)
170 T.M. Puvirajesinghe, F. Bertucci, A. Jain, P. Scerbo, E. Belotti, S. Audebert, M. Sebbagh, M. Lopez, A. BrechP.J.N.c. Finetti, Identification of p62/SQSTM1 as a component of non-canonical Wnt VANGL2–JNK signalling in breast cancer. **7**, 1-15 (2016)
171 A. Schwob, E. Teruel, L. Dubuisson, F. Lormières, P. Verlhac, Y.P. Abudu, J. Gauthier, M. Naoumenko, F.-M. Cloarec-UngM.J.S.r. Faure, SQSTM-1/p62 potentiates HTLV-1 Tax-mediated NF-κB activation through its ubiquitin binding function. **9**, 1-17 (2019)
172 I. Joung, H.J. Kim, Y.K.J.B. Kwonb.r. communications, p62 modulates Akt activity via association with PKCζ in neuronal survival and differentiation. **334**, 654-660 (2005)
173 K. Kühn, C. Cott, S. Bohler, S. Aigal, S. Zheng, S. Villringer, A. Imberty, J. ClaudinonW.J.C.d.d. Römer, The interplay of autophagy and β-Catenin signaling regulates differentiation in acute myeloid leukemia. **1**, 1-10 (2015)
174 Y. Shen, X. Li, D. Dong, B. Zhang, Y. XueP.J.A.j.o.c.r. Shang, Transferrin receptor 1 in cancer: a new sight for cancer therapy. **8**, 916 (2018)
175 M.A. Naves, A.E. Graminha, L.C. Vegas, L. Luna-Dulcey, J. Honorato, A.C. Menezes, A.A. BatistaM.R.J.M.p. Cominetti, Transport of the ruthenium complex [Ru (GA)(dppe) 2] PF6 into triple-negative breast cancer cells is facilitated by transferrin receptors. **16**, 1167-1183 (2019)
176 A. GupteR.J.J.o.i.b. Mumper, An investigation into copper catalyzed D-penicillamine oxidation and subsequent hydrogen peroxide generation. **101**, 594-602 (2007)
177 J. Dan Dunn, L. Alvarez, X. ZhangT. Soldati,
178 H. Düßmann, M. Rehm, D. KögelJ.H.J.J.o.c.s. Prehn, Outer mitochondrial membrane permeabilization during apoptosis triggers caspase-independent mitochondrial and caspase-dependent plasma membrane potential depolarization: a single-cell analysis. **116**, 525-536 (2003)
179 S. Li, J. Zhang, H. Yang, C. Wu, X. DangY.J.S.r. Liu, Copper depletion inhibits CoCl 2-induced aggressive phenotype of MCF-7 cells via downregulation of HIF-1 and inhibition of Snail/Twist-mediated epithelial-mesenchymal transition. **5**, 1-17 (2015)
180 W.D. Smith, H.E.J.D.o.t.C. BaconRectum, Experience with a new antibiotic agent as an adjunct to colon surgery. **10**, 322-324 (1967)
181 Y.-R. Liu, L. Liang, J.M. Zhao, Y. Zhang, M. Zhang, W.-L. Zhong, Q. Zhang, J.-J. Wei, M. LiJ.J.O. Yuan, Twist1 confers multidrug resistance in colon cancer through upregulation of ATP-binding cassette transporters. **8**, 52901 (2017)
182 R.W. Robey, K.M. Pluchino, M.D. Hall, A.T. Fojo, S.E. BatesM.M.J.N.R.C. Gottesman, Revisiting the role of ABC transporters in multidrug-resistant cancer. **18**, 452-464 (2018)
183 S. Modok, H.R. MellorR.J.C.o.i.p. Callaghan, Modulation of multidrug resistance efflux pump activity to overcome chemoresistance in cancer. **6**, 350-354 (2006)
184 J. Fares, M.Y. Fares, H.H. Khachfe, H.A. Salhab, Y.J.S.t. Farest. therapy, Molecular principles of metastasis: a hallmark of cancer revisited. **5**, 1-17 (2020)
185 S.K. Golombek, J.-N. May, B. Theek, L. Appold, N. Drude, F. KiesslingT.J.A.d.d.r. Lammers, Tumor targeting via EPR: Strategies to enhance patient responses. **130**, 17-38 (2018)
186 C.E. Byrne, C.E. Astete, M. Vaithiyanathan, A.T. Melvin, M. Moradipour, S.E. Rankin, B.L. Knutson, C.M. SabliovE.C.J.N. Martin, Lignin-graft-PLGA drug-delivery system improves efficacy of MEK1/2 inhibitors in triple-negative breast cancer cell line. **15**, 981-1000 (2020)
187 A.B.J.E.M.i.M.T.U. PaiT.o.M.I.i.t. Clinic, 6. IRON OXIDE NANOPARTICLE FORMULATIONS FOR SUPPLEMENTATION. 157-180 (2019)
188 T. Matsubara, R. Saura, K. HirohataM.J.T.J.o.c.i. Ziff, Inhibition of human endothelial cell proliferation in vitro and neovascularization in vivo by D-penicillamine. **83**, 158-167 (1989)
189 R. ShomeS.S.J.A.A.B.M. Ghosh, Transferrin Coated d-penicillamine–Au-Cu Nanocluster PLGA Nanocomposite Reverses Hypoxia-Induced EMT and MDR of Triple-Negative Breast Cancers. (2021)
190 P.J.T.J.o.c.i. Lipsky, Immunosuppression by D-penicillamine in vitro. Inhibition of human T lymphocyte proliferation by copper-or ceruloplasmin-dependent generation of hydrogen peroxide and protection by monocytes. **73**, 53-65 (1984)
191 E. PanieriM. Santoro, (Nature Publishing Group, 2016),
192 D. Averill-Bates, M. GrondinF.J.C. Ouellet, Activation of apoptosis signaling pathways by reactive oxygen species. **80**, 170 (2018)

193 S.W. LoweA.W.J.C. Lin, Apoptosis in cancer. **21**, 485-495 (2000)
194 Y. Li, L.H. Wang, H.T. Zhang, Y.T. Wang, S. Liu, W.L. Zhou, X.Z. Yuan, T.Y. Li, C.F. Wu, J.Y.J.J.o.c. Yangm. medicine, Disulfiram combined with copper inhibits metastasis and epithelial–mesenchymal transition in hepatocellular carcinoma through the NF-κB and TGF-β pathways. **22**, 439-451 (2018)
195 H. ZhengY.J.O. Kang, Multilayer control of the EMT master regulators. **33**, 1755-1763 (2014)
196 M. Saxena, M.A. Stephens, H. Pathak, A.J.C.d. Rangarajandisease, Transcription factors that mediate epithelial–mesenchymal transition lead to multidrug resistance by upregulating ABC transporters. **2**, e179-e179 (2011)
197 S. Baldari, G. Di Rocco, M.C. Heffern, T.A. Su, C.J. ChangG.J.C. Toietta, Effects of copper chelation on BRAFV600E positive colon carcinoma cells. **11**, 659 (2019)
198 L.J.A.o.t.E.p.i.r.f.T.-b.-i.E.i.v.N. Xie, Law BK, Chytil AM, Brown KA, Aakre ME, Moses HL. **6**, 603-610 (2004)
199 M.L. Turski, D.C. Brady, H.J. Kim, B.-E. Kim, Y. Nose, C.M. Counter, D.R. Winge, D.J.J.M. Thielec. biology, A novel role for copper in Ras/mitogen-activated protein kinase signaling. **32**, 1284-1295 (2012)
200 S. Tanno, S. Tanno, Y. Mitsuuchi, D.A. Altomare, G.-H. XiaoJ.R.J.C.r. Testa, AKT activation up-regulates insulin-like growth factor I receptor expression and promotes invasiveness of human pancreatic cancer cells. **61**, 589-593 (2001)
201 A. Marra, D. Trapani, G. Viale, C. CriscitielloG.J.N.B.C. Curigliano, Practical classification of triple-negative breast cancer: intratumoral heterogeneity, mechanisms of drug resistance, and novel therapies. **6**, 1-16 (2020)
202 K.J. Chavez, S.V. GarimellaS.J.B.d. Lipkowitz, Triple negative breast cancer cell lines: one tool in the search for better treatment of triple negative breast cancer. **32**, 35 (2010)
203 N. Dey, B.G. Barwick, C.S. Moreno, M. Ordanic-Kodani, Z. Chen, G. Oprea-Ilies, W. Tang, C. Catzavelos, K.F. KerstannG.W.J.B.c. Sledge, Wnt signaling in triple negative breast cancer is associated with metastasis. **13**, 1-15 (2013)
204 M.K. Wendt, N. Balanis, C.R. CarlinW.P.J.J.-s. Schiemann, STAT3 and epithelial–mesenchymal transitions in carcinomas. **3**, e28975 (2014)
205 E. Valli, L. Lerra, K. Kimpton, F. Saletta, F.M. Giorgi, D. Mercatelli, J.R. Rouaen, S. Shen, J.E. MurrayA.J.C.r. Ahmed-Cox, Intratumoral Copper Modulates PD-L1 Expression and Influences Tumor Immune Evasion. **80**, 4129-4144 (2020)

Publications and Conferences

Journal Publications:

From Thesis Work-

1. Shome, R., Ghosh, S.S. Tweaking EMT and MDR dynamics to constrain triple-negative breast cancer invasiveness by EGFR and Wnt/β-catenin signaling regulation. **Cellular Oncology**, 44, 405–422 (2021). https://doi.org/10.1007/s13402-020-00576-8

2. Shome, R., Ghosh, S.S. Transferrin Coated D-penicillamine-Au-Cu Nanocluster PLGA Nanocomposite Reverses Hypoxia-Induced EMT and MDR of Triple-Negative Breast Cancers. **ACS Applied Bio Materials**, 4, 6, 5033–5048 (2021). https://doi.org/10.1021/acsabm.1c00296

3. Shome, R., Ghosh, S.S. Regulation of EMT and MDR dynamics by modulation of SQSTM1 and Wnt/β-catenin signaling to constrain invasiveness in triple-negative breast cancer. (Manuscript Communicated)

4. Shome, R., Ghosh, S.S. SQSTM1/P62 at the Crossroads of Autophagy and EMT. (Manuscript under preparation)

From Collaborative Work-

1. Selvarajan, V.; Bidkar, A. P.; **Shome, R**.; Banerjee, A.; Chaubey, N.; Ghosh, S. S.; Sanpui, P. Studying in vitro phagocytosis of apoptotic cancer cells by recombinant GMCSF-treated RAW 264.7 macrophages. **International Journal of Biological Macromolecules** 2017, 102, 1138–1145 DOI: 10.1016/j.ijbiomac.2017.05.003.

2. Ghosh S, Pal S, Rajamanickam S, **Shome R**, Mohanta PR, Ghosh SS, et al. Access to Multifunctional AEEgens via Ru(II)-Catalyzed Quinoxaline-Directed Oxidative Annulation. **ACS Omega**. 2019;4(3):5565-77.

3. Arora N, **Shome R**, Ghosh SS, et al. Deciphering Therapeutic Potential of PEgylated Recombinant PTEN-Silver Nanoclusters Ensemble on 3D Spheroids. **Molecular Biology Reports**, 2019; 46, 5103–5112(2019)

4. Prasad, N. K.; **Shome, R**.; Biswas, G.; Ghosh, S. S.; Dalal, A., Discerning the self-healing, shear-thinning characteristics and therapeutic efficacy of hydrogel drug carriers migrating through constricted microchannel resembling blood microcapillary. **Colloids and Surfaces A: Physicochemical and Engineering Aspects** 2021, 626, 127070.

5. Prasad, N. K.; **Shome, R**.; Biswas, G.; Ghosh, S. S.; Dalal, A., Transport behaviour of commercial anti-cancer drug protein-bound Paclitaxel in blood capillary sized microchannel. (Manuscript Communicated).

6. Khandelia, T.; Ghosh, S.; Panigrahia, P.; Patel, B.K.; **Shome, R**.; Ghosh, S.S.; Copper(I) Mediated Dehydrogenative Cascade Annulation via Dual C-H/C-H Activation: Access to Biocompatible Benzo[α]carbazolic AEEgens. **The Journal of Organic Chemistry** 2021, 86, 23, 16948–16964

7. Roy, S.K.; **Shome, R**.; Ghosh, S.S.; Jana, C.K.; Selective N-Terminal Proline Modification of Peptides via Amino-Oxazole Synthesis and Application in Cell Imaging. (Manuscript Communicated).

Conference Presentations:

1. **Poster presentation by Shome, R**. **"**Transferrin Coated d-penicillamine–Au-Cu Nanocluster PLGA Nanocomposite Reverses Hypoxia-Induced EMT and MDR of Triple-Negative Breast Cancers", **National Conference on "Chemistry of Chalcogenides"** (NC3-2021) organized by Department of Applied Chemistry, Defense Institute of Advanced Technology, Pune-411025, India. [***Received Best Poster Award***].

Appendix

Buffers and Their Composition:

4 X protein loading dye (for 10 ml)	2 ml 1M Tris-HCl (pH 6.8), 0.8 g SDS, 4.0 ml 100 % glycerol, 0.4 ml 14.7 M β- mercaptoethanol, 8 mg bromophenol blue in water
6 X DNA loading dye	0.25 (%) (w/v) bromophenol blue, 0.25 % (w/v) xylene cyanol FF, 30 % (v/v) glycerol in water
30% Acrylamide solution	29.2 % (w/w) Acrylamide, 0.8 % (w/w) N, N' - methylenebisacrylamide.
Blocking buffer for Western blot	4 % (w/v) BSA in PBST/ TBST
Gel running buffer(10x)	250 mM Tris base, 1.92 M glycine, and 1 % SDS
Phosphate buffer saline	137 mM NaCl, 2.68 mM KCl, 7.98 mM Na_2HPO_4, 1.4 mM KH_2PO_4, pH 7.4
Tris buffered saline	Tris-HCl (50Mm), NaCl (150 mM), pH 7.5
Tris buffered saline Tween -20 (TBST)	Tris-HCl (50Mm), NaCl (150 mM), Tween 20 (0.1% v/v) pH 7.5
Tris acetate EDTA(TAE) 50 X, (100 ml)	24.2 g Tris base, 5.71 ml of glacial acetic acid, 10 ml of 0.5 EDTA (pH 8)
Towbin Buffer (5X)	25 mM Tris base, 192 mM glycine, and 20 % methanol